



City Research Online

City, University of London Institutional Repository

Citation: Quadir, A. (2017). Finite element characterisation of plasmonic waveguides in terahertz and optical frequencies. (Unpublished Doctoral thesis, City, University of London)

This is the accepted version of the paper.

This version of the publication may differ from the final published version.

Permanent repository link: <https://openaccess.city.ac.uk/id/eprint/17568/>

Link to published version:

Copyright: City Research Online aims to make research outputs of City, University of London available to a wider audience. Copyright and Moral Rights remain with the author(s) and/or copyright holders. URLs from City Research Online may be freely distributed and linked to.

Reuse: Copies of full items can be used for personal research or study, educational, or not-for-profit purposes without prior permission or charge. Provided that the authors, title and full bibliographic details are credited, a hyperlink and/or URL is given for the original metadata page and the content is not changed in any way.

Finite Element Characterisation of Plasmonic Waveguides in Terahertz and Optical Frequencies

by

Anita QUADIR



CITY UNIVERSITY
LONDON

*A thesis submitted in fulfilment of the requirements
for the degree of Doctor of Philosophy*

in the

School of Mathematics, Computer Science and Engineering

City University London

Northampton Square, London EC1V 0HB

May 2, 2017

Declaration of Authorship

I, Anita Quadir, declare that this thesis titled, “Finite Element Characterisation of Plasmonic Waveguides in Terahertz and Optical Frequencies” and the work presented in it are my own. I confirm that:

- This work was done wholly or mainly while in candidature for a research degree at this University.
- Where any part of this thesis has previously been submitted for a degree or any other qualification at this University or any other institution, this has been clearly stated.
- Where I have consulted the published work of others, this is always clearly attributed.
- Where I have quoted from the work of others, the source is always given. With the exception of such quotations, this thesis is entirely my own work.
- I have acknowledged all main sources of help.

Signed:

Date:

Acknowledgements

First and foremost I would like to thank almighty Allah for giving me the courage and patience to undertake and complete this work.

I would like to thank my husband Dr. S. M Raiyan Kabir who has always been there in the most difficult times and I am extremely grateful to him for his continuous support and encouragement. I would like to dedicate this thesis to my parents, my husband, my sister, my in-laws and my beloved son Nihan for their love and support throughout my life and for constantly encouraging me to pursue excellence.

I am immensely indebted to Prof. B.M.A. Rahman for being an excellent and patient supervisor and for providing continuous support and encouragement over the years. I would also like to thank Prof. K.T.V. Grattan for his valuable advice and support throughout this research.

Several people have contributed in various ways and without their support it would not have been possible to complete this thesis. Most notable amongst them are my friends Mr Mohammed Moseur Rahman, Mrs Farhanaz Rahman and Mr. Md. Enayetur Rahman. I would also like to sincerely thank all my colleagues at the Photonics Research Group for maintaining a friendly and joyful work atmosphere...

Abstract

In recent years plasmonic devices have become an interesting area of research due to the sub-wavelength confinement and propagation of radiation, allowing the design of very compact structures. Compact structures are necessary to make smaller integrated optical circuits. Due to the use of metals, plasmonic guides usually show more losses compared to the conventional dielectric guides. Therefore, plasmonic waveguides are not normally used for long distance transmission. However, they are promising for inter-chip or intra-chip communication and also have seen a lot of sensor applications.

There has been considerable interest in exploiting the frequency bands in the terahertz regime to open up new frontiers of research across a diverse range of applications. An array of opportunities for creating novel technologies using this frequency band had remained largely unexplored and undeveloped for a considerable period of time due to the lack of suitable sources, as well as lack of guiding and detecting devices.

This thesis describes the design, analysis and optimisation of plasmonic devices in optical and terahertz frequencies. A fully vectorial \mathbf{H} -field based finite element method has been used in the research reported in this thesis to reveal the modal characteristics of different plasmonic structures.

A six layer planar contra-directional nano-coupler has been analysed at optical frequency. Three different modes of propagation were considered to study the characteristics of different properties of the structure, including the coupling length. A design approach has been proposed to make the coupler low loss as well as smaller in length.

For the terahertz plasmonics, a rectangular metallic hollow core guide was considered at terahertz frequency. Several modes were considered for the modal analysis of the structure. Modal analysis was performed by changing metal, introducing different dielectric coating in the hollow core, changing the thickness of the metal and dielectric layers and changing the dimensions of the guide. A dispersion analysis was also performed. The criteria for designing very low loss, compact and low dispersion guide have been presented for the structure at the end of the study.

Contents

Declaration of Authorship	i
Acknowledgements	ii
Abstract	iii
Contents	iv
List of Figures	viii
List of Abbreviations	xvi
Physical Constants	xviii
List of Symbols	xix
1 Introduction	1
1.1 History of Lightwave Technology	1
1.2 Dielectric Guidance	3
1.2.1 Snell’s Law of Refraction	4
1.2.2 Critical Angle and Total Internal Reflection	7
1.2.3 Dielectric Guidance	9
1.3 Surface Plasmon Polariton	11
1.3.1 History	11
1.3.2 Applications	13
Sensor	13
Waveguide	14
Sub Wavelength Optics	16
1.4 Terahertz	16
1.4.1 Application of Terahertz Radiation	18
Biomedical Application of Terahertz	18
Application in Security Scanning	19
Application in Spectroscopy	19
1.4.2 Terahertz Detectors	21

1.4.3	THz Sources	22
	Solid State THz Sources	22
1.5	Surface Plasmon Polaritons at THz Frequencies	25
1.6	Aims and Objectives of the work	26
1.7	Presentation of the thesis	27
2	Numerical Methods	29
2.1	Introduction	29
2.2	Analytical approximation solutions	30
	2.2.1 Marcatili's Method	30
	2.2.2 The Effective Index Method	30
2.3	Numerical Approximation Solutions	31
	2.3.1 The Variational Method	32
	2.3.2 The Finite Difference Method	32
	2.3.3 Point Matching Method	33
	2.3.4 The Boundary Element Method	34
	2.3.5 The Mode Matching or Equivalent Network Method	35
	2.3.6 The Spectral Index Method	36
	2.3.7 The Method of Lines	37
	2.3.8 The Beam Propagation Method	38
	2.3.9 The Finite Element Method	39
	2.3.10 Time Domain Analysis	40
	Finite Difference Time Domain Method	40
	Finite Element Based Techniques	41
	2.3.11 Frequency domain over Time domain	42
2.4	Theoretical Background	42
	2.4.1 Basic Equations	44
2.5	Variational Formulations	48
	2.5.1 Scalar Approximation	48
	2.5.2 Vector Approximation	49
	2.5.3 Natural Boundary Conditions	50
2.6	FEM Formulation	51
	2.6.1 Domain Discretisation	51
	2.6.2 Shape Functions	53
	2.6.3 Global and Element Matrices	57
	2.6.4 Spurious Solutions	61
	2.6.5 Mesh Resolution and Convergence	62
2.7	Summary	63

3	Surface Plasmonic Waveguides	64
3.1	Introduction	64
3.2	Surface Plasmon Polariton	65
3.3	Wave Propagation in metals	66
3.3.1	SPPs at the Metal- Dielectric Interface	68
3.3.2	Evaluation of performance	71
3.4	Simulation Results: Single metal-dielectric interface	72
3.5	Three Layer Planar Waveguides	73
3.5.1	Surface Plasmon modes in three layer planar structures	73
3.5.2	Insulator-Metal-Insulator Structure	75
3.5.3	Metal-Insulator-Metal Structure	80
3.6	Six Layer Planar Optical Waveguide	85
3.6.1	Variation of Separation	90
	SPSM ₂ mode	90
	SPSM ₁ mode	95
	SPSM ₀ mode	99
3.6.2	Coupling length calculation	103
3.6.3	Variation of core thickness	105
	SPSM ₂ mode	105
	SPSM ₀ mode	110
3.7	Summary	114
4	Hybrid Plasmonic Waveguide at Optical Frequencies	116
4.1	Introduction	116
4.2	Hybrid Plasmonic Waveguide	117
4.3	The TM Mode	118
4.3.1	Variation of Spacer Thickness h	120
4.3.2	Variation of Metal thickness t	123
4.4	The TE Mode	123
4.4.1	Variation of h	125
4.4.2	Variation of t	126
4.5	Benchmarking	128
4.6	Summary	133
5	Rectangular Plasmonic Waveguide in THz	134
5.1	Introduction	134
5.2	Dielectric coated Rectangular Waveguide	135
5.2.1	Effect of Change in Guide Height	138

5.2.2	Effect of Change in Guide Width	140
5.2.3	Effect of Change in Metal Thickness	141
5.3	Dielectric Coated Design	142
5.3.1	Choice of Dielectric	142
5.3.2	Effect of Teflon Thickness	143
5.3.3	Polystyrene vs. Teflon	148
5.3.4	Effect of changing Metal	148
5.3.5	Effect of Metal Thickness	149
5.3.6	Effect of Bending	150
	Bending Characteristics of H_{10}^x mode	151
	Bending Characteristics of H_{12}^x mode	153
	Bending Loss Comparison between H_{10}^x and H_{12}^x modes	157
5.4	Analysis of bigger rectangular guides	159
5.4.1	Effect of Dimension	159
5.5	Dispersion Characteristics of the Rectangular Guides	168
5.5.1	Effect of Frequency on Loss	170
5.6	Selective coupling to the H_{12}^x mode	174
5.7	Summary	174
6	Discussion and Future Works	175
6.1	Proposals for future work	179
A	Evaluation of Element Matrices	180
B	Calculation of Confinement Factor	193
C	List of Associated Publications	197
	Bibliography	199

List of Figures

1.1	Refraction between two media with refractive indices n_1 and n_2 , where $n_2 > n_1$	5
1.2	Refraction of wave at an air-Silica interface from a point source radiating from the air layer	5
1.3	Refraction of wave on an air-Silicon interface from a point source radiating from the air layer	6
1.4	Refraction, critical angle and total internal reflection of wave on an air-Silica interface from a point source radiating from the Silica layer	7
1.5	Critical Angle and Total internal reflection, where $n_2 > n_1$	8
1.6	Total internal reflection of wave on an air-Silicon interface from a point source radiating from the Silicon layer	9
1.7	Dielectric guidance with total internal reflection	9
1.8	Wave guiding in Air-Silicon-air waveguide with core thickness $0.2 \mu\text{m}$ with a point source of $1.55 \mu\text{m}$ wavelength	10
1.9	THz-emission power as a function of frequency. Solid lines are for the conventional THz sources [80]	22
2.1	Arbitrarily shaped optical waveguide, divided into arbitrary sub-domains, each having different type of material.	43
2.2	Boundary between two media of refractive indices n_1 and n_2 , where \mathbf{n} is the unit vector normal to the interface.	46
2.3	Finite Elements in two-dimensions	52
2.4	Finite element discretisation of a waveguide with triangular elements.	53
2.5	Pascal's triangle for complete polynomials in two dimensions.	54
2.6	Representation of a first order triangular element.	55
3.1	Schematic Diagram of the interface between two media	68

3.2	Variation of the normalized H_x field profile of the TM_0 mode with the transverse direction for two values of the refractive index of the dielectric a) for air with index $n_d = 1$ and b) for Silica with index $n_d = 1.44568$	72
3.3	Schematic setup for the IMI Structure with SiO_2 and Silver (Ag)	75
3.4	Even and odd modes for the SiO_2 - Ag - SiO_2 structure with a core thickness $t = 0.07\mu m$	76
3.5	Even and odd modes for the SiO_2 - Ag - SiO_2 structure for core thicknesses $0.045\mu m, 0.07\mu m, 0.2\mu m$ and $0.3\mu m$	77
3.6	Variation of effective index of the even and odd coupled modes for symmetric IMI structure	78
3.7	Variation of modal loss versus metal thickness for the first two supermodes for a symmetric IMI structure	79
3.8	Schematic setup for the MIM Structure with SiO_2 -Glass and Silver (Ag)	80
3.9	Even and odd modes for the Ag - SiO_2 - Ag structure with a core thickness $t = 0.07\mu m$	81
3.10	Even and odd modes for the Ag - SiO_2 - Ag structure for core thicknesses $0.045\mu m$ (even only), $0.06\mu m$ (odd only), $0.07\mu m, 0.2\mu m$ and $0.3\mu m$	82
3.11	Variation of effective index of the even and odd coupled modes for symmetric MIM structure	83
3.12	Variation of modal loss versus the dielectric thickness of the even and odd coupled modes for symmetric MIM structure	84
3.13	6 layer IMIMIM structure with Glass, Ag and SiO_2	86
3.14	$SPSM_2$ mode for the six layer structure for $t_{Ag} = t_{SiO_2} = 15nm$ and $s_{Ag} = s_{Glass} = 20nm$	87
3.15	H_x, E_y and S_z profiles of the $SPSM_1$ mode for $t_{Ag} = t_{SiO_2} = 15nm$ and $s_{Ag} = s_{Glass} = 20nm$	88
3.16	H_x, E_y and S_z profiles of the $SPSM_0$ mode for $t_{Ag} = t_{SiO_2} = 15nm$ and $s_{Ag} = s_{Glass} = 20nm$	89
3.17	Effect of variation of separation between the cores shown using the magnetic & electric fields and the Poynting vector profiles for different values of separation (s) for the $SPSM_2$ mode where $t_{Ag} = t_{SiO_2} = 25nm$	91

3.18	Variation of the real part of the Effective index of the $SPSM_2$ mode when the separation between the cores are varied from 40 nm to 90 nm	92
3.19	Loss variation when the separation between the cores are varied from 40 nm to 90 nm for the $SPSM_2$ mode	94
3.20	Power confinement in different layers when the separation between the cores are varied for the $SPSM_2$ mode	94
3.21	Effect of variation of separation between the cores shown using the magnetic & electric fields and the Poynting vector profiles for different values of separation (s) for the $SPSM_1$ mode where $t_{Ag} = t_{SiO_2} = 25\text{ nm}$	96
3.22	Variation of the real part of effective index for the $SPSM_1$ mode when the separation between the cores is varied	97
3.23	Loss variation when the separation between the cores are varied from 40 nm to 150 nm for the $SPSM_1$ mode	98
3.24	Power Confinement in different layers of the planar guide when the separation between the cores is varied from 40 nm to 150 nm for the $SPSM_1$ mode	98
3.25	Effect of variation of separation between the cores shown using the magnetic & electric fields and the Poynting vector profiles for different values of separation (s) for the $SPSM_0$ mode where $t_{Ag} = t_{SiO_2} = 25\text{ nm}$	100
3.26	Variation of the real part of effective index for the $SPSM_0$ mode when the separation between the cores is varied from 40 nm to 150 nm	101
3.27	Loss variation when the separation between the cores is varied from 40 nm to 150 nm for the $SPSM_0$ mode	102
3.28	Power confinement in different layers when the separation between the cores is varied for the $SPSM_0$ mode	102
3.29	Variation of Coupling Length as a function of the separation between the cores (s)	104
3.30	Variation of the real part of effective index for the $SPSM_2$ mode when the core thicknesses are varied from 20 nm to 32 nm	106
3.31	Variation of loss when the core thicknesses are varied from 20 nm to 32 nm for the $SPSM_2$ mode	106

3.32	Effect of variation of thickness of the cores shown using the magnetic & electric fields and the Poynting vector profiles for different values of core thickness (t) for the $SPSM_2$ mode where $s_{Ag} = s_{Glass} = 20 \text{ nm}$	108
3.33	Variation of power confinement factor when the core thicknesses are varied from 20 nm to 32 nm for the $SPSM_2$ mode	109
3.34	Variation of real part of the effective index when the core thicknesses are varied from 20 nm to 32 nm keeping the total separation constant at 40 nm for the $SPSM_0$ mode	110
3.35	Effect of variation of thickness of the cores shown using the magnetic & electric fields and the Poynting vector profiles for different values of core thickness (t) for the $SPSM_0$ mode where $s_{Ag} = s_{Glass} = 20 \text{ nm}$	112
3.36	Loss variation for the $SPSM_0$ mode when the core thicknesses are varied from 20 nm to 32 nm keeping the total separation constant at 40 nm	113
3.37	Power confinement variation for the $SPSM_0$ mode when the core thicknesses are varied from 20 nm to 32 nm keeping the total separation constant at 40 nm	113
4.1	Schematic cross-sectional diagram of the hybrid plasmonic waveguide	117
4.2	(a) Pure plasmonic and (b) pure dielectric H_x field profiles of the TM mode.	119
4.3	(a) 3-D Contour profile, (b) field through the core, (c) field through the spacer and (d) field parallel to the y-axis through the centre of the guide of the H_x field for the TM mode of the hybrid waveguide.	119
4.4	Variation of the real part of the effective index of the TM mode as a function of the spacer thickness h for three different core thicknesses (d)	121
4.5	Variation of propagation loss of the TM mode as a function of the spacer thickness h for three different core thicknesses (d)	121
4.6	Normalized (a) H_x and (c) E_y field profiles of the TM mode for spacer thickness $h = 90 \text{ nm}$ and core thickness $d = 100 \text{ nm}$. (b) and (d) shows the vertical cross-sections of the fields, respectively.	122
4.7	Variation of power confinement in different layers of the hybrid waveguide for the TM mode as a function of the spacer thickness h for a core thicknesses $d = 100 \text{ nm}$	123

4.8	Variation of the real part of the effective index of the TM mode as a function of the metal thickness t for core and spacer thicknesses of $d = 150 \text{ nm}$ and $h = 90 \text{ nm}$ respectively	124
4.9	Variation of modal loss of the TM mode as a function of the metal thickness t for core and spacer thicknesses of $d = 150 \text{ nm}$ and $h = 90 \text{ nm}$ respectively	124
4.10	Normalised (a) H_y and (c) E_x field profiles of the TE mode for spacer thickness $h = 90 \text{ nm}$ and core thickness $d = 150 \text{ nm}$. (b) and (d) shows the vertical cross-sections of the fields, respectively.	125
4.11	Variation of the real part of the effective index of the TE mode as a function of the spacer thickness h for two different core thicknesses (d)	126
4.12	Variation of propagation loss of the TE mode as a function of the spacer thickness h for two different core thicknesses (d)	127
4.13	Variation of power confinement in different layers for the TE mode as a function of the spacer thickness h for a core thickness $d = 150 \text{ nm}$	127
4.14	Variation of the real part of the effective index of the TE mode as a function of the metal thickness t for core and spacer thicknesses of $d = 150 \text{ nm}$ and $h = 90 \text{ nm}$ respectively	128
4.15	Variation of propagation loss of the TE mode as a function of the metal thickness t for core and spacer thicknesses of $d = 150 \text{ nm}$ and $h = 90 \text{ nm}$ respectively	129
4.16	Comparison of variation of the real part of the effective index of the TM mode as a function of the spacer thickness h for three different core thicknesses (d)	130
4.17	Comparison of variation of propagation distance of the TM mode as a function of the spacer thickness h for three different core thicknesses (d)	131
4.18	Variation of propagation distance of the TM mode of the hybrid waveguide as a function of the spacer thickness h for a core thickness of $d = 200 \text{ nm}$ for different values of mesh densities compared with that done in [212]	131
4.19	Variation of propagation distance of the TM mode of the hybrid waveguide as a function of the total number of mesh elements at several values of the spacer thickness h for a core thickness of $d = 200 \text{ nm}$	132

4.20	Comparison of variation of the real part of the effective index of the TE mode as a function of the spacer thickness h for two different core thicknesses (d)	132
4.21	Comparison of variation of propagation distance of the TE mode as a function of the spacer thickness h for two different core thicknesses (d)	133
5.1	Schematic diagram of the hollow core rectangular waveguide with a dielectric coating inside the air core where W is the guide width, H is the height of the guide, t_m is the metal thickness and t_d is the thickness of the dielectric coating.	136
5.2	H_{10}^x field profile along (a) the horizontal and (b) the vertical directions, respectively in the hollow core rectangular waveguide with $W = 1.0 \text{ mm}$, $H = 0.6 \text{ mm}$, $t_m = 0.7 \text{ }\mu\text{m}$ and $t_d = 0$	137
5.3	Real part of effective index of all the five modes as a function of height at $W = 1.0 \text{ mm}$, $t_m = 0.7 \text{ }\mu\text{m}$ and $t_d = 0$	138
5.4	Loss of all the five modes as a function of height at $W = 1.0 \text{ mm}$, $t_m = 0.7 \text{ }\mu\text{m}$ and $t_d = 0$	139
5.5	Real part of effective index of all the five modes as a function of guide width at $H = 0.6 \text{ mm}$, $t_m = 0.7 \text{ }\mu\text{m}$ and $t_d = 0$	140
5.6	Loss of all the five modes as a function of guide width at $H = 0.6 \text{ mm}$, $t_m = 0.7 \text{ }\mu\text{m}$ and $t_d = 0$	141
5.7	Loss of all the five modes as a function of metal thickness t_m at $W = 1.0 \text{ mm}$, $H = 0.6 \text{ mm}$, and $t_d = 0$	142
5.8	n_{eff} and loss of the H_{10}^x mode as a function of Teflon thickness at $W = 1.0 \text{ mm}$, $H = 0.6 \text{ mm}$ and $t_m = 0.7 \text{ }\mu\text{m}$	143
5.9	a) Normalized amplitude of the mode profile taken at the centre of the profile in the vertical direction as a function of Teflon thickness for the H_{10}^x mode when $W = 1.0 \text{ mm}$, $H = 0.6 \text{ mm}$ and $t_m = 0.7 \text{ }\mu\text{m}$	144
5.10	Power confinement factors in air, in Teflon (Γ_d) and in metal (Γ_m) as a function of Teflon thickness for the H_{10}^x mode when $W = 1.0 \text{ mm}$, $H = 0.6 \text{ mm}$ and $t_m = 0.7 \text{ }\mu\text{m}$	145
5.11	The normalized H^x field profiles of the H_{12}^x mode along the vertical direction for two different Teflon thicknesses, a) at $t_d = 0 \text{ }\mu\text{m}$ b) at $t_d = 21 \text{ }\mu\text{m}$ when $W = 1.0 \text{ mm}$, $H = 0.6 \text{ mm}$ and $t_m = 0.7 \text{ }\mu\text{m}$	146
5.12	n_{eff} and loss of the H_{12}^x mode as a function of Teflon thickness at $W = 1.0 \text{ mm}$, $H = 0.6 \text{ mm}$ and $t_m = 0.7 \text{ }\mu\text{m}$	147

5.13	Variation of the total Loss, loss in metal and in Teflon for the H_{12}^x mode as a function of Teflon thickness for $W = 1.0 \text{ mm}$, $H = 0.6 \text{ mm}$ and $t_m = 0.7 \text{ }\mu\text{m}$	148
5.14	Comparison of loss characteristics of the H_{12}^x mode for two dielectric coatings (Polystyrene and Teflon) as a function of the dielectric thickness t_d at a metal thickness $t_m = 0.7 \text{ }\mu\text{m}$ when $W = 1.0 \text{ mm}$ and $H = 0.6 \text{ mm}$	149
5.15	Loss of the H_{12}^x mode as a function of Teflon thickness t_d at a metal thickness $t_m = 0.7 \text{ }\mu\text{m}$, $W = 1.0 \text{ mm}$ and $H = 0.6 \text{ mm}$	150
5.16	Loss of the H_{12}^x mode as a function of metal thickness t_m when the Teflon thickness $t_d = 18 \text{ }\mu\text{m}$, $W = 1.0 \text{ mm}$ and $H = 0.6 \text{ mm}$	151
5.17	Contour field profile and the normalized field profile in the vertical (y) direction of the H_{10}^x mode for bending radius a) and b) $R = 1000 \text{ mm}$, c) and d) $R = 500 \text{ mm}$ and e) and f) $R = 150 \text{ mm}$ respectively	152
5.18	Variation of the real part of effective index of the H_{10}^x mode as a function of bending radius R	153
5.19	Variation of total loss of the H_{10}^x mode as a function of bending radius R	154
5.20	Contour field profile and the normalized field profile in the vertical (y) direction of the H_{12}^x mode for bending radius of a) and b) $R = 1000 \text{ mm}$, c) and d) $R = 100 \text{ mm}$, e) and f) $R = 50 \text{ mm}$ and g) and h) $R = 10 \text{ mm}$ respectively	155
5.21	Variation of the real part of effective index of the H_{12}^x mode as a function of bending radius R	156
5.22	Power confinement factors in air (Γ_a), in Teflon (Γ_d) and in metal (Γ_m) as a function of bending radius R for the H_{12}^x mode when $W = 1.0 \text{ mm}$, $H = 0.6 \text{ mm}$, $t_d = 18 \text{ }\mu\text{m}$ and $t_m = 2.9 \text{ }\mu\text{m}$	156
5.23	Variation of total loss and bending loss of the H_{12}^x mode as a function of bending radius R	158
5.24	Comparison of bending loss from bending radius 150 mm to 1000 mm for H_{10}^x and H_{12}^x modes	158
5.25	Variation of loss for $2.5 \text{ mm} \times 1.25 \text{ mm}$ guide with varying dielectric thickness. The inset shows a zoomed in view of the curve for a range of $7.0 \text{ }\mu\text{m}$ to $27 \text{ }\mu\text{m}$	160

5.26	H_x field of the H_{12}^x mode of the $2.5\text{ mm} \times 1.25\text{ mm}$ guide for dielectric thicknesses of (a) $25\ \mu\text{m}$, (b) $28\ \mu\text{m}$, (c) $28.8\ \mu\text{m}$ and (d) $29\ \mu\text{m}$	161
5.27	Line plots of the H_x field of the H_{12}^x mode (a) horizontal cross section with no Teflon layer, (b) vertical cross section with no Teflon layer, (c) horizontal cross section with $11.6\ \mu\text{m}$ Teflon thickness, (d) vertical cross section with $11.6\ \mu\text{m}$ Teflon thickness, (e) horizontal cross section with $20\ \mu\text{m}$ Teflon thickness, (f) vertical cross section with $20\ \mu\text{m}$ Teflon thickness	163
5.28	Line plots of H_{12}^x field for Teflon thickness (a), (b) $25\ \mu\text{m}$, (c), (d) $27\ \mu\text{m}$, (e), (f) $28.8\ \mu\text{m}$ and (g), (h) $28.9\ \mu\text{m}$. Among these plots a), c), e), g) show the line plots along the horizontal direction and b), d), f), h) show the line plots along the vertical direction	164
5.29	Loss characteristics of guides from $2.0\text{ mm} \times 1.0\text{ mm}$ to $2.9\text{ mm} \times 1.45\text{ mm}$	165
5.30	Dispersion curves for $1.0\text{ mm} \times 0.6\text{ mm}$ rectangular guide (red dotted line) and the $2.5\text{ mm} \times 1.25\text{ mm}$ rectangular guide (green solid line).	169
5.31	Dispersion curves for $1.0\text{ mm} \times 0.6\text{ mm}$ rectangular guide (red dotted line), the $2.5\text{ mm} \times 1.25\text{ mm}$ rectangular guide (green solid line) and the $2.0\text{ mm} \times 1.0\text{ mm}$ rectangular guide (purple dashed line). The inset shows a closer look of the dispersion characteristics of the $2.0\text{ mm} \times 1.0\text{ mm}$ rectangular guide	169
5.32	Loss of the optimal $2.5\text{ mm} \times 1.25\text{ mm}$ guide for the frequency band 2.0 THz to 3.0 THz	171
5.33	Contour field profile along with the vertical and horizontal cross-sections of the H_{12}^x and the H_{21}^y modes	172
5.34	Real part of effective indices of the H_{12}^x and the H_{21}^y modes of the optimal $2.5\text{ mm} \times 1.25\text{ mm}$ guide for the frequency band 2.0 THz to 3.0 THz	173
5.35	Loss comparison of the H_{12}^x and the H_{21}^y modes of the optimal $2.5\text{ mm} \times 1.25\text{ mm}$ guide for the frequency band 2.0 THz to 3.0 THz	173

List of Abbreviations

IOC	I ntegrated O ptical C ircuits
IEC	I ntegrated E lectronic C ircuits
TIR	T otal I nternal R eflection
SP	S urface P lasmon
SPP	S urface P lasmon P olariton
SPR	S urface P lasmon R esonance
SERS	S urface E nhanced R aman S cattering
EM	E lectro M agnetic
TM	T ransverse M agnetic
TE	T ransverse E lectric
THz	T erahertz
TDS	T ime D omain S pectroscopy
THz-TDS	T era H ertz T ime D omain S pectroscopy
SBD	S chottky B arrier D iode
GHz	G igahertz
QCL	Q uantum C ascade L aser
RAM	R ay A pproximation M ethod
WKB	W entzel K ramers B rillouin
ENM	E quivalent N etwork M ethod
MM	M arcatili's M ethod
EIM	E ffective I ndex M ethod
VM	V ariational M ethod
FEM	F inite E lement M ethod
FDM	F inite D ifference M ethod
MAM	M ultilayer A pproximation M ethod
BEM	B oundary E lement M ethod
PMM	P oint M atching M ethod
MMM	M ode M atching M ethod
SIM	S pectral I ndex M ethod
MOL	M ethod O f L ines
BPM	B eam P ropagation M ethod

FDTD	Finite Difference Time Domain
FFT	Fast Fourier Transform
SPSM	Surface Plasmon Supermode
IMI	Insulator Metal Insulator
MIM	Metal Insulator Metal
IMIMIM	Insulator Metal Insulator Metal Insulator Metal
CMOS	Complementary Metal Oxide Semiconductor

Physical Constants

Speed of Light $c = 2.997\,924\,58 \times 10^8 \text{ m/s}$

Permittivity of the vacuum $\epsilon_0 = 8.854 \times 10^{-12} \text{ F/m}$

Permeability of the vacuum $\mu_0 = 4\pi \times 10^{-7} \text{ H/m}$

List of Symbols

n	Refractive index	
H	Magnetic field intensity	A/m
E	Electric field intensity	V/m
n_r	Real part of complex refractive index	
k	Wave number	rad/m
D	Electric flux density	C/m ²
B	Magnetic flux density	T
J	Current density	
λ	Wavelength	m
ω	angular frequency	rad
ϵ	Dielectric permittivity	
μ	Dielectric permeability	
ϵ_r	Relative dielectric permittivity of a medium	
μ_r	Relative dielectric permeability of a medium	
ϵ'	Real part of complex dielectric permittivity	
ϵ''	Imaginary part of complex dielectric permittivity	
γ	Complex propagation constant	
α	Attenuation constant	
β	Phase constant	
σ	Conductivity	
δ	Skin depth	
ρ	Electric charge density	C/m ³
Γ	Power Confinement	

Chapter 1

Introduction

1.1 History of Lightwave Technology

Glass dates back at least 4500 years to ancient Egypt and Mesopotamia [1]. 3500 years ago, Egyptians were sculpting miniature heads of transparent glass, which the years have since turned milky white.

The phenomenon of the guidance of light along transparent cylinders by multiple total internal reflections had been observed and used in the ancient world by Greek and later by Venetian glassblowers, in fabricating their decorative glassware. In fact, the basic techniques used then form an important aspect of present-day fibre optic technology. For 2000 years, glass blowers have thrust glass tubes into glowing furnaces to soften them. Workers pausing to relax from the hot, hard job must have seen the fiery glow of the furnace emerging from the glass. Master glass makers noted total internal reflection as they made sparkling ornaments for the bright glass chandeliers that illuminated the great rooms of the rich. But they kept their secrets to themselves. Scientists began to study total internal reflection in medieval times as they sought to understand the mystery of the rainbow, but they did not understand it until the laws of refraction were formulated in the seventeenth century [2].

The earliest recorded scientific demonstration of light confinement, was given by John Tyndall at the Royal Society in England in 1870, where he used an illuminated vessel of water and showed that, when a stream of water was allowed to flow through a hole in the side of the vessel, light was conducted along the curved path of the stream [3]. Ten years later, in 1880, Alexander Graham Bell invented the “photophone”, a device that varied the intensity of sunlight incident upon it in response to the amplitude of speech vibrations. The light variations were reconverted into electrical signal and then into sound, at the receiver end, via a selenium detector. Although the photophone was impractical due to propagation losses, it provided the idea for transmission of signals

over a specified distance by modulation of an optical wave: in other words, the concept of optical communication. This brought new ideas in the early years of the last century, and in 1910, Hondros and Debye presented the first form of an optical waveguide, the dielectric circular rod, in an attempt to guide electromagnetic waves through a dielectric medium [4]. The dielectric losses of the non-radiative modes propagating along the dielectric circular rod, were computed much later, by Elsasser in 1949 [5].

The term “fibre optic” was first used by Kapany in mid 50s, when the fibre of higher refractive index core and lower refractive index cladding was developed. He defined “fibre optic” as, ‘the art of the active and passive guidance of light (rays and waveguide modes), in the ultraviolet, visible, and infrared regions of the spectrum, along transparent fibres through predetermined paths [3]. A few years later, Snitzer and Osterberg [6] recorded dielectric waveguide modes in the visible region of the spectrum of various optical fibres and Kapany and Burke [7] investigated the coupling phenomenon in adjacent optical fibres. These observations were followed by further work in the field, which established the use of optical fibres in long distance telecommunications [8].

Along with the research for higher transmission capacity, larger bandwidth and lower losses in optical fibres, some other major developments were achieved in the 1960s, which revolutionised lightwave technology and the telecommunication industry. In 1960, T.H. Maiman first demonstrated laser action in ruby, by applying Einstein’s ideas for stimulated emission, dated back to 1917 [9]. The implementation of low-loss silica fibres [10], and the use of lasers as a CW coherent source of light at optical frequencies, in the range $1.3 - 1.55 \mu m$, where such fibres exhibit minimum dispersion, had given a new dimension in the field of optical communication.

The invention of the laser gave an enormous stimulus to the entire field of optics. The requirement for more compact and more economical optical transmission systems, less vulnerable to environmental changes, in order to replace the existing laser beam transit in a system via mirrors and lenses, then emerged. These requirements stimulated the development of improved thin-film fabrication techniques and studies on new materials for both active and passive function [11, 12], and led eventually to the idea of integrated optics. As a concept, it was first visualised by Miller in 1969 [13]. Integrated optics is based on the guiding of electromagnetic energy at optical frequencies by thin films, which can be placed one next to the other on a single substrate. Semiconductors had played an important role in the effort to develop monolithic integrated optical

circuits (IOC), that would serve as miniature optical counterparts of microwave devices and networks.

The period that followed initiated new activities, which aimed as an ultimate goal for the replacement of the existing integrated electronic circuits (IEC) by integrated optical circuits (IOC), in order to benefit from the advantages of larger bandwidth and negligible sensitivity to interference by natural or man-made electromagnetic fields of lower frequencies, that optical communication systems can offer.

Recent advances in integrated optics demonstrated a rich variety of optical components and devices, such as directional couplers, Y-branches, waveguide crossings, Bragg gratings, transmission gratings, acousto-optical filters, optical filters, modulators, optical amplifiers and others. Also, recent technological achievements such as laser copiers, laser printers, laser bar-code readers, CD players and others have entered our households and have become part of everyday life.

The development of more sophisticated integrated optical communication systems requires a knowledge of the properties of the basic elements, such as the optical waveguides.

1.2 Dielectric Guidance

Dielectric guidance is achieved using only dielectrics of different refractive indices. Refractive index n of a material is a dimensionless number that describes how light propagates through that medium and can be defined as the ratio of speed of light in vacuum and the speed of light in the medium as,

$$n = \frac{c}{v} \quad (1.1)$$

Where, $c = 2.99792458 \times 10^8 \text{ m/s}$ is the speed of light in vacuum and v is the speed of light in the medium.

The velocity of light in a medium can be calculated using its permittivity, ϵ and permeability, μ using,

$$v = \frac{1}{\sqrt{\mu\epsilon}} \quad (1.2)$$

The guidance of light in dielectrics can be explained with both ray optics and full-wave electromagnetic theory.

Geometric/Ray Optics Geometrical optics, or ray optics, describes light propagation in terms of rays. The ray in geometric optics approximates the paths along which light propagates. Ray optics assumes the following,

1. light propagates in rectilinear paths in homogeneous medium,
2. light bends at the interface of two dissimilar medium,
3. light follows curved paths in a medium in which the refractive index changes
4. light may be absorbed or reflected

Full-wave Electromagnetics Although ray optics makes explanations of some properties of light it cannot explain many properties like diffraction, interference etc. To explain the light properly, full-wave electromagnetic theory is needed. In electromagnetics, light is considered to be a wave combining electric and magnetic fields and is a part of the electromagnetic spectrum. Electromagnetic force is also one of the fundamental forces of nature.

1.2.1 Snell's Law of Refraction

As light passes the interface between the two refractive media, the light will either be refracted to a lesser angle, or a greater one depending upon the relative refractive indices of the two media. These angles are measured with respect to the normal line, represented by the perpendicular to the boundary. In mathematical form,

$$\frac{\sin \theta_1}{\sin \theta_2} = \frac{n_2}{n_1} \quad (1.3)$$

Here, n_1 and n_2 are the refractive indices of the two media and θ_1 and θ_2 are the angles involved in refraction.

Figure 1.1 describes the phenomena graphically. In Fig. 1.1a, the light ray is incident on the surface of refraction from the lighter medium with refractive index n_1 at an angle θ_1 , and after crossing the interface the light ray will travel inside the denser medium with refractive index n_2 at an angle θ_2 which is less than θ_1 in this case. Here, θ_1 is the angle of incidence and θ_2 is the angle of refraction. Figure 1.1b shows the opposite phenomenon of light ray travelling from a denser to a lighter medium.

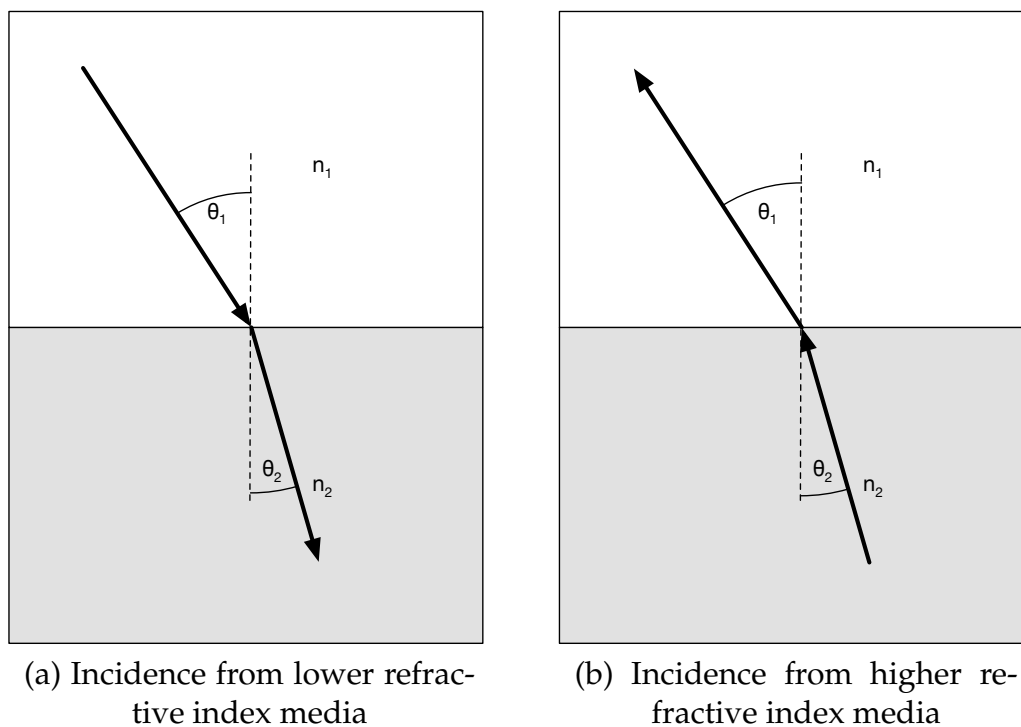


FIGURE 1.1: Refraction between two media with refractive indices n_1 and n_2 , where $n_2 > n_1$

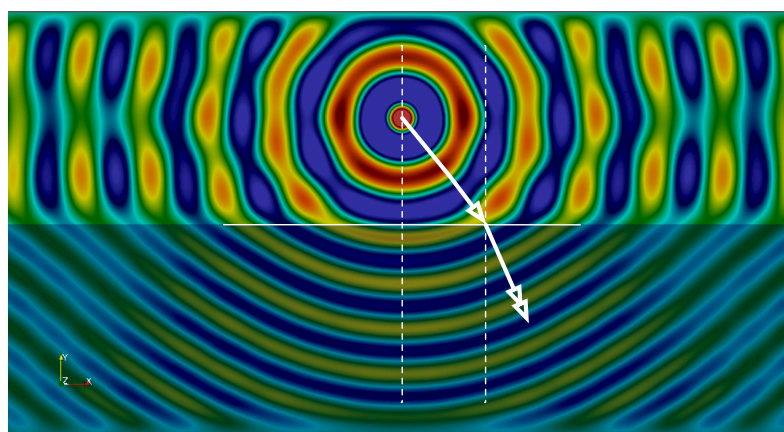


FIGURE 1.2: Refraction of wave at an air-Silica interface from a point source radiating from the air layer

Figure 1.2¹ shows refraction when a point source (wavelength, $\lambda = 1.55 \mu m$) is placed inside a lower index medium, in this case air ($n_{air} = 1$) and the wave travels into a higher index medium, in this case Silica ($n_{SiO_2} = 1.4440$ [15] at a wavelength of $1.55 \mu m$). It can be seen in the figure that when the wave crosses the interface and goes into the Silica layer, the wavefront compresses in space. This is because the speed of propagation is less inside the higher index medium.

Figure 1.2 also shows some reflected wave into the air interfering with the circular wavefront of the air layer. This interference is not visible inside the Silica layer as the reflection is from the air-Silica interface and the wave is approaching from the air layer. The reflection is due to the impedance mismatch of the two media. Both the refraction and the reflection can be better observed when an even higher index material like Silicon ($n_{Si} = 3.4777$ [16] at $1.55 \mu m$ wavelength) is used instead of the Silica. Figure 1.3 shows what happens when light with $1.55 \mu m$ wavelength is incident on an air-Silicon interface. As can be seen, the wavefront inside the Silicon layer is more compressed due to the reduction of speed of propagation. Therefore the sudden change of angle is also visible for angular incidence. It also shows higher reflection into the air layer due to the higher impedance mismatch between air and Silicon.

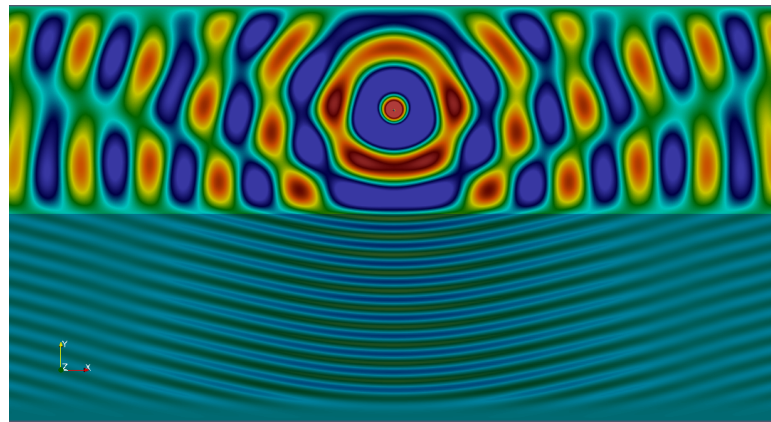


FIGURE 1.3: Refraction of wave on an air-Silicon interface from a point source radiating from the air layer

The change of angle of propagation on top of the wave front is also shown in Fig. 1.2. It can be observed that when light is incident on the interface at an angle (the single headed arrow from the point source to the interface), due to the compression of the wavefront and sudden decrease in speed of propagation, the direction of the propagation changes (double headed arrow from to interface into the Silica layer).

¹The wave representations of refraction in this chapter were simulated using the Finite Element Time Domain method presented in [14]

In Fig. 1.1b, it is shown that if the light ray is incident on the surface of refraction from the denser medium with refractive index n_2 at an angle θ_2 , after crossing the interface, the light ray will travel inside the medium with refractive index n_1 at an angle θ_1 which is greater than θ_2 . In this case, θ_2 is the angle of incidence and θ_1 is the angle of refraction.

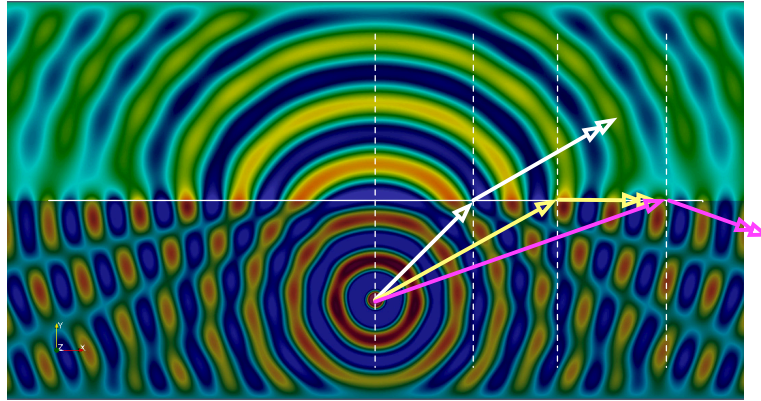


FIGURE 1.4: Refraction, critical angle and total internal reflection of wave on an air-Silica interface from a point source radiating from the Silica layer

Figure 1.4 shows the refraction characteristics when the point source of Fig. 1.2 is moved inside the Silica layer. When the point source is inside the Silica layer, the wave approaches the interface from the Silica side. It can be observed that the wavefronts inside the air layer become expanded. This is due to the higher speed inside the medium compared to the Silica. With the white arrows it can also be observed that the angle of refraction becomes larger compared to the angle of incidence.

In both the occasions, the relation between the angles and the refractive indices can be determined as explained by Eq. 1.3. For both cases, $\theta_1 > \theta_2$ when $n_2 > n_1$.

1.2.2 Critical Angle and Total Internal Reflection

As required by the Snell's law when light travels from a higher refractive index medium into a lower refractive index medium, the angle of refraction needs to be greater than the angle of incidence. Therefore, there should be an angle of incidence lower than 90° for which the angle of refraction equals 90° . This angle of incidence is called the critical angle. If a light ray is incident on a refraction interface at a critical angle, no light will come out of the interface, rather the

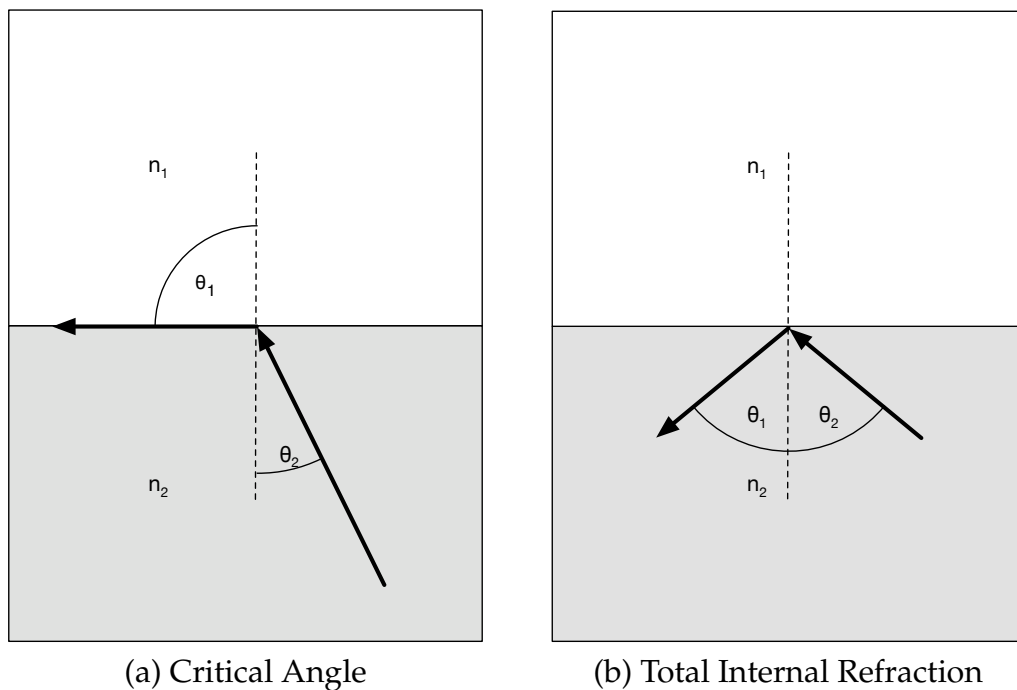


FIGURE 1.5: Critical Angle and Total internal reflection, where $n_2 > n_1$

light ray will propagate along the interface. Figure 1.5a, shows the critical angle when the refractive indices are n_1 and n_2 , $n_2 > n_1$.

In the same manner, when the angle of incidence is increased beyond the critical angle, the angle of refraction becomes more than 90° , as shown in Figure 1.5b. At this stage no light escapes the higher index medium and is totally reflected back into it. This phenomenon is called total internal reflection (TIR).

In Fig. 1.4, at the point of incidence of the white arrow the wave leaks into the air layer. But when moved further from that point, the single headed yellow arrow shows the critical angle of incidence and the double headed yellow arrow shows the propagation along the interface. When moved even further, the pink arrows show the total internal reflection. Beyond the point of critical angle all waves reflect back to the Silica layer. Although there is some reflection visible near the point source due to impedance mismatch, in this occasion the main reflection starts after the critical angle.

The phenomena can be better viewed with an air-Silicon interface. Figure 1.6 shows total internal reflection for an air-Silicon interface. This time the reflection due to impedance mismatch is barely visible. This is because the critical angle for this setup is much lower than that of the air-Silica interface. The figure clearly shows that there is no wave in the air due to total internal reflection

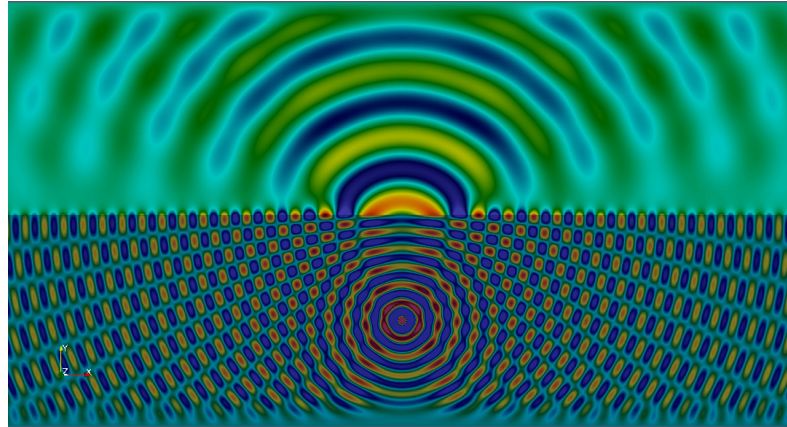


FIGURE 1.6: Total internal reflection of wave on an air-Silicon interface from a point source radiating from the Silicon layer

inside the Silicon layer.

1.2.3 Dielectric Guidance

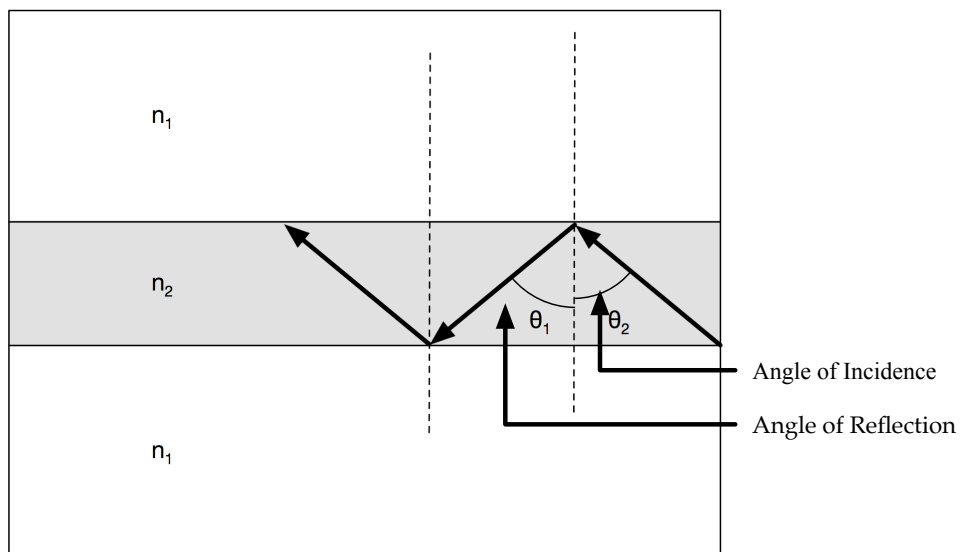


FIGURE 1.7: Dielectric guidance with total internal reflection

As total internal reflection reflects all incident light over the critical angle into the higher index medium, if a thin higher index dielectric film is surrounded by lower index medium as shown in Fig. 1.7, the total internal reflection will happen on both the interfaces and the light will be trapped inside the high index film. The trapped light will only be able to escape at the end of the high index film. This arrangement is called a dielectric waveguide.

Although dielectric guidance can be realised with ray optics, to explain a waveguide properly and also to investigate many wave related aspects of the

guidance and propagation, full-wave electromagnetics needs to be used. As can be seen in Figs. 1.2, 1.3, 1.4 and 1.6, the distribution of the wave near the boundary follows a specific pattern. According to ray optics the light should reflect into the higher index medium without any leakage into air.

But when the wave nature of light is considered in full-wave electromagnetics, part of the wave extends into air. In practice the pattern or wave profile near the interface follows the interface and never moves into the air. In other words, the field profile near the interface is guided by the interface.

When two interfaces are involved as shown in schematic diagram Fig. 1.7 both the interfaces will show the same profile across the interface. As the interfaces also guide the wave along themselves, the wave will propagate through the medium in parallel to the interface. Due to the total internal reflection from both the interfaces, moving profiles will be generated. These patterns are called modes of propagation.

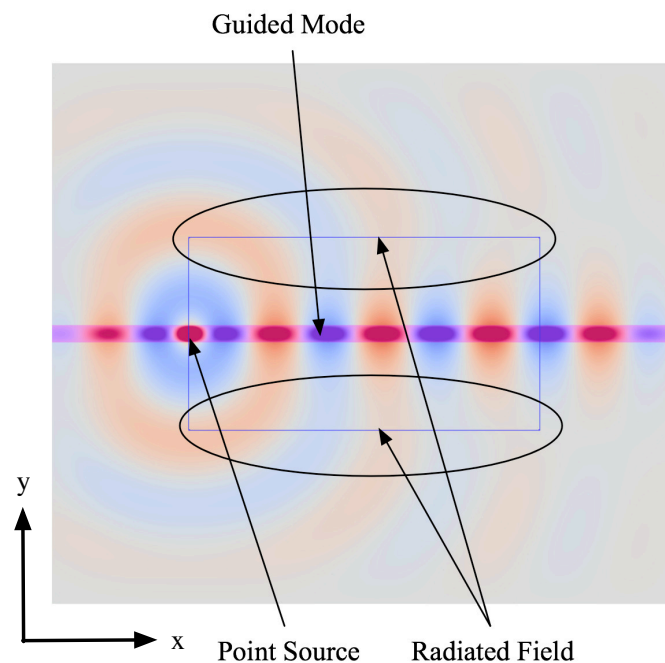


FIGURE 1.8: Wave guiding in Air-Silicon-air waveguide with core thickness $0.2 \mu\text{m}$ with a point source of $1.55 \mu\text{m}$ wavelength

Figure 1.8 shows the E_z field profile for air-Silicon-air waveguide with a point source of $1.55 \mu\text{m}$ wavelength. The Silicon core is $0.2 \mu\text{m}$ thick. As can be observed, most of the field from the point source is guided inside the Silicon core of the waveguide. Some field is also leaked out of the guide and is propagating outside the guide. Compared to the outside wave, field inside the guide is compressed.

In this work modal analysis is the primary analysis to study and analyse different properties of different guiding structures.

1.3 Surface Plasmon Polariton

Surface plasmon polaritons (SPPs), are electromagnetic waves which travel along a metal-dielectric interface. The term “surface plasmon polariton” explains that the wave involves both charge motion in the metal (“surface plasmon”) and electromagnetic waves in the dielectric (“polariton”) [17].

They are surface waves propagated along the surface of a metallic structure. SPPs are shorter in wavelength than the incident light (photons). Hence, perpendicular to the interface, SPPs can have tighter subwavelength-scale spatial confinement and higher local field intensity [18]. An SPP will propagate along the interface until its energy is lost.

1.3.1 History

Well before scientists set out to study the unique optical properties of metal, they were employed by artists to generate vibrant colours in glass artifacts and in the staining of church windows. One of the most famous examples is the Lycurgus cup dating back to the Byzantine Empire (4 century A.D.). Some of the first scientific studies in which surface plasmons were observed date back to the beginning of the twentieth century.

R.M. Wood noticed that when he shone polarised light onto a metal-backed diffraction grating, a pattern of unusual dark and light bands appeared in the reflected light [19, 20]. Around that same time, in 1904, Maxwell Garnett describes the bright colours observed in metal doped glasses [21] using the then newly developed Drude theory of metals, and the electromagnetic properties of small spheres as derived by Lord Rayleigh.

The first theoretical treatment of these anomalies was by Lord Rayleigh in 1907 [22]. He based his “dynamical theory of the grating” on an expansion of the scattered electromagnetic field in terms of outgoing waves only. With this assumption, he found that the scattered field was singular at wavelengths for which one of the spectral orders emerged from the grating at the grazing angle. He then observed that these wavelengths, which have come to be called the Rayleigh wavelengths λ_R , correspond to the Wood anomalies. Furthermore,

these singularities appeared only when the electric field was polarized perpendicular to the rulings, and thus accounted for the S anomalies; for P polarization, his theory predicted a normal behaviour near λ_R [23].

In the fifties many experimentations were carried out on electron energy losses in gasses and on thin foils [24, 25]. Pines and Bohm suggested [26, 27, 28] that the energy losses were due to the excitation of conducting electrons creating plasma oscillations or plasmons. Further research [25] revealed that the energy loss resulted from excitation of a surface plasma oscillation, in which part of the restoring electric field extended beyond the specimen boundary. Therefore, the presence of any film or contaminant on the specimen surface affects the surface plasma oscillation. This effect was later described in terms of excitation of electromagnetic 'evanescent' waves at the surface of the metal, and in the 1970s evanescent waves were described as a means to study ultra-thin metal films and coatings [29].

In the late sixties, optical excitation of surface plasmons by means of attenuated total reflection was demonstrated by Kretschmann [30, 31] and Otto [32]. Their methods for the optical excitation of surface plasmons on metal films, making experiments on surface plasmons easily accessible to many researchers.

At this point the properties of surface plasmons were well known, however the connection to the optical properties of metal nanoparticles had not yet been made. In 1970, more than sixty years after Garnett's work on the colours of metal doped glasses, Uwe Kreibig and Peter Zacharias performed a study in which they compared the electronic and optical response of gold and silver nanoparticles [33]. In their work, they for the first time describe the optical properties of metal nanoparticles in terms of surface plasmons. As the field continued to develop and the importance of the coupling between the oscillating electrons and the electromagnetic field became more apparent, Stephen Cunningham and his colleagues introduced the term surface-plasmon-polariton (SPP) in 1974 [34].

Another major discovery in the area of metal optics occurred in that same year, when Martin Fleischmann and coworkers observed strong Raman scattering from pyridine molecules in the vicinity of roughened silver surfaces [35]. Although it was not realised at the time, the Raman scattering, an exchange of energy between photons and molecular vibrations, was enhanced by electromagnetic fields near the rough silver surface due to the presence of surface plasmons. This observation led to the now well established field of Surface Enhanced Raman Scattering (SERS). All these discoveries have set the stage for

the current surge in surface plasmon research.

1.3.2 Applications

Following the fundamental studies of light-metal interaction in the early days (late 1950s to late 1960s), SPs have been extensively explored in thin film characterisation, chemical sensing and biodetection since the late 1970s. In recent years, interest in SPs has expanded from sensing technology to a wide range of fields, including subwavelength optics, nanophotonics, information storage, nanolithography, light generation and engineering left-handed metamaterials at optical wavelengths, etc. The reformed interest was stimulated by the recent progress in electromagnetic simulations, micro/nanofabrication and characterisation techniques, which provide the necessary tools to revive and exploit remarkable properties of SPs in the domains of both fundamental physics and application development. The dynamic growth of the field of plasmonics is clearly reflected in the fact that since 1990 the annual number of publications on SPs has doubled every five years [36].

Sensor

A great deal of work in SP applications has been done in the exploitation of surface plasmon resonance (SPR) sensing for physical [37], chemical [38] and biological detection [39]. The simplest form of SPR sensing is based on reflectivity measurement, which was pioneered by Nylander and co-workers in the early 1980s for gas detection and biosensing [40, 41]. In recent years SPR sensing has become a leading technology for affinity-based biosensing, owing to its label-free, noninvasive real-time analysis nature. At present about 50% of all publications on SPs involve the use of plasmons for biodetection [36], covering fields as diverse as molecular engineering, cell biology, proteomics, clinical diagnosis, drug discovery and environmental monitoring [42].

The working principle behind the SPR sensing technique is that the SPP's resonance conditions, such as wavelength and penetration depth, are highly sensitive to the immediate environment of the metal/dielectric interface. An SPR sensing system generally involves four elemental modules: an optical system comprising a light source and an optical detector; a flow system for sample delivery; a sensor surface formed by an SPP-active metal film (normally 50 ~ 100-nm-thick Au or Ag); and an electronic system for data processing. All these elements vary depending on the intended application.

Subsequent to the prism-coupler-based SPR sensor, grating-coupler-based system [43] and optical-waveguide-based systems [44, 45] have also been introduced. However, the Kretschmann-Raether configuration is still the most widely used geometry in SPR sensors [46]. Currently there are several manufacturers offering a wide variety of commercial SPR biosensors [47], which has made it possible for potential users to choose the appropriate system according to the specific requirements, such as sensitivity, selectivity, speed, portability and price.

Waveguide

Recent resurgence of interest in SPs is not only limited to sensing technology. SPs have also attracted increasing attention as useful tools for the construction of deep subwavelength optical and photonic devices.

It is well known that the spatial confinement of free propagating waves is limited to about $\lambda_0/2n$ (here, λ_0 is the freespace wavelength and n is the refractive index of the medium), that is, about half of the wavelength in the medium. This so-called “diffraction limit” of light is the primary factor that limits the minimum sizes of optical elements in conventional far-field optics and has imposed a major challenge in the development of highly integrated optical devices. The origin of the diffraction limit lies in the three-dimensional nature of the free propagating waves, *i.e.*, k_x , k_y , k_z of the wavevector k of these waves are all real. Since $|\mathbf{k}|^2 = k_x^2 + k_y^2 + k_z^2$, there is an upper limit on k_i ($i = x, y, z$) such that $k_i \leq |\mathbf{k}|$. According to the uncertainty relation of Fourier transforms, this spatial frequency upper limit leads directly to the lower limit in the variation of the wave in real space as $d_i \geq \lambda_0/2n$.

However, if one (or more than one) component(s) of \mathbf{k} become purely imaginary (e.g., an evanescent wave), then $k_i > |\mathbf{k}|$ can be achieved. This thus provides a means to conquer the diffraction limit. Depending on the number of real components in \mathbf{k} , EM waves can be defined as 3-D (three real components in \mathbf{k}), 2-D (two real, one pure imaginary components in \mathbf{k}), 1-D (one real, two pure imaginary components in \mathbf{k}) and 0-D (no real components in \mathbf{k}) waves [48]. In this sense, SPPs propagating along planar metal surfaces or metallic nanowires surfaces can be classified as 2-D or 1-D waves, respectively; and LSPs confined on the metallic nanoparticles or nanovoids can be considered as 0-D waves. Clearly, while 3-D waves suffer from conventional diffraction limits, 2-D, 1-D, and 0-D waves have the ability to provide one-, two-, and three-dimensional field confinements in real space without such constraints.

Interest in exploiting SPs for opto-electronic device applications is happening at a time when continuous miniaturisation of integrated electronic circuits is approaching fundamental limitations. For example, ever since the semiconductor industry entered the sub-100 *nm* technology nodes, there has been growing concern over the issues associated with electronic interconnects [49, 50], such as signal delay and heat generation. While conventional fibre-optic interconnects offer speed-of-light propagation, large band-width and low power consumption, the dimensions of these dielectric components are generally at the microscale. This has severely limited their applications in nanoscale integrated electronic circuits.

In contrast to the free propagating light, SPs can be sustained and guided by nanoscale metallic structures without the constraint of the diffraction limits. In 1997 Takahara and co-workers first proposed the use of metallic nanowires to guide 1-D optical beams with nanometer diameter [48]. They suggested that in visible and near-infrared ranges the negative dielectric constants of metal removes the constraints of conventional dielectric waveguides:

$$0 < \epsilon_{clad} < \epsilon_{core}$$

$$\beta, k_x, k_y, \kappa_x, \kappa_y \leq \omega \sqrt{\epsilon_{core} \mu_0} \quad (1.4)$$

where ϵ_{clad} and ϵ_{core} are the dielectric constants of the core and cladding; β is the wave vector component along the propagation direction (z-direction); k_x and k_y are the transverse components of the wavevector inside the core and κ_x and κ_y are those in the cladding. As k_x and k_y become imaginary in metallic nanowires, the beam diameter is free from the limitation of the wavelength. Simulation [48] reveals that for the lowest order TM mode β increases as the core radius decreases and there is no transmission cut off in the core size.

The concept of nanoscale 1-D metallic waveguides has motivated many new researches in the field of plasmonics. However, currently realising such structures still presents an engineering challenge. On the other hand, various 2-D SPP waveguides (waveguides of 2-D SPP waves) have been experimentally demonstrated in recent years, including: metallic stripes [51, 52, 53, 54] and wedges [55, 56] (insulator-metal-insulator configuration), metallic gaps [57, 58] and grooves [59] (metal-insulator-metal configuration), etc. Moreover, some complex SPP waveguiding elements based on the principle of straight waveguides, such as S-bent waveguides, four-port coupler, Y-splitter and coupler have also been reported [60].

Sub Wavelength Optics

Controlling the propagation of SPs is of fundamental importance to achieve SP-based subwavelength optics. The concept of using 2-D optical elements for SP manipulation was published in the same year as the metallic nanowire waveguide was proposed. When Smolyaninov *et al.* investigated SP scattering by surface defects, they suggested the design of subwavelength mirrors or lenses for SPP focusing [61]. The experimental demonstration of SP optical elements came in 2002; Ditzel and co-workers [62] reported the manipulation of SPP propagation in a 70-nm-thick Ag film by introducing various nanoscale optical elements through height modulation on the film. The influence of these elements on the SPP field distribution were detected through fluorescence imaging.

1.4 Terahertz

Terahertz waves are increasingly redefining our view of the world by opening up new frontiers of research across a wide domain of applications. Despite being in the early stages of development, the use of THz technologies have been proven to hold great potential for application areas such as imaging, spectroscopy and sensing. The recent breakthroughs achieved in designing novel components for integrated THz systems will certainly augment and potentially replace X-ray and infrared technologies in scanning and spectroscopic applications. X-ray technology is mature, having come a long way since its first demonstration more than a century ago. In comparison, systems utilising THz waves are still very much in their infancy, and thus offer significant potential.

In terms of definition, terahertz radiation is commonly referred to as the intermediate band of frequency lying between the microwave and infrared band in the electromagnetic spectrum. In quantitative terms this is defined as the range of frequencies between 300 GHz - 10 THz or, in terms of wavelength, the range can also be defined as $1\text{ mm} - 30.0\ \mu\text{m}$.

An ever-increasing list of breakthroughs achieved in THz technology has triggered a flurry of research activities in diverse fields. Most notable and indeed ground breaking milestones achieved in THz research include the demonstration of a fully functional THz time domain spectrometer by Grischkowsky *et al.* [63] although the first demonstration of THz time domain spectroscopy dates back to the mid 1980s [64, 65]. On the other hand, the first imaging device exploiting THz radiation was demonstrated in 1995 by Hu *et al.* [66]. Ever

since then some of the most remarkable developments in the field of imaging have included the development of three dimensional tomographic imaging by exploiting the temporal coherence of THz pulses [67]. In addition to that, more recently various synthetic aperture imaging configurations have also been proposed [68, 69, 70] which offers imaging with remarkable resolution. Despite the breakthroughs achieved, developments in advanced sensing and imaging with THz band remain largely unexplored compared to the relatively well-developed science and technology in the microwave and optical frequency region.

Since the demonstration of THz wave time-domain spectroscopy in the mid 1980s [64, 65], there have been a series of significant advances, as more powerful and stable THz sources and higher sensitivity detectors emerged which provide new opportunities for extending the applications in the THz frequency range.

As more and more technologies underpinning device characterisation and fabrication emerge, THz technology will not only be seen to have an impact on material characterisation and identification but its impact will also be felt in applications such as communications, imaging, medical diagnosis, health monitoring, environmental control, and chemical and biological sensing, as well as security and quality-control applications. Thus twenty-first century research in the THz band region is one of the most promising areas of study for transformational advances in imaging [71] and in other fields such as biology and medicine [72].

While interest in THz technology continues to grow throughout the whole scientific community, its usage in many real life applications still remains strictly limited due to a lack of sources and guidance medium. The lack of a high-power, low-cost and portable THz source that operates at room temperature (or even at lower temperatures for which sophisticated coolant is not necessary) is by far the most significant limitation of modern THz systems. There is an array of potential sources each with relative advantages, and advances in high-speed electronics, laser and materials research continue to provide new candidates. To set the context, before going into details about the background of the research carried out here and the results achieved, it is necessary to provide an overview of the applications of THz waves in many critically important areas of science.

1.4.1 Application of Terahertz Radiation

Applications involving exploiting THz radiation may be classified into two broad domains for this work: communications and sensing. Analytical techniques in the frequency and time domains are currently being used to identify and characterise various materials in this context. These techniques have the potential to open up new frontiers of research in many fields including biology, pharmacy, medicine, industrial non-destructive evaluation, meteorology, environment monitoring and fundamental science. The list of applications where the true potential of THz radiation can be harnessed is indeed a wide spanning one. Some of the key areas of application where the possibility of using THz waves are currently being explored has been discussed in the following subsections.

Biomedical Application of Terahertz

Time domain spectroscopic techniques based on THz waves have come a long way ever since they were first established in the early 1990s [63]. Modern THz-TDS systems may be applied to identify and characterise many biological materials such as cancer tissues, DNA, biomolecules and proteins [73, 74]. The study of proteins, DNA and other biomolecules and various cancers using THz systems is providing major insights into these critically important areas. Label free DNA sensing using THz waves has attracted considerable interest in the last decade amongst medical professionals and physicists. Several breakthroughs have also been achieved in these areas, most notably in proposing THz biochips and label free probing of genes [75, 76, 77, 74].

The application of THz spectroscopy and imaging techniques has also been extended to the diagnosis of cancer [78]. A system using a THz reflection geometry [79] has been used to study frequency and time domain based 2-dimensional images of cancerous skin cells. The high sensitivity of THz waves to hydration levels of materials were exploited in this technique to perform detection since the water content in cancerous cells is different to that in normal cells [80]. Skin cancer is visualised by the reflection of THz-TDS at a lateral and vertical resolution of about $350\ \mu\text{m}$ and $40\ \mu\text{m}$, respectively, and a penetration depth of about a millimetre has been realised.

Application in Security Scanning

Most common explosive and narcotic substances have distinct signatures in the THz band compared to other parts of the electromagnetic spectrum. This discreet advantage offered by THz waves can potentially make THz scanners useful in security systems for airports and transport hubs. THz signatures of illicit substances allow their identification of specific chemicals through the analysis of their transmission spectra. As radiation below 3.0 THz can generally pass through normal envelopes, materials can be identified using THz multispectral images and component spatial-pattern analysis without having to open the mail [81, 82]. The emergence of the THz camera has also added a new dimension to the security scanning application. For instance, a passive THz camera made up of an SBD (Schottky Barrier Diode) array with a silicon photonic bandgap crystal and a heterodyne detection method operating at a frequency of about 500 GHz is now available for use in airport security [80]. Active THz cameras on the other hand will extend the range of application range to the area of biometrics. Hazardous-gas detection using THz sensing is also expected to become more common as, for instance, a new detection technique for detecting gases, such as carbon monoxide, is required at fire sites where infrared gas detection is sometimes blocked, for example by concrete walls.

Application in Spectroscopy

By far the most successful application of THz waves (apart from in the field of astronomy) has been in spectroscopy and in imaging. The most widely employed spectroscopic technique using THz techniques is the time domain spectroscopy (or THz-TDS for short). In such a system, an ultrafast laser source (a Ti:sapphire laser operating in pulsed mode at $\lambda \sim 800$ nm with a pulse duration of about 100 fs) is split into a pump and a probe beam using beam splitters. The pump beam is shone on an appropriate THz emitter to generate THz pulses, whereas the probe is used to detect the pulses generated by the emitter. The probe pulses are then propagated along a channel of optical delay lines to sample the THz pulses and record the electric field as a function of delay time. For detecting THz waves in a TDS system, coherent detectors are required. Two of the most common methods are based on photoconductive sampling and free-space electro-optic sampling [83]. After the interaction of the terahertz pulse with a target, it can be recorded and analysed by extracting its spectrum. This

provides the THz response of the target within the THz-pulse covered bandwidth. Since the above spectroscopic measurement is carried out recording the THz waveform in the time-domain, this technique is called time-domain spectroscopy (also abbreviated TDS) [84].

There are clear advantages of using THz in TDS systems over other radiation bands of the electromagnetic spectrum. First, THz-TDS provides coherent spectroscopic detection over a wide range at THz. THz-TDS utilises coherent detection methods, which can be used to measure coherent processes in carriers. Coherent detection techniques offer the advantage of providing both the amplitude and phase of the waveform, whereas incoherent detection techniques only offer information about the intensity of the waveform/signal. Coherent detection techniques facilitate a rigorous investigation of the material under investigation. This is difficult to access using other methods. Second, using the pulsed form of THz waves in TDS systems gives a high temporal resolution due to the very short duration (measured in picoseconds) of the pulses. It is thus very well suited for measurement in dynamic spectroscopy applications. Third, THz-TDS uses time-gating in sampling the THz pulses that significantly suppresses any background noise. As a result, THz-TDS usually has a very high signal-to-noise ratio. This is especially useful to spectroscopic applications with high background radiation, which is comparable or even stronger than the signal [84].

THz-TDS also presents several challenges. THz-TDS is usually slow, due to the temporal sampling of the THz pulses. Techniques have been developed in order to improve the speed of THz-TDS measurements [85]. Today, THz-TDS can perform a single measurement in less than one second with a fairly high SNR. THz-TDS also suffers from poor spectral resolution (1 – 10 GHz) [86, 87] due to the limited temporal scanning range seen in real measurements. In principle, one can scan a THz pulse for as long a time period as it is needed. However, a longer scan not only takes more data acquisition time, but also reduces the dynamic range of the spectrometer. The limited spectral resolution is not a problem when measuring the spectrum of a target in a condensed state, whose spectral features often have a bandwidth of a few tenths of THz. The spectral resolution could, however, be insufficient when gases are measured. For such a measurement, a continuous wave THz source with narrow line width is preferred.

1.4.2 Terahertz Detectors

The detection of THz-frequency signals is a critical part of any THz system. Highly sensitive and reliable detection mechanisms are often required for THz systems due to the low output power of the available sources and the relatively high levels of thermal background radiation that can lead to erroneous detected signals.

Direct detectors such as InSb, Ge or Si bolometers based on thermal absorption are often utilised for broadband detection of THz waves. For these systems it is critical to incorporate a cryogenic cooling system to eliminate the interfering thermal background effects. Other commonly used detectors include pyroelectric infrared detectors and superconductor (such as niobium) based detectors and also through using interferometric techniques. Some major advancement has been seen recently in developing THz detection techniques. One such major leap was the demonstration of a Ge based single photon detector by Komiyama *et al.* [88]. The underlying system for this detector consists of a quantum dot based single electron transistor in the presence of a high magnetic field. Plasmonic detectors incorporating monolithic bolometers were also proposed more recently as part of a greater effort to miniaturise THz devices [89].

Heterodyne detection is often preferred over the use of bolometric detectors for applications that require a high degree of spectral resolution. Heterodyne detection utilises a nonlinear device called a mixer. Schottky diodes are commonly used as mixers. The key process in a mixer is frequency down conversion, which is carried out by mixing a THz signal ω_S with reference radiation at a fixed frequency ω_{LO} . The mixer produces an output signal at the difference frequency called the intermediate frequency, $\omega_D = |\omega_S - \omega_{LO}|$. The amplitude of the output signal is proportional to the THz amplitude [90].

In THz-TDS systems, coherent detection mechanisms are utilised which measure both the amplitude and phase of the detected THz signal. Two of the most commonly used coherent detection mechanism includes photoconductive and free-space electro-optic sampling. Electro-optic sampling relies on coupling between THz and optical pulses (from a femtosecond laser) in a non-linear sensor crystal typically ZnTe or GaSe. The birefringence of the sensor crystal gets perturbed due to the incident electric field of the THz pulse, which in turn modulates the polarisation ellipticity of the optical beam passing through the crystal. This change in ellipticity is then analysed to reveal key features of the amplitude and the phase of the THz beam [91].

1.4.3 THz Sources

Generating coherent radiation is one of the key requirements that must be met for a source before it can be used in any THz system. Coherent generation of THz has long been performed by either up or down converting radiation emitted from electronic or photonic sources. The resistive limitation of electronic sources operating beyond 100 GHz proved to strictly limit the range of frequencies offered by such sources. On the other hand using photonic sources such as semiconductor lasers appeared to be an unprecedented challenge due to limitations in achieving population inversion at small energy level separation (for THz emission, it is roughly around 40 meV) in the conduction band of many materials. An ideal THz source would undoubtedly offer the benefit of high power emission in narrowband with greater frequency tunability. In addition to that, ability to operate at low cost and high temperature are also critical. However, presently it is nearly impossible to achieve all of these from a single source. The output power from many conventional THz sources can be compared in the figure shown in Fig. 1.9 [80]

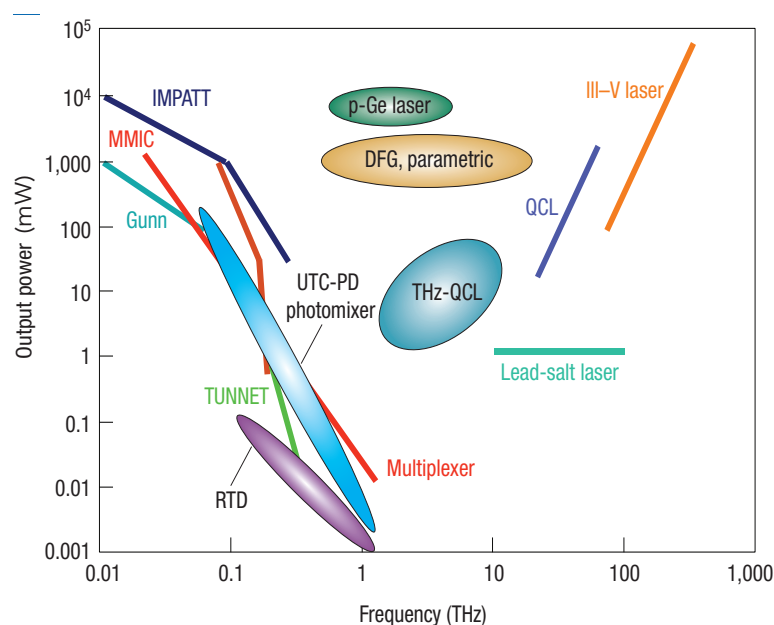


FIGURE 1.9: THz-emission power as a function of frequency. Solid lines are for the conventional THz sources [80]

Solid State THz Sources

Generating radiation at the lower end of the THz band is best performed through the use of solid-state electronic sources, like oscillators and amplifiers which

are generally limited in frequency due to the transit time of carriers through the semiconductor junctions, which causes high frequency roll-off. Several research groups have developed high frequency Gunn, IMPATT and TUNNET diodes designed for generating THz waves within the range of 0.3 THz and above [92]. Such sources were hailed as the most powerful solid-state THz oscillators operating at room temperature. Their high level of emission makes these devices suitable for several applications but by contrast the output powers of these devices are known to fall as an inverse square of the emitted frequency. Hence for frequencies above 0.1 THz, such sources are able to provide several hundreds of milliwatts of output power. However, near 1 THz the output power may reduce down to a few milliwatts or less. Due to their relative compactness, it may be appealing to use such devices in THz integrated circuits. In fact, a 0.2 THz GUNN diode is currently being used in a low cost THz imaging system [93].

THz Emitters: Generating pulsed THz radiation is more commonly performed using laser driven THz emitters by down converting the emitted radiation in the optical frequency range. The most widely used techniques are: (i) by shining femtosecond laser pulses on a photoconductive emitter such GaAs or Si on sapphire electrodes [94] (ii) by shining sub picosecond laser pulses on a non-linear crystal such as ZnTe or GaSe [95].

Free Electron Lasers: Achieving extremely high power THz emission has been recently performed using Free electron lasers [96]. The device using a 40 MeV electron beam is able to achieve up to a 5 times more intensified THz beam compared to photoconductive or optical rectifier emitter. Free-electron lasers generate continuous or pulsed variants of THz waves, providing up to six times more intensified beams than photoconductive emitters. This means that free-electron lasers have significant potential for applications where an improved signal-to-noise ratio is essential, or in the investigation of effects in non-linear THz spectroscopy.

THz Gas Laser: The gas laser has long been a prominent source of far-IR radiation, indeed since the very first lasers were developed in the early 1960's. Such gas lasers include optically pumped lasers in which a CO_2 laser is used to excite the rotational-vibrational states of low-pressure molecular gases. Methanol is a commonly used gas in such lasers, which are able to provide hundreds of milliwatts of THz emission at 0.11 THz. Gas lasers are also tuneable within a range

of 0.3 – 5 THz with a very limited power. Frequency tailoring in such lasers relies on the selection of the optimum gases that are available, which causes such devices to suffer from lack of frequency agility. In addition to that, gas lasers are also limited by the scalability factor due to their bulky size and they are expensive to maintain and operate.

THz Semiconductor Laser: Photonic devices such as semiconductor lasers diodes, which are typically compact sources of radiation in near-IR and optical range are also used to generate THz waves. In a semiconductor laser diode, emission takes place due to electric-dipole oscillation at the quantum level. For most material the band gap energy lies in the near-IR and optical frequencies. In long wavelength emission, the low band gap energy is required which most conventional semiconductors are unable to provide. As a result the THz spectrum has long remained inaccessible through conventional interband lasers, as it is difficult to achieve population inversion at a very small energy level separation between the bands. Apart from the quantum cascade laser (discussed in the next paragraph), the only other semiconductor lasers able to emit THz constitutes of p-type Ge laser or Si impurity lasers. In germanium lasers, lasing is achieved through population inversion between heavy and light holes of an electrically pumped p-doped Ge crystal. An external magnetic field is used in these devices to facilitate the process of population inversion. In a different variant of these lasers, lasing is also achievable between heavy and light holes in impurity states of a strained p-type crystal. Such variants do not require the presence of an external magnetic field to assist with achieving population inversion.

Quantum Cascade Lasers: The term quantum cascade laser (QCL) was first coined in 1994 [97] it being a novel mid IR source based on a series of juxtaposed quantum wells fabricated on a dielectric waveguide resonator. The quantum cascade consists of a repeating structure in which each repeat unit is made up of an injector and an active region. In the active region, the population inversion is created due to electrical pumping and electron transitions to a lower energy level occur accompanied by emitting photons at a specific wavelength. The electrons then tunnel between quantum wells and the injector region couples them to the higher energy level in the active region of the subsequent repeat unit. QCL has a lot of potential but may have operating temperature problem. One major issue faced by researchers developing long wavelength QCL's is the

lack of suitable waveguides. At long wavelengths, the intrinsic losses of most materials are substantially higher, hence it is important to reduce waveguide losses in THz QCL's that operate on low current threshold. Designing a suitable low loss and high confinement waveguide is still a critical challenge for many THz QCL developers.

1.5 Surface Plasmon Polaritons at THz Frequencies

SPPs at the interface between a conductor and a dielectric with refractive index n are due to a large SPP propagation constant $\beta > k_0 n$, leading to evanescent decay of the fields perpendicular to the interface. The amount of confinement increases with β . Conversely, localisation significantly decreases for frequencies $\omega \ll \omega_p$, where $\beta \rightarrow k_0 n$ [98].

The THz frequency regime has negligible field penetration into the conductor and thus highly delocalized fields. For metals, SPPs at these frequencies therefore nearly resemble a homogeneous light field in air incident under a grazing angle to the interface, and are also known as Sommerfeld-Zenneck waves [99, 100].

Due to the lower free electron density, semiconductors can exhibit a SPP propagation constant $\beta > k_0 n$ and thus field-localisation at THz frequencies resembling that for metals at visible frequencies, however with accompanying large absorption. Plasmon propagation of broadband THz pulses at the interface of a highly doped silicon grating has indeed been observed [101]. One intriguing aspect of using semiconductors for low-frequency SPP propagation apart from the enhanced confinement is the possibility to tune the carrier density and thus ω_p by either thermal excitation, photocarrier generation or direct carrier injection. Thus, active devices for switching applications seem possible. As a first step in this direction, Gómez- Rivas and co-workers have demonstrated the modification of Bragg scattering of THz SPPs on a *InSb* grating using thermal tuning [102].

The excitation and detection of broadband THz pulses, also known as THz time-domain spectroscopy, usually employs a coherent generation and detection scheme [84]. This allows a direct investigation of both amplitude and phase of the propagating SPPs.

The propagation of THz SPPs on flat metal films has been investigated using these broadband techniques, confirming the highly delocalized nature of the modes. For example, their penetration into the air space above a gold film

up to distances of multiple centimetres has been demonstrated for frequencies around 1 THz [103].

In addition to flat films, also cylindrical structures such as metallic wires can efficiently guide delocalized THz SPPs. Using a typical time-domain spectroscopy setup, Wang and Mittleman investigated the propagation of SPPs on a thin stainless-steel wire [104].

1.6 Aims and Objectives of the work

The discussion provided so far has provided an overview of the significant potential offered by surface plasmon polariton in both optical and THz frequencies. Hence the introductory information presented emphasises the motivation for conducting this research. To do so, the primary aims and objectives of this research work can be summarised as follows:

1. To develop and implement effectively a numerical simulation tool suitable to design plasmonic devices for optical and THz frequencies.
2. To use the tool to characterise different features of a plasmonic planar contra-directional coupler in nano scale in the optical frequency range.
3. To optimise the contra-directional coupler to minimise loss and device size.
4. To design a hybrid plasmonic waveguide and study its propagation characteristics with varying structural properties.
5. To design a rectangular dielectric coated plasmonic waveguide at THz frequency using the tool.
6. To study different aspects of the rectangular plasmonic guide to characterise its behaviour with structural and frequency change.

1.7 Presentation of the thesis

The work presented in this thesis is based on the research carried out by the author into the use of the versatile finite element method tailored specifically to handle the complex dielectric permittivity of materials. Further, the research reported here has been devoted essentially to the study of wave propagation in plasmonic waveguides at THz and optical frequencies. The discussion given in this section provides an outline of the structure of the thesis. Beginning with a general introduction, the first chapter introduces the reader to the historical development of light wave propagation, history and applications of surface plasmon, the benefits of the THz technology and surface plasmon application in THz frequencies. Several key areas of application have been identified which have the potential to provide a significant enhancement of the areas of every day applications of the technology.

The theoretical formulation of the Finite Element Method as a powerful numerical tool in analysing waveguide for THz and optical frequencies is described in Chapter 2. To do so, first a brief overview of the numerical techniques commonly used in waveguide analysis is presented outlining their advantages and limitations in analysing any type of waveguide. A brief history of the finite element method is also presented focusing on its importance in analysing waveguide problems. The fundamental mathematical relations derived from Maxwell's equations for the application of this approach in the solution of waveguides is also derived. Further, a comparison of several variational formulations is presented with an emphasis on the vector H field finite element formulation. The utilisation of triangular elements, the shape functions, and the infinite elements is undertaken in order to obtain the propagation constants and the field profiles of various modes supported by a uniform waveguide. The problem of spurious solutions is also investigated and the penalty function method is implemented to avoid the appearance of non-physical solutions.

Chapter 3 begins with a brief introduction to the physics underpinning the operation of a surface plasmon polariton. A brief introduction on the electron transition that occurs in a single metal-dielectric interface which lays the foundation for a novel plasmonic waveguide is shown in this chapter. Following that, brief analysis on three layer planar plasmonic structures are presented. The finite element simulation results presented here show the detailed dynamics of mode formation in these basic plasmonic structures. Finally, a rigorous analysis of a six-layer planar waveguide is also presented here where certain

parameters of the guide were varied to obtain the propagation and loss characteristics of the guide.

Chapter 4 presents a detailed analysis of a hybrid plasmonic waveguide at optical frequency. The structure and the underlying theory of the HPWG and its mode characteristics were investigated. In order to understand the properties and suitable applications of the waveguide, the confinement and propagation loss of the plasmonic waveguide have also been presented in this chapter. The results are then benchmarked with the results of a published paper which seemed in good agreement.

Chapter 5 provides a detailed insight into mode formation that can take place in plasmonic rectangular waveguides. The Chapter begins with an introduction to the various modes formed in this structure and their performances upon variation of width, height and metal layer thickness of the guide. By performing a rigorous analysis of the modes supported by the rectangular waveguide after introducing a dielectric coated layer, it is shown that the loss characteristics of the waveguide can be controlled by varying several parameters. It is further discussed in this chapter that the loss values of the guide ceases to virtually negligible values when the dimension of the waveguide was varied. It is shown that this enables the possibility of the waveguide to be used in many applications in integrated-optic devices and THz communications systems.

Finally in Chapter 6, general conclusions derived from this research work are summarised and explored further. Possible future prospects for this work are also suggested. Included within this thesis are three appendices. Appendix A provides the detailed analysis on the evaluation of the element matrices. Appendix B provides a detailed analysis for deriving the power confinement factor. The thesis concludes with a list of relevant publications in the major international literature by the author presented in Appendix C followed by a list of references cited in this work.

Chapter 2

Numerical Methods

2.1 Introduction

Advances made in modern device fabrication techniques and the continuous emergence of novel exotic materials have resulted in waveguides and related components used in today's photonics circuits having an intricate geometry and having materials with complex refractive indices. A robust and highly accurate simulation method is often required to address the challenges in defining and characterising such waveguides and devices. Defining and characterising such waveguides can be performed with various methods which can be classified into analytical approximation solutions and numerical solutions through computer aided simulations.

Analytical solutions can only be obtained for stepped 2-D optical waveguides and stepped optical fibres, where the refractive index changes gradually in the thickness and the radial direction respectively. Such solutions use the Ray Approximation Method (RAM) [105], and the Wentzel, Kramers Brillouin (WKB) method [106].

For three dimensional waveguides which are more commonly used in today's photonics systems and circuits, analytical solutions in compact form are not always obtainable. In addition, the analytical solutions do not always treat the modes in complex waveguides as hybrid modes but rather as purely of a single polarization. For that reason their accuracies are sometimes questionable in certain cases. Whenever exact analytical solutions are not available, approximate methods are often sought. Most engineering problems involve the derivation of partial differential equations, relating the variables of interest, which are based on physics and engineering principles. The development of approximate methods for the numerical solution of partial differential equations has attracted the attention of mathematicians, physicists and engineers for

a long time. There are a number of approximate theoretical and numerical techniques that could be used to determine the useful characteristics of propagation in waveguides.

2.2 Analytical approximation solutions

Analytical approximation solutions are very widely used in many applications for the determination of the propagation characteristics of various types of optical waveguides, with relatively simple geometry. Such solutions are the Marcatili Method [107] and the Effective Index Method [108].

2.2.1 Marcatili's Method

In the Marcatili's method (MM) [107], the field in a rectangular dielectric waveguide (a dielectric rod with rectangular cross-section, surrounded by four different dielectrics of lower refractive indices), is approximated to the fields in two slab waveguides, obtained by extending the width and the height of the rectangular core to infinity. The rectangular dielectric waveguide is assumed to support a well-confined mode, therefore, only the regions on each side of the dielectric rod are considered to carry appreciable amount of field, and the problem is then decoupled in two slab waveguides, one at each transverse direction. The field in the centre region is assumed to vary sinusoidally, while that in the substrates is considered to decay exponentially. Transcendental equations [109] are then derived for each transverse direction, each of them giving a transverse propagation constant. The axial propagation constant of the waveguide is then calculated from the transverse propagation constants, obtained by solving simultaneously the two transcendental equations. In a similar way, the MM can also be applied to the solution of the directional coupler problem. The above approach works well in the far-from cut-off region but gives poor results in the near-cut-off region [110].

2.2.2 The Effective Index Method

The Effective Index Method (EIM), is an improvement of the Marcatili's method, proposed by Knox and Toullos (1970) [108]. In this approach, the core of a rectangular dielectric waveguide is replaced by an equivalent slab with an effective index obtained from another slab. The dielectric core is decoupled into two slab waveguides, one at each transverse direction, and the transcendental equation

is first solved in one direction, by applying the appropriate boundary conditions. The effective index calculated is then used as the refractive index of the centre region in the solution of the transcendental equation in the other transverse direction, which is obtained by applying boundary conditions in that direction. The new effective index obtained corresponds to the overall effective index of the waveguide.

The above approach does not give satisfactory results near the cut-off region, therefore, several techniques have been proposed to improve the accuracy of the method. Zhou and Itoh (1982) [111] used the approach for a trapped image guide, where they replaced the original waveguide by an equivalent structure. Then they imposed the transverse resonance at the dielectric-air interface, to include the free-space regions of the guide and solved the problem in terms of the surface impedances in an approximate manner, with an improved accuracy at low frequencies. Chiang *et al.* [112] derived an expression for the error in the propagation constant of a rectangular waveguide, which occurs by using the conventional EIM, and proposed a new effective-index approach with a built-in perturbation correction of the above error, suitable for rectangular dielectric waveguides, channel waveguides, strip waveguides and arrays of such waveguide structures. Chiang *et al.* [113], proposed a dual effective index approach, in which, by combining two solutions, corresponding to two different ways of applying the EIM to the waveguide, they achieved the elimination of the errors occurring by applying each solution separately.

2.3 Numerical Approximation Solutions

The numerical solutions of waveguides can be classified into two groups. These are the domain solutions, also known as differential solutions, in which the whole domain of the optical waveguide is considered as the operational area, and the boundary solutions, also known as integral solutions, which include only the boundaries as the operational area. The Variational Method (VM), the Finite Element Method (FEM), the Finite Difference Method (FDM), and the Multilayer Approximation Method (MAM) are some of the most commonly used domain solutions, while, the Boundary Element Method (BEM), the Point Matching Method (PMM) and the Mode Matching Method (MMM), are typical boundary solutions [114].

Most of the numerical solutions are concerned with methods of finding a

numerical solution to the Helmholtz wave equation, which can be derived directly from Maxwell's equations and can be expressed as [115]:

$$\nabla^2\Phi + k^2\Phi = 0 \quad (2.1)$$

Equation (2.1) is valid over the entire cross section of an arbitrarily shaped waveguide, bounded by the closed curve. The equation is also subject to boundary conditions which can be of both Dirichlet and Neumann type.

2.3.1 The Variational Method

In the variational approach, a field solution of the optical waveguide problem, usually based on the wave equation is assumed, where the unknown parameters are chosen to match the assumed field to the actual field solution. The above solution is then expressed in integral form, in terms of a functional satisfying the boundary conditions of the problem. The stationary value of the functional about the correct solution, with respect to small variation of the field values, is achieved by minimizing the integral expression. Then by using trial functions to represent the field solutions, the integral equations are reduced to a set of linear equations which can be solved by standard numerical techniques. The accuracy of the results depends on the choice of the trial functions [116], which must be sufficiently differentiable and satisfy the boundary conditions. The variational method forms the basis of other fundamental numerical techniques, such as the Finite-Element and the Finite-Difference methods, which are discussed in the following sections.

2.3.2 The Finite Difference Method

The finite difference method (FDM) [117], is one of the most rigorous and perhaps the most commonly used numerical method used for the solution of boundary value problems. In FDM, a finite cross-section is defined by enclosing the optical waveguide under investigation in a rectangular box, where the side walls may be either electric or magnetic walls, in order to include coupled structures. At the boundaries of the enclosing rectangular box, the fields are assumed to be negligibly small, therefore infinite elements with an associated decay factor can be introduced, to approximate the infinite exterior region. The cross-section of any non-homogeneous optical waveguide is implemented by a rectangular grid, where it is essential that all the dielectric boundaries must lie on points of the above grid. By considering any arbitrary nodal point of the

rectangular grid, the corresponding nodal field value can be expressed in terms of the neighbouring nodes, in the two transverse directions, by the five-point formula of finite differences, which is based on a Taylor series expansion. The Helmholtz wave equation (shown earlier in equation (2.1)), or a variational expression, can be arranged into a set of two coupled wave equations, one for each transverse direction H_x and H_y , which can be discretized in the five-point finite difference form. By imposing the correct continuity conditions of the fields between the adjacent cells of the grid, an eigenvalue matrix equation of the type $[A]x - \lambda[B]x = 0$ can be formed (where λ is the eigenvalue), which can be solved by using sparse matrix techniques.

The main disadvantage of finite difference methods are the lack of geometrical flexibility in fitting irregular boundary shapes, and in concentrating points in regions of the solution domain where the variable changes rapidly. Moreover, using the finite difference methods difficulties also arise in treating singular points and when any boundary or interface boundary does not coincide with constant coordinate surfaces.

2.3.3 Point Matching Method

The point matching method (PMM) can be classified as a typical boundary solution of the optical waveguide problem, and as an approach in which the electromagnetic field is expanded in a series of orthonormal functions (basis functions). It was first proposed by Goell [118] for the solution of the rectangular optical waveguide, where the radial variation of the longitudinal electromagnetic fields of the modes can be represented by a series of circular harmonics. In the above approach the electromagnetic fields inside the waveguide core are expressed by a sum of Bessel functions and their derivatives, with the fields outside the core by a sum of modified Bessel functions and their derivatives, both multiplied by trigonometric functions. Solutions can be obtained by imposing boundary conditions of the above fields at a finite number of points, named matching points, placed symmetrically along the boundary of the waveguide core. The matching of the tangential electromagnetic fields leads to continuity equations, arranged into matrix form, from which the eigenvalues and the expansion coefficients can be determined.

The above approach can be applied to dielectric waveguides having arbitrary cross sections, composite dielectric waveguides having multiple dielectric materials and coupled dielectric waveguides composed of multiple waveguides. The number of matching points lies only on the boundaries of the structures, and therefore, less computational time and memory capacity are required for the solution of the problem, compared to the use of other numerical approaches, such as the FEM and the FDM, where nodal points are required, not only for the boundaries, but for the whole waveguide cross section, as well. However, it is difficult to apply the method to structures with a three-dimensional boundary surface, or to structures with an index distribution within the waveguides, such as graded index fibers [119].

Cullen *et al.* [120] improved the approach, by rotating the grid of equiangularly spaced matching points, in order to place matching points at the corner of a rectangular dielectric waveguide, to reduce the overall mismatch at the boundary. Bates and Ng [121], in a review of the method, examined the validity of the expansions in the approach, the accuracy and the convergence as the number of matching points increases.

2.3.4 The Boundary Element Method

The boundary element method (BEM) [122] is a computer technique, where the basic equations are boundary integral equations, which are solved numerically, by dividing the integration domain into a set of elements. The approach has similar features with the FEM, but instead of taking unknown nodal field values throughout the waveguide region, as in the FEM, in the BEM the unknowns are taken only along the boundary. The solution of the problem, is accomplished by first deriving integral equations with respect to unknowns taken on the boundaries. The integral equations are then discretized to linear equations, to obtain numerical solutions, which are again expressed in integral forms in order to represent the values of various physical quantities. Integral representations play a key role throughout the process, not only in the derivation of integral but also in the evaluation of the physical quantities. Various integral representations can be used, depending on the particular case, with the Green's formula being the most popular for many applications.

The BEM offers the ability to deal with odd-shaped boundaries, as the FEM, but with far less number of unknowns, since unknown values are considered only along the boundary, while in the FEM, these are considered for the whole waveguide cross-section, less memory storage and less computational time are

required. Unlike the FEM, the BEM automatically incorporates the boundary conditions at infinity and no infinite elements are required. Additionally, both approaches may have the same discretization schemes, thus enabling the FEM to be used for the same case. The BEM is limited though to homogeneous structures, while some unphysical solutions, known as resonant solutions, may be involved. Another drawback of the BEM is that it may require some analytical treatment and more programming, in some cases where the Green's function has some singularities with respect to the integral equations. Also the BEM formulation yields dense matrices, while in the FEM they remain sparse, therefore offering a more efficient matrix solution.

Zhu and Zhang [123] reported a modified BEM for the solution of waveguide problems, named the eigenweighted boundary integral equation method, in which a fictitious boundary and a set of eigenfunctions satisfying the boundary conditions were introduced, but they reduced the weighting of eigenfunction in only one term, rather than an infinite series in modified Green's functions, thus increasing the computational efficiency. Nallo *et al.* [124] developed a BEM formulation, for cylindrical dielectric structures, by expressing the fields inside and outside the cylinder by means of free space dyadic Green's functions, enabling a great flexibility in the choice of basis functions for the unknowns, thus enlarging significantly the class of algorithms for the numerical solution of the integral equations.

2.3.5 The Mode Matching or Equivalent Network Method

The mode matching method (MMM) [125], which is also known as the equivalent network method (ENM), is an approximate analysis used for the determination of the propagation characteristics of an open dielectric waveguide. In the above approach, the open waveguide structure is considered artificially bounded, therefore the TE-TM coupling and the continuous spectrum distribution at the sides of the waveguide are neglected [126]. The waveguide cross section is viewed in terms of its constituent parts or building blocks, which are usually portions of uniform dielectric layered structures interfaced by dielectric step discontinuities. The fields in the various regions are then expanded in terms of transverse modal expansions over each region, thus resulting in a microwave equivalent circuit representation of the waveguide. The uniform dielectric regions are then represented by uniform transmission lines with their characteristic impedances, and the various step discontinuities are modelled by a set of transformers, where equivalent network admittances take into account

the effects of the outer region. Therefore, it is possible to model the whole spectrum of open waveguide structures as a cascade of uniform regions and step discontinuities. By applying boundary conditions to the above modes and a transverse-resonance condition, which requires that, for a particular mode, the total admittance seen at any of the ports is zero, the dispersion relation for the propagation constant can be obtained.

For more accurate analysis of open waveguide structures, which exhibit continuous and discrete modal spectra, the continuous spectrum should be discretised by suitable basis function expansions, rather than by artificially bounding the structure [127]. Additionally, the effects of the TE-TM coupling at the sides of such structures, must be taken into account. Koshiya and Suzuki [128] reported a vectorial wave analysis of optical waveguides with a rectangular structure by the ENM, where by taking into consideration the discrete-continuous spectrum coupling and the TE-TM coupling, they calculated the propagation characteristics. Dagli and Fonstand [127] extended the ENM to GaAs Rib waveguides, directional and three guide couplers, by cascading the models of single waveguide structures.

2.3.6 The Spectral Index Method

The spectral index method (SIM), is a relatively fast and accurate approach, in which the wave equation is expressed in terms of Fourier transforms and Fourier series. It has been applied in the solution of the simple semiconductor rib waveguide [129][130] and the strip loaded directional coupler [131]. Recently, Pola *et al.* [132] have extended the approach to multiple rib waveguides. By considering a simple semiconductor rib waveguide, the SIM replaces the original rib structure by an effective structure, by displacing the actual physical dimensions to new ones on which the optical field is zero, in order to model the penetration of the optical field into the cladding. The method consists of expanding the fields in terms of local modes and matching the fields along the base of the rib. The E- or H-field (depending on the polarization) inside the rib region, is expressed in terms of trial functions, such as cosine and sine Fourier series, representing the symmetric and antisymmetric modes respectively. In the region below the rib, the wave equation is expressed in terms of its Fourier Transform and the problem is reduced to a 1-D slab problem, where the refractive indices of the layers below the rib are represented by their corresponding spectral indices. The equations for the two regions are then linked via a transfer

relation and a transcendental equation is formed, which determines the propagation constant of the waveguide. In order to overcome the field discontinuities in the rib region, an effective width is introduced, while in the Fourier transform for the region below the rib, the evanescent regions are expressed by imaginary spectral indices.

Although the method requires much less computational time than other numerical methods, such as the FDM and the FEM, in the presence of dielectric corners the electric field exhibits a singular behaviour produced by its transverse components. This makes the design of rapidly converging numerical algorithms for vector mode field computations difficult [133].

2.3.7 The Method of Lines

The method of lines (MOL) is a semi-analytical approach, suitable for the analysis of the hybrid modes of optical waveguide structures. The method was first applied to microwave devices by Schulz and Pregla [134], for the analysis of the dispersion characteristics of isotropic planar waveguides and microstrips. Later on a modified version of the method was proposed [135] to treat cases having uniaxially anisotropic regions, such as finline/strip configurations on an anisotropic substrate. Rogge and Pregla [136] applied the method for the analysis of strip-loaded film and rib waveguides, and Gerdes *et al.* [137] to optimize broad-band electro-optic modulators with asymmetric co-planar strip electrodes. Also, this approach was used for the analysis of multilayered gyrotropic waveguide structures, where a complex permittivity and susceptibility were considered for the magnetised gyromagnetic and gyroelectric media, respectively [138]. Recently, the application of the MOL was reported in modelling optical waveguides with lossy inhomogeneous anisotropic media [139].

In the MOL, the optical waveguide is enclosed in a rectangular box, with electric or magnetic walls at the sides, satisfying the boundary conditions of the required polarization. The waveguide cross section is then divided into a set of equidistant lines along the one transverse direction, resulting in the discretisation of the electromagnetic fields, which are calculated on the lines along the other transverse direction. By substituting difference operators for the second derivatives of the electromagnetic wave equations, a system of coupled ordinary differential equations, for each dielectric layer, is obtained. By suitable matrix transformations, the above system is uncoupled and the equations can

be solved analytically. Further application of boundary conditions at waveguide discontinuities leads to a matrix equation, from which the eigenvalues can be determined.

The above approach is related to a discrete Fourier transformation, therefore the calculation of the fields on the discretisation lines is very accurate. Since the interface conditions on dielectric steps are included, discontinuous field curves can be described accurately [140]. Nevertheless, it is difficult to apply for waveguides with curved boundaries and the accuracy in the near cut-off region is limited to the finite size of the rectangular box, as in the finite-difference method [141].

2.3.8 The Beam Propagation Method

The research on integrated optical circuits (IOC) and optical planar devices, has emerged from the necessity of calculating the propagation of a light wave in an optical circuit having an arbitrary refractive index distribution. This type of field propagation can be simulated numerically by the beam propagation method (BPM), an approach that was developed in underwater acoustics and seismology before it was adapted to optical waveguide problems by Feit and Fleck [142]. Since then, it has been widely used for analysing the performance of a light beam propagated in an optical planar circuit that has a nearly stripelike waveguiding structure and in which the refractive index varies smoothly compared with the wavelength. The main features of the BPM are that the electromagnetic fields are Fourier transformed with respect to the direction normal to that of light propagation and that a stepwise method is used for successively calculating the electromagnetic field along the axial direction.

In the BPM, the optical field is transported within one propagation step, from the transverse plane at the longitudinal coordinate z , to the transverse plane at $z + \Delta z$. Calculations are performed, to relate the optical fields at the input and output planes, which are based on the assumption that the dielectric profile within one step, Δz , remains unchanged [143]. As the optical field propagates through a medium, it is subject to diffraction due to its wave nature, and the light rays of the wave experience a certain amount of phase shift, depending on their x, y positions. The above influences can be applied one at a time, provided that the space along the path is subdivided into very small sections. By doing so, the continuous medium can then be realised as a series of lenses separated by short sections of homogeneous space, where the contribution of the lenses in the phase shift is expressed in the solution of the wave equation.

For computational purposes, the wave between the lenses can be decomposed into its spectrum of plane waves by applying a Fast Fourier Transform (FFT) algorithm, and then it is reconstructed halfway, $(\Delta z/2)$, before the next lens, by applying the inverse FFT. The above process is repeated for each section along the whole propagation path. The propagation step size Δz , which must be at most one wavelength of the light beam, must ensure that the contribution of evanescent waves, which are part of the plane wave, is negligible, and that the rays associated to the wave, travel parallel to the z -axis, with minimum phase shift.

The BPM is widely accepted as a powerful method for the analysis of non-uniform structures. But this method requires more computational resources as discretizations in both the transverse and the longitudinal planes are required [141]. To handle the discretization in the transverse plane, two-dimensional methods can be employed, such as the FDM [144] and the FEM [145]. The latter can be used in many devices, such as directional couplers, optical fibers, bent optical waveguides, Bragg and diffraction gratings, tapered optical waveguides and optical Y -junctions. It can also be used in conjunction with other numerical techniques such as the Fresnel approximation [144].

2.3.9 The Finite Element Method

The finite element method (FEM) has emerged as one of the most successful numerical methods for the analysis of waveguides from low frequency to microwave to optical region. It is indeed capable of solving waveguides of arbitrary refractive index distribution. In the work presented in this thesis, a full-vectorial \mathbf{H} field based FEM has been used to characterise waveguides operating at terahertz and optical frequencies. Such methods are capable of handling a wide range of inhomogenous problems with greater ease. It is also capable of solving anisotropic problems.

In this approach, any waveguide cross-section can be divided into a patchwork of triangular elements, where the appropriate field components are approximated by polynomial expressions over these elements. Each element can have different dielectric material, which may be anisotropic, non-linear or lossy. The FEM, which is based on the Ritz-Galerkin approach, converts a continuous system into a discretized model. By applying the variational principle [146] to the functional of the system, the problem reduces to a standard eigenvalue matrix equation $[A]x - \lambda[B]x = 0$, which can then be solved by using standard matrix solver algorithms. The FEM can be used effectively for the analysis

of various optical waveguides, with any shape, including 2D and 3D optical waveguides, axisymmetrical and non-axisymmetrical optical fiber, and non-linear optical waveguides. The FEM is based on the same principles as the FDM, therefore a comparison of the two methods can be attempted. Although in the FDM simpler matrix eigenvalue equations are formed, which are formulated with less computer programming, less computer memory storage and execution time, and the solution is free of spurious modes ($H_x - H_y$) formulation, the above approach cannot be easily applied to structures with odd-shaped boundaries. The triangular elements used in the FEM can give a better fit to such structures and also the change of the density or the order of the elements, in regions where there is more rapid field variation, is performed more easily with the FEM. Additionally, in the FEM, the field is defined explicitly everywhere and this makes for easier manipulation, such as when evaluating spatial derivatives to give related fields [146].

2.3.10 Time Domain Analysis

All methods discussed up to now produces a steady state field distribution of one specific frequency. Transient or time varying responses of the photonic devices cannot be studied by the above mentioned methods. Study of broadband characteristics of photonic devices is also difficult using the above mentioned methods because any broadband signal will contain more than one frequency and the shape of the signal may vary with time depending on the type of the signal used to excite the device. To tackle such problems, time domain analysis methods were developed. The time domain analysis of EM and photonics started with Yee's algorithm [147] for Finite Difference analysis of time domain problems. Followed by Finite Integration [148, 149, 150], Finite Volume [151, 152] and Finite Element [153, 154, 155, 156, 157, 158, 159, 160] based methods.

Finite Difference Time Domain Method

In 1966 Yee [147] proposed a finite difference based technique to solve Maxwell's equations over time to analyse time domain properties of Electromagnetics. The method he proposed is widely known as Finite Difference Time Domain or the FDTD method. The method solves the Maxwell's equations in their differential form on a rectangular grid for 2D and cuboid grid for 3D. The method uses a special staggered distribution of field components to solve the Maxwell's

coupled equations. It calculates \mathbf{E} and \mathbf{H} field components at different space nodes and \mathbf{E} and \mathbf{H} fields at different time-steps.

The advantages of the FDTD methods are as follows,

1. It can handle broadband signals. Therefore, frequency response of a structure can be calculated by performing a single simulation.
2. As the field from the injecting source evolves with time, transient response of a device can be observed.
3. Effect of non uniform structure, bending, truncation, fracture etc. can be observed and measured using the FDTD method.
4. It also solves an explicit form of Maxwell's equation in localised manner for each cell which results in a highly data parallel technique.

The FDTD method has the following disadvantages,

1. The method supports all possible modes in the same simulation. Therefore, it is not possible to characterise each mode without explicitly injecting the mode into the structure.
2. It is a finite difference method. Therefore, using dense and coarse regions in one computational domain could be less efficient compared to finite element techniques.
3. Due to the use of FD grid, it has numerical dispersion issues.

Finite Element Based Techniques

As mentioned in the above section, the problems associated with the FDTD methods mostly arise from the grid. Therefore, the general idea is that a better grid or meshing technique could improve the performance of the grid and improve the overall performance of the time domain analysis.

To represent the structure more accurately, researchers have considered the FEM for time domain analysis [156, 154, 155, 161, 162, 159]. Although these methods are sometimes more accurate in structural representation, however some of them may require an implicit solution of the computational domain for each time step [163], some require the solution of large matrices [156] and some require higher order solutions of Maxwell's equations [154, 162, 159].

2.3.11 Frequency domain over Time domain

To analyse characteristics of the plasmonic waveguides in this thesis both the FEM method or the FDTD time domain could be used. However, for this work, the FEM method was chosen over the time domain method because of the following reasons.

1. The time domain method requires a 3D grid to solve the problem and to get the steady state solution it needs to solve the entire computational domain many times. Therefore, it is a slow process. On the other hand, the FEM method needs to solve only a 2D cross-section of the computational domain. Therefore it is much faster in getting the solution.
2. Time domain cannot separate modes with different propagation constants. Therefore, to analyse the characteristics of one single mode, that mode profile needs to be injected into the input of the waveguide. To get that appropriate mode profile, the FEM method is needed in the first place. The steady state parameters could be calculated directly from the FEM results.
3. Time domain method can calculate the dispersion characteristics of a broad band signal in one simulation. But that leaves a possibility of generation of other modes. This is because the mode profiles for all frequencies are not the same. As a result, with time domain the propagating wave will evolve into the supported modes. Therefore, more than one mode could couple into the guide. This will lead to a less accurate solution.
4. Similar problem exists for bending analysis as the reflected wave from the boundary could couple into other unwanted modes leading to less accurate results. On the other hand a simple coordinate transformation could allow us to calculate the bending characteristics for one mode using the FEM.

2.4 Theoretical Background

Mathematically, the FEM is a numerical technique for obtaining approximate solutions to boundary-value problems, and it is the extension of two classical methods, the Raleigh-Ritz variational method, and the Galerkin method of weighted residuals. A boundary value problem can be defined by a governing differential equation in a domain, together with the boundary conditions

on the boundary that encloses the domain. In the variational approach the boundary-problem is formulated in terms of variational expressions, referred to as functionals, whose minimum corresponds to the governing differential equation. The approximate solution is obtained by minimising the functional with respect to its variables [164]. The Galerkin method is based on the method of weighted residuals [146], in which the domain of the differential equation is discretized, and the solution is approximated by the summation of the unknown solutions for each subdomain weighted by known functions, relating them to the domain. The overall solution is obtained by minimising the error residual of the differential equation.

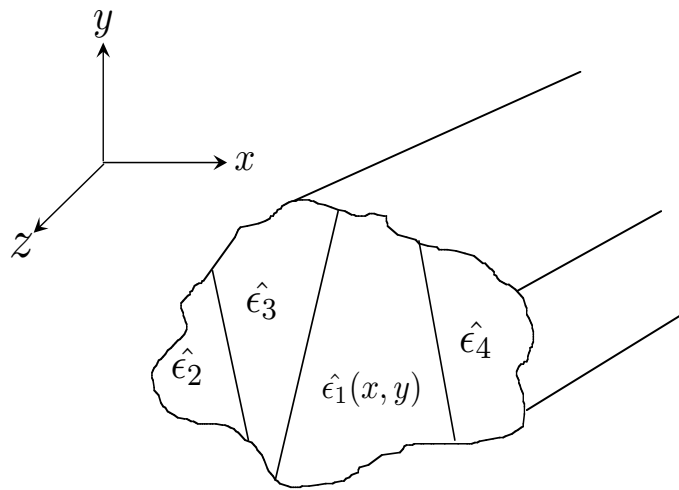


FIGURE 2.1: Arbitrarily shaped optical waveguide, divided into arbitrary sub-domains, each having different type of material.

Research on the application of the FEM to electromagnetic-wave engineering began during the last years of the 1960s and since then, with the availability of larger and faster computers, it has been established as a very powerful tool dealing with the analysis of optical waveguides, particularly structures with arbitrary shapes, index profiles, nonlinearities and anisotropies. A cross section of an arbitrarily shaped optical waveguide, Ω , in the $x - y$ transverse plane as shown in Fig. 2.1 is considered, divided into a number of sub-domains, called elements, being composed of several different materials, each of which can be described by arbitrary permittivity and permeability tensors, $\hat{\epsilon}(x, y)$ and $\hat{\mu}(x, y)$ respectively. A uniform shape of the waveguide along the longitudinal z axis, is assumed and time and axial dependencies are given by $e^{j\omega t}$ and $e^{-\gamma z}$, where,

ω is the angular frequency and the complex propagation constant, γ , given by:

$$\gamma = \alpha + j\beta \quad (2.2)$$

where α (Np/m) is the attenuation constant and β (rad/m) is the phase constant. For a lossless case, the propagation constant is considered to be equal to the phase constant, $j\beta$. The electric, $\mathbf{E}(x, y, z, t)$ and the magnetic $\mathbf{H}(x, y, z, t)$ fields over the region of the waveguide can be expressed by:

$$\mathbf{E}(x, y, z, t) = \mathbf{E}(x, y)e^{j(\omega t - \beta z)} \quad (2.3)$$

$$\mathbf{H}(x, y, z, t) = \mathbf{H}(x, y)e^{j(\omega t - \beta z)} \quad (2.4)$$

where $\mathbf{E}(x, y)$ and $\mathbf{H}(x, y)$ are the spatial time-independent electric and magnetic fields respectively.

2.4.1 Basic Equations

Maxwell's Equations

Maxwell's equations comprise a set of four electromagnetic field vectors, which represent the governing laws of the electromagnetic wave phenomena. The four vectors are: the electric field intensity \mathbf{E} (Volts/metre), the magnetic field intensity \mathbf{H} (Amperes/metre), the electric flux density \mathbf{D} (Coulomb/metre²) and the magnetic flux density \mathbf{B} (Tesla). For time dependent fields they can be written in differential or integral forms. Since the FEM is a boundary-value problem which is defined by differential equations, Maxwell's equations are presented in differential form as follows:

$$\nabla \times \mathbf{E} = -\frac{\partial \mathbf{B}}{\partial t} \quad (2.5)$$

$$\nabla \times \mathbf{H} = \frac{\partial \mathbf{D}}{\partial t} + \mathbf{J} \quad (2.6)$$

$$\nabla \cdot \mathbf{D} = \rho \quad (2.7)$$

$$\nabla \cdot \mathbf{B} = 0 \quad (2.8)$$

where ρ , is the scalar volume electric charge density (coulomb/metre³) and \mathbf{J} is the electric current density (Amperes/metre).

The associated constitutive equations for the medium can be written as:

$$\mathbf{D} = \epsilon \mathbf{E} \quad (2.9)$$

$$\mathbf{B} = \mu \mathbf{H} \quad (2.10)$$

where ϵ is the permittivity and μ is the permeability of the medium and can be defined by:

$$\epsilon = \epsilon_0 \epsilon_r \quad (2.11)$$

$$\mu = \mu_0 \mu_r \quad (2.12)$$

where ϵ_0 , ϵ_r , μ_0 and μ_r are the permittivity of the vacuum (8.854×10^{-12} Farad/metre), the relative permittivity of the medium, the permeability of the vacuum ($4\pi \times 10^{-7}$ Henry/metre) and the relative permeability of the medium respectively.

Boundary Conditions

Boundary Conditions are conditions that must be met at the boundary surface when two different media 1 and 2 come into contact. If the unit normal vector \mathbf{n} , is directed from medium 1 to medium 2 as shown in Fig. 2.2 in the absence of any surface currents ($\mathbf{J} = 0$) and surface charges ($\rho = 0$), the following boundary conditions apply:

1. The tangential component of the electric field must be continuous.

$$\mathbf{n} \times (\mathbf{E}_1 - \mathbf{E}_2) = 0 \quad (2.13)$$

2. The tangential component of the magnetic field must be continuous.

$$\mathbf{n} \times (\mathbf{H}_1 - \mathbf{H}_2) = 0 \quad (2.14)$$

3. The normal component of the electric flux must be continuous.

$$\mathbf{n} \cdot (\mathbf{D}_1 - \mathbf{D}_2) = 0 \quad (2.15)$$

4. The normal component of the magnetic flux density must be continuous.

$$\mathbf{n} \cdot (\mathbf{B}_1 - \mathbf{B}_2) = 0 \quad (2.16)$$

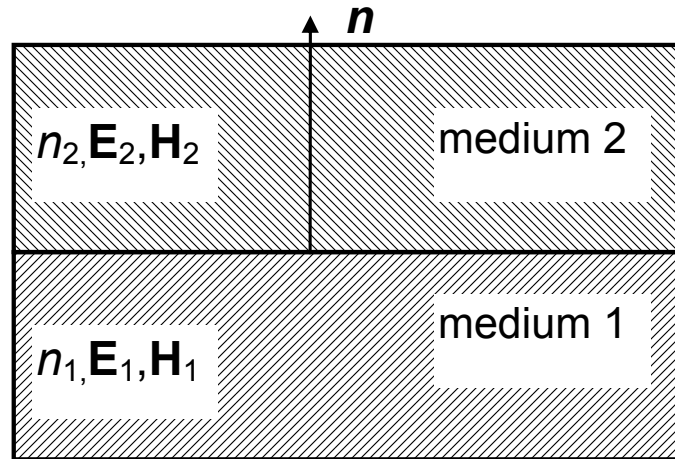


FIGURE 2.2: Boundary between two media of refractive indices n_1 and n_2 , where \mathbf{n} is the unit vector normal to the interface.

In certain cases, one of the two media can be considered either as a perfect electric conductor or a perfect magnetic conductor. When one of the two media becomes a perfect electric conductor, an electric wall boundary condition is imposed as:

$$\mathbf{n} \times \mathbf{E} = 0 \quad \mathbf{n} \cdot \mathbf{H} = 0 \quad (2.17)$$

Such a condition ensures the continuity of the normal component of the electric field vector, \mathbf{E} , and vanishes the magnetic field vector, \mathbf{H} , at the boundary.

When one of the two media becomes a perfect magnetic conductor, a magnetic wall boundary condition is imposed as:

$$\mathbf{n} \times \mathbf{H} = 0 \quad \mathbf{n} \cdot \mathbf{E} = 0 \quad (2.18)$$

The above condition, vanishes the electric field vector, \mathbf{E} , and ensures the continuity of the normal component of the magnetic field \mathbf{H} at the boundary.

In the case of a closed surface, such as the boundary of an optical waveguide, additional boundary conditions are considered. These boundary conditions can be natural, in cases where the field decays at the boundary, therefore they can be left free. In some other cases they can be forced, in order to take advantage

of the symmetry of a waveguide, to reduce the number of elements in FEM (and the order of the matrices), or to impose complementary symmetry to the waveguide, in order to achieve the required polarization. The above boundary conditions can be classified as follows [146]:

$$\Phi = 0 \quad \text{Homogenous Dirichlet} \quad (2.19)$$

$$\Phi = k \quad \text{Inhomogenous Dirichlet} \quad (2.20)$$

$$\frac{\partial \Phi}{\partial \mathbf{n}} = 0 \quad \text{Homogenous Neumann} \quad (2.21)$$

where Φ can be the electric or magnetic field, k is a prescribed constant value and \mathbf{n} is the unit vector normal to the surface.

The Neumann boundary condition represents the rate of change of the field when it is directed out of the surface and it can be used in the FEM to impose the field decay along finite-elements, adjacent to the boundary elements of a waveguide structure.

Wave Equations

In an isotropic lossless medium with no wave source ($\mathbf{J} = 0$, $\rho = 0$), with uniform permeability $\mu = \mu_0$, and uniform and constant permittivity, by eliminating the magnetic flux density and the electric flux density components from Maxwell's equations 2.5 and 2.6, these can be written as:

$$\nabla^2 E + k^2 E = 0 \quad (2.22)$$

$$\nabla^2 H + k^2 H = 0 \quad (2.23)$$

where the wavenumber, k (rad/m) is given as:

$$k = \omega \sqrt{\epsilon \mu_0} \quad (2.24)$$

If $\epsilon = \epsilon_0$, then the wavenumber k_0 is called the free space wavenumber and is defined by:

$$k_0 = \omega \sqrt{\epsilon_0 \mu_0} \quad (2.25)$$

Equations 2.22 and 2.23 are known as vector Helmholtz wave equations [165] for homogeneous media, and in addition to the physical solutions, they also support non-physical, spurious solutions, since the condition $\nabla \cdot \mathbf{B} = 0$, is not satisfied. In a rectangular coordinate system, if only one component of the electric or magnetic field is considered, suppose E_x , the vector Helmholtz wave equation can lead to the scalar Helmholtz wave equation as [115]:

$$\nabla^2 E_x + k^2 E_x = 0 \quad (2.26)$$

2.5 Variational Formulations

The finite-element formulation is based on the variational or Raleigh-Ritz approach, therefore, several variational formulations have been proposed for the analysis of the optical waveguide problem. These can be in a scalar form [166], where the Electric or Magnetic field is expressed only in terms of one component, according to the predominant field component, or, can be in vector form, where the Electric or Magnetic field is expressed in terms of at least two of the constituent field components.

It should be noted that most of the formulations applied in the FEM, yield to a standard eigenvalue problem:

$$[\mathbf{A}]\{x\} - \lambda[\mathbf{B}]\{x\} = 0 \quad (2.27)$$

where $[\mathbf{A}]$ and $[\mathbf{B}]$ are real symmetric sparse matrices, and \mathbf{B} is also positive definite. The eigenvalue λ can be chosen as β^2 or k^2 depending on the formulation, and the eigenvalues represent the nodal field values of the finite-elements. It is desirable for the above matrix equation to be of this canonical form, to allow an efficient solution.

2.5.1 Scalar Approximation

The scalar approximation can be applied in situations where the field can be described as predominantly TE or TM and it can be expressed in terms of the longitudinal components of the above modes. It has been used for the solution of homogeneous waveguide problems [167], open boundary problems [168], and for the analysis of anisotropic waveguides [169]. For the quasi-TE modes

over a region Ω , where the dominant field component is E_x , the formulation can be written as [166]:

$$L = \int \int_{\Omega} \left[\left(\frac{\partial E_x}{\partial x} \right)^2 + \left(\frac{\partial E_x}{\partial y} \right)^2 - k_0 n^2 E_x^2 + \beta^2 E_x^2 \right] d\Omega \quad (2.28)$$

where, β is the propagation constant and n is the refractive index. For the quasi-TM modes, where H_x is the dominant field, the formulation can be written as [166]:

$$L = \int \int_{\Omega} \left[\frac{1}{n^2} \left(\frac{\partial H_x}{\partial x} \right)^2 + \frac{1}{n^2} \left(\frac{\partial H_x}{\partial y} \right)^2 - k_0 H_x^2 + \frac{1}{n^2} \beta^2 H_x^2 \right] d\Omega \quad (2.29)$$

2.5.2 Vector Approximation

The scalar formulation is inadequate to handle general anisotropic or inhomogeneous problems and it can be used only as an approximation in such cases. For a more accurate representation of general waveguide fields, a vector formulation, with at least two components is essential. Several vector formulations dealing with optical waveguide problems have been proposed by many authors. However, some of them are affected by non-physical spurious solutions, which appear mixed with the correct ones in the computations, and therefore several methods have also been proposed to overcome such problems.

The $E_z - H_z$ formulation which was one of the first formulations used in finite-element analysis [170], [166] cannot treat general anisotropic problems without destroying the canonical form of the eigenvalue equation A.1. In addition to that, some problems also arise whilst enforcing boundary conditions for a waveguide with an arbitrary dielectric distribution. Additionally, this approach is based on the axial field components which are the least important of the \mathbf{E} and \mathbf{H} fields.

A vector \mathbf{E} -field formulation [171, 172, 173] which can handle general anisotropy, but loss-less problems, has also been applied to the solution of several types of optical waveguides. For such a formulation, the natural boundary conditions correspond to a magnetic wall, and therefore it is essential to enforce the electric wall ($\mathbf{n} \times \mathbf{E} = 0$) as a boundary condition, which is difficult to implement for irregularly shaped structures. Also in this case, the field is not continuous at the dielectric interfaces.

The vector \mathbf{H} -field formulation is more suitable for dielectric waveguide problems, because the magnetic field is continuous everywhere, and the natural boundary conditions correspond to those of the electric wall, therefore no forced boundary conditions at the boundaries are required. This formulation can be written as [174, 175]:

$$\omega^2 = \frac{\int (\nabla \times \mathbf{H})^* \cdot \hat{\epsilon}^{-1} \cdot (\nabla \times \mathbf{H}) d\Omega}{\int \mathbf{H}^* \cdot \hat{\mu} \cdot \mathbf{H} d\Omega} \quad (2.30)$$

where ω is the natural frequency, Ω is the waveguide cross-section, $\hat{\epsilon}$ and $\hat{\mu}$ are the permittivity and permeability tensors, respectively. To obtain the stationary solution of the functional 2.30, the expression is minimised with respect to each of the variables, which are the unknown nodal field components H_x , H_y and H_z . This minimisation leads to a matrix eigenvalue equation as stated in equation A.1, where $[\mathbf{A}]$ is a complex Hermitian matrix and $[\mathbf{B}]$ is a real symmetric and positive-definite matrix. Because of the general 90° phase difference between the axial and transverse components of \mathbf{H} [176] the Hermitian matrix $[\mathbf{A}]$ can be transformed to a real symmetric matrix for a loss-less problem. In general, the matrices $[\mathbf{A}]$ and $[\mathbf{B}]$ are quite sparse. The eigenvectors $\{x\}$ represent the unknown field components at the nodal points for different modes with λ as their corresponding eigenvalues and also λ is proportional to ω^2 . In order to obtain a solution for a given wavelength, the propagation constant, β value has to be changed iteratively until the output eigenvalue corresponds to that wavelength. By varying β over the range of interest, it is possible to calculate the dispersion characteristics for the various modes.

However, the above formulation (as well as the \mathbf{E} -field), yields spurious solutions, because the divergence condition, $\nabla \cdot \mathbf{H} = 0$ is not satisfied, therefore alternative approaches, such as the penalty coefficient method [174, 128] have been proposed to eliminate those non-physical solutions. This method will be discussed in a later section of this chapter.

2.5.3 Natural Boundary Conditions

The term 'natural boundary condition' arises in the calculus of variations, and since the finite element method is fundamentally one of minimisation of an error functional, the term arises also in this context. The boundary condition, which is automatically satisfied in the variational procedure, is called the 'natural boundary condition'. In variational formulations these can be automatically satisfied, if left free. The scalar functional defined earlier in equation 2.28 has

the continuity of $\frac{\partial E_x}{\partial n}$ as the natural boundary condition, and the functional defined in equation 2.29 has the continuity $(\frac{1}{n^2}) (\frac{\partial H_x}{\partial n})$ as the natural boundary condition, where \mathbf{n} is the outward normal unit vector. The vector \mathbf{H} -field formulation described in equation 2.30, has the natural boundary condition of an electric wall, *i.e.* $\mathbf{n} \cdot \mathbf{H} = 0$. Therefore there is no need to force any boundary condition on conducting guide walls. But for regular shaped waveguides, and at the symmetric walls (if applicable) the natural boundary condition can be imposed to reduce the matrix problem size. However, it may be necessary to analyse the structure with complementary symmetry conditions to obtain all the modes, although the exploitation of the symmetry greatly reduces the computational cost.

2.6 FEM Formulation

The key to using the finite element method is to find the solution of a complicated problem by replacing it with a simpler one. The differential operator equations which describe the physical problem are replaced by an appropriate extremum functional J , which is the variational for the desired quantity. The problem can be regarded as obtaining the solution \mathbf{H} over a specified region in the transverse plane so that the boundary conditions and also the extremum requirement are satisfied. The axial dependence is assumed in the form $e^{-j\beta z}$ and the transverse plane is used for the discretisation.

2.6.1 Domain Discretisation

The discretisation of the domain into sub-regions (finite elements) is considered as the initial step in the finite element method. The shapes, sizes, number and configurations of the elements have to be chosen carefully such that the original body or domain is simulated as closely as possible without increasing the computational effort needed for the solution. Each element is essentially a simple unit within which the unknown can be described in a simple manner. There are various types of elements available for use in finite element formulations. These elements can be defined to be as one, two and three dimensional elements. When the geometry and material properties can be described in terms of only one spatial coordinate, then a one-dimensional element can be used. However, when the configuration and other details of the problem can be described in terms of two independent spatial coordinates, the two-dimensional

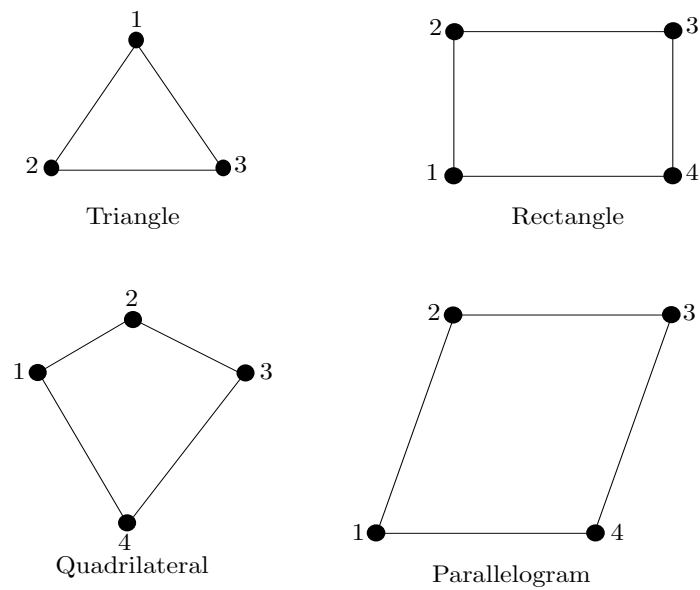


FIGURE 2.3: Finite Elements in two-dimensions

elements shown in Fig. 2.3 can be used. The use of a rectangle as a basic finite element to discretise an irregular domain is certainly the simplest but not the most suitable choice because an assembly of rectangles cannot accurately represent the arbitrary geometrical shape of the domain. In such a case, the discretisation error is significant, although it tends to decrease as the size of rectangles in the domain becomes smaller. The simplest and indeed the most basic element typically considered for two-dimensional analysis is the triangular element. If a triangle is used instead of a rectangle as the basic element for the meshing of the 2-D domain, the discretisation error would be effectively much smaller. The size of the element also dictates the accuracy of the final solution as the higher order elements tend to provide more accurate solutions. A typical representation of an arbitrary waveguide structure using triangular elements is shown in Fig. 2.4. By dividing the waveguide cross section into triangular elements, the unknown \mathbf{H} is discretised into corresponding sub-regions. These elements are easier to analyse rather than analysing the distribution over the whole cross section. As shown in Fig. 2.4, the transverse plane is covered with a grid of discrete nodes which are the vertices of each triangular element. The values of \mathbf{H} at these nodal points are the basic unknowns. The intersections of the sides of the triangular elements are called the nodal lines.

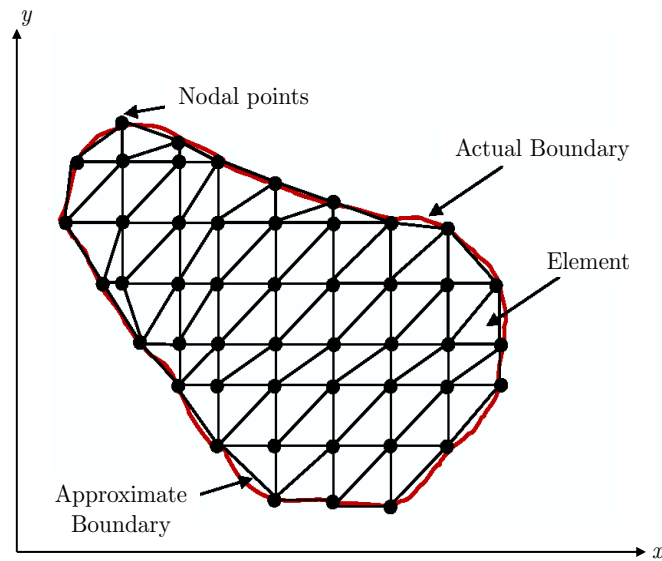


FIGURE 2.4: Finite element discretisation of a waveguide with triangular elements.

2.6.2 Shape Functions

In two-dimensional problems, the element assumes a linear interpolation between the field values at the vertices of the triangle. Within each element the unknown field \mathbf{H} , is approximated by means of suitably chosen set of polynomials. These functions are called 'shape functions'. For a simple triangular element the interpolation polynomial should include a constant term and both the x and y terms rather than only one of them. The field variable representation within an element should not alter the local coordinate system. In order to achieve this 'geometric isotropy', the polynomial should be completed according to Pascal's triangle as shown in Fig. 2.5. The final consideration in selecting the order of the interpolation polynomial is to make the total number of terms in the polynomial equal to the number of nodal degrees of freedom of the element. For example, the first degree polynomial involves three coefficients and so can be expressed in terms of three nodal values at the triangle vertices. The second degree polynomial needs six coefficients and can similarly be expressed in terms of values of six nodes as shown in Fig. 2.5.

The continuous field function $\phi(x, y)$ in the problem domain may be replaced by a set of discrete values $(\phi_i, i = 1, 2, 3, \dots, m)$, where m is the total number of nodes. The shape functions must guarantee the continuity of the primary unknowns across interelement boundaries. To be admissible functions, they must satisfy some specific conditions between the elements; usually the

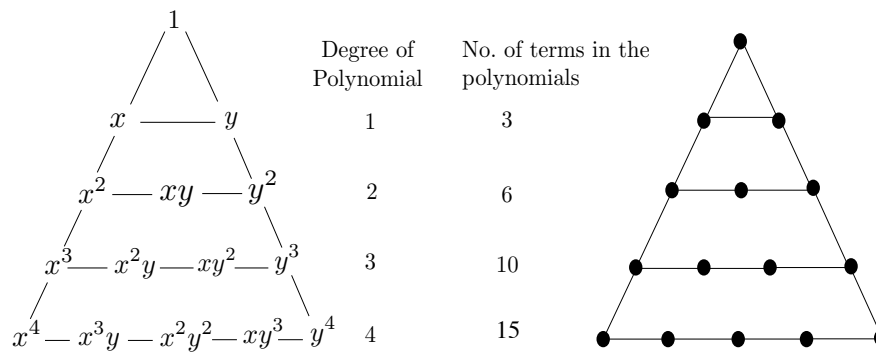


FIGURE 2.5: Pascal's triangle for complete polynomials in two dimensions.

continuity of the field across the boundaries is preferred. A typical first order triangular element used in finite element discretisation is shown in Fig. 2.6. Inside each first order element, the nodal field values ϕ are interpolated continuously. This can be achieved by introducing the interpolation functions, $N_i(x, y)$. Thus, using the interpolation functions, the elemental field values can be written as:

$$\phi_e(x, y) = \sum_{i=1}^3 N_i(x, y) \cdot \phi_i \quad (2.31)$$

$$\Rightarrow \phi_e(x, y) = N_1(x, y) \cdot \phi_1 + N_2(x, y) \cdot \phi_2 + N_3(x, y) \cdot \phi_3$$

where ϕ_i are the nodal field values. The functions $N_i(x, y)$ are called 'shape functions'. Equation 2.31 can also be written in matrix form as:

$$\phi_e(x, y) = \begin{bmatrix} N_1 & N_2 & N_3 \end{bmatrix} \begin{Bmatrix} \phi_1 \\ \phi_2 \\ \phi_3 \end{Bmatrix} \quad (2.32)$$

$$\phi_e(x, y) = [N] \{\phi_e\} \quad (2.33)$$

where $[N]$ is the shape function matrix and the column vector $\{\phi_e\}$ is the vector corresponding to the field values at the 3 vertices of the triangular element. In order to obtain the shape functions, $N_i(x, y)$ (where $i = 1, 2, 3$), a linear approximation of the of the field inside the element must be performed:

$$\phi_e(x, y) = \alpha_1 + \alpha_2 x + \alpha_3 y \quad (2.34)$$

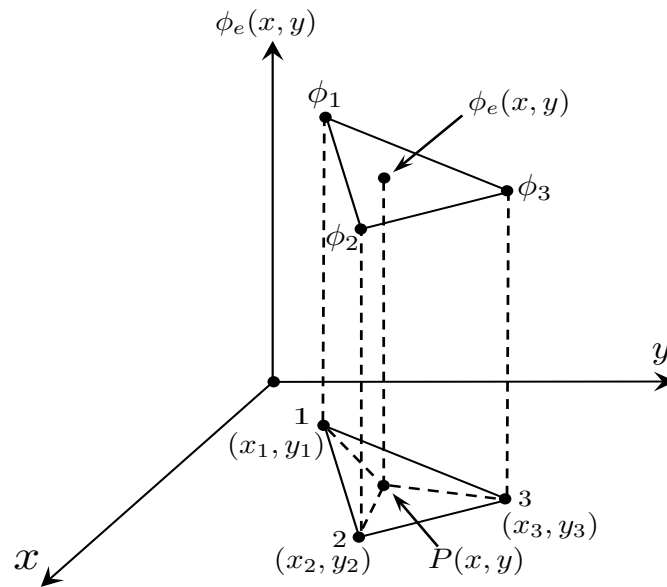


FIGURE 2.6: Representation of a first order triangular element.

for which α_1 , α_2 and α_3 are constants. By re-writing the above relation, such that the following conditions are satisfied:

$$\phi_e(x_i, y_i) = \phi_i \quad i = 1, 2, 3 \quad (2.35)$$

where $(x_i, y_i)(i = 1, 2, 3)$ are the global co-ordinates of the three vertices of the triangle. Hence the nodal field values ϕ_i can be expressed as:

$$\begin{aligned} \phi_1 &\equiv \phi_e(x_1, y_1) = \alpha_1 + \alpha_2 x_1 + \alpha_3 y_1 \\ \phi_2 &\equiv \phi_e(x_2, y_2) = \alpha_1 + \alpha_2 x_2 + \alpha_3 y_2 \\ \phi_3 &\equiv \phi_e(x_3, y_3) = \alpha_1 + \alpha_2 x_3 + \alpha_3 y_3 \end{aligned} \quad (2.36)$$

This can also be written in the matrix form as:

$$\begin{Bmatrix} \phi_1 \\ \phi_2 \\ \phi_3 \end{Bmatrix} = \begin{bmatrix} 1 & x_1 & y_1 \\ 1 & x_2 & y_2 \\ 1 & x_3 & y_3 \end{bmatrix} \begin{Bmatrix} \alpha_1 \\ \alpha_2 \\ \alpha_3 \end{Bmatrix} \quad (2.37)$$

By solving the above matrix, the constants $\alpha_1, \alpha_2, \alpha_3$ can be determined in terms of $\phi_i, i = 1, 2, 3$:

$$\begin{aligned}
\alpha_1 &= \frac{1}{2A_e} [\phi_1(x_2y_3 - x_3y_2) + \phi_2(x_3y_1 - x_1y_3) + \phi_3(x_1y_2 - x_2y_1)] \\
\alpha_2 &= \frac{1}{2A_e} [\phi_1(y_2 - y_3) + \phi_2(y_3 - y_1) + \phi_3(y_1 - y_2)] \\
\alpha_3 &= \frac{1}{2A_e} [\phi_1(x_3 - x_2) + \phi_2(x_1 - x_3) + \phi_3(x_2 - x_1)]
\end{aligned} \tag{2.38}$$

where A_e is the area of the triangular element given by:

$$A_e = \frac{1}{2} \begin{vmatrix} 1 & x_1 & y_1 \\ 1 & x_2 & y_2 \\ 1 & x_3 & y_3 \end{vmatrix} = \frac{1}{2} [(x_2y_3 - x_3y_2) + (x_3y_1 - x_1y_3) + (x_1y_2 - x_2y_1)] \tag{2.39}$$

Substituting the values of α_i from equation 2.38 into equation 2.34 results in the formation of the following equation:

$$\begin{aligned}
\phi_e(x, y) &= \frac{1}{2A_e} [\phi_1(x_2y_3 - x_3y_2) + \phi_2(x_3y_1 - x_1y_3) + \phi_3(x_1y_2 - x_2y_1)] \\
&+ \frac{1}{2A_e} [\phi_1(y_2 - y_3) + \phi_2(y_3 - y_1) + \phi_3(y_1 - y_2)] x \\
&+ \frac{1}{2A_e} [\phi_1(x_3 - x_2) + \phi_2(x_1 - x_3) + \phi_3(x_2 - x_1)] y
\end{aligned} \tag{2.40}$$

The above relation has close resemblance to the matrix relation given earlier in equation 2.31. Now comparing equation 2.31 with equation 2.40, the shape functions $N_i(x, y)$ $i = 1, 2, 3$ are given by the matrix notation [146]:

$$[N]^T = \begin{bmatrix} N_1 \\ N_2 \\ N_3 \end{bmatrix} = \frac{1}{2A_e} \begin{bmatrix} x_2y_3 - x_3y_2 & y_2 - y_3 & x_3 - x_2 \\ x_3y_1 - x_1y_3 & y_3 - y_1 & x_1 - x_3 \\ x_1y_2 - x_2y_1 & y_1 - y_2 & x_2 - x_1 \end{bmatrix} \begin{bmatrix} 1 \\ x \\ y \end{bmatrix} \tag{2.41}$$

where N_1 , N_2 and N_3 are shape functions at the three nodal points of the triangular element and N^T denotes a transpose of the N matrix. The shape function matrix can also be re-written as:

$$[N]^T = \begin{bmatrix} N_1 \\ N_2 \\ N_3 \end{bmatrix} = \begin{bmatrix} a_1 + b_1x + c_1y \\ a_2 + b_2x + c_2y \\ a_3 + b_3x + c_3y \end{bmatrix} \tag{2.42}$$

and a_i, b_i, c_i ($i = 1, 2, 3$) are the constants calculated as:

$$\begin{aligned} a_1 &= \frac{x_2 y_3 - x_3 y_2}{2A_e} \\ b_1 &= \frac{y_2 - y_3}{2A_e} \\ c_1 &= \frac{x_3 - x_2}{2A_e} \end{aligned} \quad (2.43)$$

Similarly a_2, b_2, c_2, a_3, b_3 and c_3 , can be calculated by cyclic exchange of $1 \rightarrow 2 \rightarrow 3$ in equation 2.43. The shape functions N_i can also be expressed in terms of the areas of the triangle shown earlier in Fig. 2.6 as:

$$N_i = \frac{\text{area of sub triangle } P23}{\text{area of sub triangle } 123} \quad (2.44)$$

Similarly N_2 and N_3 can be defined in the same way. Hence, N_i has the following property:

$$\sum_{i=1}^3 N_i = 1 \quad (2.45)$$

Thus evaluating the shape function N_1 gives a value of 1 at the node $1(x_1, y_1)$, whereas at nodes 2 and 3 a value of 0 is obtained. Hence it is the unique first-degree interpolation function for node 1. Similarly the shape functions N_2 and N_3 gives a value of 1 at nodes 2 and 3 respectively and 0 at other nodes.

2.6.3 Global and Element Matrices

The solution of the optical waveguide problem by the FEM can be transformed to a standard eigenvalue problem as in equation A.1 where matrices $[A]$ and $[B]$ are known as global matrices and consist of the summation of the element matrices for each triangular element of the discretised cross-section of the optical waveguide. In this section, the assembly of the element and global matrices is shown, with respect to the shape functions and the nodal field values of each triangular element, based on the variational formulation. Throughout the procedure, the full vectorial \mathbf{H} - field formulation in terms of the three axial components is assumed and first-order triangular elements are being used. Within each of the triangular elements the three unknown field \mathbf{H} - components H_x, H_y

and H_z of the magnetic field can be represented as following:

$$\begin{aligned}
 H_x(x, y) &= \begin{bmatrix} N_1 & N_2 & N_3 \end{bmatrix} \begin{bmatrix} H_{x1} \\ H_{x2} \\ H_{x3} \end{bmatrix} \\
 H_y(x, y) &= \begin{bmatrix} N_1 & N_2 & N_3 \end{bmatrix} \begin{bmatrix} H_{y1} \\ H_{y2} \\ H_{y3} \end{bmatrix} \\
 H_z(x, y) &= \begin{bmatrix} N_1 & N_2 & N_3 \end{bmatrix} \begin{bmatrix} H_{z1} \\ H_{z2} \\ H_{z3} \end{bmatrix}
 \end{aligned} \tag{2.46}$$

where H_{xi} , H_{yi} and H_{zi} for $i = 1, 2, 3$ are the x , y and z components of the nodal magnetic fields. Hence the magnetic field over the element $[H]_e$ can be described as:

$$[H]_e = \begin{bmatrix} H_x(x, y) \\ H_y(x, y) \\ H_z(x, y) \end{bmatrix} = \begin{bmatrix} N_1 & N_2 & N_3 & 0 & 0 & 0 & 0 & 0 & 0 \\ 0 & 0 & 0 & N_1 & N_2 & N_3 & 0 & 0 & 0 \\ 0 & 0 & 0 & 0 & 0 & 0 & N_1 & N_2 & N_3 \end{bmatrix} \begin{bmatrix} H_{x1} \\ H_{x2} \\ H_{x3} \\ H_{y1} \\ H_{y2} \\ H_{y3} \\ H_{z1} \\ H_{z2} \\ H_{z3} \end{bmatrix} \tag{2.47}$$

In a more compact form, the above equation 2.47 can be written as:

$$[\mathbf{H}]_e = [\mathbf{N}]\{\mathbf{H}\}_e \tag{2.48}$$

where $\{\mathbf{H}\}_e$ is the column vector representing the three components of the nodal field values in the element and $[\mathbf{N}]$ is the shape function matrix. Also

using equation 2.48 , the curl of \mathbf{H} equation can be written as:

$$\nabla \times [\mathbf{H}]_e = \nabla \times [\mathbf{N}]\{\mathbf{H}\}_e = \begin{bmatrix} 0 & -\partial/\partial z & \partial/\partial y \\ \partial/\partial z & 0 & -\partial/\partial x \\ -\partial/\partial y & \partial/\partial x & 0 \end{bmatrix} [\mathbf{N}]\{\mathbf{H}\}_e = [Q]\{\tilde{H}\}_e \quad (2.49)$$

where the matrix $[Q]$ can be written as:

$$[Q] = \begin{bmatrix} [0] & \frac{-\partial[N]}{\partial z} & \frac{\partial[N]}{\partial y} \\ \frac{\partial[N]}{\partial z} & [0] & \frac{-\partial[N]}{\partial x} \\ \frac{-\partial[N]}{\partial y} & \frac{\partial[N]}{\partial x} & [0] \end{bmatrix} \quad (2.50)$$

where $[0] = \begin{bmatrix} 0 & 0 & 0 \end{bmatrix}$ and $[N] = \begin{bmatrix} N_1 & N_2 & N_3 \end{bmatrix}$ and some of the shape function derivatives are substituted using equation 2.42 as shown:

$$\begin{aligned} \frac{\partial N_1}{\partial x} &= b_1, & \frac{\partial N_2}{\partial x} &= b_2, & \frac{\partial N_3}{\partial x} &= b_3 \\ \frac{\partial N_1}{\partial y} &= c_1, & \frac{\partial N_2}{\partial y} &= c_2, & \frac{\partial N_3}{\partial y} &= c_3 \end{aligned} \quad (2.51)$$

The values of the constants b_1, b_2, b_3, c_1, c_2 and c_3 were given earlier in equation 2.43. By substituting the expressions shown in equations 2.48 and 2.49 in to the variational formulation of equation 2.30, the vector \mathbf{H} -field formulation functional for an element can be obtained as:

$$\begin{aligned} \omega^2 &= \frac{\int (\nabla \times \mathbf{H})^* \cdot \hat{\epsilon}^{-1} \cdot (\nabla \times \mathbf{H}) d\Omega}{\int (\mathbf{H}^* \cdot \hat{\mu} \cdot \mathbf{H}) d\Omega} \\ \Rightarrow \omega^2 &= \frac{\int_{\Delta} ([Q]\{\mathbf{H}\}_e)^* \cdot \hat{\epsilon}^{-1} \cdot ([Q]\{\mathbf{H}\}_e) d\Omega}{\int_{\Delta} ([N]\{\mathbf{H}\}_e)^* \cdot \hat{\mu} \cdot ([N]\{\mathbf{H}\}_e) d\Omega} \\ \Rightarrow \omega^2 &= \frac{\int_{\Delta} \{\mathbf{H}\}_e^T [Q]^* \cdot \hat{\epsilon}^{-1} [Q] \{\mathbf{H}\}_e d\Omega}{\int_{\Delta} \{\mathbf{H}\}_e^T [N]^T \cdot \hat{\mu} [N] \{\mathbf{H}\}_e d\Omega} \end{aligned} \quad (2.52)$$

Re-arranging the last part of the above equation 2.52, the following can be obtained:

$$J_e = \int_{\Delta} \{\mathbf{H}\}_e^T [Q]^* \cdot \hat{\epsilon}^{-1}[Q] \{\mathbf{H}\}_e d\Omega - \omega^2 \int_{\Delta} \{\mathbf{H}\}_e^T [N]^T \cdot \hat{\mu}[N] \{\mathbf{H}\}_e d\Omega \quad (2.53)$$

where Δ represents the integration over the triangular element domain. T and $*$ denote the transpose of a matrix and the complex conjugate transpose, respectively. The $[Q]$ matrix was defined earlier in equation 2.50. A transpose operation on this matrix would define the $[Q]^*$ matrix. For isotropic material, the relative permittivity ϵ is a scalar quantity. For waveguides consisting of anisotropic material the relative permittivity ϵ can be taken as a tensor represented by a 3×3 matrix and the inverse of the matrix should be implemented. The total function, J , associated with the whole cross section of the waveguide can be obtained by summing J_e of all the individual elements as:

$$J = \sum_{e=1}^n J_e \quad (2.54)$$

where n is the number of elements.

The minimisation of the functional given in equation 2.54 can be performed by differentiating with respect to the field nodal values and equating it to zero as below:

$$\frac{\partial J}{\partial \{H\}_e} = 0 \quad (2.55)$$

Thus the following relation can be obtained:

$$\begin{aligned} \frac{\partial J}{\partial \{H\}_e} &= 2 \int_{\Delta} \{\mathbf{H}\}_e [Q]^* \cdot [Q] \hat{\epsilon}^{-1} d\Omega - \omega^2 2 \int_{\Delta} [N]^T \hat{\mu}[N] \{\mathbf{H}\}_e d\Omega = 0 \\ \therefore \int_{\Delta} \hat{\epsilon}^{-1} [Q]^* [Q] d\Omega \cdot \{\mathbf{H}\}_e - \omega^2 \int_{\Delta} \hat{\mu}[N]^T [N] d\Omega \cdot \{\mathbf{H}\}_e &= 0 \end{aligned} \quad (2.56)$$

Thus the following eigenvalue equation can be obtained:

$$[\mathbf{A}]\{\mathbf{H}\} - \omega^2[\mathbf{B}]\{\mathbf{H}\} = 0 \quad (2.57)$$

where the matrices $[\mathbf{A}]$ and $[\mathbf{B}]$ can be defined as:

$$\begin{aligned} [\mathbf{A}] &= \sum_{e=1}^n [\mathbf{A}]_e = \sum_{e=1}^n \int_{\Delta} \frac{1}{\hat{\epsilon}} [Q]^* [Q] d\Omega \\ [\mathbf{B}] &= \sum_{e=1}^n [\mathbf{B}]_e = \sum_{e=1}^n \hat{\mu} \int_{\Delta} [N]^T [N] d\Omega \end{aligned} \quad (2.58)$$

Matrix $\{\mathbf{H}\}$ contains all the \mathbf{H} -field nodal values over the whole cross section of the waveguide considered. $[\mathbf{A}]_e$ and $[\mathbf{B}]_e$ represent the element matrices whose assemblage over the whole cross section result in formation of the so called global matrices of the eigenvalue equation, given by $[\mathbf{A}]$ and $[\mathbf{B}]$, respectively. The calculation of the element matrices, $[\mathbf{A}]_e$ and $[\mathbf{B}]_e$ are shown in Appendix A.

When solving waveguide problems by using finite elements, the key factor affecting storage requirements and computational effort is the choice of algorithm to solve the matrix equation. The global matrices $[\mathbf{A}]$ and $[\mathbf{B}]$ shown in equation 2.58 are highly sparse. The sparsity increases with the order of the matrices and decreases with the polynomial order of the shape functions. It is obvious that using higher order basis functions, one may obtain a more accurate solution of the problem under consideration. However, the added disadvantage to that is that the process involves increasing programming effort, particularly when considering waveguide problems with material anisotropy, infinite elements and penalty functions. In addition to that, using higher order polynomials for a given matrix order increases the density of the matrix although this can be handled with reasonable effort by using a sophisticated matrix solver.

2.6.4 Spurious Solutions

The usage of vector formulations in analysing waveguide problems, results in generating some non-physical, spurious solutions along with the physical solutions of the system. Spurious solutions may evolve due to several reasons such as: (i) enforcement of boundary condition (ii) positive definiteness of the operator and (iii) non-zero divergence of the trial fields. In the \mathbf{H} -field formulation, the associated Euler equation is consistent with the two curl equations 2.5, 2.6 of Maxwell, but does not satisfy the $\nabla \cdot \mathbf{B} = 0$ condition which may be the reason behind the appearance of spurious modes [174].

The identification of the spurious modes amongst the physical modes can be difficult, when a set of eigen modes are computed. Sometimes spurious

modes can be spotted, from their dispersion curves, or by their eigenvectors, where the field varies in an unreasonable, sometimes in a random way along the cross section of the waveguide. Rahman and Davies [177] have developed a procedure which gives a reasonable identification of the spurious modes. In the above approach, the divergence of the magnetic field, $\nabla \cdot \mathbf{H}$, is calculated for each eigenvector, and when the value obtained is high, it is assumed that the eigen mode does not satisfy the divergence condition, and therefore it is a spurious mode.

Several approaches have been used, most of them aiming to force the condition $\nabla \cdot \mathbf{H} = 0$, which is considered the main cause of spurious modes. In the method developed by Rahman and Davies [177] an integral is added to the \mathbf{H} -field formulation, so that the resulting Euler equation is the Helmholtz equation, plus the $\nabla \cdot \mathbf{B} = 0$ condition. The variational formulation then becomes as [174, 177]:

$$\omega^2 = \frac{\int (\nabla \times \mathbf{H})^* \frac{1}{\epsilon} \cdot (\nabla \times \mathbf{H}) d\Omega + \frac{\alpha}{\epsilon_0} \int (\nabla \cdot \mathbf{H})^* \cdot (\nabla \cdot \mathbf{H}) d\Omega}{\int \mathbf{H}^* \cdot \hat{\mu} \mathbf{H} d\Omega} \quad (2.59)$$

where α is the dimensionless penalty factor. The value of α is often taken to be around $\frac{1}{\epsilon_n}$, where ϵ_n is the dielectric constant of the core of the waveguide. In this method the divergence free constraint is imposed in a least-squared sense and the larger the penalty factor the more heavily the constraint is implemented, giving a further reduction of the spurious modes from the spectrum. The penalty function also improves the quality of the eigenvectors without increasing the order of the matrix in the eigenvalue problem.

2.6.5 Mesh Resolution and Convergence

Due to the discretisation of the computational domain the effective index obtained by the method might deviate from the actual value depending on the resolution of the mesh. To obtain the accurate value of the effective index using the above mentioned FEM technique, same structure could be simulated with different resolutions. Results from these simulations can be used in Aitkin's extrapolation [178, 179] to improve the accuracy of the solution. According to Aitkin's technique,

$$\omega_\infty = \omega_3 - \frac{(\omega_3 - \omega_2)^2}{\omega_3 - 2\omega_2 + \omega_1} \quad (2.60)$$

Here, ω_1 , ω_2 and ω_3 are results obtained by using successive higher mesh refinement for the same structure and ω_∞ is the extrapolated result equivalent to infinite mesh division.

To validate the accuracy, a much higher resolution simulation could be performed and the result can be compared to the extrapolated result.

2.7 Summary

The aim of this chapter was to present a theoretical background of the Finite Element Method based on the variational principle to perform modal analysis of various waveguide structures. The properties of various numerical methods often used in analysing waveguide problems has been examined. An elaborate mathematical description is given for the vector **H**-field based FEM formulation. Several aspects of the method such as the boundary conditions, shape functions and methods aimed at eliminating spurious solutions have been extensively analysed. This chapter thus serves as the underlying principle of the numerical method used to analyse waveguides used in Terahertz and optical plasmonic waveguides details of which will be presented in the subsequent chapters.

Chapter 3

Surface Plasmonic Waveguides

3.1 Introduction

In recent years there has been considerable interest shown in the field of the surface plasmon polariton (SPP) [48, 180, 181, 182] that emerged from the need to have miniaturized structures and to provide optical waveguides having increased functionality and efficiency. Surface Plasmon Polaritons (SPPs) are electromagnetic waves that are located at the dielectric metal interface and are created due to the coupling between the electromagnetic field and free electrons in the metal [183], decaying evanescently on both sides of the interface. In case of SPPs, large electromagnetic fields can be confined within the subwavelength region of the interface thus breaking the diffraction limit of light. It enables plasmonic waveguides to guide light much below the diffraction limit by controlling and adjusting the interface parameters [181, 184, 185, 186, 187, 188]. These unique properties have enabled the use of SPP structures for several fiber-optic and optoelectronic devices, such as optical polarizers [189], fiber-optic sensors [190], scanning microscopy [191, 181, 192] and also for subwavelength laser devices namely visible nanolasers [193, 194] and terahertz lasers [195].

Metals such as silver, gold, copper which are commonly termed as noble metals almost resemble the properties of an ideal plasma and have negative permittivity when they are properly excited. A metal film, having certain thickness sandwiched between dielectrics on both sides or a thin layer of dielectric bounded by metals above and below, can be used as a planar plasmonic waveguide of infinite width [196]. These structures can guide plasmonic modes which are formed due to the combination of the surface waves at the two metal-dielectric interfaces. A hybrid waveguide having the configuration I-M-I-M-I-M can be formed by placing two such plasmonic structures (described above) close to each other. The strongly confined modal properties of the SPM's created at the metal-dielectric interfaces enable the formation of highly coupled

surface plasmon super modes (SPSMs).

In the first two sections we present a general overview on surface plasmons and then followed by relating the optical properties of metals to the interaction of EM waves with metals, which can be derived from Maxwell's equations at the macro scale. The discussion is further extended to three layer structures and a six-layer metal-dielectric waveguide in the latter sections of this chapter.

3.2 Surface Plasmon Polariton

An electromagnetic wave travelling through a polarizable medium is modified by the polarization it induces and becomes coupled to it. This coupled mode of excitation is called a polariton and if the polarizable medium is identified, then the polariton is qualified. In the case of an electron plasma, the coupled modes are often called plasmon-polaritons [197]. Bulk polaritons propagate in an unbounded medium, while surface polaritons can be defined as the coupling of electromagnetic radiation to surface dipole excitation, which propagates in a wave-like manner along the interface between the two media. Surface plasmons exist in the boundary of a solid metal or semiconductor whose electrons behave like those of a quasi-free electron gas. These plasmons represent the quanta of the oscillations of surface charges, which are produced by exterior electric fields in the boundary [198]. The Electromagnetic fields of the surface polariton can be either evanescent away from the interface (non-radiative surface polariton) or they can be oscillatory fields away from the interface (radiative surface polariton). In the first case, the amplitude of the field is maximum at the interface and decays exponentially away from it in a non-oscillatory manner in a direction perpendicular to the propagation, while in the second, the field modes are unbound but maintained by balancing the energy radiating away from the surface with energy radiating to the surface. The surface plasmon-polaritons or surface plasma waves occur at the interface of a dielectric with a positive dielectric constant and a metal with a negative real part of the dielectric constant. In 1941 Fano pointed out that for non-magnetic media evanescent surface waves could exist for TM polarization only [199].

The properties of these waves are based on the solution of Maxwell's equations for an interface between two semi-infinite and isotropic dielectric media. They can be classified in four categories according to their dielectric function, $\epsilon(\omega)$, which are the 'Fano', 'Brewster', 'Evanescent' and the 'Zenneck modes'. The 'Fano modes' are the only surface normal modes since the existence of the

other three modes depends in an essential way of damping and they are usually associated with $\epsilon(\omega) < 0$ [200]. In this work surface plasmon modes have been examined for different types of optical and terahertz waveguide structures, like planar metal-clad waveguides, two-dimensional metal-clad waveguides, multi-layer planar structure and metal-clad waveguides.

3.3 Wave Propagation in metals

The propagation of the EM waves in a material medium can be described by Maxwell's equations, which are:

$$\nabla \times \mathbf{H} = \frac{\partial \mathbf{D}}{\partial t} + \mathbf{J}_f \quad (3.1)$$

$$\nabla \times \mathbf{E} = -\frac{\partial \mathbf{B}}{\partial t} \quad (3.2)$$

$$\nabla \cdot \mathbf{D} = \rho_f \quad (3.3)$$

$$\nabla \cdot \mathbf{B} = 0 \quad (3.4)$$

where \mathbf{E} , \mathbf{D} , \mathbf{H} and \mathbf{B} are electric field density, electric flux density (electric displacement), magnetic field density and (magnetic induction) and magnetic flux density, respectively.

Equations 3.1 to 3.4 describe the fields due to free current density \mathbf{J}_f and free charge density ρ_f . In order to determine the field vectors inside a medium, the material equations that describe the behaviour of the medium in the given fields (also called constitutive equations) are necessary. For metals these equations are:

$$\mathbf{D} = \epsilon \mathbf{E} \quad (3.5)$$

$$\mathbf{B} = \mu \mathbf{H} \quad (3.6)$$

$$\mathbf{J} = \sigma \mathbf{E} \quad (3.7)$$

where $\epsilon = \epsilon_r \epsilon_0$ and $\mu = \mu_r \mu_0$ with ϵ_0 and μ_0 being the permittivity and the permeability of free space, respectively; ϵ_r is the relative permittivity including the effects of both vacuum and metal core polarization; μ_r is the relative permeability of the material; and σ is the conductivity of the material.

Combining equations 3.1 and 3.2 with material equations 3.5 and 3.6 we have a differential wave equation for the \mathbf{E} -field in the metal:

$$\nabla^2 \mathbf{E} = \epsilon_r \epsilon_0 \mu_r \mu_0 \frac{\partial^2 \mathbf{E}}{\partial t^2} + \mu_r \mu_0 \sigma \frac{\partial \mathbf{E}}{\partial t} \quad (3.8)$$

A solution for equation 3.8 has the form

$$\mathbf{E}(\mathbf{r}, t) = \mathbf{E}_0 e^{j(\mathbf{k} \cdot \mathbf{r} - \omega t)} \quad (3.9)$$

where \mathbf{k} is called the propagation vector of the waves and $\mathbf{k} = [k_x, k_y, k_z]$; \mathbf{r} is the position vector, where $\mathbf{r} = [x, y, z]$.

Substituting equation 3.9 into equation 3.8 and using $\mu_r = 1$ for non-magnetic metals at optical frequencies, the propagation constant $k = |\mathbf{k}|$ of the wave in the metal can be expressed as:

$$k^2(\omega) = \epsilon_0 \mu_0 \omega^2 \left(\epsilon_r(\omega) + j \frac{\sigma(\omega)}{\epsilon_0 \omega} \right) \quad (3.10)$$

The bracketed term is the effective dielectric constant of the metal, which includes the contribution from both bound electrons and conduction electrons. However, it is common to assume that the valency electrons and the corresponding ions are tightly bound, consequently, they have no considerable contribution to the polarization of the metal (*i.e.*, metal core polarization due to an incident EM wave is zero). Therefore, the effective dielectric constant of the metal is often expressed as:

$$\epsilon_{eff} = 1 + j \frac{\sigma(\omega)}{\epsilon_0 \omega} \quad (3.11)$$

The propagation constant in equation 3.10 can also be expressed as:

$$k^2 = (k' + jk'')^2 = \frac{\omega^2}{c^2} (n + j\kappa)^2 \quad (3.12)$$

where k' represents the real part of k (it describes how the waves propagate in the metal); k'' is the imaginary part of k (it tells how the waves attenuate while propagating in the metal); $c = 1/\sqrt{(\epsilon_0 \mu_0)}$ is the speed of light in free space; and $(n + j\kappa)$ is the complex refractive index of the material.

The time averaged field intensity in the metal follows the relation $I \propto \langle |\mathbf{E}(\mathbf{r}, \mathbf{t})|^2 \rangle = |\mathbf{E}_0|^2 e^{-2k''|\mathbf{r}|} = |\mathbf{E}_0|^2 e^{-\alpha|\mathbf{r}|}$, where $\alpha = 2k''$ is the absorption coefficient and the quantity $1/\alpha$ is known as the skin depth or penetration depth of the metal which is the propagation distance at which field intensity drops by a factor of $1/e$. The skin depth for metal is usually a very small number.

3.3.1 SPPs at the Metal- Dielectric Interface

To understand the phenomenon of SPP, it is instructive to examine the EM-waves at the interface of a metal and a dielectric. First we consider TM polarized light incident on a planar interface of two media whose dielectric constants are ϵ_1 and ϵ_2 respectively, as illustrated in Fig. 3.1. Assuming the interface plane is at $y = 0$, the fields in two media can be described as:

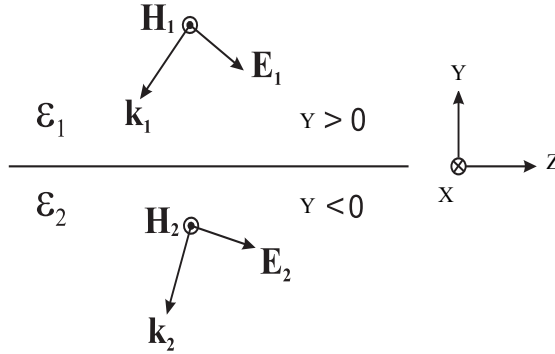


FIGURE 3.1: Schematic Diagram of the interface between two media

$$\mathbf{E}_1 = (0, E_{y1}, E_{z1})e^{j(k_{y1}y+k_{z1}z-\omega t)} \quad (3.13)$$

$$\mathbf{H}_1 = (H_{x1}, 0, 0)e^{j(k_{y1}y+k_{z1}z-\omega t)} \quad (3.14)$$

$$\mathbf{E}_2 = (0, E_{y2}, E_{z2})e^{j(k_{y2}y+k_{z2}z-\omega t)} \quad (3.15)$$

$$\mathbf{H}_2 = (H_{x2}, 0, 0)e^{j(k_{y2}y+k_{z2}z-\omega t)} \quad (3.16)$$

Solving Maxwell's equations with appropriate boundary conditions leads to the implicit dispersion relation for EM waves existing at the interface, which is

$$\frac{k_{y1}}{\epsilon_1} + \frac{k_{y2}}{\epsilon_2} = 0 \quad (3.17)$$

For EM waves to be localized to the interface, both k_{y1} and k_{y2} must be positive imaginary numbers, which follows that ϵ_1 and ϵ_2 must have opposite signs.

Combining equation 3.17 with the following relation

$$\epsilon_i \left(\frac{\omega}{c} \right)^2 = k_z^2 + k_{yi}^2 \quad (i = 1, 2) \quad (3.18)$$

the dispersion relation for surface EM waves at the interface can be expressed as:

$$k_z = \frac{\omega}{c} \sqrt{\frac{\epsilon_1 \epsilon_2}{\epsilon_1 + \epsilon_2}} \quad (3.19)$$

which indicates that in addition to the requirement of $\epsilon_1 \epsilon_2 < 0$ for EM waves existing at the interface, $\epsilon_1 + \epsilon_2 < 0$ is essential for waves to propagate along the interface (z -direction), *i.e.*, the real part of k_z is positive. At optical frequencies these two conditions can be fulfilled simultaneously if one medium is a dielectric and the other one is a metal. In the literature, surface EM waves that satisfy the above descriptions are often termed surface plasmon polaritons (SPPs) to manifest their plasma oscillation and EM wave propagation hybrid nature.

Assuming $\epsilon_1 > 0$ and $\epsilon_2 = \epsilon'_2 + j\epsilon''_2$ with $\epsilon'_2 < 0$ and $|\epsilon'_2| > \epsilon_1$, the real and imaginary parts of k_z can be expressed as [183]

$$\{k_z\}_{Re} = \frac{\omega}{c} \sqrt{\frac{\epsilon_1 \epsilon'_2}{\epsilon_1 + \epsilon'_2}} \quad (3.20)$$

and

$$\{k_z\}_{Im} = \frac{\omega}{c} \sqrt{\left(\frac{\epsilon_1 \epsilon'_2}{\epsilon_1 + \epsilon'_2} \right)^3 \frac{\epsilon''_2}{2(\epsilon'_2)^2}} \quad (3.21)$$

Equation 3.20 is generally referred to as the explicit dispersion relation of the SPPs, in which $\{k_z\}_{Re}$ is often replaced by the notation k_{sp} . Since $\epsilon_1 < |\epsilon_1 + \epsilon'_2| < |\epsilon'_2|$, the surface plasma frequency $k_{sp} > \frac{\omega}{c}$ and the SPP dispersion curve is situated below the dispersion curve of light in the dielectric medium. This shows that the in-plane wavevector of the SPPs is always larger than that of the light at same frequency, therefore light-SPPs interaction cannot occur spontaneously on a flat metal surface due to the fact that the energy and momentum conservation cannot be satisfied simultaneously in such system.

Equation 3.20 also implies that the wavevector k_{yi} ($i = 1, 2$) are pure imaginary as $k_{sp} > \frac{\omega}{c}$, which indicates that SPP waves are evanescent waves whose field intensity peaks at the interface ($y = 0$) and decreases exponentially away from the interface. Owing to the Ohmic loss of the metal (ϵ''_2), the field intensity also attenuates exponentially while SPs propagate along the interface

(z -direction). The $1/e$ intensity decay length along the z -direction, which is known as the propagation length of the SPPs, is given by $L = (2\{k_z\}_{Im})^{-1}$. At an Ag/air interface this is about $22 \mu\text{m}$ at $\lambda = 514 \text{ nm}$ and $500 \mu\text{m}$ at $\lambda = 1060 \text{ nm}$ [183].

The E -field component E_{yi} ($i = 1, 2$) at the interface can also be obtained by solving Maxwell's equations with appropriate boundary conditions, which leads to

$$\frac{E_{y1}}{E_{y2}} = \frac{\epsilon_2}{\epsilon_1} \quad (3.22)$$

This indicates that within two different media, both amplitude and phase of SPPs can be different at the interface. Since the dielectric constant of the metal is generally greater than that of the dielectric, the amplitude of the SPP field at the dielectric side of the interface is usually larger than that at the metal side of the interface. The penetration depth of the SPPs, which refers to $1/e$ intensity decay length in the direction normal to the interface (z -direction), is given by $y_i = (|k_{yi}|)^{-1}$, is also different in the two media. For example, at $\lambda = 600 \text{ nm}$ the penetration depth of the SPPs at an Ag/air interface is 24 nm in Ag and 390 nm in air.

It is also worth noting that for a very large k_{sp} , the group velocity and phase velocity of SPP waves both approach zero. In this case, the waves resemble electrostatic surface waves, that is, a non-propagating fluctuation of the electron plasma near the metal surface; and the frequency of this collective oscillation can be expressed as:

$$\omega_{sp} = \frac{\omega_p}{\sqrt{\epsilon_d + 1}} \quad (3.23)$$

Finally, we note that for TE polarized light, the fields in two media in Fig. 3.1 becomes:

$$\mathbf{E}_1 = (E_{x1}, 0, 0)e^{j(k_{z1}z+k_{y1}y-\omega t)} \quad (3.24)$$

$$\mathbf{H}_1 = (0, H_{y1}, H_{z1})e^{j(k_{z1}z+k_{y1}y-\omega t)} \quad (3.25)$$

$$\mathbf{E}_2 = (E_{x2}, 0, 0)e^{j(k_{z2}z+k_{y2}y-\omega t)} \quad (3.26)$$

$$\mathbf{H}_2 = (0, H_{y2}, H_{z2})e^{j(k_{z2}z+k_{y2}y-\omega t)} \quad (3.27)$$

Solving Maxwell's equations with appropriate boundary conditions leads to

$$k_{y1} + k_{y2} = 0 \quad (3.28)$$

which implies that k_{y1} and k_{y2} cannot be simultaneously positive, *i.e.*, no localized surface EM waves can be excited under TE polarized incident light.

The frequency dispersion characteristic of the relative electric permittivity of metals incorporating loss is described by Drude-Sommerfeld's theorem in

$$\epsilon_m(\omega) = 1 - \frac{\omega_p^2}{\omega^2 + j\frac{\omega}{\tau}} \quad (3.29)$$

where ω_p is the plasma frequency and τ is the relaxation time for the metal.

3.3.2 Evaluation of performance

The two key parameters which dictate the performance in a plasmonic waveguide are the waveguide loss, α_w and the fractional power confinement, Γ in the core and cladding layers. In the analysis presented here, the waveguide loss has been calculated from the complex propagation constant γ arising from the complex transcendental equation as $\alpha_w = 2\mathcal{I}(\gamma)$. The power confinement, Γ , in any particular area is obtained by integrating the Poynting vector relation which is obtained from the \mathbf{H} field as shown in equation. 3.30. The finite element implementation of the Poynting vector calculation has been presented in Appendix B.

$$\Gamma = \mathcal{R} \frac{\int \int_{\Omega_A} [E_x^* H_y - E_y^* H_x] d\Omega}{\int \int_{\Omega_\infty} [E_x^* H_y - E_y^* H_x] d\Omega} \quad (3.30)$$

where, Ω_A is taken as the area of the active region and Ω_∞ is the integration over the entire computational domain.

3.4 Simulation Results: Single metal-dielectric interface

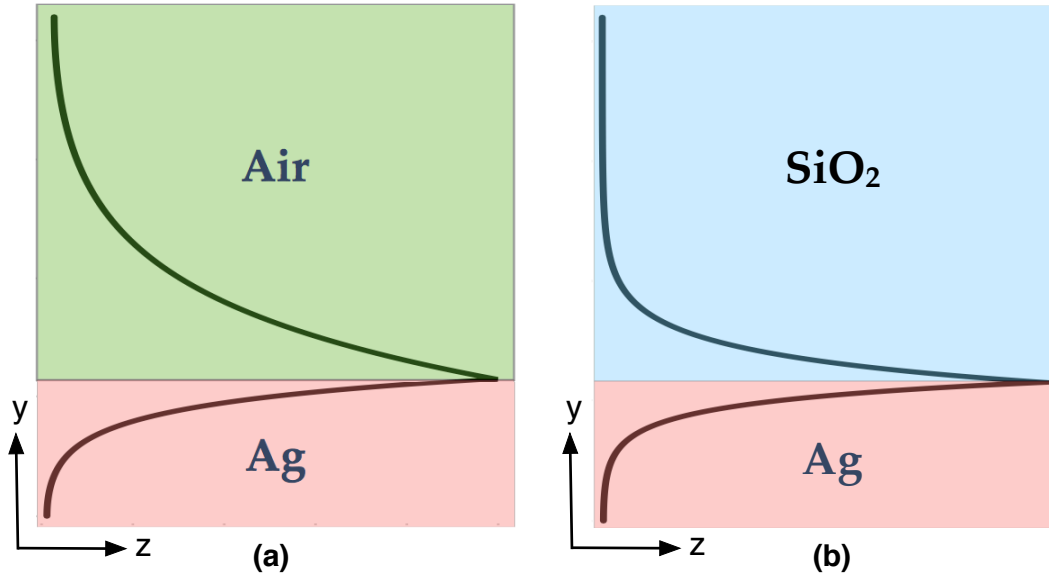


FIGURE 3.2: Variation of the normalized H_x field profile of the TM_0 mode with the transverse direction for two values of the refractive index of the dielectric a) for air with index $n_d = 1$ and b) for Silica with index $n_d = 1.44568$.

Firstly, a single metal-dielectric interface, which is the most basic structure that can support a plasmonic wave, was examined. The waveguide consisted of a Silver layer with a complex refractive index n_m , attached to a dielectric layer with a refractive index, n_d , at an operating wavelength $\lambda = 0.3 \mu m$. By solving the problem using the full-vectorial Finite Element Method (FEM) method, it was found that only the lowest TM mode, (TM_0), could propagate along the interface. This is the mode, which can be classified as a non-radiative surface plasmon mode and has a maximum amplitude at the interface and decays away from it. All the TE and the higher TM modes, were unbounded, *i.e.* they did not decay in the dielectric material region.

Figure 3.2 shows the normalised H_x field profile of single metal-dielectric structure in the transverse direction to the propagation (y), of the TM_0 optical mode, for two different values of the refractive index of the dielectric material and the metal is Ag. It can be observed in both Figs. 3.2 (a) and (b) that in

the metal region, the field decays very rapidly, while in the dielectric region the decay depends on the value of the refractive index, n_d , of the dielectric material. As the refractive index, n_d , increases, the mode becomes more confined near the interface, with a faster decay of the field in the dielectric region, while the rapid decay in the metal region remains unchanged. That is why the magnetic field in Silica (having higher refractive index) shown in Fig. 3.2(b) decays at a much faster rate than that in air as shown in Fig. 3.2(a).

The TM_0 mode propagates with an effective index, β/k_0 , very close to the refractive index of the dielectric material, n_d , so therefore, any increase of the refractive index, n_d , is followed by a linear increase of the effective index of the mode. The optical field of the TM_0 mode is concentrated at the metal/dielectric interface, where the proportion of the optical power in the lossy metal region gives rise to the attenuation characteristics. As the refractive index of the dielectric material increases, the mode becomes more confined in the dielectric region and the maximum field is higher at the metal/dielectric interface. Therefore, the proportion of the optical power in the metal region increases, resulting in an increase of loss. The normalised attenuation constant, α/k_0 , of the TM_0 optical mode increases with the increase of the refractive index, n_d , of the dielectric material, following a second order function.

3.5 Three Layer Planar Waveguides

The propagation characteristics and field profiles, for different types of three layer planar waveguides are examined in this section. The interaction of metallic films with dielectric materials in order to accommodate guided optical waves is also examined, since, such structures play an important role in many optoelectronic applications. Practical metallic elements are not perfect conductors, but suffer a small amount of loss, and therefore, in the analysis of waveguides incorporating metal films, the attenuation characteristics should be taken into consideration. In waveguide analysis metallic elements are represented by a complex refractive index, n_m .

3.5.1 Surface Plasmon modes in three layer planar structures

As discussed in the previous section, surface-plasmon waves are guided electromagnetic waves supported by a single or multiple metal/dielectric interface, where the refractive index of the metal film is considered to have an almost

purely imaginary part at the operating wavelength, thus giving a high negative dielectric constant. Surface-plasmon mode properties are used in a wide range of device applications, such as in optical polarizers or highly sensitive evanescent optical sensors.

After single interface, the simplest possible planar structure for plasmonic guidance could be a three layer structure consisting of two dielectric-metal interfaces. There could be only two types of arrangement of the dielectric and metals that could produce two dielectric-metal interfaces. The two media around the interface have dielectric constants of opposite sign and thus these structures can support SPPs to form at the interface. They are,

IMI Structures: In this type of structure a metal film is sandwiched between two dielectric (insulator) layers. Hence the name Insulator-Metal-Insulator (IMI). Here, the metal film is considered as the core and the dielectric layers work as claddings.

MIM Structures: In this type of structure a dielectric (insulator) layer is sandwiched between two metal layers. Therefore this type of structure is named Metal-Insulator-Metal (MIM). Here, the dielectric layer works as the core and the metals are the claddings.

As was shown in Section. 3.4, a single metal/dielectric interface can support only one TM-polarized mode, which is a surface-plasmon mode, where the field intensity is high at the interface and it decays exponentially away from it. When two such interfaces are placed together to form a composite structure, the two surface waves at the two dielectric-metal interfaces begin to couple through the metal or the dielectric and thus supermodes are created. Usually, there can be two types of bound surface modes for these kind of structures, one is symmetric and the other one is antisymmetric bound. These modes are known as symmetric bound modes, s_b or even modes and antisymmetric bound modes a_b or odd modes respectively. The symmetric bound mode or even mode corresponds to the two separate surface modes having amplitude of same polarity being coupled whereas the antisymmetric bound mode or odd mode resembles the coupling of two surface modes with opposite polarities. Their properties depend on the arrangement of the dielectric and metallic films and the separation between the two metal-dielectric interfaces.

Since metallic films are lossy materials, an investigation of the attenuation characteristics is important. The full-vectorial FEM has been used to calculate

the complex propagation constants of the above structures. To keep the characterisation simple both the IMI and the MIM structures were symmetrical, hence, the cladding materials used were kept the same.

3.5.2 Insulator-Metal-Insulator Structure

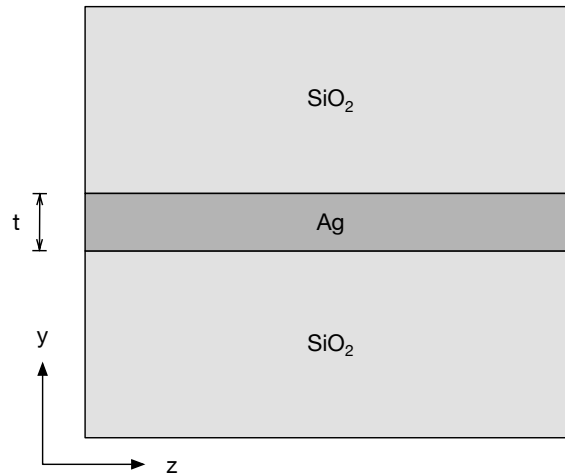


FIGURE 3.3: Schematic setup for the IMI Structure with SiO_2 and Silver (Ag)

The IMI structure considered in the section has Ag film core. The Ag film is surrounded by two semi-infinite dielectric materials which is SiO_2 -Glass in this case of the symmetrical structure. The thickness of the Ag core was taken to be t . The wavelength considered for the simulation was $0.3 \mu m$ and the refractive indices at this wavelength for Ag and SiO_2 are $n_{Ag} = 0.013109 + j1.847482$ [201] and $n_{SiO_2} = 1.44568$ [202], respectively. As mentioned before, the structure considered here is symmetric, so both the claddings for the structure were SiO_2 , hence the refractive indices are the same. Figure 3.3 shows a schematic diagram of the structure considered. The cross section shown in the figure is taken on the yz plane. The direction of propagation is z . The guide is considered uniform in the x direction.

As discussed in Section 3.5.1 the structure supports only two types of supermodes: even and odd. Figure 3.4 shows both the odd and even supermodes for a core thickness of $0.07 \mu m$. From this point onwards the word ‘**mode**’ will be used to denote “supermodes” alongside usual modes. This is because in most cases plasmonic modes are supermodes formed by multiple surface-plasmon modes (sp-modes). As can be seen in Fig. 3.4a, two sp-modes at the two interfaces are in the same direction and they are coupling to each other in the core

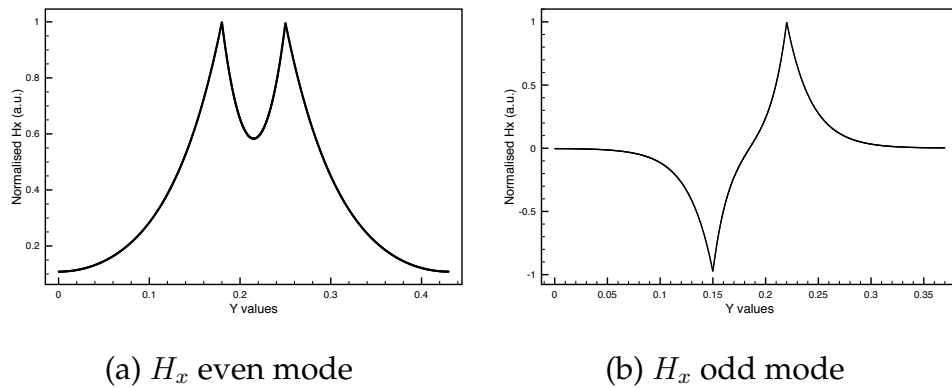


FIGURE 3.4: Even and odd modes for the SiO_2 - Ag - SiO_2 structure with a core thickness $t = 0.07\mu m$

in a constructive manner. Therefore, the field amplitude at the core is always positive and never crosses zero.

On the other hand the two sp-modes are in the opposite direction for the odd mode and in the core they are coupling in a destructive manner and forcing each of the sp-mode amplitude to fall rapidly and cross zero at the centre of the core to obtain opposite value. This is clearly visible in Fig. 3.4b.

To characterise the structure, the thickness t of the core was varied from $0.035\mu m$ to $0.3\mu m$. Figure 3.5 shows the even and odd mode profiles of the H_x field for the core thickness of $0.045\mu m$, $0.07\mu m$, $0.2\mu m$ and $0.3\mu m$. For both modes, the sp-modes at the two interfaces decouple with increasing core thickness t . At a very low core thickness, the even mode shows very little dip and the odd mode shows almost linear field profile inside the core. This is due to the fact that the fields of the odd mode penetrate progressively deeper into the metal as its thickness is reduced. In the case of the even mode, a decreasing film thickness causes the opposite effect, that is, the fields penetrate progressively more into the top and bottom dielectric regions and less into the metal. But as the thickness increases the even mode becomes more confined showing larger dip at the centre of the core as the two metal/dielectric interfaces move apart, whereas the odd mode started to show non-linear profile inside the core as the mode becomes less confined and the field spreads further into the cladding. For a very large thickness the sp-modes at the two interfaces decouple and behave like two weakly coupled surface modes, one at each metal/dielectric interface, propagating with almost identical propagation constants and an exponential decay is visible in both the cladding and the core for both the modes.

Figure 3.6 shows the characteristics of the real part of the effective index

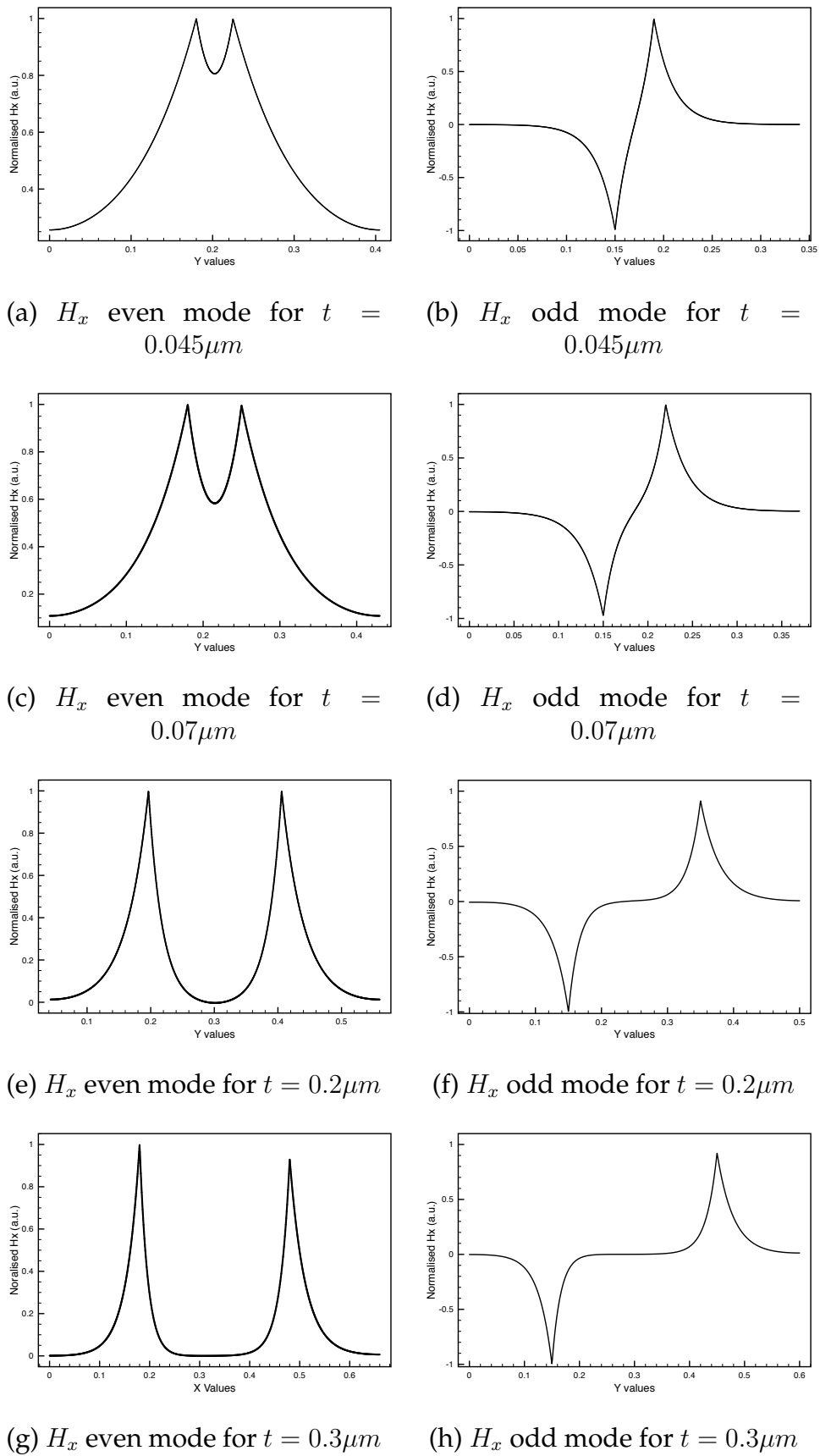


FIGURE 3.5: Even and odd modes for the $\text{SiO}_2\text{-Ag-SiO}_2$ structure for core thicknesses $0.045\mu\text{m}$, $0.07\mu\text{m}$, $0.2\mu\text{m}$ and $0.3\mu\text{m}$

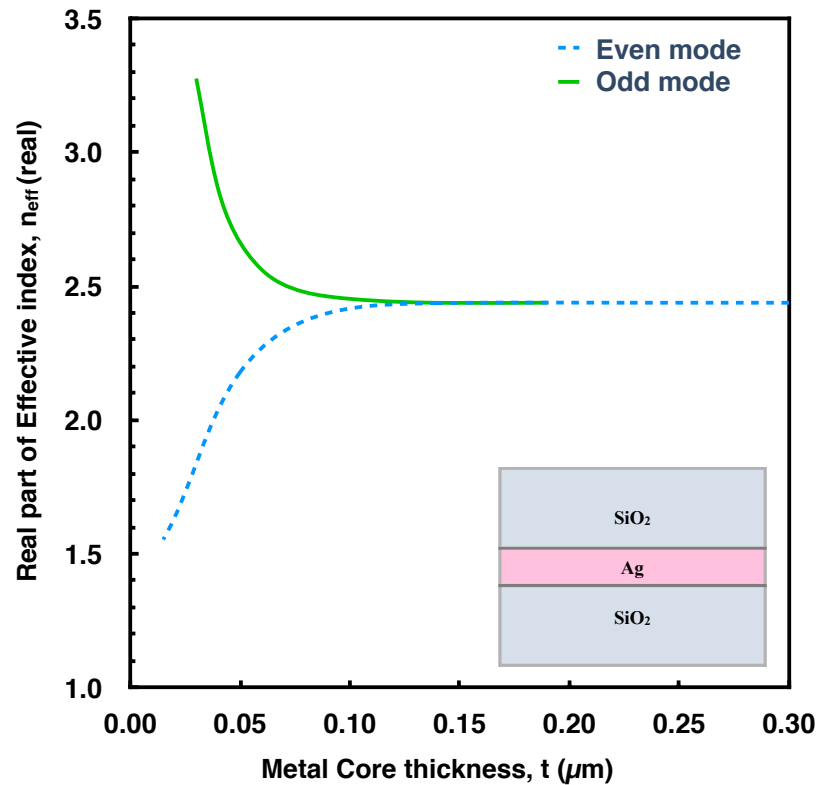


FIGURE 3.6: Variation of effective index of the even and odd coupled modes for symmetric IMI structure

of the even and odd modes of the SiO_2 - Ag - SiO_2 guide. Both the modes have higher effective indices than the common cladding refractive index of the two (top and bottom) cladding regions. When the thickness of the core of the guide is very small the real part of the complex effective indices of the even and odd modes are far apart. The real part of the index of the even mode is lower than that of a single interface of the same materials. In this occasion Ag and SiO_2 is considered. The real part of the effective index of the odd mode for very thin metal core is much higher than that of the single interface. The effective index of the even mode reduces and approaches the cladding refractive index value, as the metal thickness decreases and the mode becomes more weakly bounded. When the thickness increases the real part of the effective index of the even mode increases and the mode becomes more confined, showing a larger central dip as the two metal/dielectric interfaces move apart. However, as the film thickness increases, the odd mode becomes less confined since effective index of the odd mode decreases. When the film thickness becomes wide enough, the two supermodes behave like two weakly coupled surface modes, one at each metal/dielectric interface, propagating with almost identical propagation constants. As the metal thickness increases further, the two effective indices tend to

reach the effective index of the mode supported by a single metal dielectric interface and both indices saturate at the value of the index of the single interface. As the (identical) refractive index of both the cladding regions is increased, the effective index of each mode is shifted upwards by an amount equal to that increase.

It can be seen from the figure that the indices of the even and the odd modes at a thickness of $0.035\mu\text{m}$ are 1.918457 and 2.96971, respectively. For a thickness of $0.07\mu\text{m}$ the indices for even and odd modes are 1.956179 and 2.378496, respectively. At a thickness of $0.2\mu\text{m}$ both the indices approach saturation index with index of even mode 2.301209 and that of odd mode 2.316047. After $0.2\mu\text{m}$ both the modes come even closer and remain at saturation.

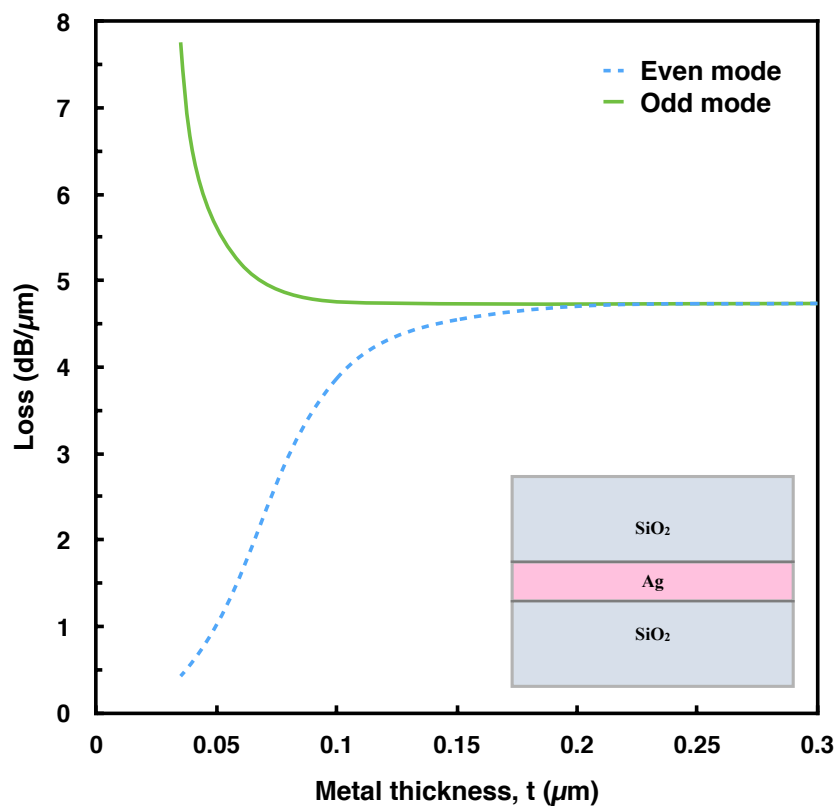


FIGURE 3.7: Variation of modal loss versus metal thickness for the first two supermodes for a symmetric IMI structure

The loss characteristics of the $\text{SiO}_2\text{-Ag-SiO}_2$ guide was also studied and shown in Fig. 3.7. The loss value decreases monotonically for the odd mode, with the metal thickness, whereas for the even mode, it increases. The loss of the even mode is lower for thinner metal cores and for the odd mode, it is higher. The modal loss for the even mode is less than that of the odd mode, hence the even (or even-like) mode is also known as the long range mode. Similarly the odd (or odd-like) modes are known as short range modes. When the

thickness is increased the loss of the even mode increases and the odd mode decreases. The modal loss values reach that of the surface mode supported by a single metal/dielectric interface when t is large. At a higher thickness both the modes converge to the same value of loss.

At a thickness of $0.035\mu\text{m}$ the loss value for the even mode is $0.42316\text{ dB}/\mu\text{m}$ and for odd mode the value is $7.7573\text{ dB}/\mu\text{m}$. For a thickness of $0.07\mu\text{m}$ the loss value of the even mode is $2.3285\text{ dB}/\mu\text{m}$ and for odd mode is $4.9672\text{ dB}/\mu\text{m}$. For a thickness of $0.2\mu\text{m}$ the loss for even mode is $4.7243\text{ dB}/\mu\text{m}$ and that for the odd mode is $4.7359\text{ dB}/\mu\text{m}$. After $0.2\mu\text{m}$ the loss of the even and odd modes become even closer and approach the same value, that of the single interface.

3.5.3 Metal-Insulator-Metal Structure

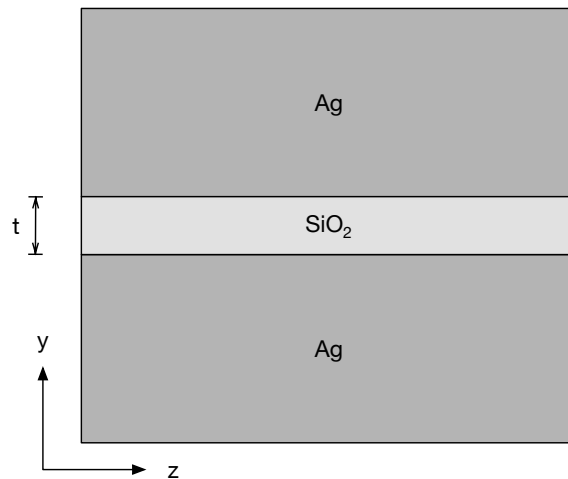


FIGURE 3.8: Schematic setup for the MIM Structure with SiO_2 -Glass and Silver (Ag)

The MIM structure considered in this section consists of a SiO_2 -core and Ag claddings. Similar to the IMI structure described in Section 3.5.2, in MIM structures the optical guided modes propagate along the metal/dielectric interfaces, where the field intensity is high and decays exponentially away from them. These modes are coupled to form a supermode and the coupling depends on the thickness of the dielectric film. The thickness of the core of the guide was considered to be t . The wavelength considered was $0.3\mu\text{m}$, which is the same as Section 3.5.2 for the IMI structure with the same refractive indices of Ag and SiO_2 . Figure 3.8 shows the schematic diagram of the MIM planar structure. Similar to the IMI simulation, the schematic diagram shows the yz plane and z is the direction of propagation whereas x direction is considered to be uniform.

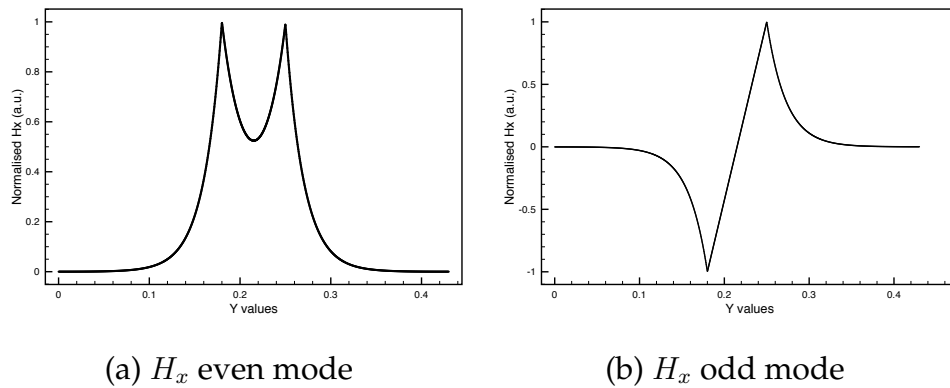


FIGURE 3.9: Even and odd modes for the $Ag-SiO_2-Ag$ structure with a core thickness $t = 0.07 \mu m$

As discussed before, the MIM guide can produce even and odd supermodes similar to the IMI structure. Figure 3.9 shows the even and odd supermodes obtained for the core thickness of $0.07 \mu m$. Although similar in nature to the IMI structure, the shape of the modes inside the core and also in the cladding are different.

To characterise the structure, the thickness of the core t was varied from $0.035 \mu m$ - $0.3 \mu m$. Figure 3.10 shows H_x field profiles of the even and odd supermodes for the core thicknesses of $0.045 \mu m$ (even only), $0.06 \mu m$ (odd only), $0.07 \mu m$, $0.2 \mu m$ and $0.3 \mu m$. As can be observed from the field profiles, with the increasing core thickness, the dip at the centre of the even mode becomes more profound and after nearly approaching 0 two single interface sp's move away from each other if the thickness of the guide is further increased. For the MIM structure, the rate of decoupling is slower than that of the IMI structure considered in Section 3.5.2. The odd mode shows a similar effect when the thickness is increased.

Figure 3.11 shows the effective index characteristics of the $Ag-SiO_2-Ag$ guide. The effective index characteristics are however different from that of the IMI structure. In case of the MIM structure, the even mode has higher effective index (real part) than that of the odd mode for thin core structures. When the core thickness is increased the effective index of the even mode reduces. However, for small values of the dielectric film thickness, the odd mode is in the cut-off region and although the effective index of the even mode could be found for the thickness of $0.015 \mu m$, the odd mode was not found until the core thickness of $0.06 \mu m$. The effective index of the odd mode increases as the film thickness increases. For higher values of the core thickness, both the effective index curves

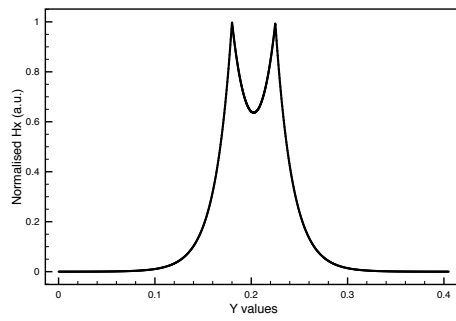
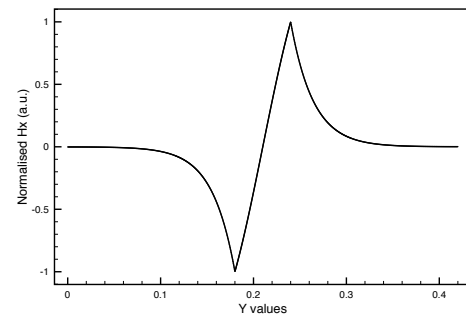
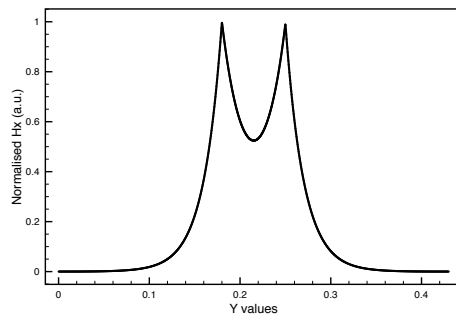
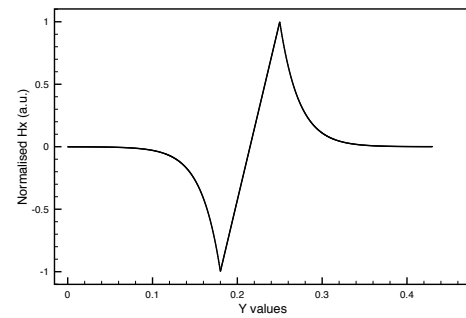
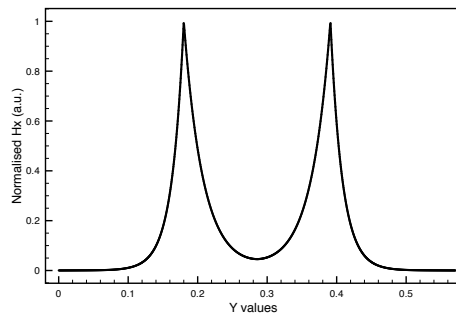
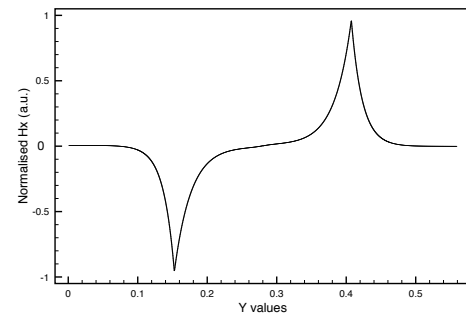
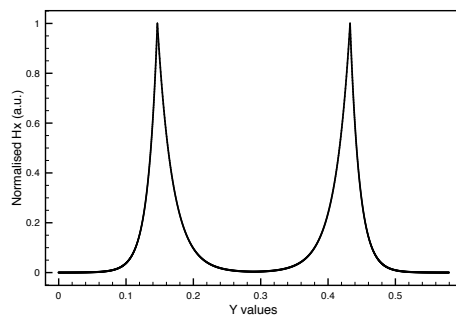
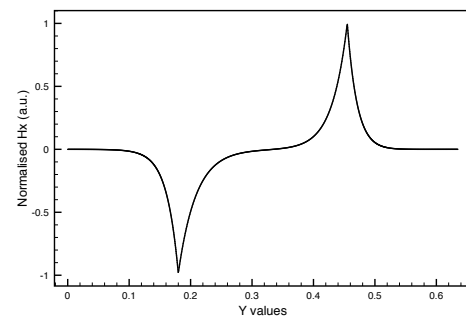
(a) H_x even mode for $t = 0.045\mu m$ (b) H_x odd mode for $t = 0.06\mu m$ (c) H_x even mode for $t = 0.07\mu m$ (d) H_x odd mode for $t = 0.07\mu m$ (e) H_x even mode for $t = 0.2\mu m$ (f) H_x odd mode for $t = 0.2\mu m$ (g) H_x even mode for $t = 0.3\mu m$ (h) H_x odd mode for $t = 0.3\mu m$

FIGURE 3.10: Even and odd modes for the $Ag-SiO_2-Ag$ structure for core thicknesses $0.045\mu m$ (even only), $0.06\mu m$ (odd only), $0.07\mu m$, $0.2\mu m$ and $0.3\mu m$

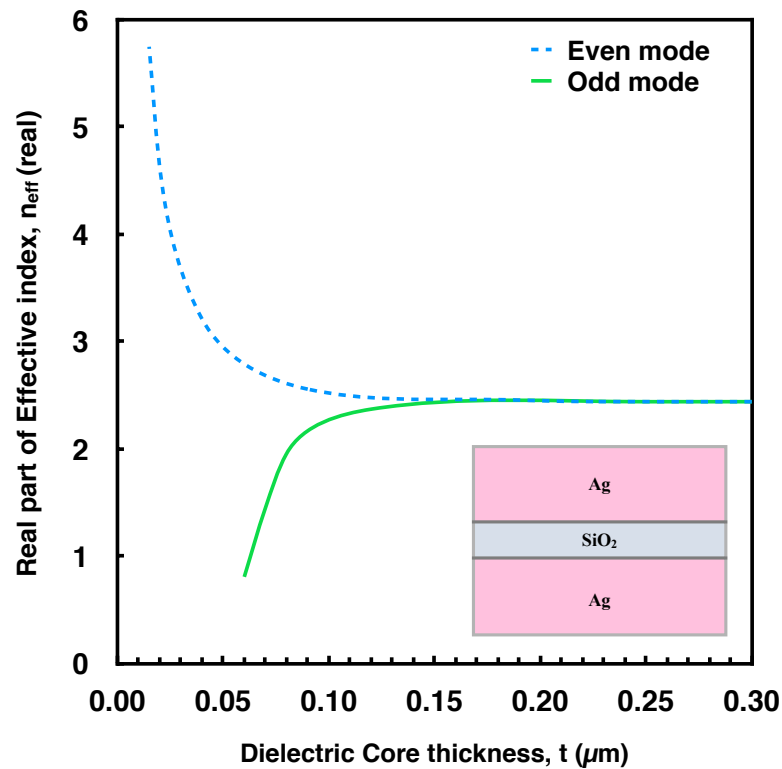


FIGURE 3.11: Variation of effective index of the even and odd coupled modes for symmetric MIM structure

converge at a single real effective index value.

As can be seen from the figure (fig 3.11), the effective index of the even mode was very high, 3.068346 at the thickness of $0.045\mu\text{m}$. The odd mode at $0.06\mu\text{m}$ has an effective index of 0.974461. When the thickness of the guide is increased the effective index of the even mode reduces and the effective index of odd mode increases. Eventually the effective indices of both modes converge to a single effective index value of 2.43784.

The propagation characteristics shown in Fig. 3.11 can be explained from the observation of the field profiles of the two supermodes, for different values of the dielectric thickness. The normalized field profile of the even supermode, for a small film thickness of $0.045\mu\text{m}$, is shown in Fig. 3.10(a), where it can be seen that the field intensity is equally high at the two metal/dielectric interfaces and quite strong in the center of the dielectric film as well. The supermode behaves like two strongly coupled surface plasmon modes which propagate at the two metal/dielectric interfaces. For a larger film thickness of $0.2\mu\text{m}$, the field intensity at the centre of the even supermode reduces, as shown in Fig. 3.10(e). As the two metal/dielectric interfaces are moved apart, the supermode decouples into two independent surface modes. Due to symmetry, these modes then

propagate with an identical effective index. This effective index corresponds to the effective index of a single metal/dielectric interface, which was calculated to be 2.43784. This value corresponds to the value at which the effective index of the supermode converges, at a large film thickness, as shown in Fig. 3.11.

Similar features can also be observed from the normalized field profiles of the odd supermode, for different values of dielectric thickness. For a small dielectric thickness of $0.06\mu\text{m}$, as shown in Fig. 3.10(b), there is an appreciable amount of field intensity in the dielectric region and the transition of the field intensity from positive to negative, from the two opposite peaks at the metal/dielectric interfaces, or vice versa, is nearly linear. For a larger film thickness of $0.2\mu\text{m}$, as shown in Fig. 3.10(f), the supermode is more confined at each of the two interfaces, and the field intensity in the core of the waveguide flattens. The supermode decouples into two surface plasmon modes, which propagate at each metal/dielectric interface, but at opposite polarity, with an effective index equal to that of a single metal/dielectric interface, 2.43784. The effective indices of the odd and the even supermodes, converge to that value, as shown in Fig. 3.11, one from below and the other from above, respectively.

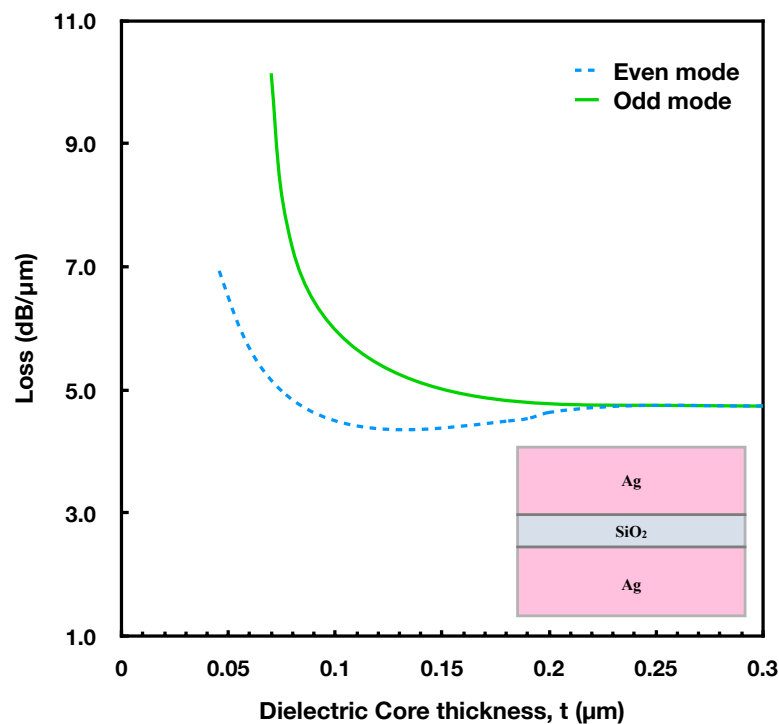


FIGURE 3.12: Variation of modal loss versus the dielectric thickness of the even and odd coupled modes for symmetric MIM structure

The loss characteristics are significantly different from the IMI loss characteristics and it is presented in Fig. 3.12. The loss values for both the modes reduce from two different points and converge to a single lower value when the dielectric core thickness increases. This is unlike the opposite structure in the previous section, where the loss values were seen to be increasing for the even mode and decreasing for the odd one. The even mode loss curve creates a minima lower than the converged loss value.

In this type of structure the thickness of the two metal-claddings, which are the lossy regions, does not change, and therefore the loss values depend mostly on the optical field intensity at the metal/dielectric interfaces. As mentioned earlier, For the even supermode, the loss is lower than that for the odd supermode. As the dielectric film thickness increases, the two loss values converge to a certain value which corresponds to the loss of a single metal/dielectric interface, as in the propagation characteristics, and this was calculated as $4.75 \text{ dB}/\mu\text{m}$. This can be explained, again, from the field profiles of the two supermodes, which are decoupled into two independent surface plasmon modes, which propagate at the two interfaces, for large dielectric film thickness.

It can be observed from Fig. 3.12 that both the loss curves start from higher loss values. The even mode curve starts early as it starts from $0.04\mu\text{m}$ core thickness. The loss value for $0.045\mu\text{m}$ is $7.005 \text{ dB}/\mu\text{m}$. The odd mode starts at $0.06\mu\text{m}$ core thickness and it has a loss value of $10.145 \text{ dB}/\mu\text{m}$ at a core thickness of $0.070\mu\text{m}$ which is much higher than that of the even mode loss values. When the core thickness increases both the loss values started to drop exponentially and converge to a single loss value of $4.75 \text{ dB}/\mu\text{m}$ after the thickness of $0.225\mu\text{m}$.

3.6 Six Layer Planar Optical Waveguide

Directional couplers are devices that couple fields from two different waveguides. Depending on the direction of power flow, directional couplers can be of two types, co-directional and contra-directional couplers. In a co-directional coupler, the power flow from the two devices have the same direction. But in case of a contra-directional coupler, power flow is in the opposite direction. At optical frequencies, waveguides that support plasmonic modes like the IMI and MIM structures, propagate light in the backward and forward directions respectively. Thus the coupling of these two types of structures forming IMIM waveguide leads to contra-directional coupling between the two guides. As SPPs can operate much below the diffraction limit, optical contra-directional

couplers based on SPPs can show very short coupling length resulting in higher integration density and much better confinement.

To investigate contra-directional coupling and the performance of plasmonic planar structures further, the six layer structure presented in [203] has been studied. Figure 3.13 shows the schematic diagram of the six layer guide. Numerical simulations were performed using the full vectorial (\mathbf{H} field formulation) finite element method (as presented earlier in Chapter 2) at an operating wavelength of $0.3 \mu\text{m}$.

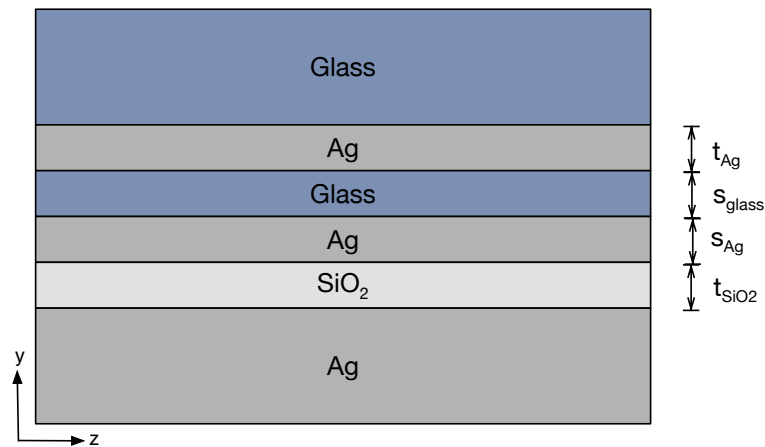


FIGURE 3.13: 6 layer IMIMIM structure with Glass, Ag and SiO_2

In the work, Wang *et al.* investigated the contra-directional coupler property of the structure for a specific mode. It can be clearly observed in Fig. 3.13 that the structure is constructed using one IMI and one MIM structure. Therefore there is one metal core and another dielectric core and as can be seen there are five metal dielectric interfaces. As discussed in Section 3.5, both the IMI and MIM sub-structures can support both even and odd supermodes. The six layer structure in this section has one extra metal dielectric interface between the two substructures which could also produce even and odd coupling with the supermodes of the substructures. Therefore, there could be 2^5 possible modes in theory.

In [203], Wang *et al.* considered the $SPSM_2$ supermode. The H_x magnetic field of the mode can be seen in Fig. 3.14a and the electric field is shown in Fig. 3.14b. The article highlights the direction of the Poynting vector in the two cores. It can be seen in Fig. 3.14c, the Poynting vector in the Ag core and the SiO_2 core are pointing towards the opposite direction. The structure evaluated in the work had $t_{Ag} = t_{SiO_2} = 15 \text{ nm}$ and $s_{Glass} = s_{Ag} = 20 \text{ nm}$.

In this section a more in-depth characterisation of the structure was performed for the mode analysed in [203] and two other modes namely $SPSM_1$

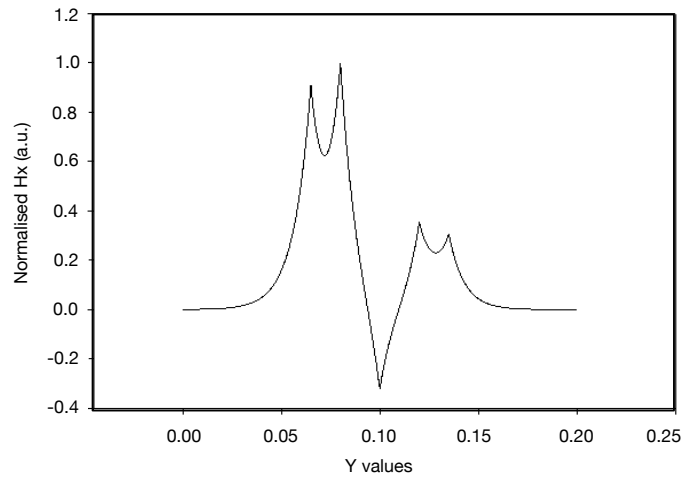
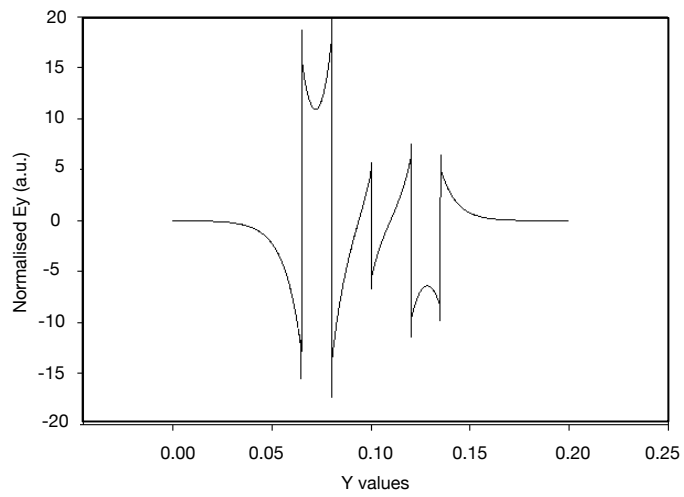
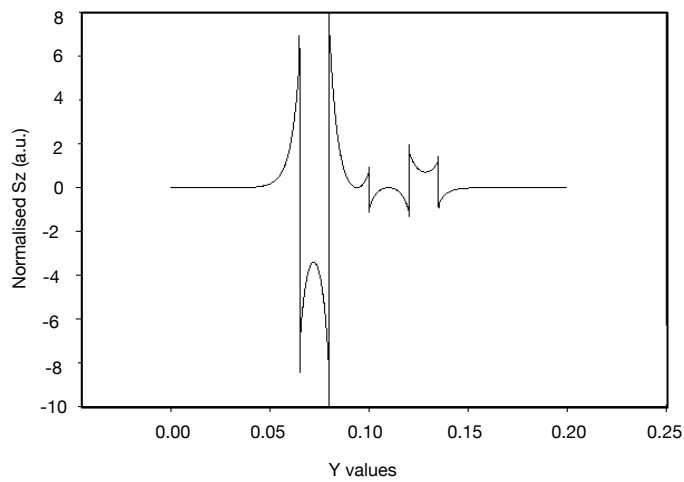
(a) H_x field profile of the $SPSM_2$ mode(b) E_y field profile of the $SPSM_2$ mode(c) S_z profile of the $SPSM_2$ mode

FIGURE 3.14: $SPSM_2$ mode for the six layer structure for $t_{Ag} = t_{SiO_2} = 15 \text{ nm}$ and $s_{Ag} = s_{Glass} = 20 \text{ nm}$

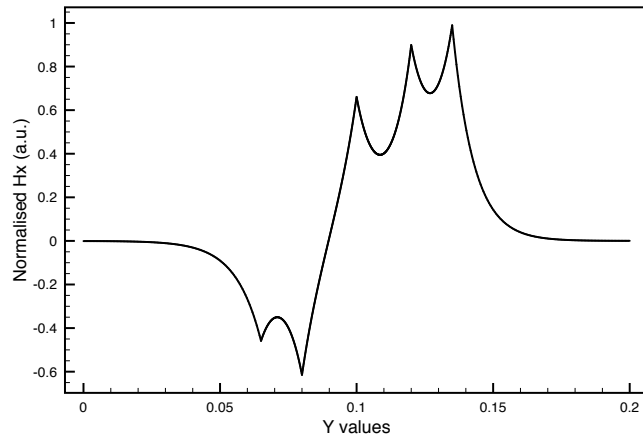
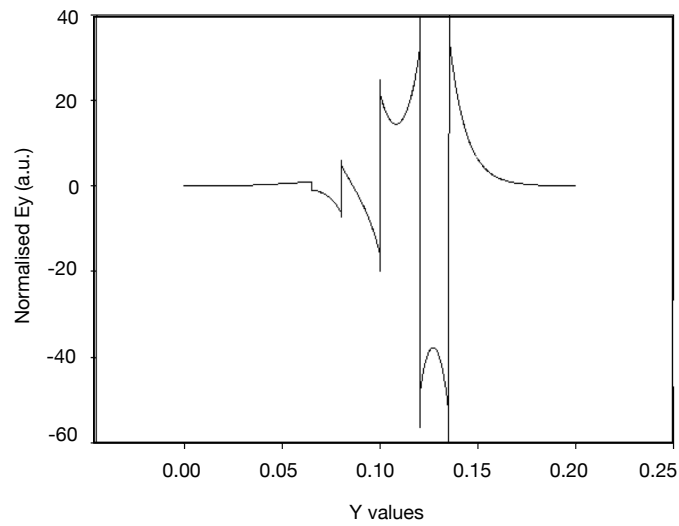
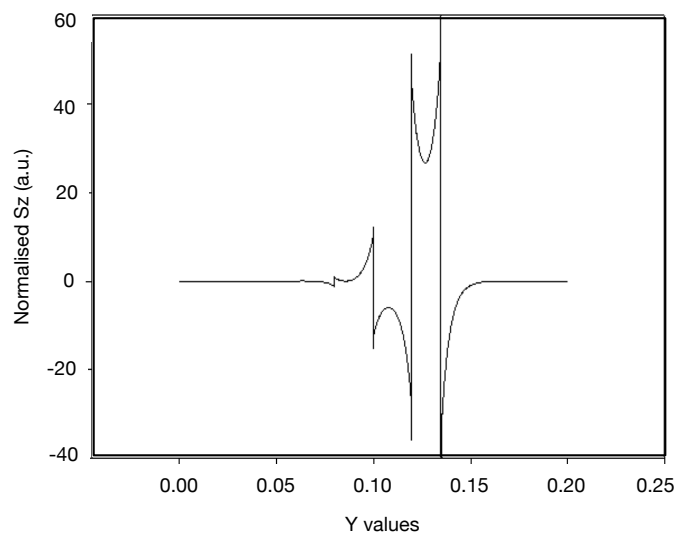
(a) H_x field profile of the $SPSM_1$ mode(b) E_y field profile of the $SPSM_1$ mode(c) S_z profile of the $SPSM_1$ mode

FIGURE 3.15: H_x , E_y and S_z profiles of the $SPSM_1$ mode for $t_{Ag} = t_{SiO_2} = 15 \text{ nm}$ and $s_{Ag} = s_{Glass} = 20 \text{ nm}$

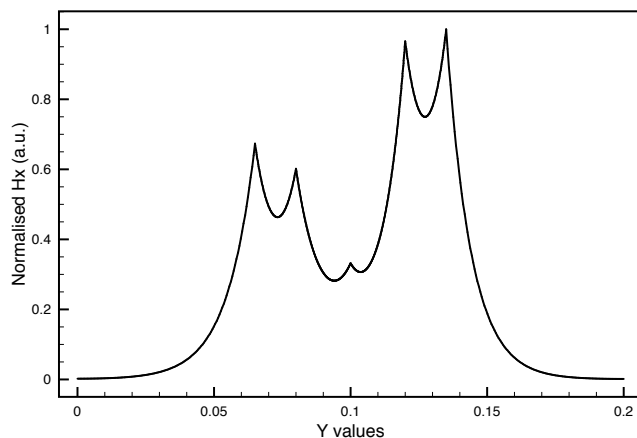
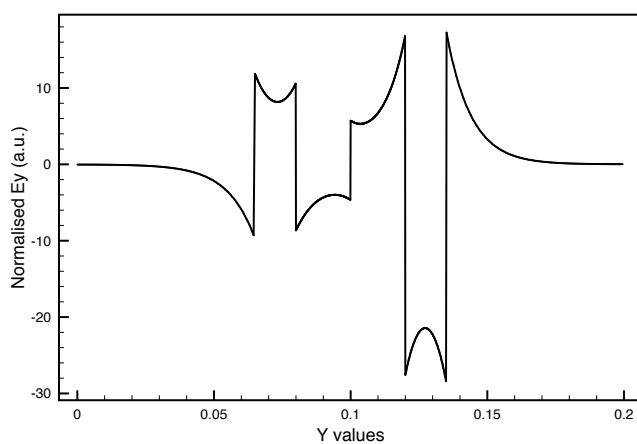
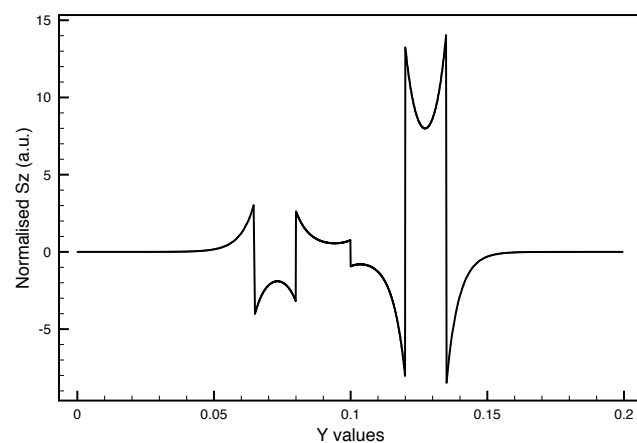
(a) H_x field profile of the $SPSM_0$ mode(b) E_y field profile of the $SPSM_0$ mode(c) S_z profile of the $SPSM_0$ mode

FIGURE 3.16: H_x , E_y and S_z profiles of the $SPSM_0$ mode for $t_{Ag} = t_{SiO_2} = 15 \text{ nm}$ and $s_{Ag} = s_{Glass} = 20 \text{ nm}$

and $SPSM_0$ shown in Figs. 3.15 and 3.16 respectively, where the subscripts used in the mode names denote the zero crossings of the field distribution. The magnetic field H_x , electric field E_y and the Poynting vector S_z profile of both the modes are shown in these two figures. To study the characteristics of each mode, the thickness of the cores and the separation between the cores of the substructures were varied. To make things simple, the core thicknesses and the separations between the substructures were taken to be equal ($t_{Ag} = t_{SiO_2}$ and $s_{Ag} = s_{Glass}$). The wavelength considered was $0.3 \mu m$. The material indices are $n_{Ag} = 0.013109 + j1.847482$ [201], $n_{SiO_2} = 1.44568$ [202] and $n_{Glass} = 2.04939$ [202].

3.6.1 Variation of Separation

Separation between the two cores was varied to characterise the structure for the three modes mentioned before. To make things simple s_{Ag} and s_{Glass} were kept equal for all the simulations.

SPSM₂ mode

Figure 3.14a shows the $SPSM_2$ mode. In this supermode the two single-interface plasmonic modes on the left side couple together in an even manner. The second and the third interfaces couple in odd manner. The third and the fourth interfaces also couple in odd manner whereas the fourth and the fifth interfaces couple in even manner.

To study the mode characteristics with separation, the width of separation layers were varied from $s_{Ag} + s_{Glass} = 40 \text{ nm}$ to 90 nm keeping the widths equal, $s_{Ag} = s_{Glass}$.

For examining the propagation and attenuation characteristics of the structure, it is necessary to observe the field profiles of the mode for the different values of separation. Figure 3.17 shows the H_x , E_y field profiles and the corresponding Poynting vectors S_z for the $SPSM_2$ mode for four different values of the separation, s , whereas the thicknesses of the cores were kept constant at $t_{Ag} = t_{SiO_2} = 25 \text{ nm}$. The left side core denotes the SiO_2 core whereas the right handed one refers to the Ag core in all of the profiles in this figure.

At $s = 45 \text{ nm}$, the H_x field is more confined in the SiO_2 core although a considerable amount of field is concentrated in the Ag core as well. As the separation increases, field confined in the SiO_2 core slightly increases along with the field confinement in the Ag cladding and that in the Ag core gradually

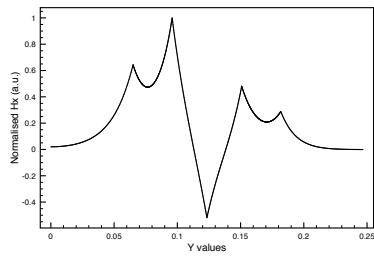
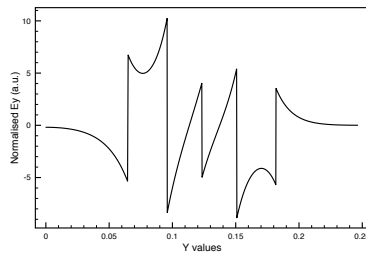
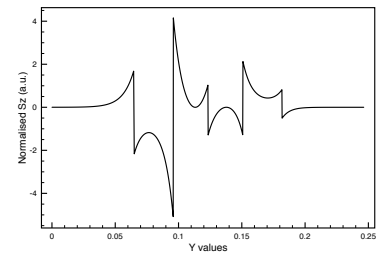
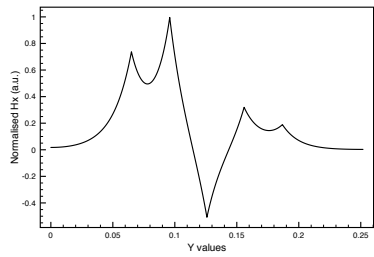
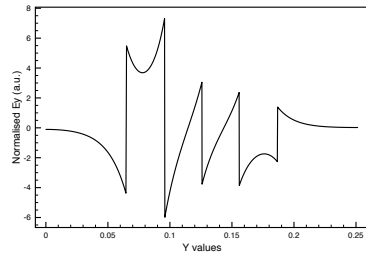
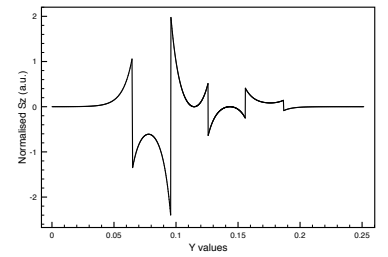
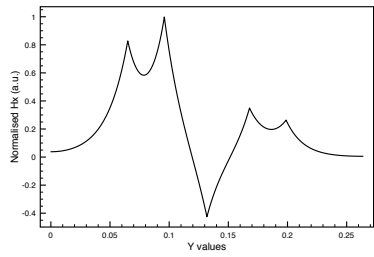
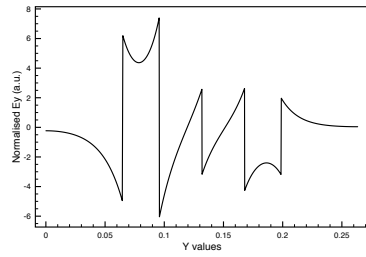
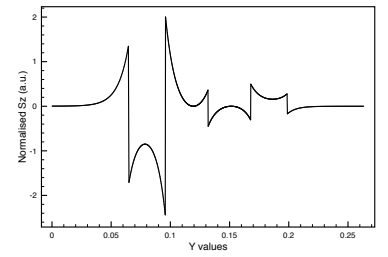
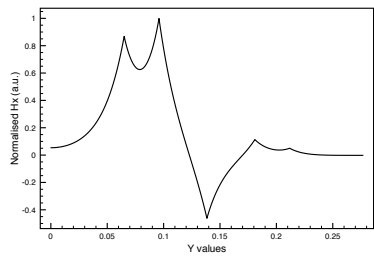
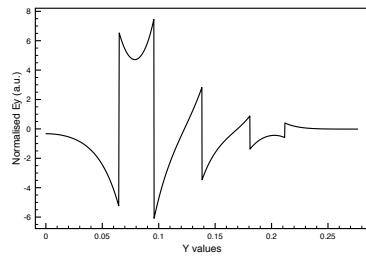
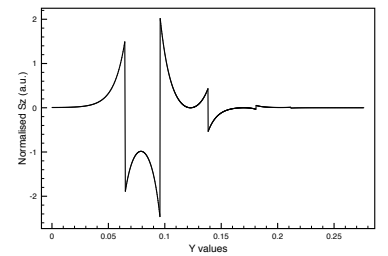
(a) H_x field profile at $s = 45$ nm(b) E_y field profile at $s = 45$ nm(c) S_z profile at $s = 45$ nm(d) H_x field profile mode at $s = 60$ nm(e) E_y field profile at $s = 60$ nm(f) S_z profile at $s = 60$ nm(g) H_x field profile at $s = 72$ nm(h) E_y field profile at $s = 72$ nm(i) S_z profile at $s = 72$ nm(j) H_x field profile at $s = 85$ nm(k) E_y field profile at $s = 85$ nm(l) S_z profile at $s = 85$ nm

FIGURE 3.17: Effect of variation of separation between the cores shown using the magnetic & electric fields and the Poynting vector profiles for different values of separation (s) for the $SPSM_2$ mode where $t_{Ag} = t_{SiO_2} = 25$ nm

becomes smaller. When the value of the separation is larger, the even mode in the MIM substructure becomes dominant than the even mode in the IMI substructure and the difference in confinement in the two cores start to increase. At a separation of $s = 80$ nm, power confined in the *Ag* core becomes very small as can be observed in Figs. 3.17j, 3.17k and 3.17l. After this value of separation, the fields in the IMI substructure almost vanishes and majority of the power is drawn into the MIM substructure.

Variation of the real part of the effective index of this mode is shown in Fig. 3.18. It can be noticed from the figure that the real part of the effective index decreases steadily as the separation between the core layers increases. Figure 3.19 shows the loss curve for the mode when the separation is varied. Power confinement in different layers of cores and claddings are presented in Fig. 3.20. It can be observed in Fig. 3.20, that the confinement factor characteristics change in 3 stages when the separation between the MIM and IMI parts is increased. Throughout the variation of separation, the glass cladding confinement factor drops steadily almost in a straight line. However the confinement in the *Ag* cladding increases rapidly and confinement in the *Ag* core decreases also in a rapid pattern. The confinement in *SiO*₂ core increases with the increasing values of separation.

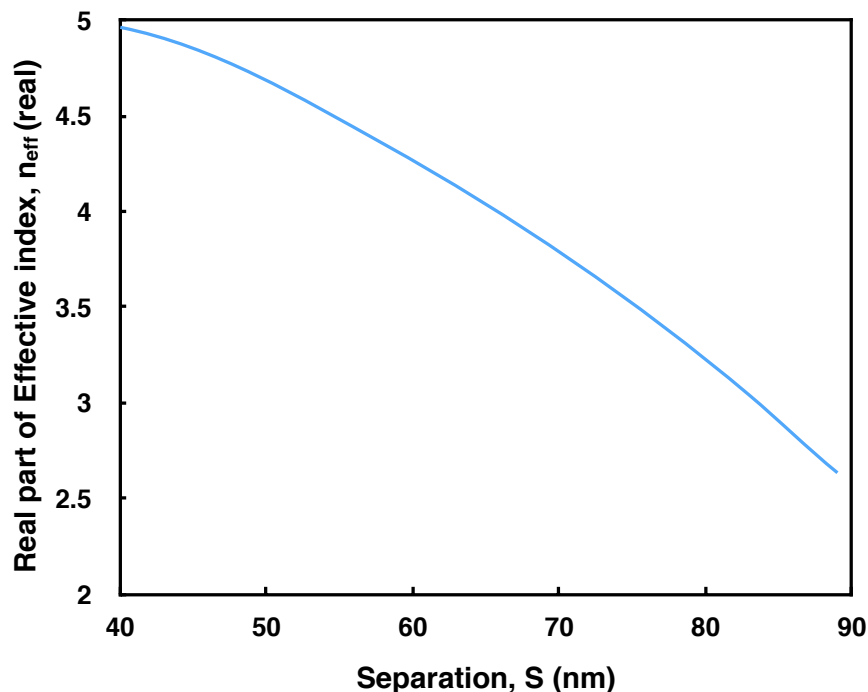


FIGURE 3.18: Variation of the real part of the Effective index of the $SPSM_2$ mode when the separation between the cores are varied from 40 nm to 90 nm

The effective index and the loss characteristics can be described using the field profiles of Fig. 3.17 and the power confinement plot for different layers shown in Fig. 3.20. As can be observed from the power confinement curve, the confinements in the two cores initially have almost same values. Hence the effective index is high for lower values of separation. Effective index is mostly governed by the dielectric core confinement and is not much affected by the metal core. For all values of separation, the mode is a MIM dominated mode where the SiO_2 core maintains higher confinement factor. When the separation between the MIM and the IMI parts increases more power moves into the MIM part as the power in the IMI part gets increasingly smaller which is depicted in the field profiles of Fig. 3.17 and can also be seen in Fig. 3.20. As the MIM substructure becomes more predominant, the effective index of the $SPSM_2$ mode approaches the effective index of the MIM mode. Therefore the effective index curve shows a decreasing pattern with increasing separation.

The loss characteristics shown in Fig. 3.19 shows that the loss values initially increase when the separation is increased upto $s = 56$ nm. After this value, the curve starts to follow a decreasing pattern with increasing values of separation. The confinement factor characteristics of Fig. 3.20 and the field distribution plots of Fig. 3.17 can be used to explain the attenuation characteristics. At the initial stage when the separation is increased, the loss of the guide increases due to the high confinement in the Ag core and also the rapid increase in power confinement in the Ag cladding. High field intensity in the metal layers, which is the lossy material, causes the loss values to rise high for the initial values of separation. But the confinement in the glass cladding and the Ag core decreases gradually as the evanescent tail of the Ag cladding of the MIM part leaks less power into the glass cladding of the IMI part. Moreover, as the field inside the Ag cladding is evanescent in nature, the increase in power confinement in this layer slows down as the separation increases. At a separation of 56 nm the loss peaks at a value 116.1 dB/mm. After this value of separation, the Ag core continues to lose confinement more rapidly as the rate of decrease of confinement is much greater than the increase in the Ag cladding and hence the loss values drop exponentially. The confinement in the Ag core decreases rapidly beyond the separation of 80 nm as the right hand side interface of the IMI substructure started to lose power rapidly. Due to the increased separation, the mode gets mainly confined in the MIM part and field in the metal core almost vanishes. Hence, the decrease in loss is continued as dielectric confinement increases.

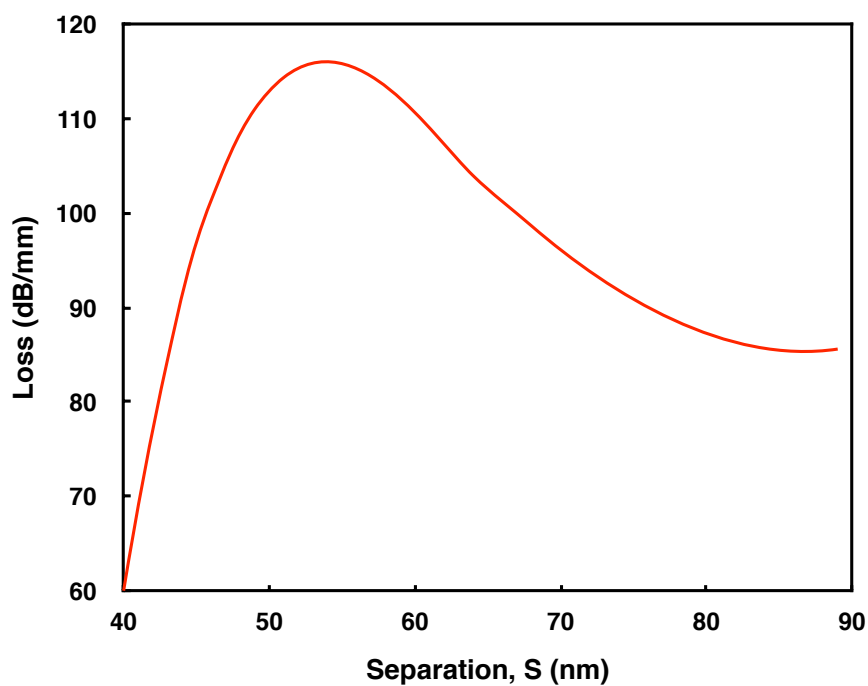


FIGURE 3.19: Loss variation when the separation between the cores are varied from 40 nm to 90 nm for the $SPSM_2$ mode

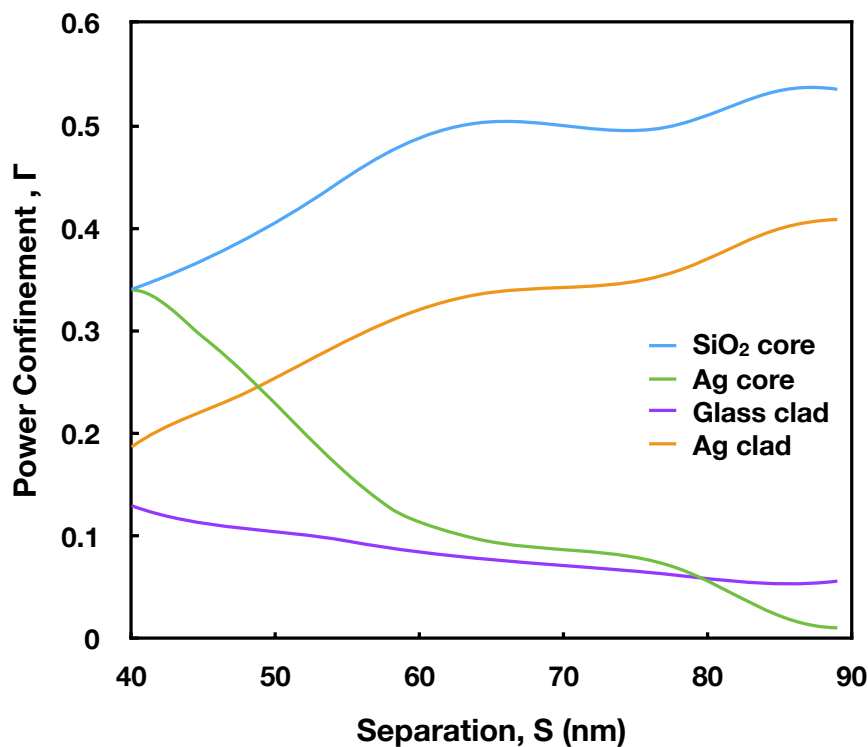


FIGURE 3.20: Power confinement in different layers when the separation between the cores are varied for the $SPSM_2$ mode

SPSM₁ mode

Figure 3.15a shows the $SPSM_1$ mode. In this supermode the two plasmonic modes at the leftside single interface couple together in an even manner. The modes at the second and the third interfaces couple in odd manner, those on the third and fourth interfaces couple in even manner and the modes on the fourth and fifth interfaces couple in even manner.

To obtain the propagation and loss characteristics of the mode by varying the separation of the two cores, $s_{Ag} + s_{Glass}$ was varied from 40 nm to 150 nm keeping s_{Ag} and s_{Glass} equal. These characteristics can be properly explained using the field profiles and the confinement factors of each layer. The $SPSM_1$ mode profiles for various values of separation are shown in Fig. 3.21. The effective index and loss characteristics of the mode are presented in Fig. 3.22 and 3.23 respectively. Figure 3.24 shows the confinement factors for the variation of separation for the mode under consideration.

The field profiles exhibit that when the separation is small, field amplitude in the Ag core and Glass cladding (right hand side core and cladding) is higher compared to the field amplitude for greater values of separation (Fig. 3.21a). As a result, at smaller separation the power confined in the Ag core is also higher. The power confinement in the glass cladding is high as well. This is because it is supporting the Ag core profile. This phenomenon can be observed in Fig. 3.21c. When the separation is increased field amplitude in the Ag core starts to decrease and the field starts to penetrate into the Ag cladding. Hence, field confined in the Silica core also takes a rise. At 53 nm separation, the power confined in the Silica core and the Glass cladding rises to a higher value which is almost same as that in the Ag core. Figure 3.21f shows the almost equal distribution of Poynting vector for the mode at 53 nm separation. When separation is further increased, the field rapidly moves into the Silica core and the confinement in the Ag core rapidly decreases. The power transfer from the IMI to MIM part continues until most of the power is transferred to the SiO_2 core and the mode effectively becomes three layer MIM mode at separation of 130 nm.

The effect of varying the separation on the effective index of the mode is depicted in Fig. 3.22. The effective index of the mode is mainly governed by the field intensity and power confinement in the dielectric layers. Initially the real part of the effective index increases rapidly as the separation increases. Figure 3.21c shows the Poynting vector distribution plot of the guide when the separation is 40 nm. It can be clearly seen that initially the power is mostly in the IMI structure for this mode. The confinement in the Glass claddings increase

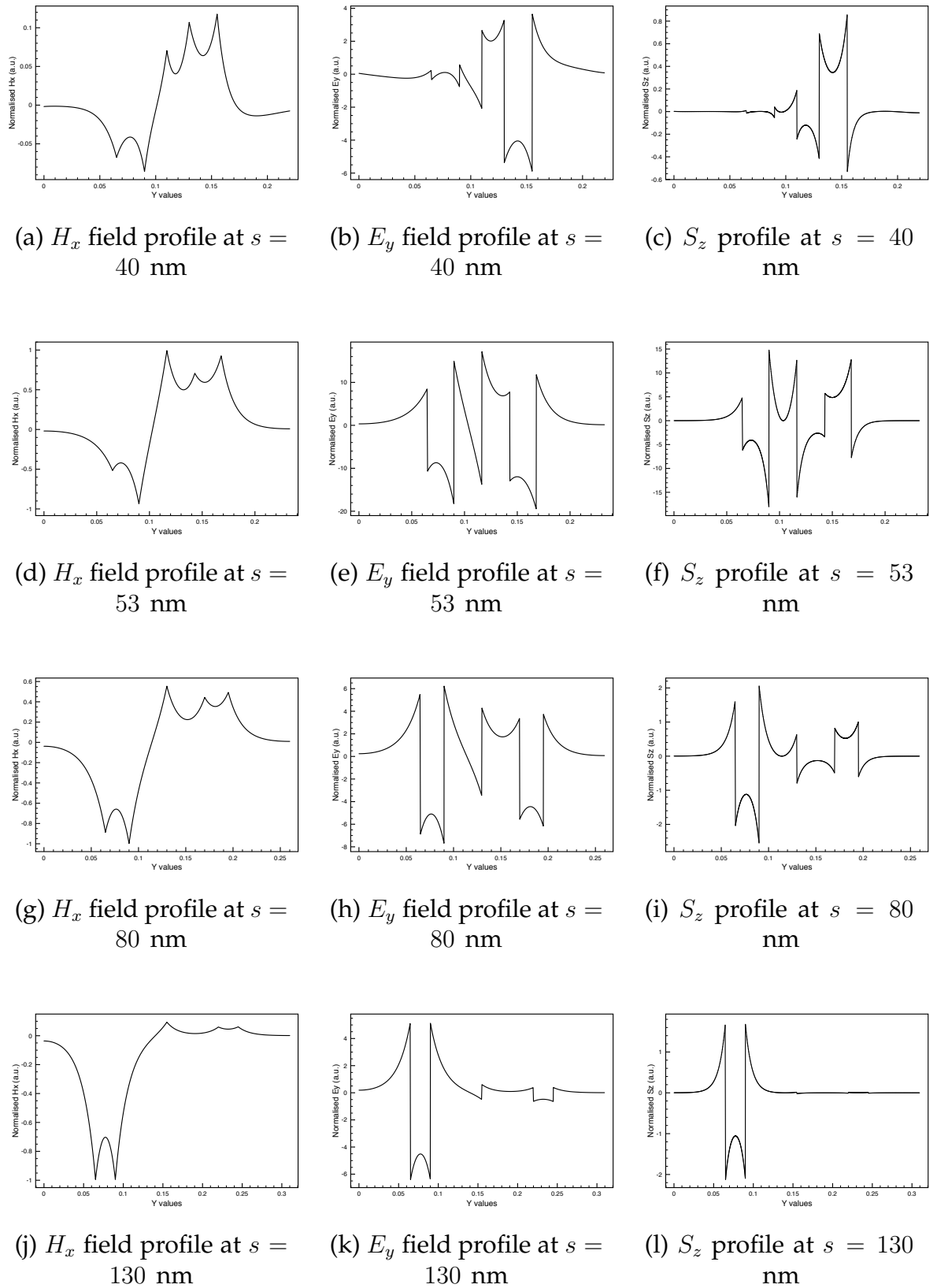


FIGURE 3.21: Effect of variation of separation between the cores shown using the magnetic & electric fields and the Poynting vector profiles for different values of separation (s) for the $SPSM_1$ mode where $t_{Ag} = t_{SiO_2} = 25$ nm

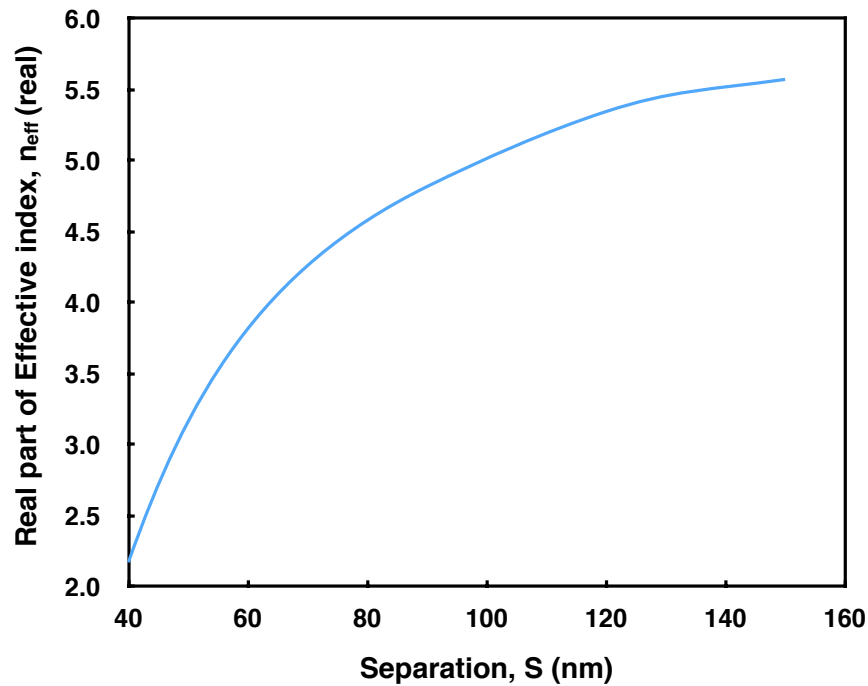


FIGURE 3.22: Variation of the real part of effective index for the $SPSM_1$ mode when the separation between the cores is varied

for initial values of separation. Hence the effective index also increases. When the separation increases the power starts to move into the MIM structure and hence the power confinement in the Silica core increases. The rate of increase of the effective index curve is slowed down as the separation increases mainly due to the rapid decrease in confinement of the glass claddings. After this value of separation the confinement in the Silica core rapidly goes to a higher value. This phenomena can be seen in the power confinement characteristics in Fig. 3.24. Figure 3.21f shows higher Poynting vector in SiO_2 core than that in Fig. 3.21c. Hence, the effective index continues to show an increasing pattern.

The loss characteristics of the mode for variation of separation is shown in Fig. 3.23 which is mostly dominated by the confinement in the cores of the structure. As can be seen in the figure, the loss decreases exponentially when the separation between the cores increases. In the power confinement factor characteristics (Fig. 3.24) it can be seen that at the initial stage the mode is dominated by the IMI structure and most of the power is confined in the Ag core. At this stage there is very little power confined in the SiO_2 core. Therefore due to the high confinement in the metal core at smaller separation values, the loss of the mode is the highest. When the separation is increased, power confinement of the Ag core starts to decrease. Initially confinement in the Silica core also decreases. Power confinement of the Ag cladding increases almost linearly

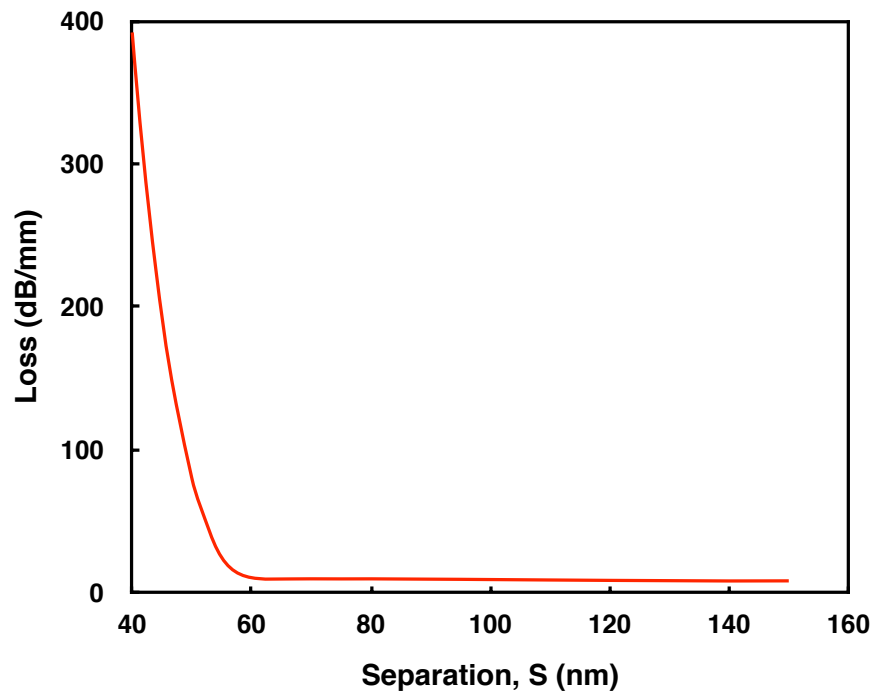


FIGURE 3.23: Loss variation when the separation between the cores are varied from 40 nm to 150 nm for the $SPSM_1$ mode

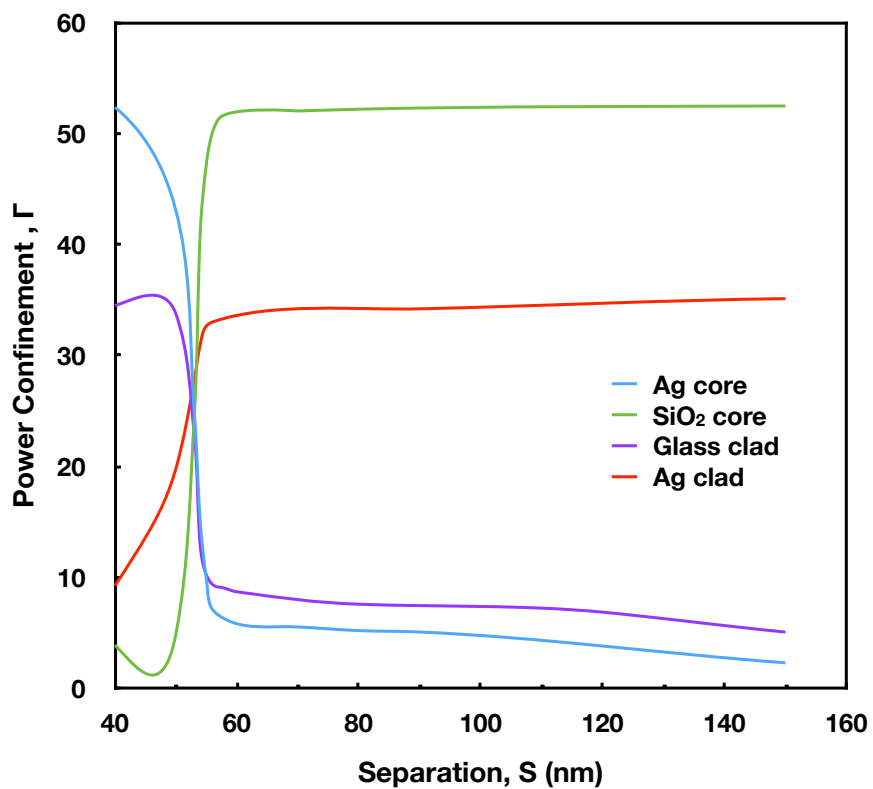


FIGURE 3.24: Power Confinement in different layers of the planar guide when the separation between the cores is varied from 40 nm to 150 nm for the $SPSM_1$ mode

as the power from the *Ag* core moves to the middle *Ag* cladding. Power confinement in the glass cladding also increases initially, specially at the middle plasmonic mode on glass-*Ag* cladding interface. When the separation is further increased the power confinements change rapidly. More power moves from the *Ag* core (or IMI) to the *SiO₂* core (MIM). The confinement in the *Ag* core rapidly decreases and this started after 45 nm of separation which can be observed in Fig. 3.24. The confinement in the glass cladding rapidly decreases at this stage. This is mostly due to the rapid fall of confinement in the *Ag* core. At this stage, confinement in the *Ag* cladding also increases more rapidly than before. But the confinement in the Silica core takes over more power at a much faster rate than any other layer. As a result, the loss of the mode exhibits a rapid decrease. At around 53 nm separation, the power confinement in all the cores and cladding layers become almost equal. Figure 3.21f shows the almost equal distribution of Poynting vector for the mode at 53 nm separation. The power transfer from the IMI to MIM part continues until most of the power is transferred to the *SiO₂* core and the mode effectively becomes three layer MIM mode at separation of 130 nm which can be observed in Figs. 3.21j, 3.21k and 3.21l. The decreasing loss of the mode tend to exhibit a saturating behaviour starting at a value of 9.31 dB/mm at a separation of 70 nm. This is aligned with the power confinement saturation at 70 nm separation presented in Fig. 3.24.

SPSM₀ mode

For the *SPSM₀* supermode, the H_x field profiles of all the SP's couple with each other in an even manner (Fig. 3.16a).

Figures 3.25a, 3.25d, 3.25g and 3.25j shows the H_x field profiles of the *SPSM₀* mode with the separations of 50 nm, 70 nm, 100 nm and 130 nm, respectively. It can be observed that when the separation is low at 50 nm, the field amplitudes in both the cores dominate and the SP mode at the middle single interface between *Ag* cladding and glass cladding is not visible in Fig. 3.25a. The field amplitudes in both the cores are almost equal.

When the separation is increased, the field amplitude in the *Ag* core starts to fall and the middle interface couples more field than before and become visible. Figure 3.25d, shows the H_x field profile with a separation of 70 nm. The middle SP is clearly visible in Fig. 3.25d.

With further increase in separation, the field amplitude in the *Ag* core falls sharply. Figures 3.25g and 3.25j, shows the H_x field profiles for 100 nm and 130 nm values of separation, respectively. It can be seen that amplitude for both

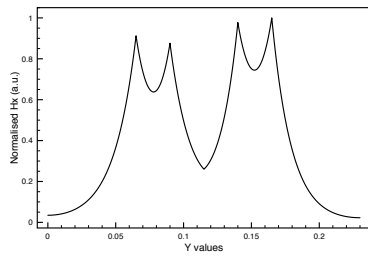
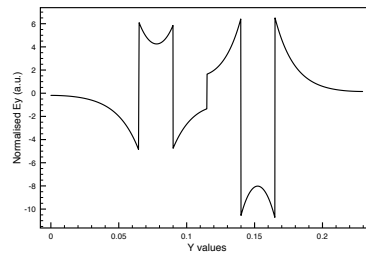
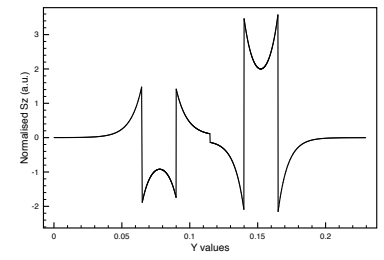
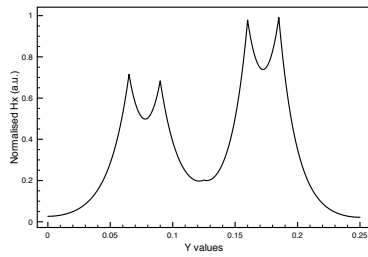
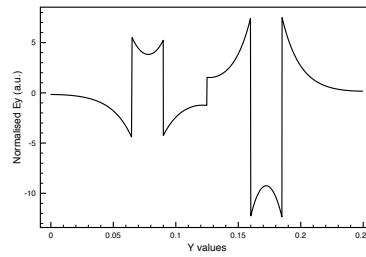
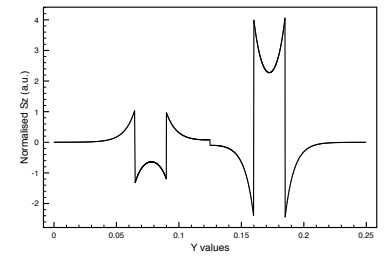
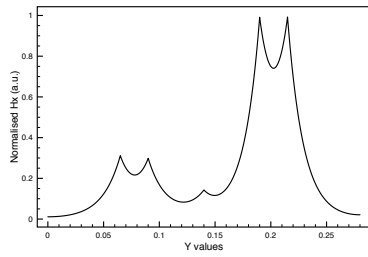
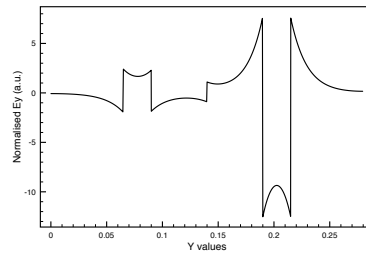
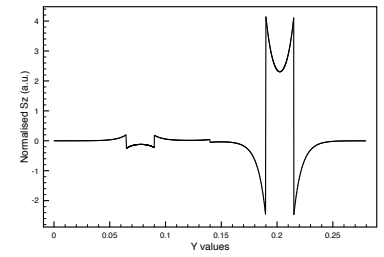
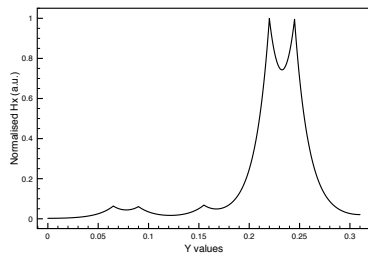
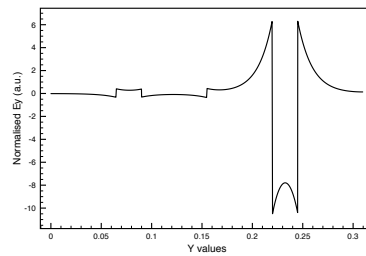
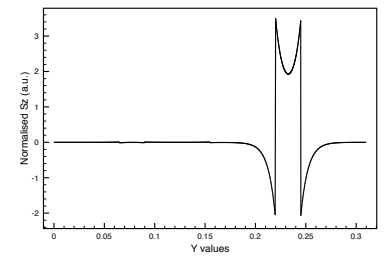
(a) H_x field profile at $s = 50$ nm(b) E_y field profile at $s = 50$ nm(c) S_z profile at $s = 50$ nm(d) H_x field profile at $s = 70$ nm(e) E_y field profile at $s = 70$ nm(f) S_z profile at $s = 70$ nm(g) H_x field profile at $s = 100$ nm(h) E_y field profile at $s = 100$ nm(i) S_z profile at $s = 100$ nm(j) H_x field profile at $s = 130$ nm(k) E_y field profile at $s = 130$ nm(l) S_z profile at $s = 130$ nm

FIGURE 3.25: Effect of variation of separation between the cores shown using the magnetic & electric fields and the Poynting vector profiles for different values of separation (s) for the $SPSM_0$ mode where $t_{Ag} = t_{SiO_2} = 25$ nm

the Ag core and the middle interface SP mode becomes significantly lower than the dominant amplitude in Silica core.

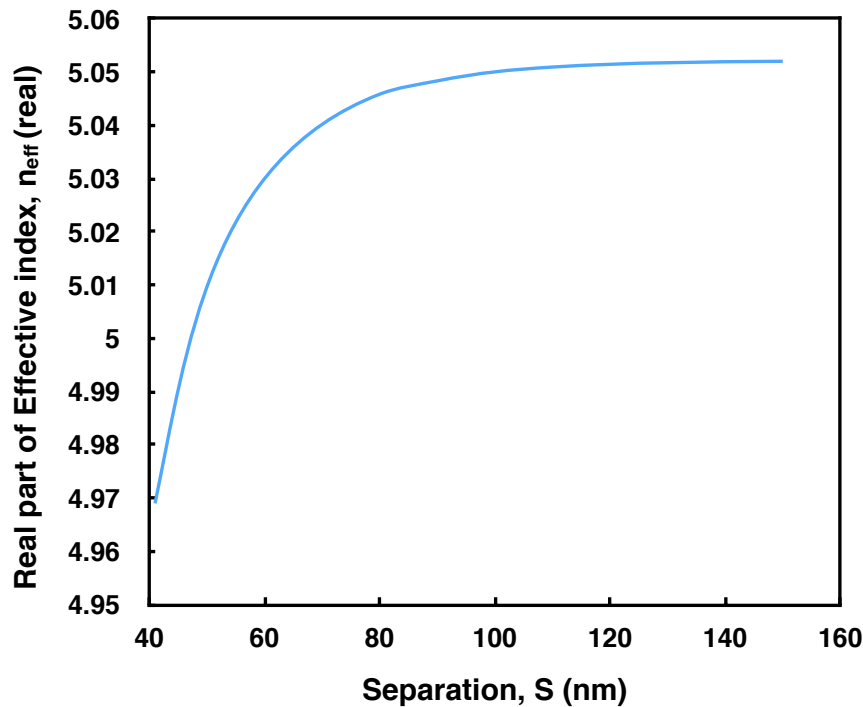


FIGURE 3.26: Variation of the real part of effective index for the $SPSM_0$ mode when the separation between the cores is varied from 40 nm to 150 nm

Figures 3.26 and 3.27 shows the variations of effective index and the loss with separation from 40 nm to 150 nm. Power confinement in different layers are presented in Fig. 3.28. It can be seen in Fig. 3.26 that the effective index increases with the increase of separation and saturates around a value of 5.05 for higher values of separation. As the field moves away from the Ag core, the index of the $SPSM_0$ supermode exponentially moves towards a higher index which is greater than the total index of the mode itself at a lower separation. The mode gains noticeable amplitude when the Ag core started to lose field to the Silica core. The middle interface SP also loses amplitude to the Silica core when the separation is further increased. The impact of the middle interface SP on the effective index is thus insignificant.

However, the loss of the $SPSM_0$ mode, as shown in Fig. 3.27 initially increases in an exponential manner. The loss reaches a peak value of 41.86 dB/mm at a separation of 60 nm then started to fall again and nearly stabilises at 36.599 dB/mm after a separation of 120 nm. The loss characteristics can be better explained with the field profiles and the power confinement of different layers.

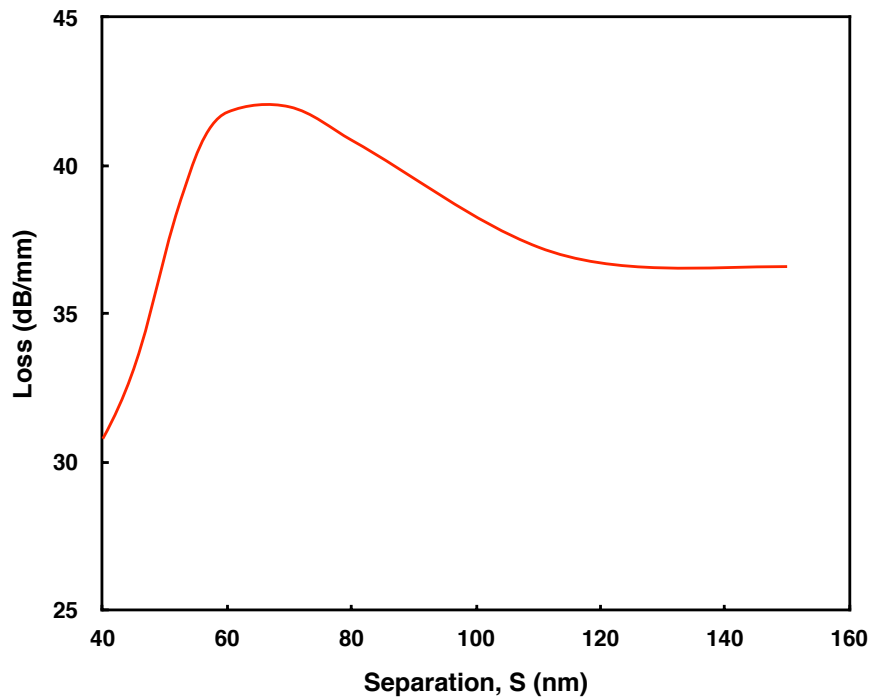


FIGURE 3.27: Loss variation when the separation between the cores is varied from 40 nm to 150 nm for the $SPSM_0$ mode

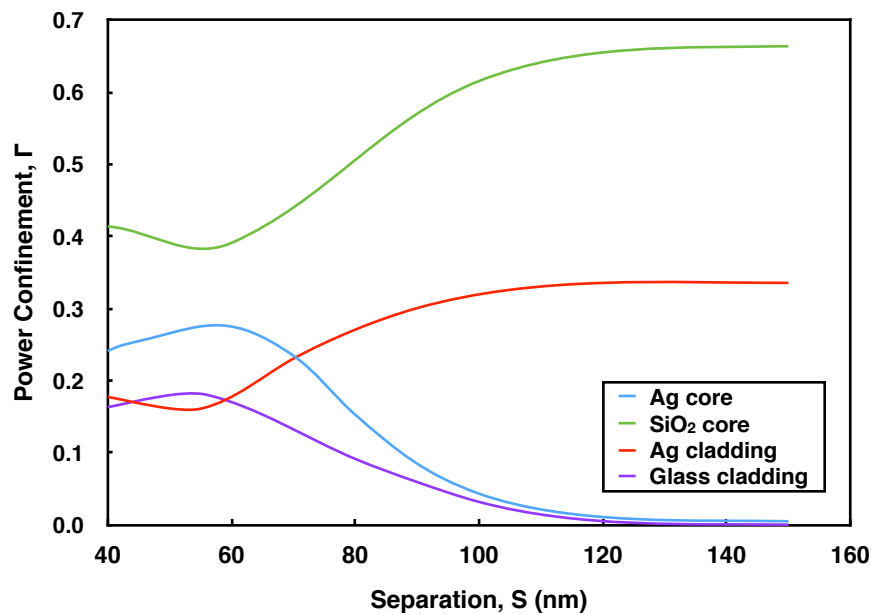


FIGURE 3.28: Power confinement in different layers when the separation between the cores is varied for the $SPSM_0$ mode

Figure 3.28 shows the power confinement in the two cores and the claddings with the variation of separation. It can be observed that initially the confinement of the *Ag* core and that of the Glass cladding increases whereas confinement in the Silica core and in the *Ag* cladding decreases and this trend continues up to 60 nm of separation. This is inline with the maximum amplitude of the middle interface SP at this separation. From Fig. 3.25 it can be seen that for lower values of separation, field intensity in the lossy *Ag* layers are more and the power inside the metal layers tend to get lower for higher values of separation. For separation values upto 60 nm, the increase in *Ag* core confinement is much more than the decrease of confinement in the *Ag* cladding. As a result the loss values increase for these values of separation. Hence, it coincides with the peak in the loss curve (Fig. 3.25d). Beyond 60 nm of separation, both the *Ag* core and the middle interface SP lose field to the Silica core. After this separation, power in both the *Ag* core and the Glass cladding start to decrease whereas the Silica core and the *Ag* cladding start to gain more power. Hence there is significant reduction in amplitude in the *Ag* core and middle interface SP. This phenomenon causes the drop in the loss curve. It can also be seen that at higher values of separation, the power confinement in Silica is significantly higher than the other layers and hence the loss of the guide reduces. As the confinement of power in Silica core saturates at around 66% the loss also stabilises at 36.599 dB/mm.

3.6.2 Coupling length calculation

The coupling length, L_c between two modes is defined as:

$$L_c = \frac{\lambda}{2(n_1 - n_2)} \quad (3.31)$$

where λ is the wavelength and n_1 and n_2 are generally the effective indices of the fundamental (even) and first order (odd) modes of the two coupled waveguides operated at the specific wavelength.

The $SPSM_0$ and the $SPSM_2$ modes are primarily even in nature. This is because both the fields inside the two cores are in the same direction. On the other hand, for the $SPSM_1$ mode the field inside the two cores are pointing in the opposite directions. Therefore to calculate the coupling length, both the $SPSM_0$ and the $SPSM_2$ modes were used as the even mode and the $SPSM_1$ mode was considered to be the odd mode. Separation was varied to characterise the coupling length for the two combinations. Figure 3.29 shows the variation of

coupling length for both the combinations described above with separation between the cores.

It can be seen that the coupling length of $SPSM_1$ and $SPSM_2$ increases in a non linear function. On the other hand the coupling length of $SPSM_0$ and $SPSM_1$ increases with a linear function. At the initial stage of the separation of 40 nm both pairs show the same coupling length. But when the separation is increased at 55 nm the coupling length of $SPSM_1$ and $SPSM_2$ shows 63% higher coupling length than that of the combination of $SPSM_0$ and $SPSM_1$ modes. Therefore, for higher separation the $SPSM_0$ and $SPSM_1$ pair is better if the size of the device is considered.

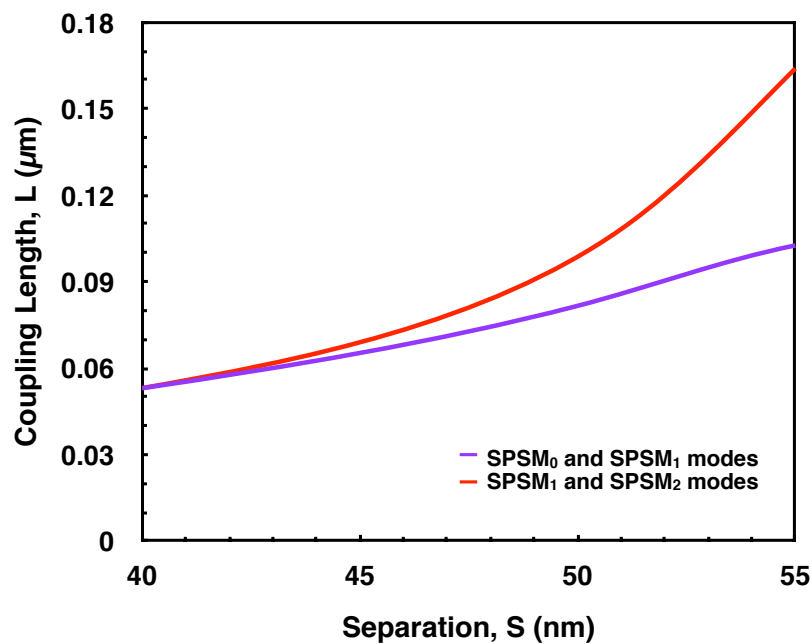


FIGURE 3.29: Variation of Coupling Length as a function of the separation between the cores (s)

Coupling between the modes can also be analysed considering the loss values of all the modes. Figures 3.19 and 3.27 show the loss curves for the $SPSM_2$ and $SPSM_0$ modes respectively. As can be seen in the figures, for both modes the loss increase with the increase in separation. Loss of $SPSM_2$ mode is higher than the loss of $SPSM_0$ mode for all the values of separation. For $SPSM_2$ mode loss at 40 nm separation is 60 dB/mm and at 55 nm separation the loss is 116 dB/mm . On the other hand, for $SPSM_0$ mode the loss at 40 nm is 30.78 dB/mm and at 55 nm the loss is 43.13 dB/mm . Therefore, for all thicknesses, $SPSM_0$ mode is preferable compared to the $SPSM_2$ mode when loss is considered.

Figure 3.23 shows the loss curve of $SPSM_1$ mode. As can be observed, the loss for lower separation is extremely high compared to the loss of higher separation. For 40 nm separation the loss is 392 dB/mm and for 60 nm separation the loss is 10.15 dB/mm. Therefore, for $SPSM_1$ mode higher separation is preferable when loss is considered.

Although the loss of the $SPSM_0$ and $SPSM_2$ modes are lower for smaller separations, due to extremely high loss of the $SPSM_1$ mode for smaller separation the overall loss for the contra directional coupler will be very high. On the other hand, for higher separation the loss of the $SPSM_2$ mode is significantly higher. But the loss of the $SPSM_0$ mode is comparatively lower. The loss for the $SPSM_1$ mode is significantly lower for higher separation.

Therefore, overall loss could be minimised if the coupling pair of $SPSM_0$ and $SPSM_1$ modes are considered. As the loss of the $SPSM_1$ mode saturates after 55 nm, the optimised separation for the structure with core thickness 25 nm is 55 nm. As described earlier, the $SPSM_0$ and $SPSM_1$ pair is also preferable when coupling length is considered.

3.6.3 Variation of core thickness

To analyse the impact of variation of thickness of the cores on the characteristics of the guide, the thicknesses of the cores were varied keeping the thickness of each core equal $t_{Ag} = t_{SiO_2}$. For this analysis only the core thicknesses were varied while the value of the separation was kept constant.

$SPSM_2$ mode

The propagation and loss characteristics for the $SPSM_2$ mode, with the variation of the core thickness, t , of the 6-layer planar guide were calculated using the full-vectorial FEM method. Figure 3.30 presents the variation of the effective index of the waveguide with the variation of the core thickness of 20 nm to 32 nm, t , for the $SPSM_2$ mode. As can be observed from the figure, the real part of the effective index of the mode varies in a decreasing pattern for increasing values of the core thickness.

In order to examine the propagation and attenuation characteristics of the structure, it is essential to observe the field profiles of the mode for the different values of the core thickness. Figure. 3.32 shows the H_x , E_y field profiles and the corresponding Poynting vector S_z for the $SPSM_2$ mode for four different values of the core thickness, t , whereas the separation between the cores were

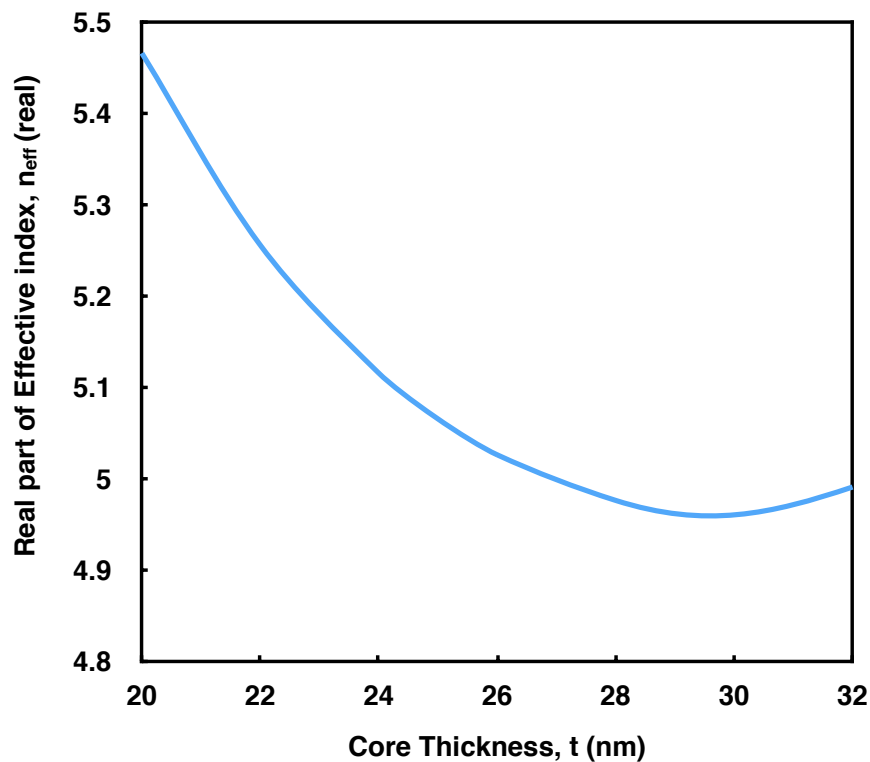


FIGURE 3.30: Variation of the real part of effective index for the $SPSM_2$ mode when the core thicknesses are varied from 20 nm to 32 nm

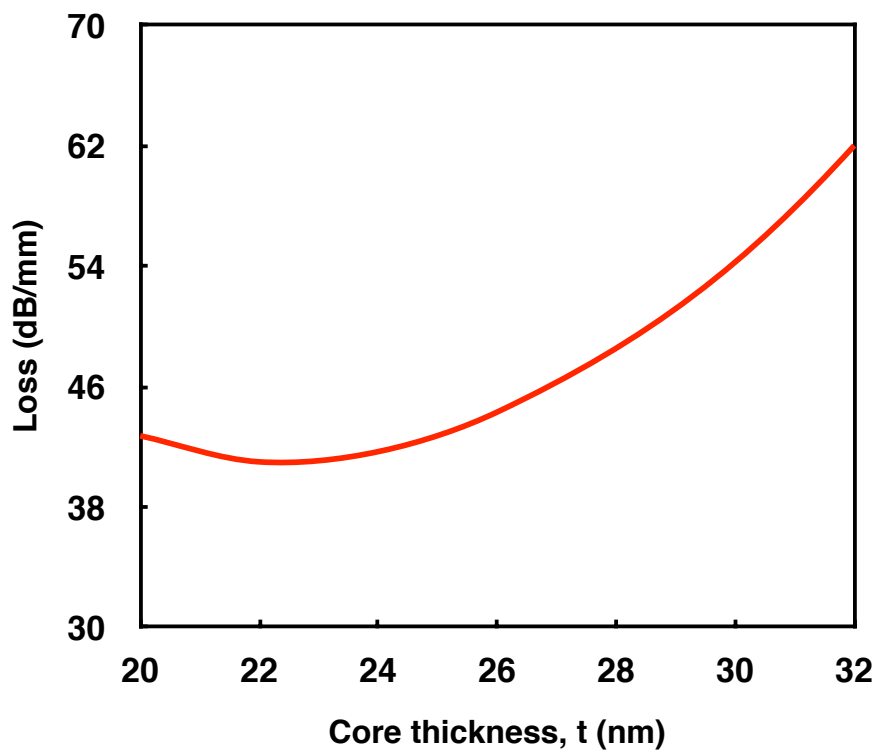


FIGURE 3.31: Variation of loss when the core thicknesses are varied from 20 nm to 32 nm for the $SPSM_2$ mode

kept constant at $s_{Ag} = s_{Glass} = 20 \text{ nm}$. The left side core denotes the SiO_2 core whereas the right handed one refers to the Ag core in all of the profiles in this figure.

For $t = 16 \text{ nm}$, the H_x field is more confined in the SiO_2 core and small amount of field is concentrated in the Ag core. As the thickness increases, more field is confined in the Ag core and that in the SiO_2 core gradually becomes smaller. When the value of the core thickness is larger, the even mode in the IMI substructure becomes comparable with the even mode in the MIM substructure and the confinement in the two cores come closer. At a core thickness of $t = 30.75 \text{ nm}$, power confined in both the cores become equal as can be observed in figs. 3.32j, 3.32k and 3.32l. After this value of core thickness, the IMI substructure becomes dominant and higher field intensity and power is drawn into the Ag core.

The propagation characteristics shown in Fig. 3.30 can be explained using the field profiles in Fig. 3.32. When the thickness of both the cores are smaller, the $SPSM_2$ mode is dominated by the power confined in the SiO_2 core. This can be seen in the Poynting vector plot in Figs. 3.32c and 3.32f. Therefore, the effective index characteristics follows the MIM characteristics described in section 3.5.3. As it is shown in Figs. 3.32a, 3.32d and 3.32g, the amplitude of the H_x field in the SiO_2 core decreases with the increase of the core thickness. Hence, when the thickness of the cores is increased, the overall effective index of the mode decreases. Fig. 3.32i shows that at 28 nm thickness, the power in both the SiO_2 and the Ag cores become almost equal. The effective index curve decreases to a minimum at $t = 30.75 \text{ nm}$ when both the cores hold equal amount of power. After this minimum, the effective index of the mode starts to increase again. This is because beyond this core thickness the power inside the Ag core becomes greater than that of the SiO_2 core. This can be seen in Fig. 3.32j.

Figure 3.31 presents the loss characteristics of the mode for core thicknesses of 20 nm to 32 nm . The power confinement in the two cores and the claddings are shown in Fig. 3.33.

The attenuation characteristics of the $SPSM_2$ mode in Fig. 3.31 can be explained by analysing the field profiles in Fig. 3.32 and variation of power confinement factor in Fig. 3.33. The loss values are mainly governed by the field intensity and power confinement in the metal layers. At the initial stage when the thickness of the cores is small, more field is confined in the SiO_2 core. Hence the losses are lower for low values of core thickness. For increasing values of

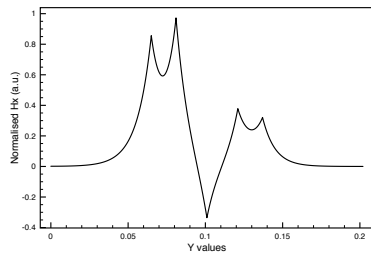
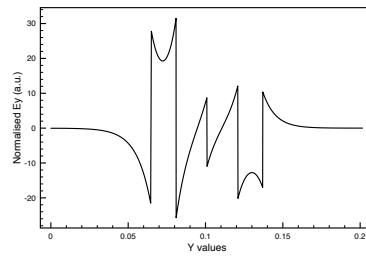
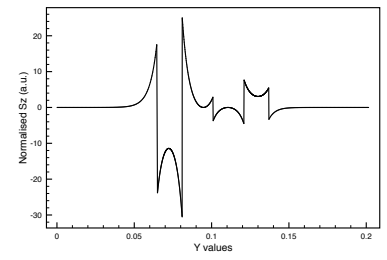
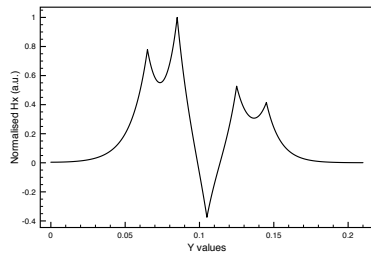
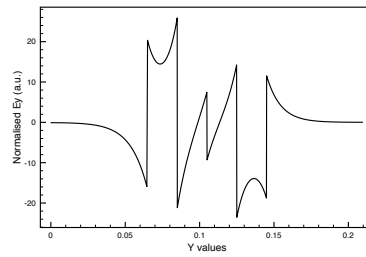
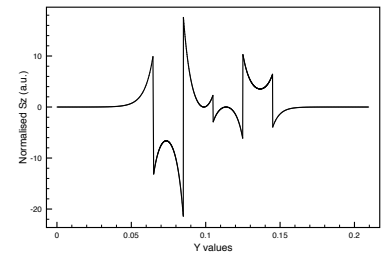
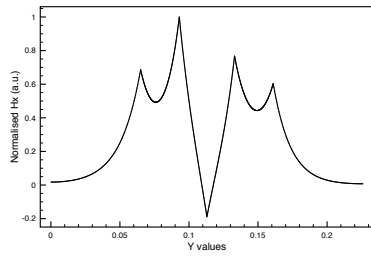
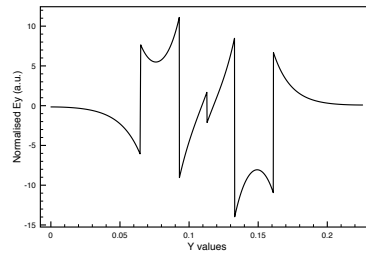
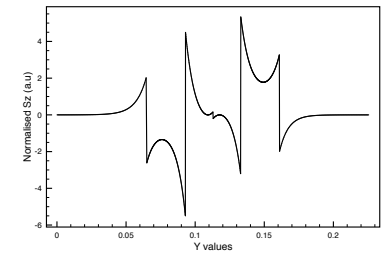
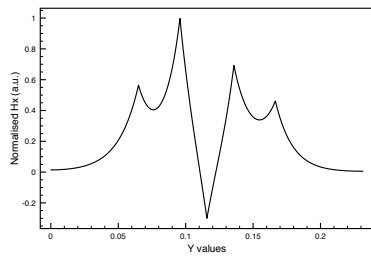
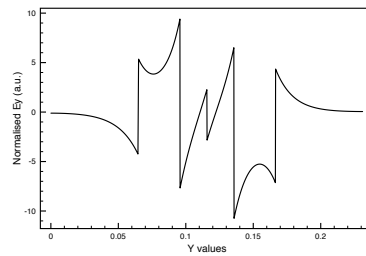
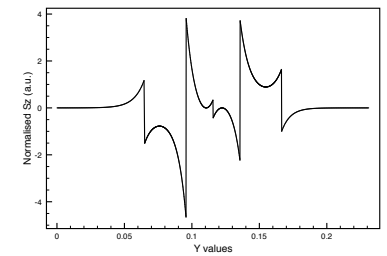
(a) H_x field profile at $t = 16$ nm(b) E_y field profile at $t = 16$ nm(c) S_z profile at $t = 16$ nm(d) H_x field profile mode at $t = 20$ nm(e) E_y field profile at $t = 20$ nm(f) S_z profile at $t = 20$ nm(g) H_x field profile at $t = 28$ nm(h) E_y field profile at $t = 28$ nm(i) S_z profile at $t = 28$ nm(j) H_x field profile at $t = 30.75$ nm(k) E_y field profile at $t = 30.75$ nm(l) S_z profile at $t = 30.75$ nm

FIGURE 3.32: Effect of variation of thickness of the cores shown using the magnetic & electric fields and the Poynting vector profiles for different values of core thickness (t) for the $SPSM_2$ mode where $s_{Ag} = s_{Glass} = 20$ nm

the thickness, confinement in the *Ag* core increases, but the increase in confinement in the *Ag* core is almost cancelled by the decrease in confinement in the *Ag* cladding. The power confinement in the *SiO₂* core decreases steadily in almost a linear pattern. Therefore, the initial stage is dominated by the decrease in confinement in *SiO₂*. The loss values reach a minimum at $t = 22$ nm. After crossing each other, the confinement in *Ag* core increases more rapidly than the confinement in the *Ag* clad as the rate of decrease in power confinement factor in the *Ag* clad slows down. Hence, there is a net increase in power confinement in the lossy metal layers. As a result, the loss started to increase after $t = 22$ nm and the power confined in both the cores become more comparable. As the thickness of the core increases, the net increase of power in the lossy metal layers causes the loss to increase in a non-linear manner. When the core thickness becomes $t = 30.75$ nm, the power confinement in both the cores are equal and beyond this value, the confinement in *Ag* core becomes the dominant one. Therefore the rate of change of loss value increase even more. It can be seen the loss of the mode reduces slightly from 42.724377 dB/mm at 20 nm core thickness to 40.994522 dB/mm at 22 nm thickness. After that, the loss begins to climb upward in a non-linear manner. At a core thickness of 32 nm, the loss of the mode becomes 61.986688 dB/mm.

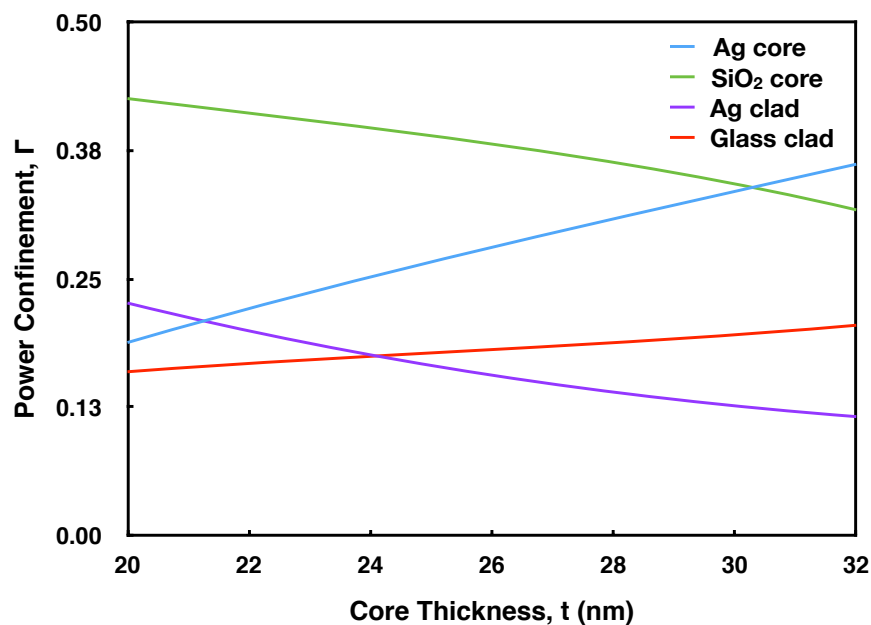


FIGURE 3.33: Variation of power confinement factor when the core thicknesses are varied from 20 nm to 32 nm for the $SPSM_2$ mode

SPSM₀ mode

Similar to the $SPSM_2$ mode, the variation of the effective index of the $SPSM_0$ mode with the variation of the core thickness was examined and the results obtained are presented in Fig. 3.34. As it can be seen from the graph, for small values of core thickness, t , the effective index, n_{eff} , is quite high, but as the core thickness increases, the effective index, n_{eff} , reduces to the value $n_{eff} = 4.916369$. Figure 3.36 shows the loss characteristics of the $SPSM_0$ mode. As can be observed in the figure, the loss of the mode also decreases in a non-linear manner. The variation of power confinement in the cores and the claddings with the variation of core thickness is presented in Fig. 3.37.

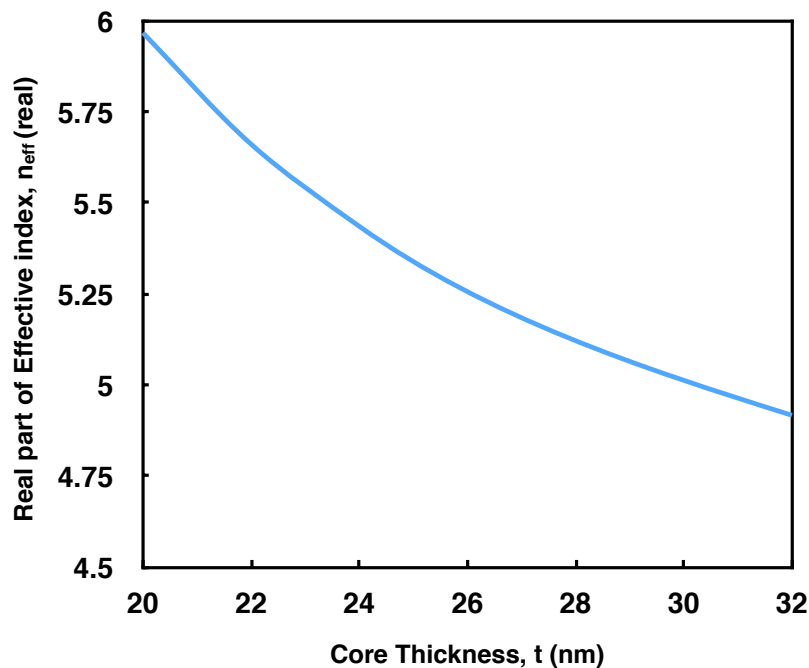


FIGURE 3.34: Variation of real part of the effective index when the core thicknesses are varied from 20 nm to 32 nm keeping the total separation constant at 40 nm for the $SPSM_0$ mode

For explaining the propagation and attenuation characteristics of the structure, the field profiles of the $SPSM_0$ mode for the different values of the core thickness were observed. Figure. 3.35 shows the H_x , E_y field profiles and the corresponding Poynting vector S_z for the $SPSM_0$ mode for four different values of the core thickness, t , whereas the separation between the cores were kept constant at $s_{Ag} = s_{Glass} = 20$ nm. The left side core denotes the Ag core whereas the right handed one refers to the SiO_2 core in all of the profiles in this figure.

Similar to the $SPSM_2$ mode, for $t = 15$ nm, the H_x field intensity is more in the SiO_2 core and small amount of field is concentrated in the Ag core. As the

thickness increases, field intensity in the Ag core increases and that in the SiO_2 core gradually becomes smaller. When the value of the core thickness is larger, the amplitude of the third peak start to reduce significantly and the amplitude difference between the even modes in the IMI and the MIM substructures also decreases. At a thickness of 24 nm , the third peak almost disappears. After this point, the third peak takes a flip and shows odd like coupling and further increase in thickness causes the amplitude of the third peak to increase in an odd manner. At a core thickness of 26 nm , the field intensity in the two cores are almost equal and the confinements come closer.

The effective index characteristics in Fig. 3.34 can be explained using the field profiles and the confinement factor curve. Similar to the $SPSM_2$ mode, the $SPSM_0$ mode also exhibits higher field intensity at lower values of core thickness in the SiO_2 core as shown in field profiles of Figs. 3.35a, 3.35b and 3.35c. As can be seen in the confinement factor plot in Fig. 3.37 the power confinement factor in SiO_2 core and Glass cladding does not vary much with the increase in core thickness. However, the confinement factor of Ag core increases and that of the Ag cladding decreases. For the entire range of thickness variation, the confinement in the SiO_2 core is the highest of all and hence the mode is dominated by the MIM substructure surrounding the SiO_2 core. Therefore, when the core thickness is increased the effective index decreases in a pattern similar to the characteristics of the MIM substructure described in section 3.5.3.

The loss characteristics of the mode shown in Fig. 3.36 can be explained by observing the power confinement factor characteristics in Fig. 3.37 and the S_z Poynting vector profiles in Figs. 3.35c, 3.35f, 3.35i and 3.35l. It can be observed in the confinement factor curves that the confinement for the SiO_2 core and the Glass cladding are not very sensitive to change in the core thickness. But the confinements in the Ag core and in the Ag cladding increases and decreases respectively. Although the confinement factor for the Ag core increased, but in reality the power amplitude in the Ag core remains the same whereas the power amplitude in the SiO_2 reduces slightly but keeping the confinement factor same. Therefore, the field confinement in the surrounding Ag cladding layer decreases while the field confined in the Glass cladding remains almost the same. As a result, overall, field confinement in Ag layers decreases, causing a net decrease in loss. Moreover, for the entire range the mode is dominated by the MIM substructure and because of this dominance of the MIM side, the loss values decrease non-linearly with the increase of the thickness of the cores.

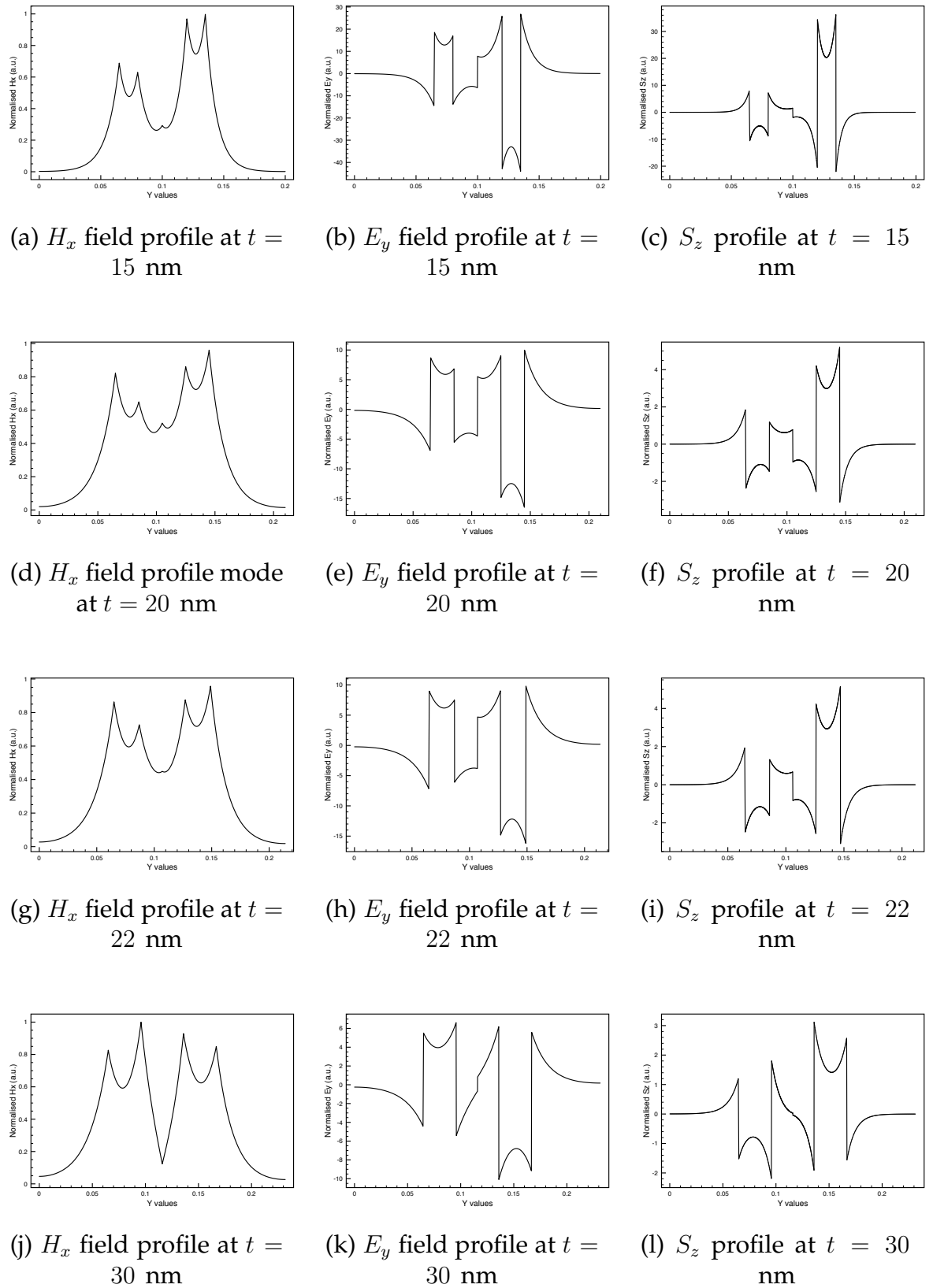


FIGURE 3.35: Effect of variation of thickness of the cores shown using the magnetic & electric fields and the Poynting vector profiles for different values of core thickness (t) for the $SPSM_0$ mode where $s_{Ag} = s_{Glass} = 20$ nm

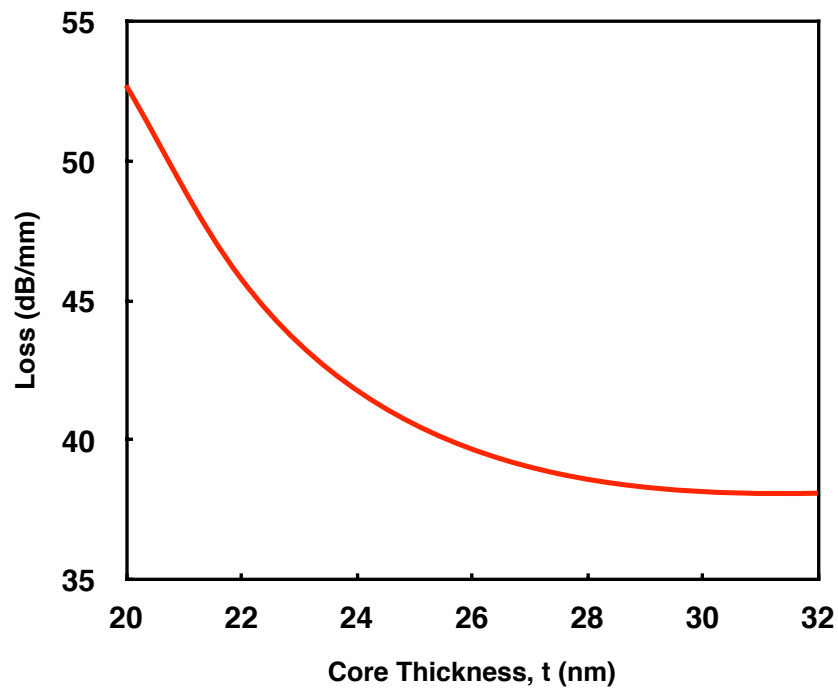


FIGURE 3.36: Loss variation for the $SPSM_0$ mode when the core thicknesses are varied from 20 nm to 32 nm keeping the total separation constant at 40 nm .

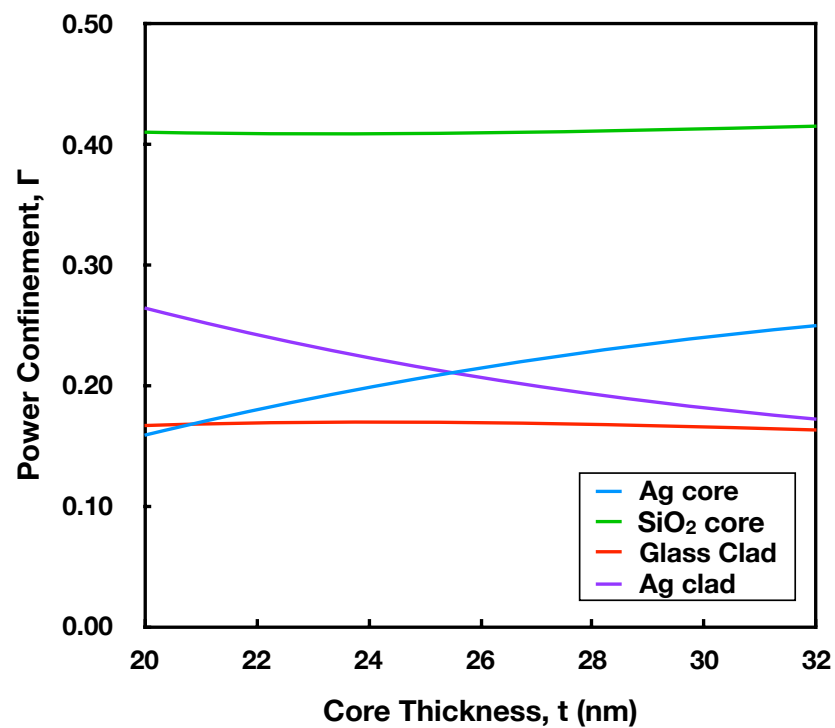


FIGURE 3.37: Power confinement variation for the $SPSM_0$ mode when the core thicknesses are varied from 20 nm to 32 nm keeping the total separation constant at 40 nm .

3.7 Summary

In this chapter, the complex propagation characteristics of certain types of planar plasmonic waveguides were investigated, by using the full-vectorial FEM. Planar structures incorporating metal and dielectric films, which exhibit loss and surface plasmon properties, were analysed, and finally a multilayer structure incorporating dielectric and metal layers suitable for contra-directional coupling applications was also examined. The analysis was carried out for three different multi-layer plasmonic modes. The propagation and attenuation characteristics along with the power confinements were studied.

For all the modes discussed above it was observed that the amplitude of the Poynting vectors in the Ag and the SiO_2 cores have opposite signs, suggesting that the direction of power flow is opposite in the two cores. Therefore, light injected in one core will couple light going in the opposite direction.

To study the loss characteristics of the contra directional coupler, the separation and the thickness of the guide was varied. It was observed that when the separation was increased for all three modes, the field confinement moved into one of the cores (the SiO_2 core) and at the end became almost like a three layer guide and lost the contra directional characteristics completely. Although $SPSM_1$ mode shows very low and stable loss at higher values of separation, the loss at low separation is extremely high where the contra directional coupling is active. The $SPSM_2$ and $SPSM_0$ modes show much lower loss in this region where separation value is low. Moreover, the shift of power to the SiO_2 core is much slower in $SPSM_2$ and $SPSM_0$ compared to the $SPSM_1$ mode. The $SPSM_0$ mode shows more stability for separations between 40 – 60 nm than the other two modes.

The $SPSM_2$ and $SPSM_0$ modes were studied with a fixed separation of 40 nm while varying the thickness of the two cores. For both the modes the contra directional coupling characteristics of the guide was present throughout the range. For the $SPSM_2$ mode, the loss initially decreases to a minimum of 41 dB/mm but it increases afterwards. The $SPSM_0$ mode shows higher loss at lower values of core thickness than the $SPSM_2$ mode. But the loss gradually reduces as the thickness increases and the loss saturates to 38 dB/mm for a thickness of around 30 nm. After that the loss moves up very slowly to remain near 38 dB/mm at the end of the range. Therefore, the loss characteristics is more stable with change of thickness for the $SPSM_0$ mode. It can also be observed that the loss for the $SPSM_0$ mode is lower compared to the $SPSM_2$ mode at higher thickness values.

The stability and the low loss of the $SPSM_0$ mode with separation and thickness variation makes it more suitable for practical use. As the mode is less sensitive to both separation and thickness variations, it is more manufacturing friendly. Lower loss of the mode means it is more likely to propagate longer in the structure.

Chapter 4

Hybrid Plasmonic Waveguide at Optical Frequencies

4.1 Introduction

Waveguides have been designed for many different applications and are important components in integrated optical circuits. To increase the integration density, compact circuits are preferred. One approach to achieve this is to use high refractive index contrast waveguides, for example, silicon waveguides with silica or air cladding. Silicon waveguides can guide light in a more confined manner than can be achieved using low index contrast waveguides. Silicon waveguides are compatible with CMOS (Complementary metal-oxide-semiconductor) technology; thus they offer the possibility for integrating electronics and photonics in the same material platform and have attracted much interest [204]. Since silicon is transparent in the near-infrared range, silicon waveguides have very low loss and are widely used in telecommunication. However, the mode size achievable with a silicon waveguide is still limited by the diffraction. As SPPs have shorter wavelength, plasmonic waveguides can operate beyond the diffraction limit. They offer the possibility of increased integration density for optical circuits. But at the same time, due to the complex refractive index of metal, plasmonic waveguides suffer from significant propagation loss. A combination of low propagation loss, high power density, and large confinement will be useful for many applications of plasmonic waveguides including nonlinear optics [205] and biosensing [206, 207]. Many kinds of plasmonic waveguides have been proposed for nanophotonic applications such as the dielectric loaded surface plasmon waveguide (DLSPW) [208], the plasmonic slot waveguide [209], and the hybrid plasmonic waveguide (HPWG) [210, 187, 211].

In this chapter a hybrid plasmonic waveguide at optical frequency will be

investigated. This chapter will focus on the complex propagation characteristics of a hybrid plasmonic waveguide (HPWG) and characterise various aspects such as the effective index, propagation loss, power confinements of the guide using the full-vectorial \mathbf{H} -field based FEM method described in Chapter 2. The results were then compared with those obtained by Alam *et al.* [212], for the same structure. From the comparison of the variation of the real part of the effective index and the propagation loss, with the spacer thickness for fixed core and metal layer thicknesses, the curves presented are found to be in good agreement, for both the TE and TM modes.

4.2 Hybrid Plasmonic Waveguide

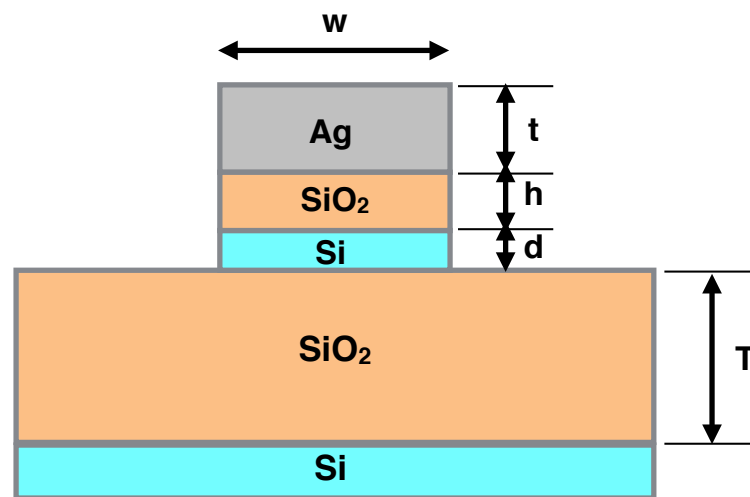


FIGURE 4.1: Schematic cross-sectional diagram of the hybrid plasmonic waveguide

The HPWG consists of a dielectric substrate with a high refractive index dielectric core sitting on the substrate, a metal layer at the top of the guide and in between the high index core and the metal cladding layer there is a low index dielectric layer called the spacer. The schematic structure is presented in Fig. 4.1.

As shown in the figure, the substrate considered for the structure is a Silica (SiO_2) layer sitting on Silicon. The high index Silicon (Si) core of the slot with width w sits on top of the Silica substrate. On top of the Silicon core there is a thin layer of Silica. This is the spacer layer. At the very top there is a Silver (Ag) layer. Silicon is chosen as the high index medium and silica is chosen as the low index spacer, so that the structure is fully compatible with silicon-on-

insulator (SOI) technology and is suitable for optical applications in the near infrared range. The thicknesses of the core, spacer and metal cladding are d , h and t respectively.

The most interesting aspect of the structure is that it combines both dielectric and plasmonic guiding schemes and forms a hybrid guiding scheme. The hybrid mode that concentrates in the low index spacer region offers a compromise between loss and confinement compared to pure plasmonic or pure dielectric modes. Therefore, the structure is more suitable for nano integrated photonic circuit design for its compactness and its low losses. Hence the HPWG offers the possibility of successful integration of silicon photonics and plasmonics on the same platform. In addition, the HPWG supports both the transverse electric (TE) and the transverse magnetic (TM) modes in two different layers and offers the possibility of developing devices which can manipulate the two polarizations independently.

In [212] the structure in Fig. 4.1 was characterised for the dimensions by varying h , d and t respectively using COMSOL multiphysics software [213]. In this chapter both the TE and the TM modes will be studied by varying h , d and t respectively using the full vectorial FEM method described in Chapter 2. Therefore, this chapter is a benchmarking exercise with our method. In addition to benchmarking, this chapter explains the phenomena by calculating the confinement factor for each layer of the structure. Material properties for silica and silicon are taken from [202] and that of the metal Silver is taken from [214].

4.3 The TM Mode

The TM mode is a hybrid supermode combining both the dielectric mode which is formed because of the lower index spacer and the substrate surrounding the core and the plasmonic mode formed at the interface between the spacer and the metal cladding on top.

Figure 4.2 shows the plasmonic and the dielectric modes separately. To obtain the plasmonic mode the core of the guide was replaced with the spacer material to obtain only a single interface. The dimensions chosen were $t = 200$ nm, $w = 350$ nm and the Silica thickness was taken as 350 nm. As there is only one interface, only the plasmonic mode develops at the single interface.

Similarly, the metal layer was replaced with the spacer material to make a pure dielectric guide. Figure 4.2(b) shows the pure dielectric TM mode.

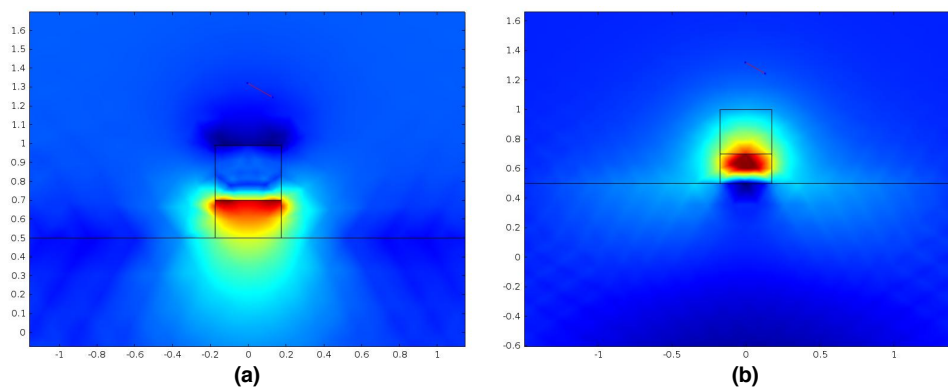


FIGURE 4.2: (a) Pure plasmonic and (b) pure dielectric H_x field profiles of the TM mode.

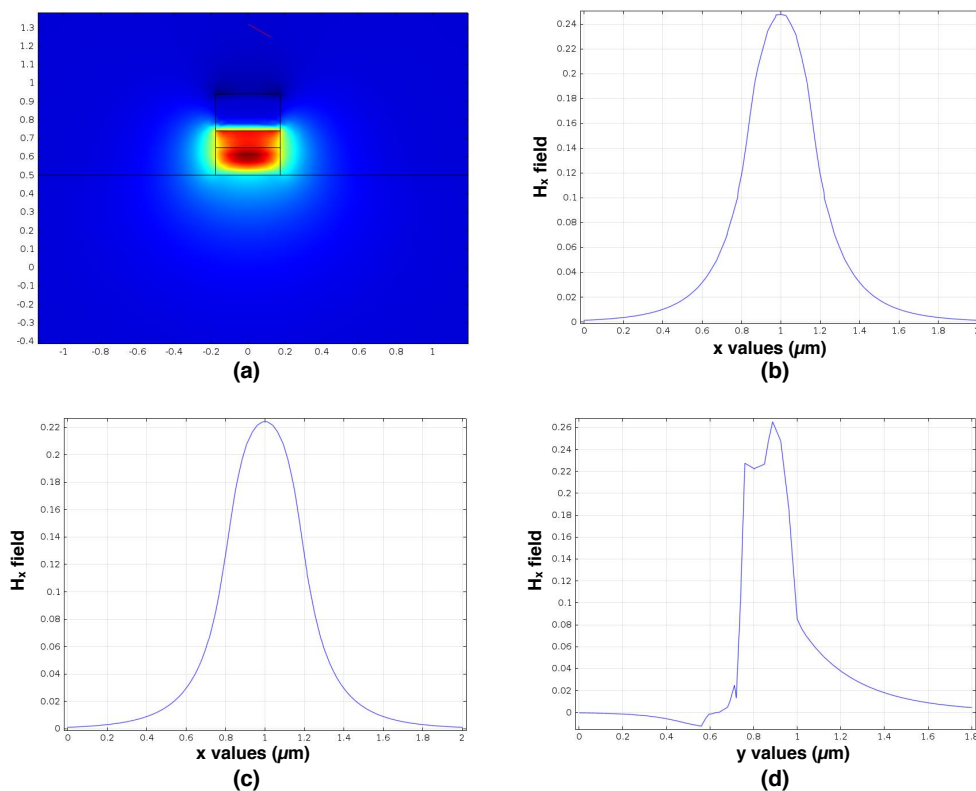


FIGURE 4.3: (a) 3-D Contour profile, (b) field through the core, (c) field through the spacer and (d) field parallel to the y -axis through the centre of the guide of the H_x field for the TM mode of the hybrid waveguide.

When the metal layer is introduced at the top of the guide, both the plasmonic and the dielectric TM modes couple to form the hybrid supermode. As both the modes couple in an even manner, the field intensity in the spacer region does not decay. Although the mode is more confined in the Silicon core, a significant part of the mode stays in the spacer region. Figure 4.3(a) shows the contour field profile of the H_x field. It clearly shows that the H_x field is continuing through the spacer to the metal surface with a lesser amplitude than the core. Figure 4.3(b), (c) and (d) show the field profiles along the cross section parallel to x-axis through the centre of the core, through the centre of the spacer and parallel to the y-axis through the centre of the guide, respectively.

As can be observed in Fig. 4.3(b) and (c), the H_x field distribution is Gaussian in shape in both the core and the spacer material. The cross section through the centre of the guide parallel to the y-axis in Fig. 4.3(d) is more interesting as it highlights the hybrid interaction between the dielectric and the plasmonic modes. It can be observed that the field distribution in the spacer is not decaying as it would be expected for a pure plasmonic mode at the Silver-Silica interface or for a pure dielectric mode in the core. When they are separately observed they show exponential decay in the spacer region. But when they couple together, the H_x field distribution remains high. After the spacer the field inside the metal layer decays very quickly in exponential manner.

4.3.1 Variation of Spacer Thickness h

In this section the thickness of the spacer h will be varied from 50 nm to 200 nm to observe the impact on the loss and the effective index of the structure. Figure 4.4, shows effective index versus h (spacer thickness) curve for three different core thicknesses of 100 nm, 150 nm and 200 nm. The thickness of the metal layer was kept constant at 200 nm. It can be observed from the figure that all of the curves show gradual decline. On the other hand the loss curve shown in Fig. 4.5 depicts a rapid fall of loss value with the increase of h .

This phenomena can be better explained by observing the power confinements in each layer.

Figure 4.6 shows the contour profile and the vertical cross sections of the H_x and E_y field distributions of the guide with a spacer thickness of $h = 90$ nm for a core thickness of $d = 100$ nm. Power Confinements in the metal layer, spacer and the core with the variation of spacer thickness h are plotted in Fig. 4.7 for a core thickness $d = 100$ nm and metal thickness $t = 200$ nm. Confinement in the layers for other core thicknesses considered in the analysis also exhibit

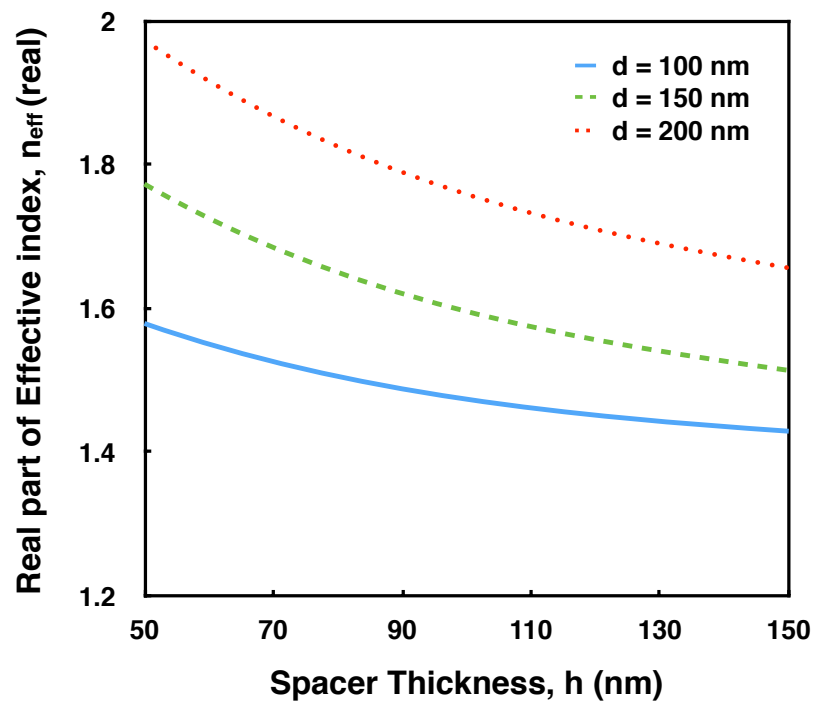


FIGURE 4.4: Variation of the real part of the effective index of the TM mode as a function of the spacer thickness h for three different core thicknesses (d)

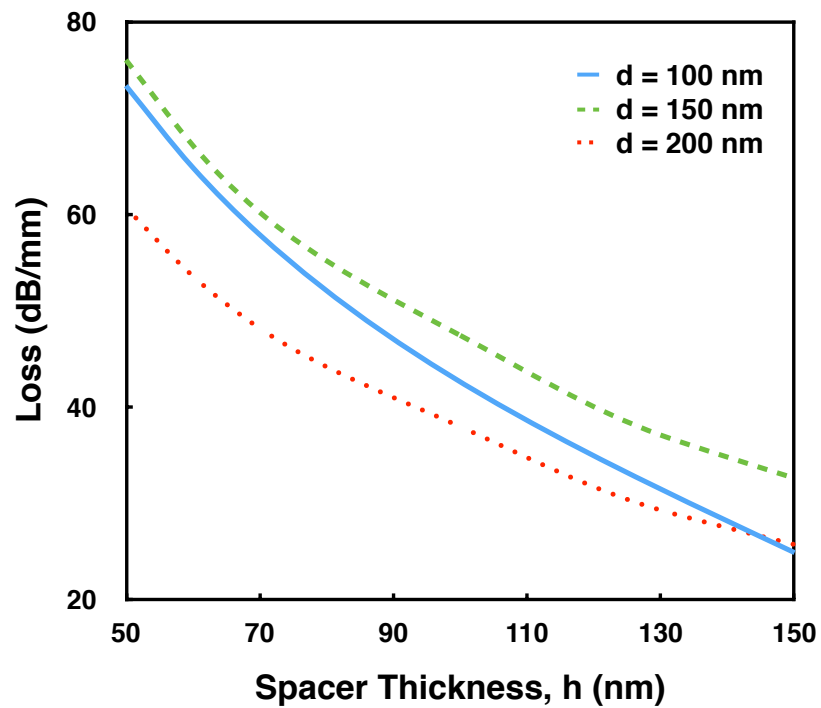


FIGURE 4.5: Variation of propagation loss of the TM mode as a function of the spacer thickness h for three different core thicknesses (d)

similar patterns. Hence only one thickness of the core is taken into account for discussing the power confinement effects. As can be observed from the Figs. 4.6 and 4.7, increasing the thickness of the spacer confines more and more field within the lower index, lower loss Silica spacer. If the confinement factor is taken into consideration, the confinement of power is only increasing in the Silica spacer region. In the metal and the Silicon core region the power confinement decreases. Although the H_x field amplitude is higher in the core region, the power confinement of the structure is dominant in the spacer region. This is because the E_y field is confined in the spacer region and E_y field in the core is insignificant. As the power is more confined in the low loss spacer and the confinement in the spacer is increasing with h , the overall loss of the structure is decreasing with h .

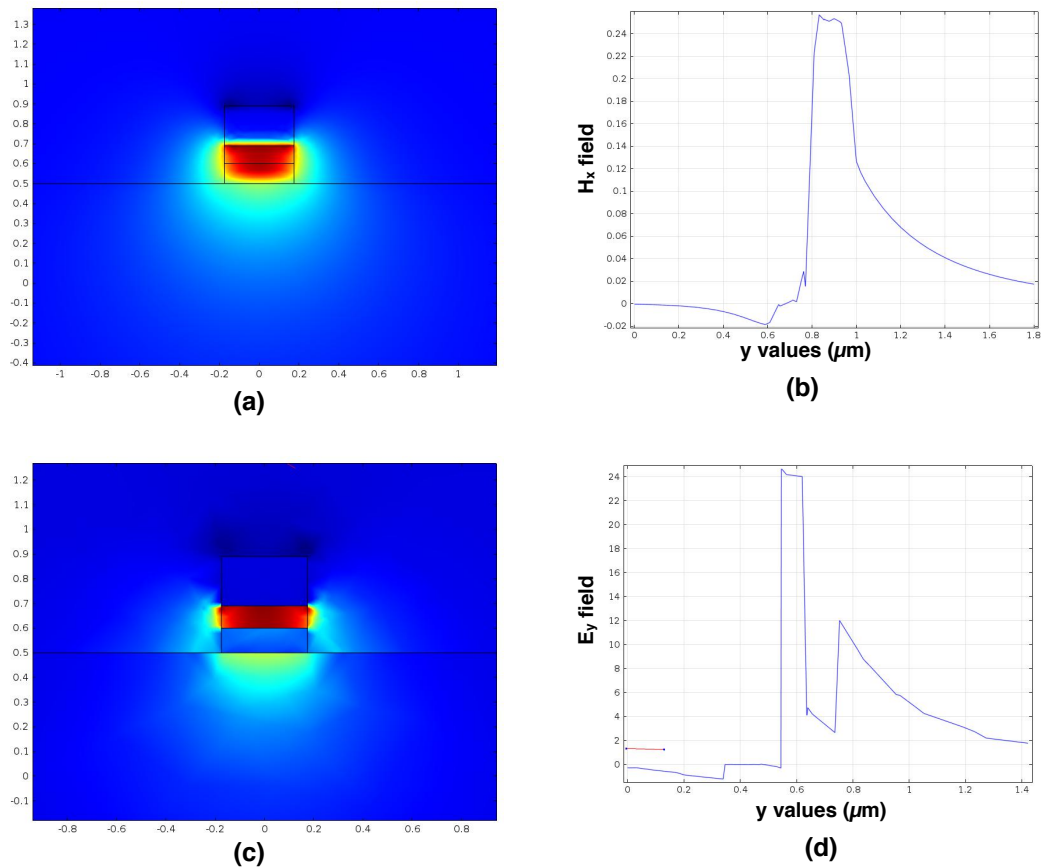


FIGURE 4.6: Normalized (a) H_x and (c) E_y field profiles of the TM mode for spacer thickness $h = 90$ nm and core thickness $d = 100$ nm. (b) and (d) shows the vertical cross-sections of the fields, respectively.

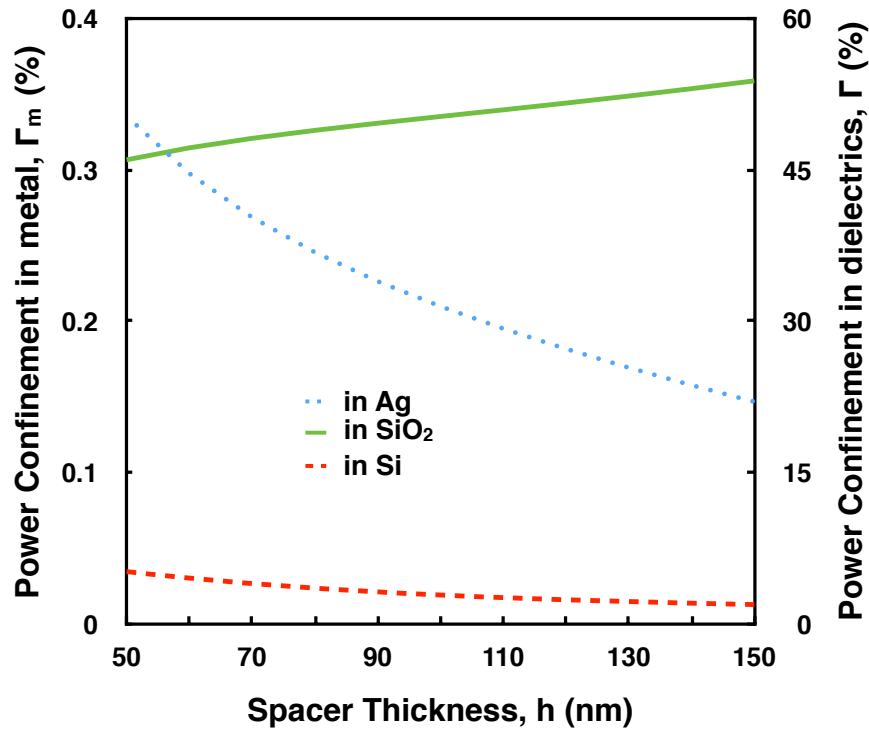


FIGURE 4.7: Variation of power confinement in different layers of the hybrid waveguide for the TM mode as a function of the spacer thickness h for a core thicknesses $d = 100$ nm

4.3.2 Variation of Metal thickness t

In this section the thickness of the Silver layer on the top has been varied from 20 nm to 400 nm. The thickness of the spacer and the core were kept constant at 100 nm and 150 nm, respectively. Figures 4.8 and 4.9 show the variations of the effective index and loss for the TM mode, respectively.

In both figures it can be observed that with the increase in metal thickness both the effective index and the loss decrease rapidly and both stabilise after the thickness of 120 nm. After this value of metal thickness ($t = 120$ nm), The value of effective index changes only 0.53% whereas the change in loss values is only 3.03%.

4.4 The TE Mode

As the TE mode is not supported on a single metal-dielectric, the TE mode of this guide is purely dielectric in nature. The wave is guided as the Silicon core is surrounded by lower index air or Silica. Figure 4.10 shows the H_y and the E_x field profiles along-with their vertical cross-sectional (parallel to the y -axis)

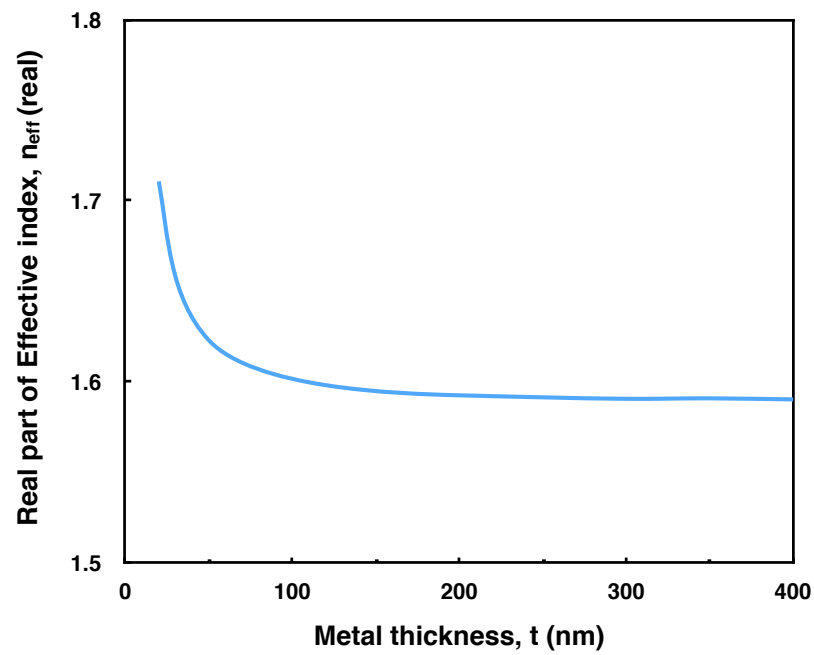


FIGURE 4.8: Variation of the real part of the effective index of the TM mode as a function of the metal thickness t for core and spacer thicknesses of $d = 150 \text{ nm}$ and $h = 90 \text{ nm}$ respectively

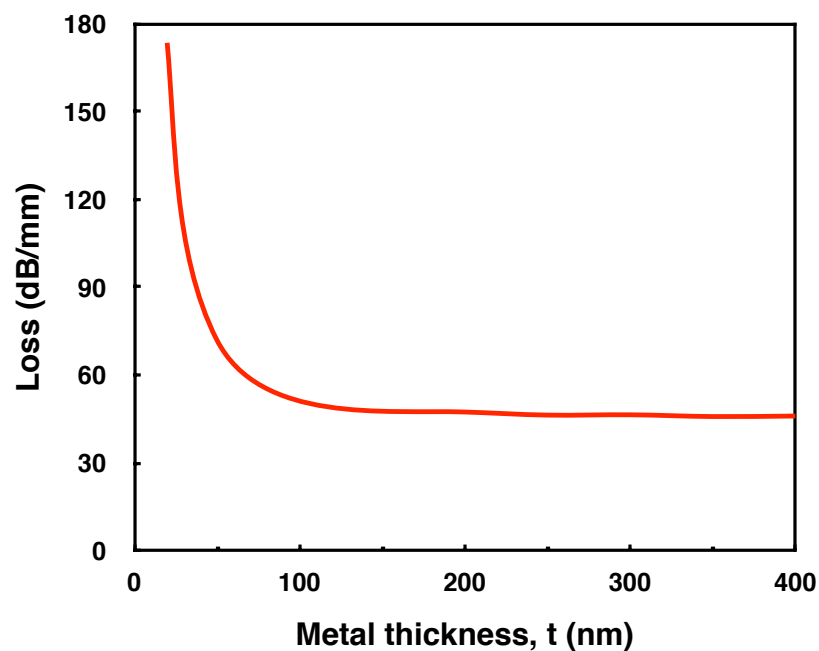


FIGURE 4.9: Variation of modal loss of the TM mode as a function of the metal thickness t for core and spacer thicknesses of $d = 150 \text{ nm}$ and $h = 90 \text{ nm}$ respectively

profiles of the TE mode supported by the hybrid plasmonic guide. Similar to the TM mode, the variation of h , d and t were observed for the TE mode as well.

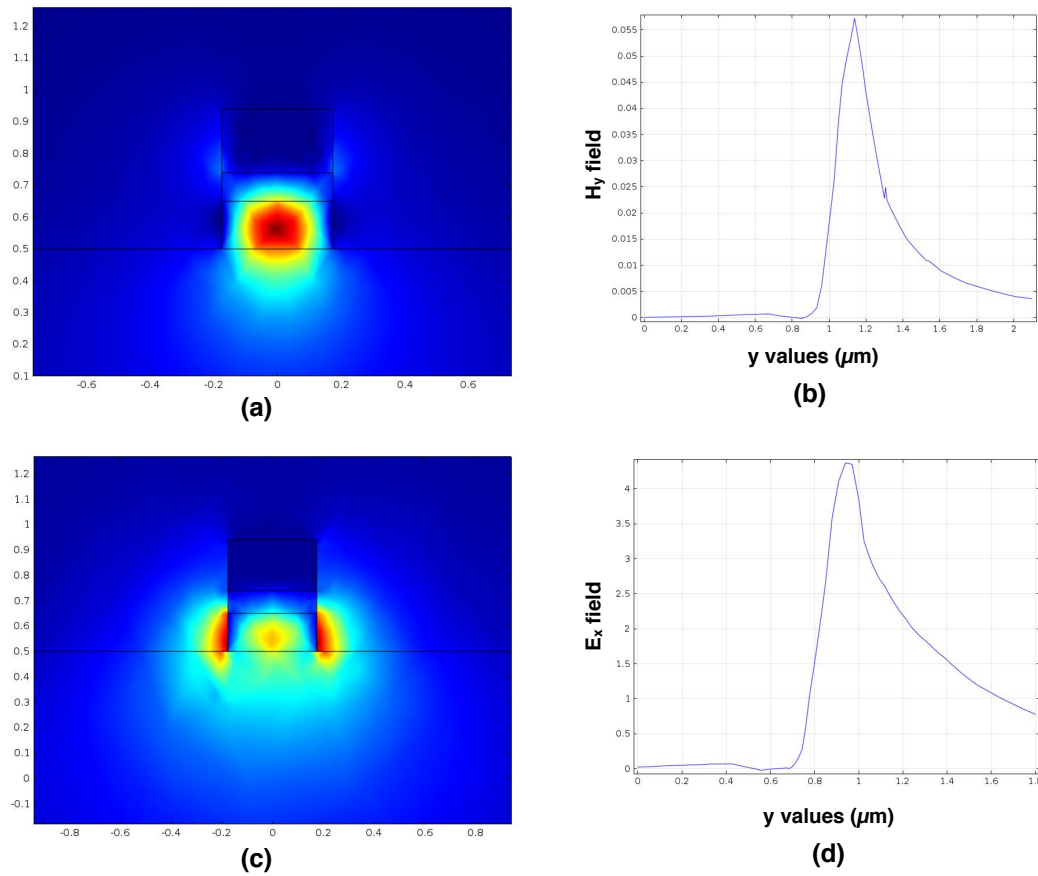


FIGURE 4.10: Normalised (a) H_y and (c) E_x field profiles of the TE mode for spacer thickness $h = 90$ nm and core thickness $d = 150$ nm. (b) and (d) shows the vertical cross-sections of the fields, respectively.

4.4.1 Variation of h

Figures 4.11 and 4.12 show the effect of varying the spacer thickness on the effective index and propagation loss when the core thicknesses are 150 nm and 200 nm and metal thickness was kept at 200 nm. As can be observed, the effective index increases with increasing spacer thickness for both the values of the core thickness. But the loss curve shows interesting behaviour. The loss curve for the 200 nm core shows regular exponential drop in loss with spacer thickness. But for the 150 nm core, the loss first increases to a maximum and then starts to drop exponentially. Therefore, for a 150 nm core, the point of maximum loss is a spacer thickness of 100 nm.

To explain the phenomenon, the power confinement distribution was studied for 50 nm to 130 nm of spacer thicknesses for 150 nm core thickness. Figure 4.13 depicts that most of the power of the TE mode is confined in the core and the spacer layers. With the increase in spacer thickness, power confinement in the core and in the spacer increase monotonously. The confinement in metal layer is very low compared to the confinement in the other two layers. Therefore, it can be concluded that with the increase of spacer thickness the field distribution of the structure becomes more confined inside the structure. The confinement curve in metal shows an interesting nature. As shown in the figure, confinement first increases with increase in h . But after 100 nm the confinement in the metal layer started to fall. This phenomenon coincides with the loss curve shown in Fig. 4.12. So it can be concluded that, although the TE mode is purely dielectric in nature, the loss of the mode follows the confinement pattern in the metal region.

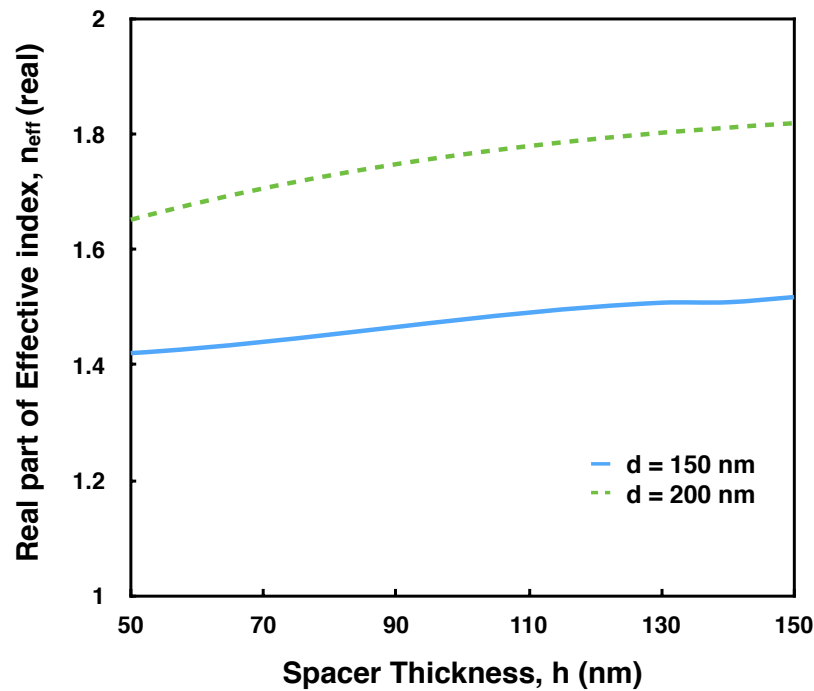


FIGURE 4.11: Variation of the real part of the effective index of the TE mode as a function of the spacer thickness h for two different core thicknesses (d)

4.4.2 Variation of t

Similar to the TM hybrid mode the metal thickness was varied for the TE mode keeping the core thickness at 150 nm and the spacer thickness at 100 nm. The

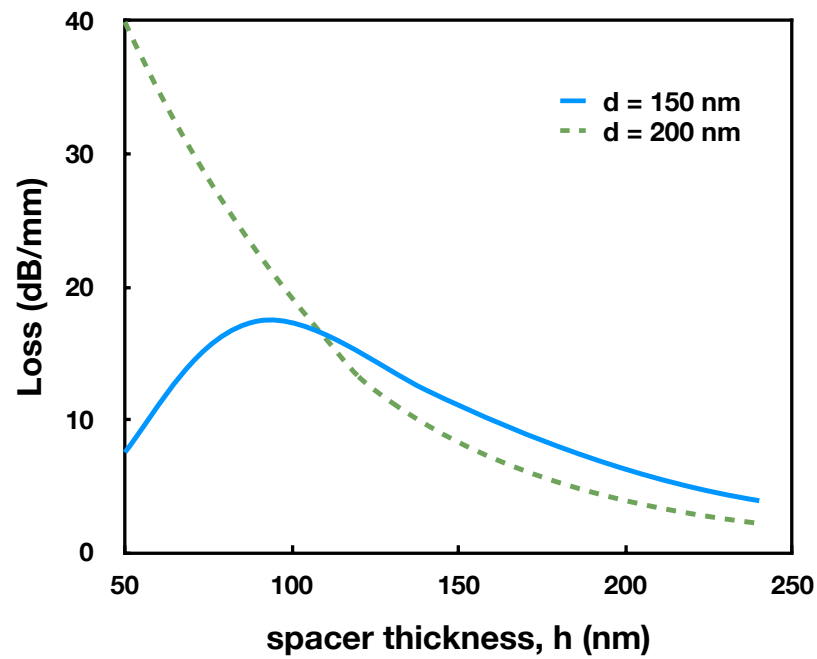


FIGURE 4.12: Variation of propagation loss of the TE mode as a function of the spacer thickness h for two different core thicknesses (d)

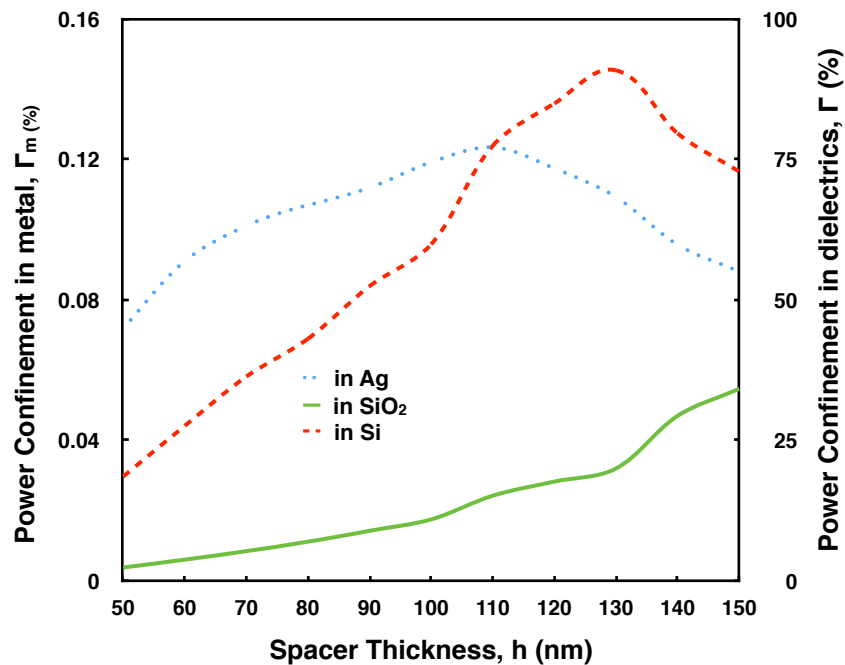


FIGURE 4.13: Variation of power confinement in different layers for the TE mode as a function of the spacer thickness h for a core thickness $d = 150$ nm

effect of the metal thickness is similar to the effect on the TM mode. After 120 nm thickness the loss saturates. The variation of the effective index and loss of the TE mode are shown in Figs. 4.14 and 4.15.

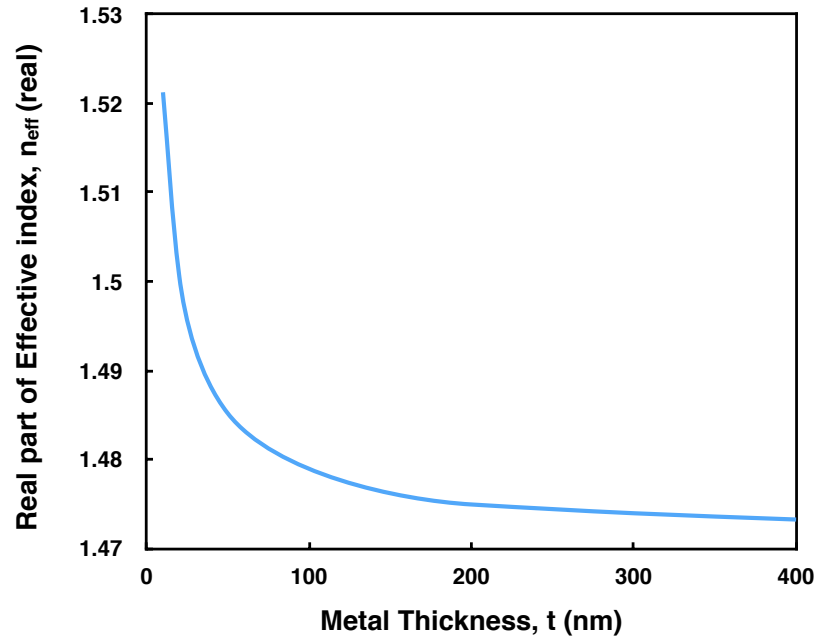


FIGURE 4.14: Variation of the real part of the effective index of the TE mode as a function of the metal thickness t for core and spacer thicknesses of $d = 150 \text{ nm}$ and $h = 90 \text{ nm}$ respectively

4.5 Benchmarking

As mentioned earlier the propagation characteristics of the structure are presented in [212]. In the previous sections, the propagation characteristics of the structure using a full-vectorial \mathbf{H} field based FEM method were described. These results are then compared to those presented in [212]. Figures 4.16 and 4.17 show the comparison of effective index and propagation distance of the TM mode. The propagation distance is defined as the distance over which guided power drops to $1/e$ of its initial magnitude. From the comparison of the variation of the real part of the effective index and the propagation distance, with the spacer thickness for fixed core and metal layer thicknesses, the curves presented are found to be in good agreement for the TE mode. The comparison curves for the TE mode are shown in Figs. 4.20 and 4.21. For the TM mode, the curves show good agreement when the thickness of the spacer layer is smaller.

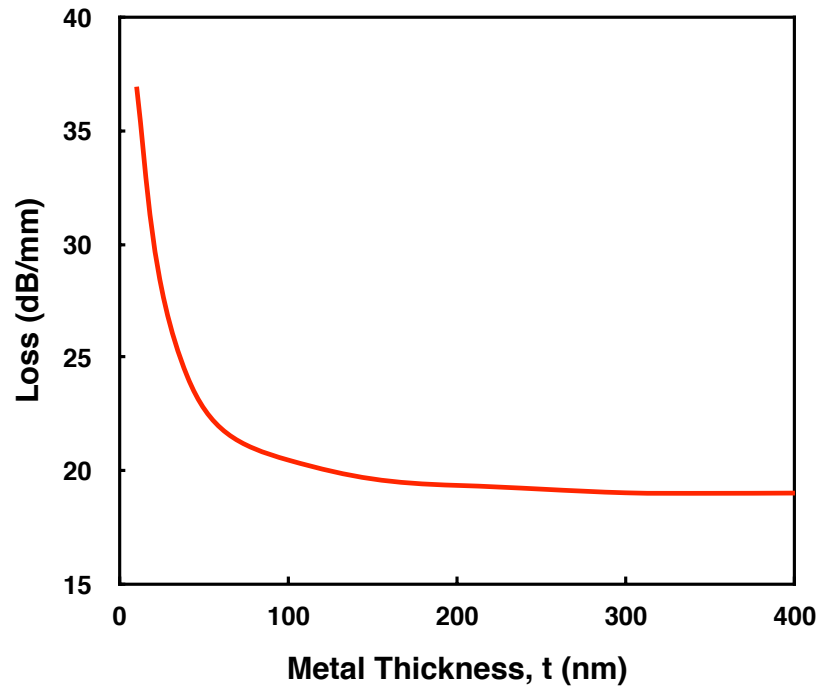


FIGURE 4.15: Variation of propagation loss of the TE mode as a function of the metal thickness t for core and spacer thicknesses of $d = 150 \text{ nm}$ and $h = 90 \text{ nm}$ respectively

But when the spacer thickness is increased beyond $h = 110 \text{ nm}$, the propagation distances calculated by the two methods started to differ slightly from each other.

To investigate the difference at higher values of spacer thickness, the spacer thickness sweep was performed with different resolutions of the mesh for the $d = 200 \text{ nm}$ core. Figure 4.18 shows the curves of several mesh resolutions along with the result from the [212] overlaid on top (denoted by purple triangles). The curve shown in grey circles is the one shown earlier in Fig. 4.17 (also in grey). It can be noticed from Fig. 4.18 that at lower spacer thicknesses, the propagation distances calculated at almost all the resolutions are very much close to each other. But as the thickness of the spacer layer was increased, curves with higher resolution mesh started to produce slightly higher propagation distance than that of the lower resolution meshes. It can be observed in the Fig. 4.18 that the results, presented in [212] started with a good agreement with all the mesh resolutions for lower spacer thicknesses upto around $h = 110 \text{ nm}$. But for spacer thicknesses greater than this value, the [212] curve drifted towards the lower resolution results produced by our method. Figure 4.19 shows the relation between the propagation distance and mesh resolution in terms of number of mesh elements for different values of the spacer thickness. It can be observed

that at lower resolution the propagation distance is lower and *****. As the resolution increases, the calculated propagation distance becomes more stable. All the results presented in this chapter using our technique were produced at 90×90 resolution where the total number of mesh elements were 16200. This resolution was used so that the produced results are more stable. The curve of propagation distance shown in Fig. 4.16 was also produced using 16200 mesh elements at a 90×90 mesh resolution which gave more stable result but created a drift with the [212] curve for higher spacer thicknesses. Therefore, it can be concluded that the difference between the propagation distance curve obtained by our method and that in [212] might be due to mesh resolution.

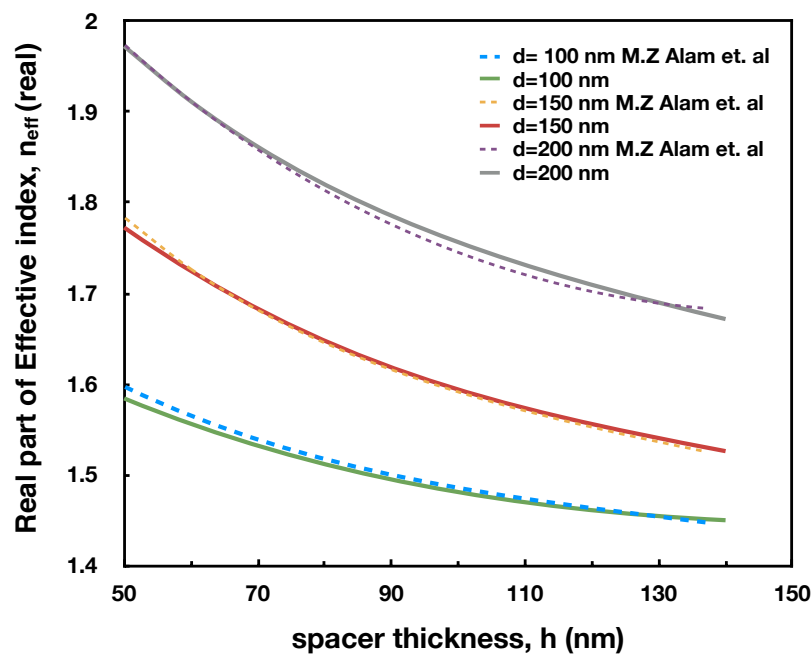


FIGURE 4.16: Comparison of variation of the real part of the effective index of the TM mode as a function of the spacer thickness h for three different core thicknesses (d)

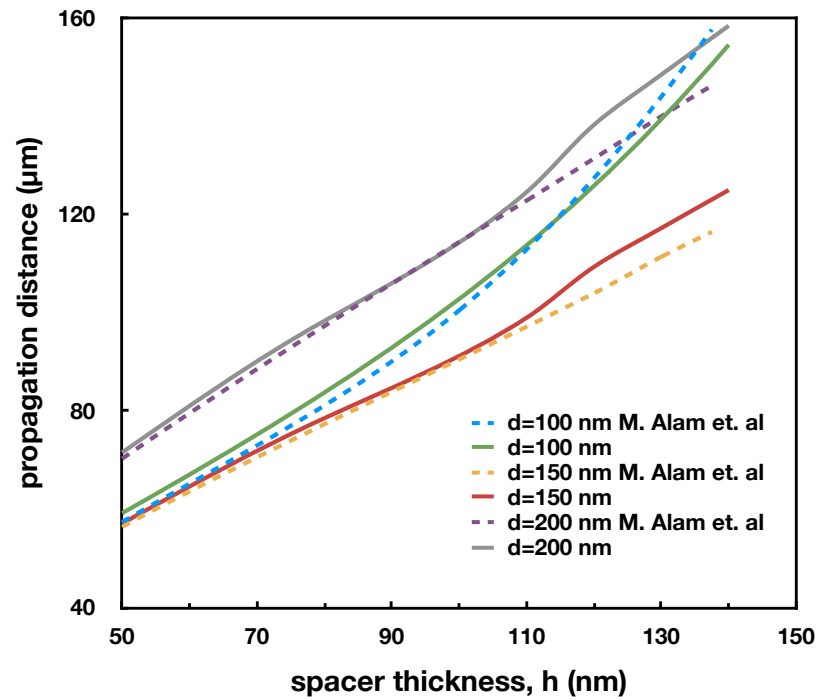


FIGURE 4.17: Comparison of variation of propagation distance of the TM mode as a function of the spacer thickness h for three different core thicknesses (d)

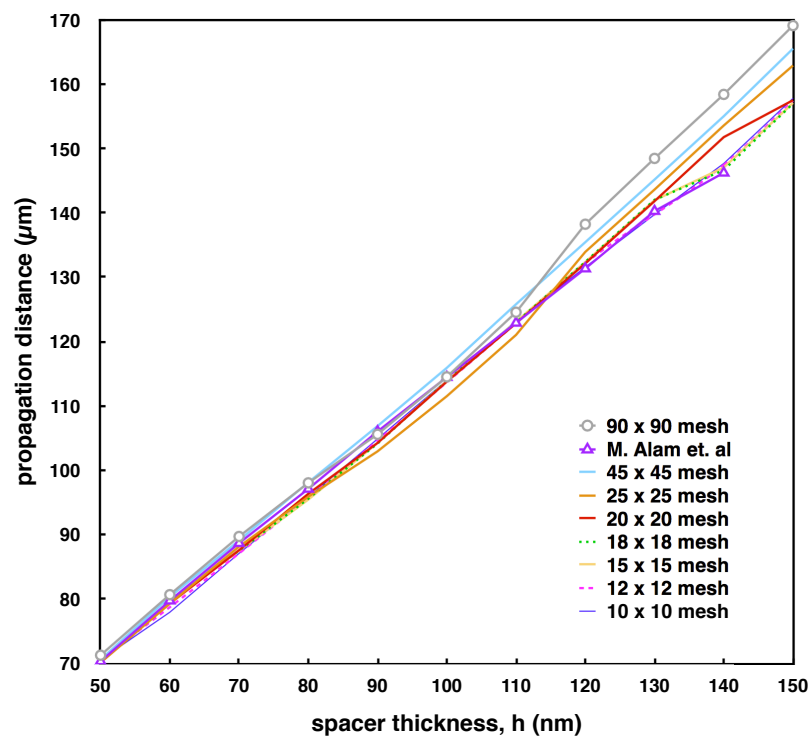


FIGURE 4.18: Variation of propagation distance of the TM mode of the hybrid waveguide as a function of the spacer thickness h for a core thickness of $d = 200$ nm for different values of mesh densities compared with that done in [212].

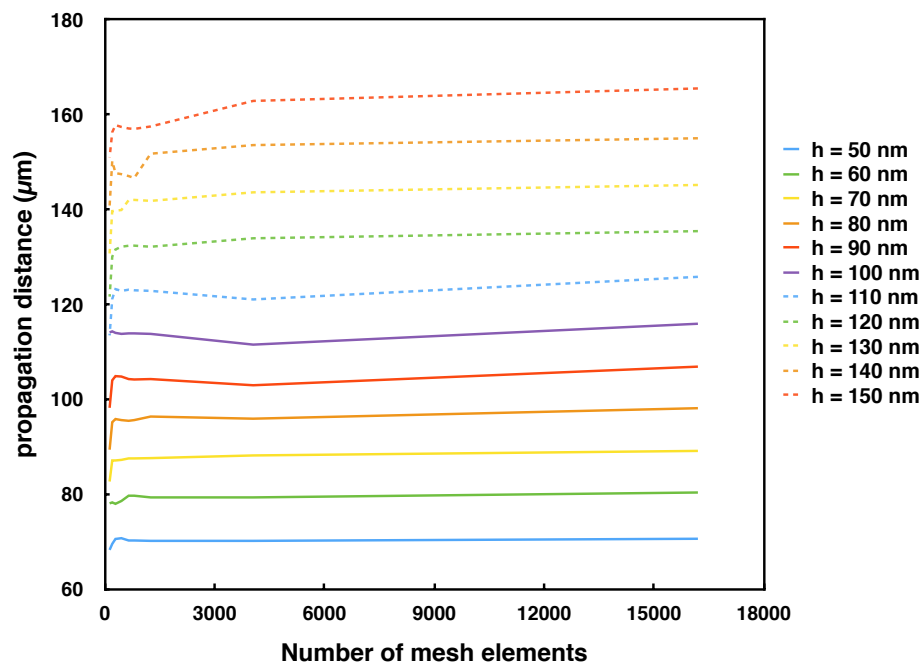


FIGURE 4.19: Variation of propagation distance of the TM mode of the hybrid waveguide as a function of the total number of mesh elements at several values of the spacer thickness h for a core thickness of $d = 200$ nm.

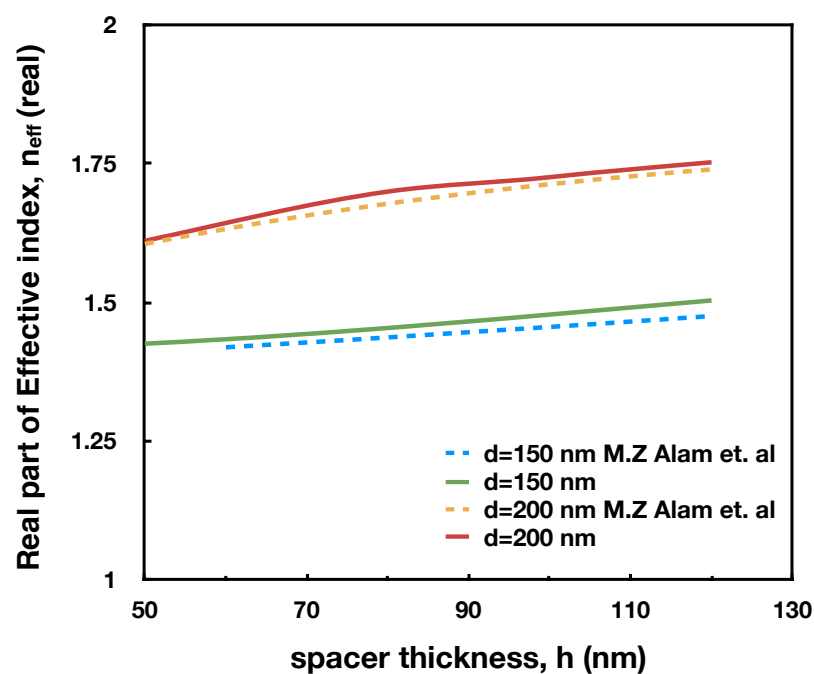


FIGURE 4.20: Comparison of variation of the real part of the effective index of the TE mode as a function of the spacer thickness h for two different core thicknesses (d)

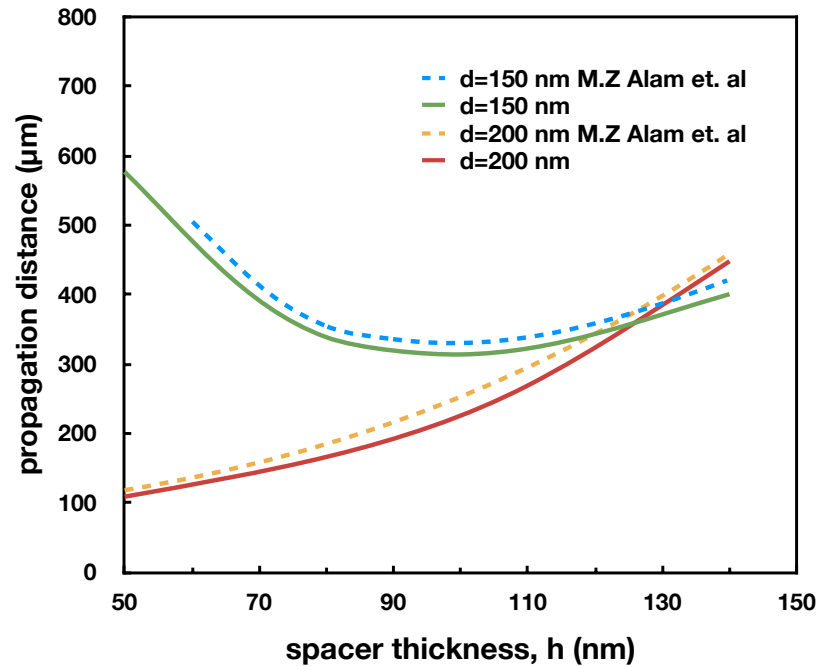


FIGURE 4.21: Comparison of variation of propagation distance of the TE mode as a function of the spacer thickness h for two different core thicknesses (d)

4.6 Summary

The HPWG offers sub-wavelength confinement in the low index region, offers a better compromise between confinement and loss compared to pure plasmonic waveguides, and is compatible with SOI technology. In addition, the propagation of the TE and TM modes can be independently controlled which opens up the possibility of implementing compact devices for manipulating polarization. In this chapter, we have analysed the properties of the HPWG by observing the confinement and propagation loss of the HPWG. The HPWG combines both dielectric and plasmonic guiding schemes, and it provides good confinement with moderate propagation loss. The HPWG supports both the TE and TM modes which can be utilised for many applications.

Chapter 5

Rectangular Plasmonic Waveguide in THz

5.1 Introduction

The terahertz (THz) frequency region has attracted a huge amount of research effort in recent years and is emerging as a key technology for a number of applications. Considerable interest in THz devices has been created in the field of imaging [215], sensing [216] and scanning microscopy [217, 191]. The development of THz sources and receivers has also increased the demand for low loss THz waveguides [218], which can be used as interconnects in integrated THz devices for higher speed and wideband communications. The lack of a compact and low loss interconnect has limited the capacity for THz components to be placed either in close proximity to each other or else to use free space as the propagation medium, which then requires bulky components [219, 220]. A low-loss waveguide can be used to replace such bulky components with compact, integrated circuits.

The major hurdle for THz guiding is that most of the materials considered exhibit high absorption losses in this region of the spectrum [221]. Conventional dielectrics tend to be lossy at terahertz frequencies, whereas metals show low propagation loss owing to their high conductivities. To reduce absorption loss, waveguides can be designed such that less power stays within the lossy material and most of the power is guided through the air [222]. Amongst the techniques used so far, photonic crystal fibre [223, 224], porous fibre [225, 226, 227], hollow Bragg fibre [228], metal clad hollow core [229, 230, 231, 218] and ferroelectric clad fibre [232, 228] can be mentioned and all these approaches guide a significant portion of the power through air.

Among various approaches considered, a metal clad guide which supports surface plasmon modes is one of the most promising contender because of low

loss in both active components and passive waveguides [218]. Recently it has been shown, both experimentally [231] and via numerical simulations [218], that a dielectric coated metal-clad hollow core circular waveguide yields low loss at THz frequencies. Such flexible guides are more suitable to deliver high power electromagnetic waves to a target, instead of using free space transmission. Previously Miyagi and Karasawa [233] have suggested that a rectangular hollow core guide would be expected to have a lower bending loss, compared to a circular waveguide of a similar bore. A previous study [218] also shows that polarized modes in circular waveguides are not circular due to the boundary conditions at the metal-dielectric interface, even though the superposition of two degenerate polarized modes produces radially symmetric unpolarized modes. With these non-circular polarized modes being degenerate, the polarization state of the beam will not be stable. It is expected that modes in a rectangular waveguide can be designed not to be degenerate and the polarization condition can be maintained in such a waveguide.

In this chapter, a two-dimensional modal analysis was performed for the characterization and optimization of a dielectric coated hollow core rectangular waveguide, by using the full vectorial \mathbf{H} -field based FEM method. Additionally, the propagation and attenuation properties of this waveguide were examined by varying several parameters of the guide.

5.2 Dielectric coated Rectangular Waveguide

Figure 5.1 shows a schematic diagram of the rectangular cross-section of the waveguide with a dielectric coating. The structure considered here is composed of a thin metal clad silica waveguide with an air core. It was suggested previously [234] that by using a soldering technique to join two sets of parallel horizontal and vertical metal-clad dielectric slabs, such a waveguide can be fabricated readily. As the decay length at the metal-air interface will be much longer than that at the metal-silica interface, the electromagnetic field at the outer surface of the guide will decay more quickly. Hence the host material, silica, in this case, has a negligible effect on the modes guided in the air core and any other suitable dielectric material can also be used. For the simulation purpose, the refractive index of silica was taken as $n_{silica} = 1.96 + j0.0061$ [202] at an operating frequency of 2.5 THz. At this operating frequency, the loss associated with the air is considered and its complex refractive index was taken

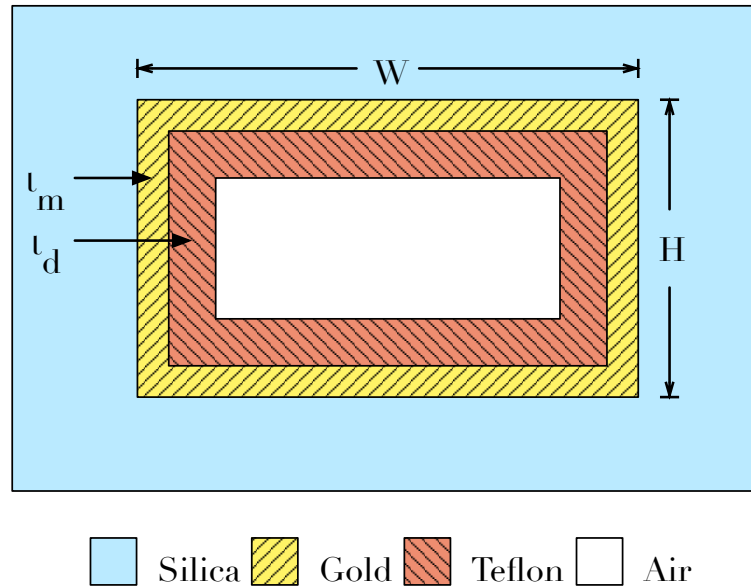


FIGURE 5.1: Schematic diagram of the hollow core rectangular waveguide with a dielectric coating inside the air core where W is the guide width, H is the height of the guide, t_m is the metal thickness and t_d is the thickness of the dielectric coating.

as $1.0 + j1.1 \times 10^{-6}$ [218]. Initially, the noble metal, gold (Au), having a refractive index $n_m = 281.55 + j419.74$ [235], has been considered as the cladding material. The width W and height H of the guide and the cladding thickness t_m were varied. To study the effect of the dielectric coating on the modal loss, a thin layer of Teflon deposited at the inner surface of the metal cladding was considered. A plasma vapour deposition process can be used to deposit Teflon on the metal during the fabrication process. A similar technique applied to a hollow core fiber has been studied [218] and fabricated [231] previously, where in that case polystyrene was used as the dielectric coating material.

Quasi-TM modes with a dominant H^x field would form SPP modes at the horizontal metal-dielectric interfaces, whereas quasi-TE modes with the dominant H^y field can form SPP modes at the vertical metal/dielectric interfaces. In this study, only the quasi-TM modes are reported; however the quasi-TE modes would show similar features. This structure supports the surface plasmon modes at two metal-dielectric interfaces; one at the outer silica-gold interface and the other at the gold-air interface inside. The decay length at the gold-air interface is much higher than that at the silica-gold interface. In this structure, at all four interfaces at the four sides, both sides of the metal cladding are surrounded by two different dielectrics. However, as the decay length at the gold-air interface will be much longer than that at the silica-gold interface, the

electromagnetic field at the outer surface of the guide will decay faster. Since the refractive indices of the inner and outer dielectrics are different, their phase velocities are also different and they do not couple effectively to form supermodes across the metal layer. On the other hand, the SPP modes at the upper and lower metal/air interfaces with longer decay lengths will couple to form supermodes as they are also phase matched. When these two modes couple in an even-like manner, an air-guided mode is formed.

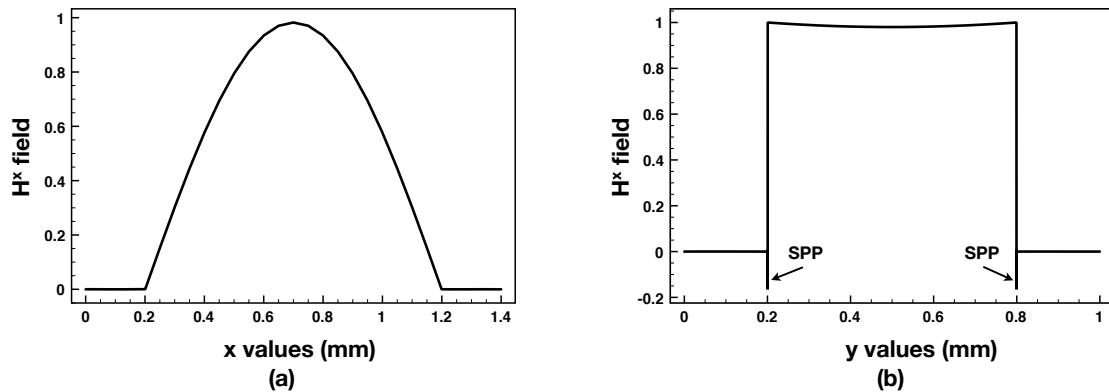


FIGURE 5.2: H_{10}^x field profile along (a) the horizontal and (b) the vertical directions, respectively in the hollow core rectangular waveguide with $W = 1.0$ mm, $H = 0.6$ mm, $t_m = 0.7$ μ m and $t_d = 0$.

It was observed that when the width and height of the waveguide were large compared to the wavelength, the waveguide supports many modes and the real part of their effective indices (n_{eff}) are closer to the refractive index of the air core. In this work, the fundamental H_{10}^x and four higher order quasi-TM modes H_{20}^x , H_{30}^x , H_{11}^x and H_{12}^x are studied. The contour profiles of these modes are shown later. Using a familiar nomenclature for the integrated optical waveguides, the waveguide modes were defined as H_{mn}^x , where H^x is the dominant \mathbf{H} -field component and the subscripts m and n depict the field maxima along the x and y coordinates, respectively. The H^x field profile of the fundamental H_{10}^x mode along the horizontal and vertical directions are shown in Figs. 5.2(a) and (b), respectively. For this mode, identical SP modes existing at the top and bottom metal-air interfaces couple together to form an even-like supermode along the vertical (y) direction, as presented in Fig. 5.2(b). Two plasmonic peaks at the gold-air interfaces are clearly visible and are shown by arrows in Fig. 5.2(b). However, the boundary condition along the vertical metal interfaces on the two side walls forces H^x to be zero there. So a half sine wave curve is formed along the horizontal direction, as can be seen in Fig. 5.2(a). On the other hand, the H_{11}^x mode is the result of the odd coupling between the SP modes of the top

and bottom claddings. However, the H_{12}^x mode has a higher order variation along the y direction. Besides showing two sharp plasmonic peaks at the metal interfaces, this mode also shows two additional zero-crossings. The H_{20}^x and H_{30}^x modes follow a similar profile as the H_{10}^x along the y direction, but their profiles change along the horizontal (x) direction showing two and three field extrema, respectively. Before considering possible dielectric coatings inside the metal cladding, several parameters of the guide, namely the height, width and the metal thickness were varied to observe their effect on the modal properties, examining the effective index and the loss values for all of the five modes mentioned above. The effective index, n_{eff} , of a given mode is a normalized propagation parameter, which can be defined by $n_{eff} = \frac{\beta}{k_0} = n_{re} + jn_{im}$, where $\beta = \beta_{re} + j\beta_{im}$ is the complex propagation constant of that mode and k_0 is the free space wavenumber defined as $k_0 = \omega\sqrt{\mu\epsilon} = \frac{2\pi}{\lambda}$. The absorption coefficient is $\alpha_{WG} = 2\beta_{im}$ [236]. From this coefficient, the value of loss (in dB/m) was calculated as $loss = 8.6858896\beta_{im}$. This expression is used for all the calculations of loss throughout this chapter.

5.2.1 Effect of Change in Guide Height

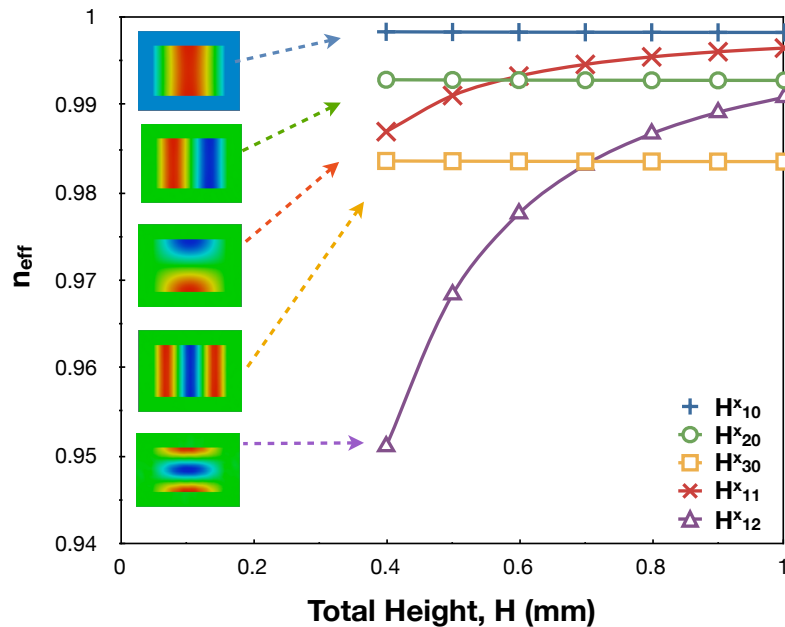


FIGURE 5.3: Real part of effective index of all the five modes as a function of height at $W = 1.0 \text{ mm}$, $t_m = 0.7 \text{ }\mu\text{m}$ and $t_d = 0$.

Figure 5.3 shows the variations of the real part of effective index (n_{eff}) with the waveguide height, H . The height of the guide was varied from 0.4 mm to

1.0 mm while keeping the width and cladding thickness constant at 1.0 mm and 0.7 μm respectively. It can be seen from this figure that for the H_{10}^x , H_{20}^x and H_{30}^x modes, n_{eff} 's do not change much with the height. When the height is gradually reduced from 1.0 mm to 0.4 mm at an interval of 0.1 mm, the deviation in effective index (from that of height 1.0 mm) is only about 0.0073%, 0.0075% and 0.0076% for the H_{10}^x , H_{20}^x and H_{30}^x modes, respectively. This is because, although these three modes have different variations along the x direction, their field profiles along the y direction are constant and these are not affected by the changing height. Due to the much larger decay length in air, compared to the change of height of the guide, these modes do not show significant variation of their effective index values. However, the higher order modes have slightly smaller effective indices than those of lower order. On the other hand, the effective index curves of the H_{11}^x and H_{12}^x modes fall more rapidly as the guide height is decreased, showing a stronger dependence on the waveguide height, H as their spatial variation is changed with the height. The H_{12}^x mode has a sharp decaying curve of its effective index when the waveguide height is reduced.

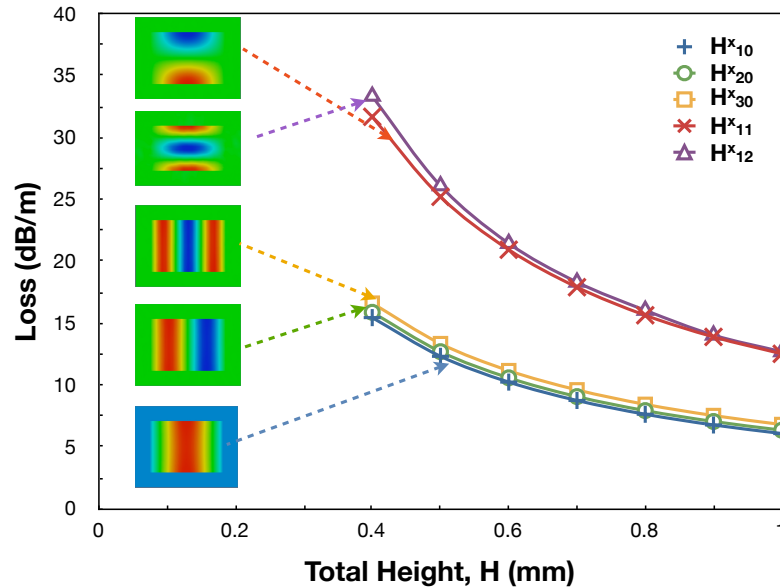


FIGURE 5.4: Loss of all the five modes as a function of height at $W = 1.0 \text{ mm}$, $t_m = 0.7 \mu\text{m}$ and $t_d = 0$.

Figure 5.4 shows the variation of the modal loss with height for all the five modes considered here. It can be observed that the modal losses of the guide increase exponentially with the reduction of height for all the modes. The loss values, for the H_{10}^x , H_{20}^x and H_{30}^x modes, are very close to each other and their rate of change is almost identical. For these three modes, it can be noted that

all the loss values are very similar when the waveguide height, H , is large but the higher order modes have slightly higher losses than those of lower order. However losses increase at a much higher rate in the case of the H_{11}^x and H_{12}^x modes where the field depends strongly on the height, H . These values are also much greater compared to the other three modes. The H_{10}^x mode has the lowest loss value among all the modes shown here. The H^x field profiles for all the five modes are shown as insets in Figs. 5.3 and 5.4.

5.2.2 Effect of Change in Guide Width

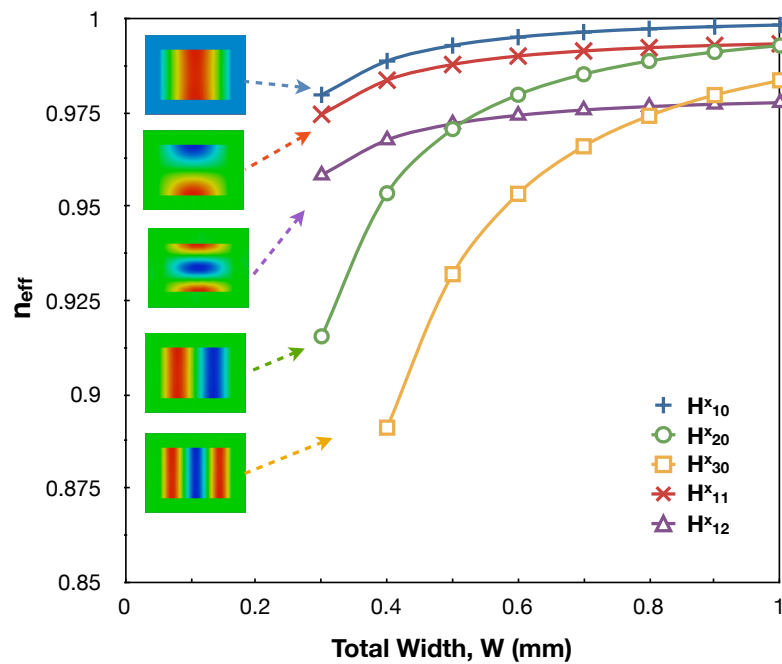


FIGURE 5.5: Real part of effective index of all the five modes as a function of guide width at $H = 0.6 \text{ mm}$, $t_m = 0.7 \text{ }\mu\text{m}$ and $t_d = 0$.

In order to observe the dependence of the effective index and the loss values on the width of the rectangular guide, this parameter (denoted by W) was varied from 0.5 mm to 1.0 mm for all the five modes. Figure 5.5 depicts the variation of n_{eff} for the five modes with respect to width for a constant height $H = 0.6 \text{ mm}$ and a metal thickness $t_m = 0.7 \text{ }\mu\text{m}$. The curves suggest that the values of n_{eff} decrease for all the modes, with decreasing width. For the H_{10}^x , H_{11}^x and H_{12}^x modes, the rate of decrement of the n_{eff} 's are similar due to the fact that, in the horizontal direction, the variation of their modal field profiles are similar. However, the lower order modes exhibit larger effective indices. On the other hand, for the H_{20}^x and H_{30}^x modes, their n_{eff} values reduce much more rapidly because of the faster change in the mode profiles in the horizontal

direction with the width variation. The rate of decrement is much greater for the higher order mode than for its lower order counterpart.

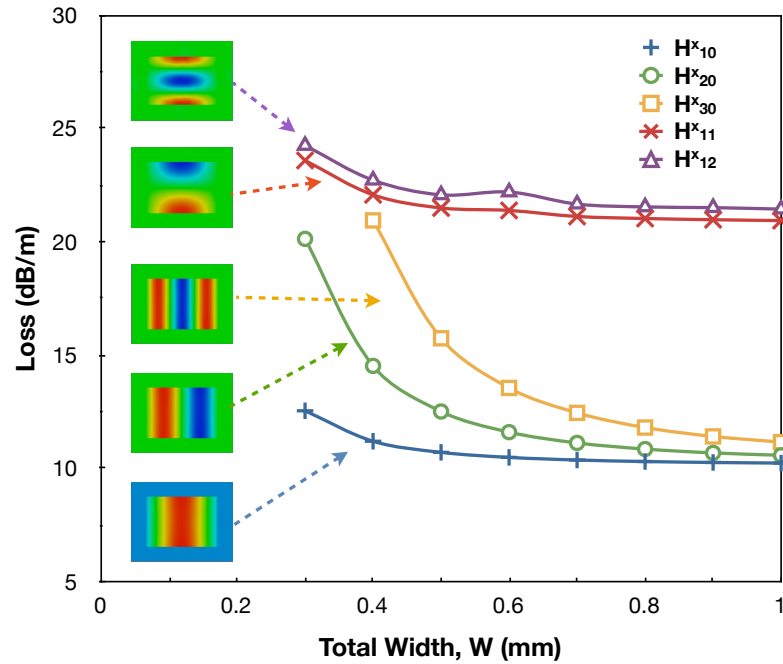


FIGURE 5.6: Loss of all the five modes as a function of guide width at $H = 0.6 \text{ mm}$, $t_m = 0.7 \text{ }\mu\text{m}$ and $t_d = 0$.

The propagation loss for the H_{10}^x , H_{11}^x and H_{12}^x modes have similar incremental rates with decreasing width, as can be seen from Fig. 5.6. The loss values for these modes do not increase significantly as the losses arise predominantly due to the metal confinement in the top and the bottom dielectric-metal interfaces. The boundary conditions at the left and right interfaces demand a zero H^x field which does not interact with the mode profile. On the other hand, for the H_{20}^x and H_{30}^x modes, the losses increase sharply while the width is decreased. This arises because the change of the mode profile in the horizontal direction also affects the interaction at the upper and lower metal-dielectric interfaces.

5.2.3 Effect of Change in Metal Thickness

Next, the effect of the metal thickness on the modal loss was also studied. When the thickness of the Au cladding layer was varied over a range $0.2 \text{ }\mu\text{m} < t_m < 0.9 \text{ }\mu\text{m}$, the loss curves for all the five modes showed a similar nature as given in Fig. 5.7. In this case, the width and the height of the guide were taken as 1.0 mm and 0.6 mm , respectively. The propagation loss values follow a decreasing trend with increasing metal thickness. However, the higher order modes

show higher values of loss than those of the lower order, particularly the higher order modes in the vertical direction. The effective indices of the modes do not change significantly with the cladding thickness and these are not shown here.

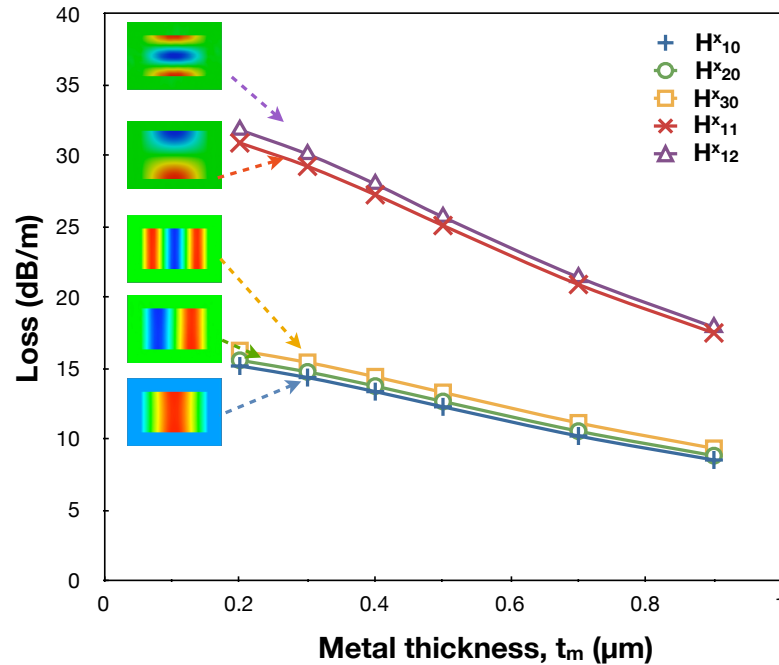


FIGURE 5.7: Loss of all the five modes as a function of metal thickness t_m at $W = 1.0 \text{ mm}$, $H = 0.6 \text{ mm}$, and $t_d = 0$.

5.3 Dielectric Coated Design

5.3.1 Choice of Dielectric

In the work previously reported by Themistos *et. al* [218], polystyrene was used as the dielectric material for the coating inside the metal cladding and the complex refractive index for this material was reported to be $1.58 + j0.0036$ at 2.5 THz. Operating at the same frequency, it has been observed that Teflon is a lower loss medium with a complex refractive index $n_d = 1.445 + j0.00119$ [237, 238]. For this reason, the effect of a layer of Teflon deposited inside the metal cladding in this structure was studied. A guide width of 1.0 mm, a height of 0.6 mm and a metal thickness of 0.7 μm were considered for incorporation in the simulation, although these parameters can also be optimized as necessary. The effect of the Teflon thickness on the different modes was observed and this is presented in the following sections.

5.3.2 Effect of Teflon Thickness

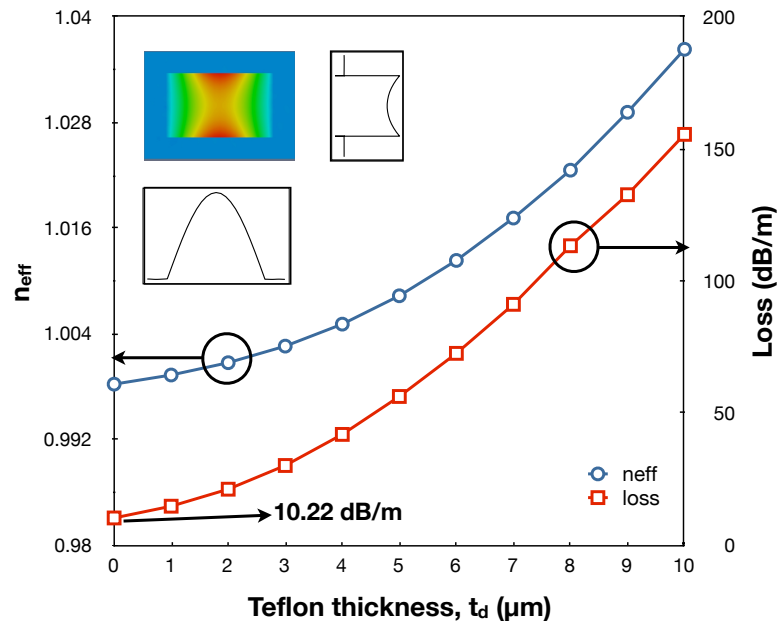


FIGURE 5.8: n_{eff} and loss of the H_{10}^x mode as a function of Teflon thickness at $W = 1.0 \text{ mm}$, $H = 0.6 \text{ mm}$ and $t_m = 0.7 \mu\text{m}$.

Initially the effect of the Teflon thickness on the fundamental H_{10}^x mode, which also shows minimum loss values, was investigated. This feature is of particular interest where low loss applications are concerned. After considering a coating of Teflon, this mode was analysed to find a possible low loss condition. It was observed that in the absence of the Teflon coating, the H^x field exhibits a sharp rise at the air-Au interfaces at the top and the bottom, but maintains a fairly constant profile at the central air core, details of which are presented in Fig. 5.2(b). As the Teflon coating was introduced inside the metal, the field profile deteriorates with a dip at the centre of the waveguide. Increasing the thickness of the Teflon layer results in a decoupling of the two surface plasmon modes of the top and bottom interfaces as a significant part of the field penetrates into the Teflon layer and interacts with the metal cladding when the Teflon coating is applied. Hence, the field inside the air core decreases with the increase in the Teflon thickness. As a result, the propagation loss also increases. Figure 5.8 presents the variation of the effective index and the loss curves of the H_{10}^x mode with the change in the Teflon thickness. This figure shows that the effective index of the mode rises exponentially with an increase in the Teflon thickness because more power is confined in the high index Teflon layer. The loss curve for the mode shows similar characteristics, as increasing the Teflon

layer suggest that the field confinement at the metal-Teflon interface increases, which gives rise to the loss value seen. The top left inset in the figure shows the contour field profile of this mode at a Teflon thickness of $t_d = 1 \mu\text{m}$, whereas the other two insets present the H^x field profiles of the same mode along the horizontal and vertical directions passing through the centre of the guide. It can be noted that the minimum loss achievable with this mode is 10.22 dB/m when no Teflon coating was applied.

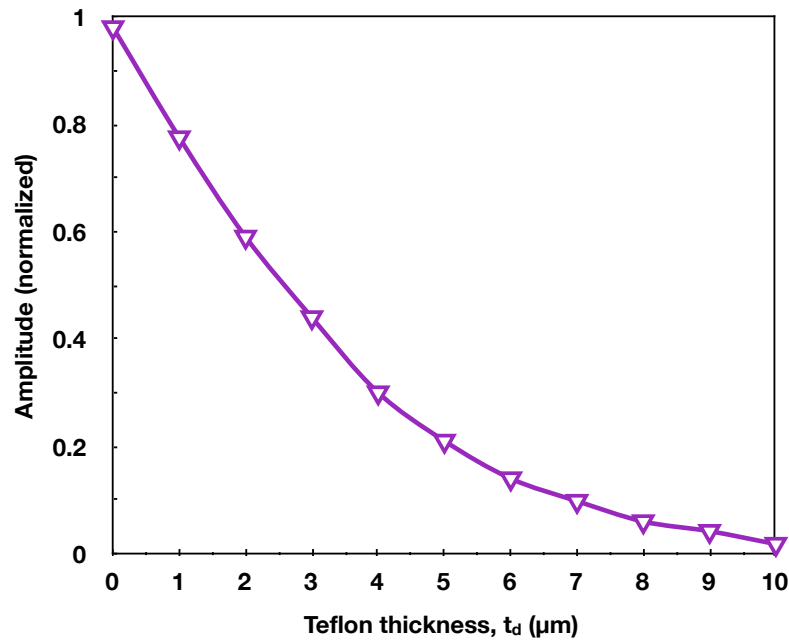


FIGURE 5.9: a) Normalized amplitude of the mode profile taken at the centre of the profile in the vertical direction as a function of Teflon thickness for the H_{10}^x mode when $W = 1.0 \text{ mm}$, $H = 0.6 \text{ mm}$ and $t_m = 0.7 \mu\text{m}$.

It has already been mentioned that the field profile at the centre of the waveguide reduces when the thickness of the Teflon layer was increased and this is shown in Fig. 5.9 where the normalised H^x field amplitude at the centre of the waveguide (normalised to its maximum value) is plotted against the Teflon thickness. It can be noted that when the Teflon thickness is $7 \mu\text{m}$, the field value at the centre of the waveguide is only 10% of the maximum field at the edges.

The propagation loss depends on the power confinement in the different layers and their corresponding loss tangent values. The power confinement in any particular layer (constituting the guide) is calculated by normalising the power in that layer to the total power. The fraction of the power confined in the air core, the Teflon and the metal cladding for the H_{10}^x mode are shown in Fig. 5.10 for different Teflon thicknesses. This figure clearly illustrates the fact

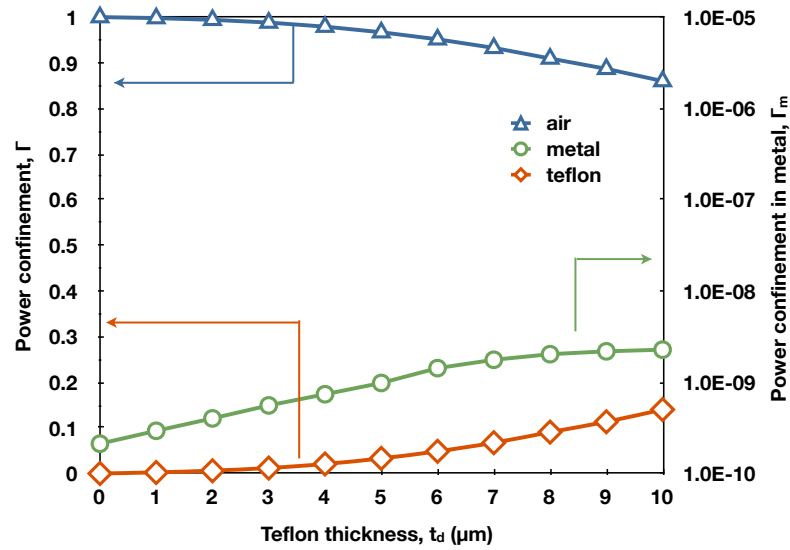


FIGURE 5.10: Power confinement factors in air, in Teflon (Γ_d) and in metal (Γ_m) as a function of Teflon thickness for the H_{10}^x mode when $W = 1.0 \text{ mm}$, $H = 0.6 \text{ mm}$ and $t_m = 0.7 \mu\text{m}$.

that as the thickness of the Teflon layer is increased, the power confinement in the Teflon increases (left hand scale) as more field is drawn into that layer. This also reduces the amount of power confined in the air core (left hand scale). The power confinement in the Au layer is also higher for a thicker Teflon layer, which strongly contributes to the modal loss values. It should be noted that the power confinement in the metal is shown with reference to the right hand scale in Fig. 5.10. Although this fractional value is smaller, the dominant loss value contribution comes from the power confinement in this layer.

The other higher order modes H_{20}^x , H_{30}^x and H_{11}^x have also been studied. They show similar characteristics to the H_{10}^x mode, with both n_{eff} and the loss increasing exponentially with increasing Teflon thickness, but these are not shown here. However, the H_{12}^x mode shows interesting modal properties after the Teflon coating is added and this is shown and discussed in the remainder of the section.

It has been noticed that the presence of the Teflon layer strongly affects the field profile of the H_{12}^x mode. The field profiles for the H_{12}^x mode for different Teflon thicknesses have also been investigated. These field profiles for the H_{12}^x mode along the y direction for Teflon thicknesses of $0 \mu\text{m}$ and $21.0 \mu\text{m}$ are shown in Figs. 5.11(a) and (b), respectively. For both these cases, the H^x field profiles show a rapid change at the metal-Teflon interface (shown by arrows), exhibiting a plasmonic nature. This mode also shows large negative fields at the Au-Teflon interfaces, in a similar way to the case when the Teflon was absent (as

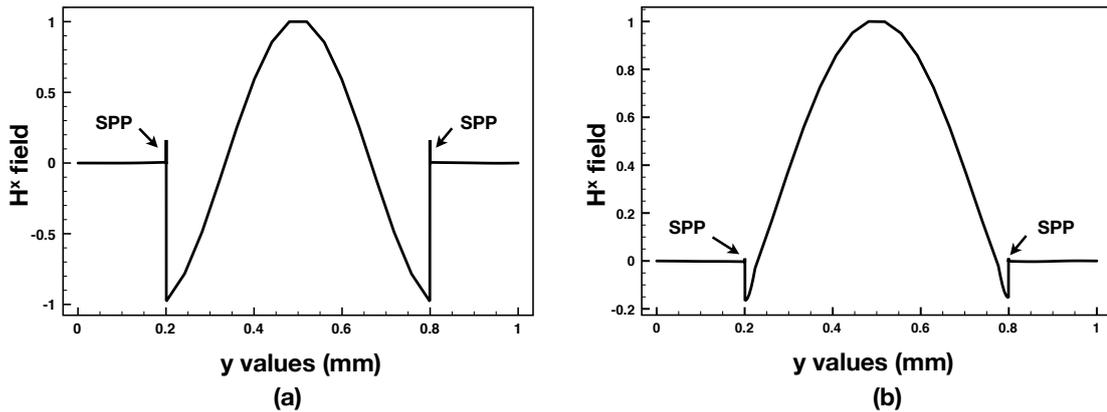


FIGURE 5.11: The normalized H^x field profiles of the H_{12}^x mode along the vertical direction for two different Teflon thicknesses, a) at $t_d = 0 \mu m$ b) at $t_d = 21 \mu m$ when $W = 1.0 mm$, $H = 0.6 mm$ and $t_m = 0.7 \mu m$.

mentioned above in Section 5.2). However, for smaller thicknesses of the Teflon layer, the field profile has significant side lobes of negative polarity and they interact mainly with the metal cladding. But when the Teflon thickness increases, a significant part of the field moves into the central air core, with the side lobes reducing in amplitude. This situation is shown in the field profile for a Teflon thickness of $21.0 \mu m$ in Fig. 5.11(b). As can be seen, it has an almost Gaussian shaped profile at the central air core region for a thick Teflon layer. Therefore, applying a Teflon coating can minimize the two negative lobes and this mode can be more suitable for launching through this waveguide from a source with Gaussian shaped profile. The smaller side lobes also generate plasmonic peaks of smaller values (shown by arrows in Fig. 5.11(b)) and in turn these lower the loss inside the metal layers.

The variation of the effective index and the loss characteristics with the change of the Teflon thickness for the H_{12}^x mode have been investigated and are presented together in Fig. 5.12. As like the H_{10}^x mode, the loss value for the H_{12}^x mode started to rise initially but then it reduces after a Teflon thickness of $3.0 \mu m$ is reached. As mentioned above, for this mode the two minor lobes of opposite polarity contain a significant amount of power. When these two lobes interact with the metal cladding, the loss in the metal layer starts to fall because a higher proportion of the field is shifted from the metal to the lower loss Teflon layer. Hence, the loss of this mode is much higher than that of the H_{10}^x mode for lower values of the Teflon thickness. The total loss is mainly governed by the attenuation in the metal for a lower Teflon thickness. However, as the Teflon thickness increases to a value above $3.0 \mu m$, the Teflon layer starts interacting

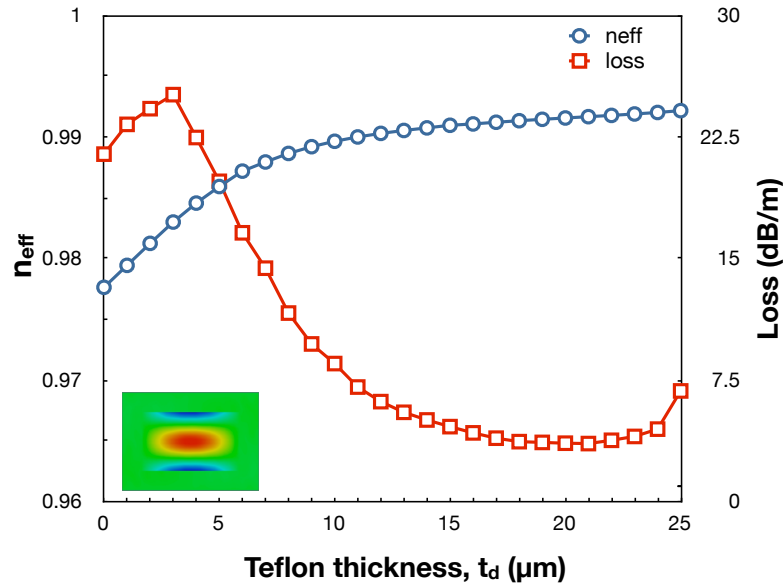


FIGURE 5.12: n_{eff} and loss of the H_{12}^x mode as a function of Teflon thickness at $W = 1.0 \text{ mm}$, $H = 0.6 \text{ mm}$ and $t_m = 0.7 \text{ }\mu\text{m}$.

with the metal cladding and the side lobes of the modal field profile start to reduce in amplitude and more field is trapped inside the air core. The central Gaussian lobe becomes predominant. The lower confinements in the metal and the Teflon layers result in a reduction of the total loss. The loss characteristics of the waveguide, along with the individual contributions of the metal and the Teflon layers, are shown in Fig. 5.13 with the variation of the Teflon thickness. The loss in the Teflon layer is shown by square symbols whereas circular symbols are used to denote the loss in the metal layer in this figure (Fig. 5.13).

When the Teflon thickness is further increased, the loss in the Teflon layer reaches the same order of magnitude of the metal losses and crosses it (the metal loss) at a Teflon thickness of $t_d = 16 \text{ }\mu\text{m}$. At a Teflon layer thickness of $21.0 \text{ }\mu\text{m}$, the minimum loss is achieved. Beyond this thickness, the loss in the Teflon starts to increase. The high refractive index of Teflon compared to that of air draws away power from the central Gaussian lobe and the confinement in Teflon becomes predominant, compared to that in metal. Thus the total loss increases again. The lowest loss found for this configuration is 3.55 dB/m , which is obtained at a Teflon layer thickness of $21.0 \text{ }\mu\text{m}$. This is only one third of the lowest loss of the H_{10}^x mode and also a significantly low value of loss compared to previously reported THz waveguides. McGowan *et. al* [239] reported a loss of about 300 dB/m , Hidaka *et. al* a loss of 6.5 dB/m [232] and Harrington *et. al* reported a loss of 3.9 dB/m [230] at THz frequency. The power confinement in the central air core was determined to be around 0.99 throughout the whole

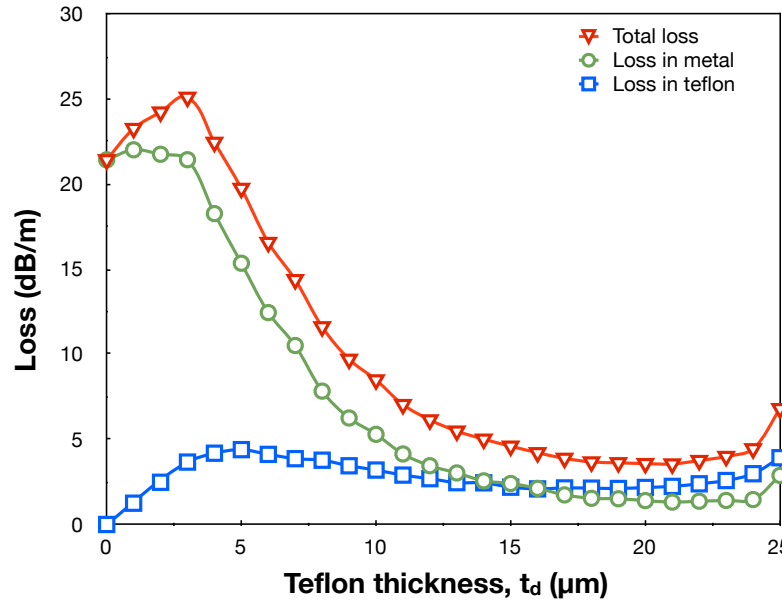


FIGURE 5.13: Variation of the total Loss, loss in metal and in Teflon for the H_{12}^x mode as a function of Teflon thickness for $W = 1.0 \text{ mm}$, $H = 0.6 \text{ mm}$ and $t_m = 0.7 \mu\text{m}$.

range of Teflon thickness studied.

5.3.3 Polystyrene vs. Teflon

A similar study was also performed with Polystyrene, and the loss comparison between the Polystyrene and the Teflon is presented in Figure 5.14. Both show a similar trend, revealing a minimum loss at $t_d = 21 \mu\text{m}$ and $t_d = 17 \mu\text{m}$, with minimum loss values of 3.55 dB/m and 6.2 dB/m for Teflon and Polystyrene, respectively. It clearly shows that the minimum loss for the H_{12}^x mode with Polystyrene is significantly higher than for a similar guide with Teflon coating, as was predicted earlier in Section 3.1. This is due to the higher loss tangent of Polystyrene than that of Teflon.

5.3.4 Effect of changing Metal

A further study of the H_{12}^x mode was performed for two other metal claddings, Ag and Cu, having effective indices of $308 + j532$ and $250.52 + j345.42$, respectively at 2.5 THz. Figure 5.15 shows the comparison of the losses for different Teflon thicknesses at a constant metal thickness $t_m = 0.7 \mu\text{m}$ for the three metals: Au, Ag and Cu. It can be seen that the minimum values of loss with the variation of the Teflon thickness is 3.55 dB/m , 2.94 dB/m and 4.21 dB/m for Au,

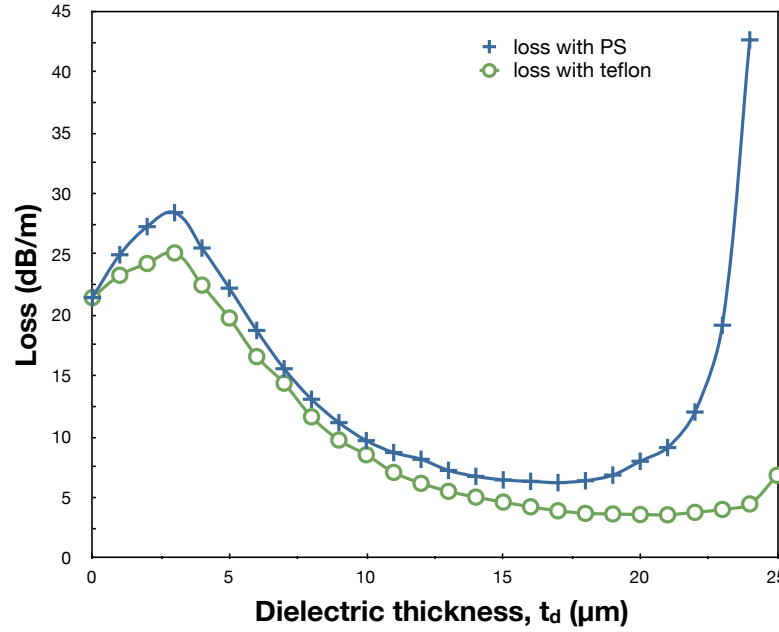


FIGURE 5.14: Comparison of loss characteristics of the H_{12}^x mode for two dielectric coatings (Polystyrene and Teflon) as a function of the dielectric thickness t_d at a metal thickness $t_m = 0.7 \mu\text{m}$ when $W = 1.0 \text{ mm}$ and $H = 0.6 \text{ mm}$.

Ag and Cu respectively, at the same Teflon thickness value, $t_d = 21 \mu\text{m}$. A pure metal with a pure imaginary refractive index does not contribute to the modal loss. On the other hand, for a lossy metal, its imaginary part (n_i) is bigger than its real part (n_r), and the real part contributes to the loss. Of the three metals mentioned above, silver (Ag) has the lowest n_r/n_i ratio, at 2.5 THz, and hence it suffers the lowest loss, as can be seen from the results obtained.

5.3.5 Effect of Metal Thickness

Further analysis on the effect of the cladding (metal) thickness on the modal characteristics of the guide for the three metals mentioned above was performed. It has been observed that changing the metal thickness has also gradually shifted the minimum loss of the guide from a Teflon thickness of $21 \mu\text{m}$ to $18 \mu\text{m}$. Figure 5.16 shows the loss characteristics of the guide with different metal thicknesses (with the Teflon thickness taken as $18 \mu\text{m}$) for three different metal claddings. As can be seen from this figure, as the metal thickness increases, the loss of the guide further decreases to a metal thickness value of $2.9 \mu\text{m}$. Beyond a metal thickness of $2.9 \mu\text{m}$, the loss of the guide starts to increase again. For a Teflon thickness $t_d = 18 \mu\text{m}$, the minimum loss was found with an Ag coated guide with a value of 2.07 dB/m , whereas using Cu and Au the losses

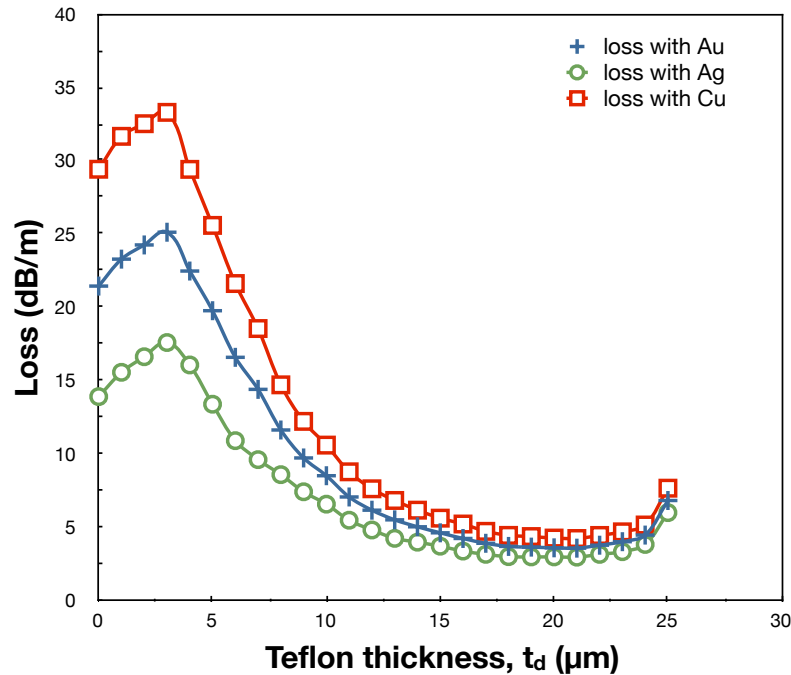


FIGURE 5.15: Loss of the H_{12}^x mode as a function of Teflon thickness t_d at a metal thickness $t_m = 0.7 \mu\text{m}$, $W = 1.0 \text{ mm}$ and $H = 0.6 \text{ mm}$.

are 2.54dB/m and 2.286dB/m , respectively. This clearly shows that the loss value can be minimised by adjusting various parameters of the waveguide.

5.3.6 Effect of Bending

Bent waveguides are important building blocks used to interconnect non-collinear straight waveguides and input/output ports, and they also are used in the designs of specialised components, such as ring resonators [240], arrayed waveguide filters [241], optical delay lines [242] and S-bend attenuators [243].

Previous research [244] has shown that the field distribution of the fundamental mode in a bent waveguide is different from that of the straight waveguide. The radiation and transition losses between the straight and the bent waveguide contribute to the propagation properties of a bent waveguide. As a result, the power loss in a bent waveguide will be higher, due to the conversion of the incident beam to the higher order modes.

Therefore it is important to analyse the bending properties of a waveguide for proper characterisation of the structure. The first step in the process is to transform the curved waveguide to an equivalent straight waveguide using the conformal transformation [245]. The coordinate transformation allows a bent

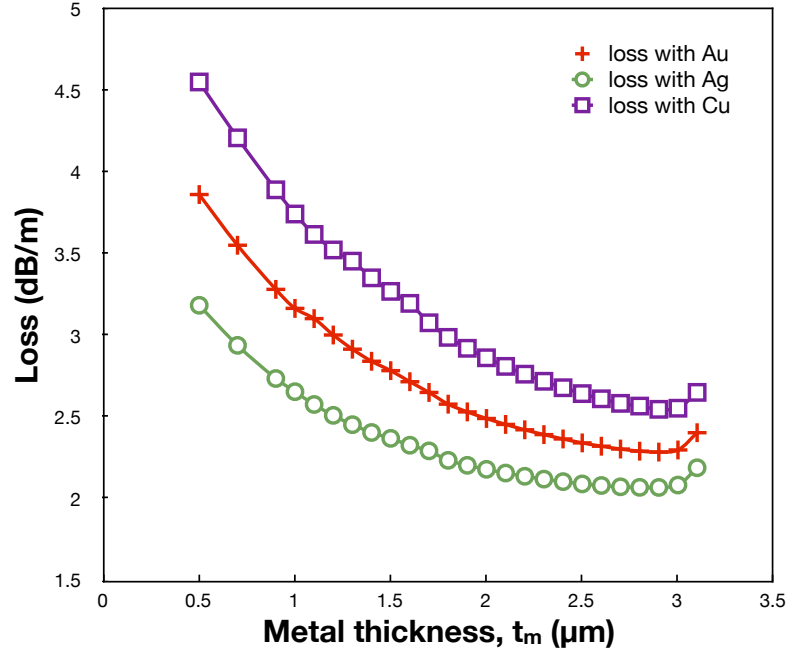


FIGURE 5.16: Loss of the H_{12}^x mode as a function of metal thickness t_m when the Teflon thickness $t_d = 18 \mu\text{m}$, $W = 1.0 \text{ mm}$ and $H = 0.6 \text{ mm}$.

waveguide in the y -plane to be represented by an equivalent straight waveguide with a modified refractive index distribution, $n'(x, y)$.

$$n'(x, y) = n_m(x, y)(1 + y/R) \quad (5.1)$$

Here, $n_m(x, y)$ is the original refractive index profile of the bent waveguide, $n'(x, y)$ is the equivalent index profile of a straight guide, R is the radius of the curvature, and y is the distance from the centre of the waveguide.

Bending Characteristics of H_{10}^x mode

To see the bending characteristics of the H_{10}^x mode of the loss optimised dielectric coated rectangular guide, the bending radius was varied from 1000 mm to 150 mm and the bending of the guide was done in the downward *i.e.* $-y$ direction. This suggests that because of the bending, the effective index of the mode will increase in the $+y$ direction and reduce in the $-y$ direction. Figure 5.17 shows the H_x field profiles of the H_{10}^x mode and the normalised line plots for a cross section on the y axis for bending radius of 1000 mm, 500 mm and 150 mm respectively.

The effect of bending is visible for even 1000 mm radius. As can be seen in Figs. 5.17a and 5.17b, the bottom interface plasmonic peak is significantly lower

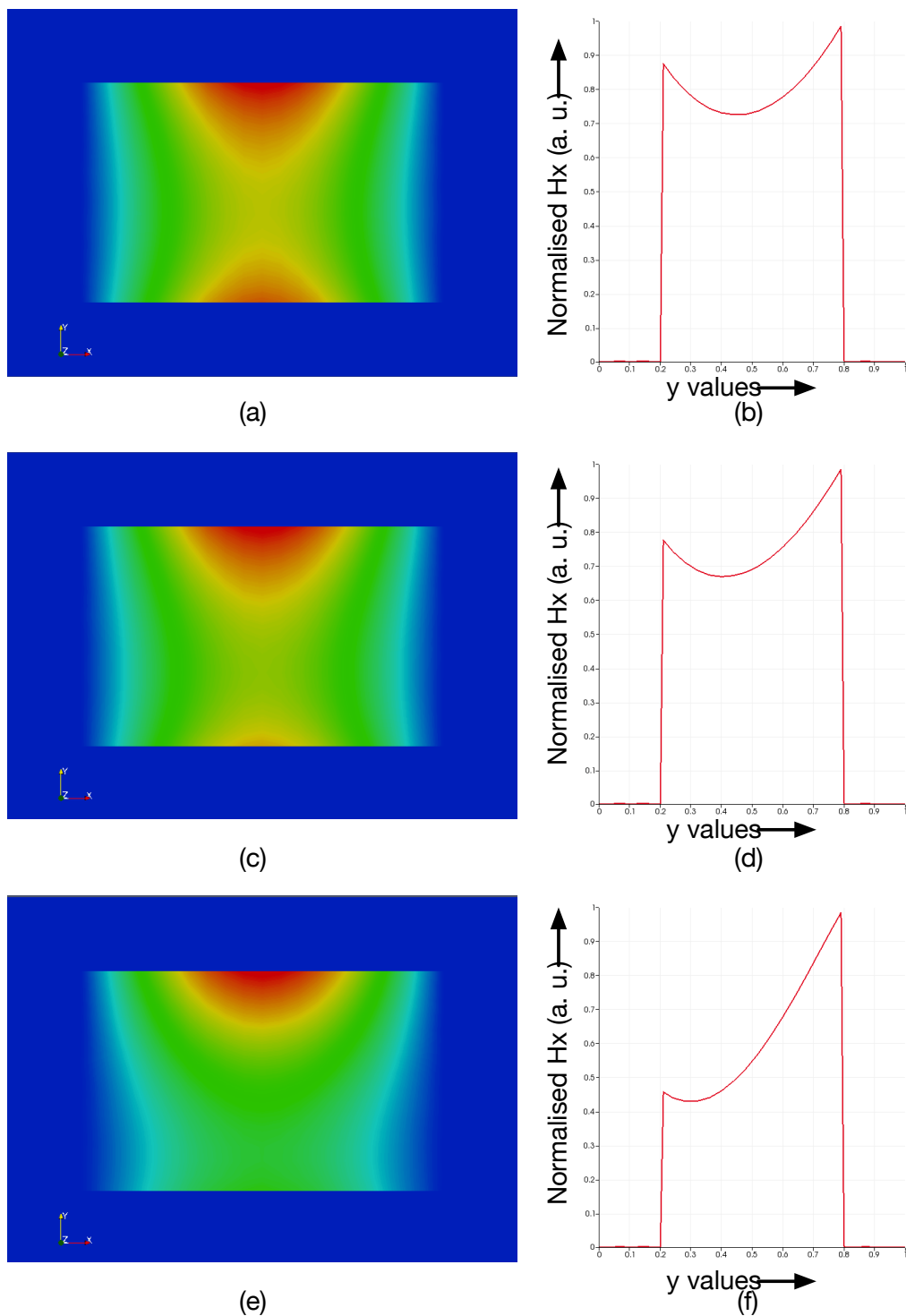


FIGURE 5.17: Contour field profile and the normalized field profile in the vertical (y) direction of the H_{10}^x mode for bending radius a) and b) $R = 1000 \text{ mm}$, c) and d) $R = 500 \text{ mm}$ and e) and f) $R = 150 \text{ mm}$ respectively

than that of the top interface depicting the fact that more field is pulled to the top interface due to the increase in effective index. When the bending radius is reduced further, the difference between the peaks increases. Figures 5.17c, 5.17d and 5.17e, 5.17f show the effect on H_x field profile of H_{10}^x mode at a bending radius of 500 mm and 150 mm. It can be clearly observed that the bottom interface peak is reducing in amplitude compared to the top interface peak amplitude. In fact the field distribution is moving towards the top interface with the decrease in bending radius.

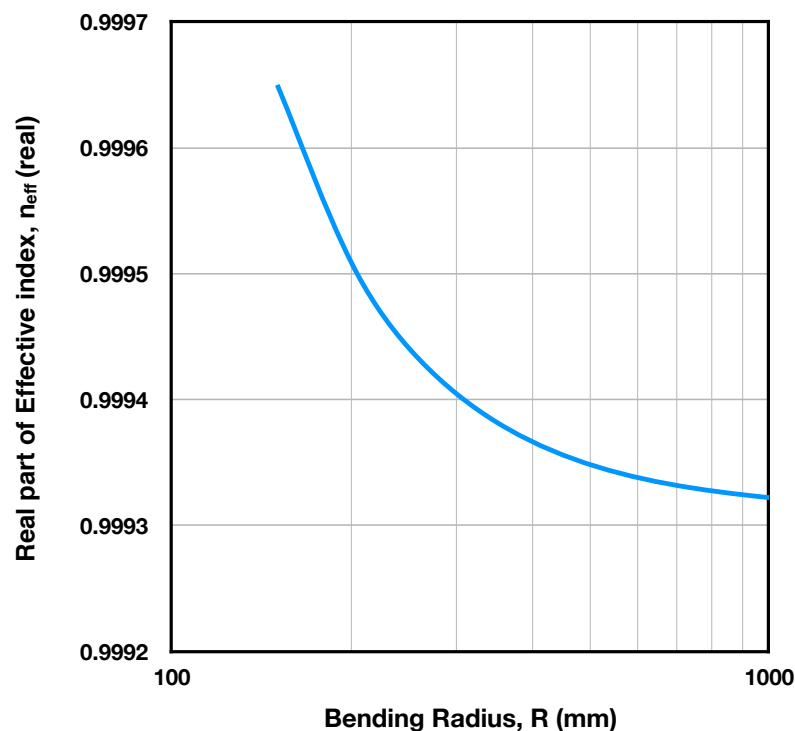


FIGURE 5.18: Variation of the real part of effective index of the H_{10}^x mode as a function of bending radius R

The effect of the bending on the real part of the effective index can be seen in Fig. 5.18. As can be seen, the real part of the effective index increases slightly as the bending radius is decreased.

The effect on loss is shown in Fig. 5.19. As can be seen the loss of guide increases exponentially with the reduction of the bending radius.

Bending Characteristics of H_{12}^x mode

To see the bending characteristics of the H_{12}^x mode of the loss optimised dielectric coated rectangular guide, the bending radius was changed from 1000 mm

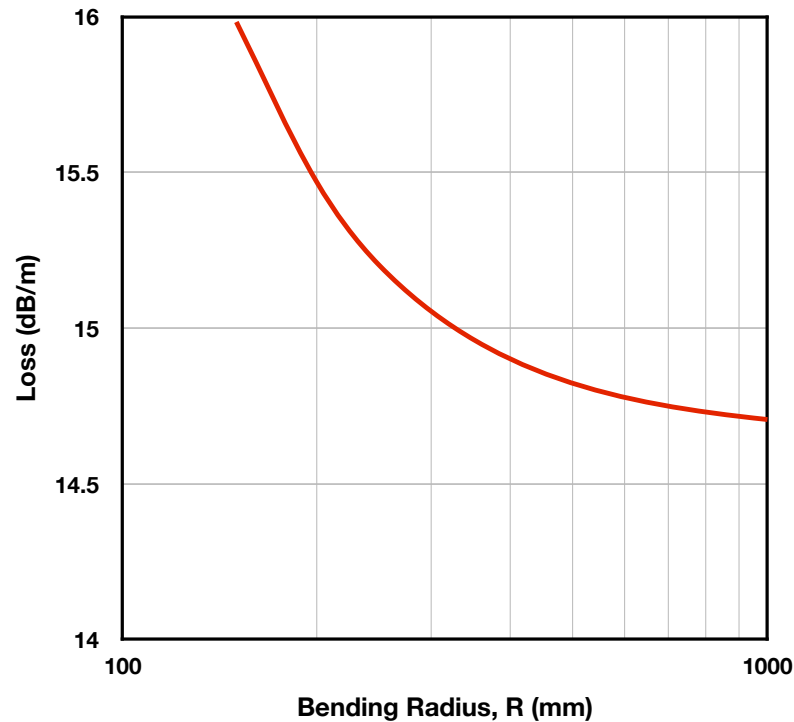


FIGURE 5.19: Variation of total loss of the H_{10}^x mode as a function of bending radius R

to 10 mm. Figure 5.20 shows the H_x field profiles of the H_{12}^x mode and the normalised line plots for a cross section on the y axis for bending radius of 1000 mm, 100 mm, 50 mm and 10 mm respectively.

It can be observed that the field profile for bending radius 1000 mm has no visual difference from the field profile of a straight guide.

For 100 mm bending radius shown in Figs. 5.20(c) and (d), although there is no visual difference in the contour plot, the line plot shows slight increase of the right side lobe compared to the left side.

With bending radius 50 mm, the imbalance between the sidelobes can clearly be seen in the 2D contour profile in Fig. 5.20(e) and the line plot of Fig. 5.20(f) confirms the higher imbalance between the two lobes compared to 100 mm bending radius. It can also be noticed in the line plot that the central lobe is also moving towards the right, as expected.

At bending radius 10 mm it can be clearly seen from the contour plot of Fig. 5.20(g) that the central lobe has also moved from the centre to the top and the top sidelobe is higher in amplitude than the bottom lobe. The line plot also confirms the same thing. The central lobe has clearly shifted to the right (which is the upperside) and the right side lobe is much bigger in amplitude than the left side lobe.

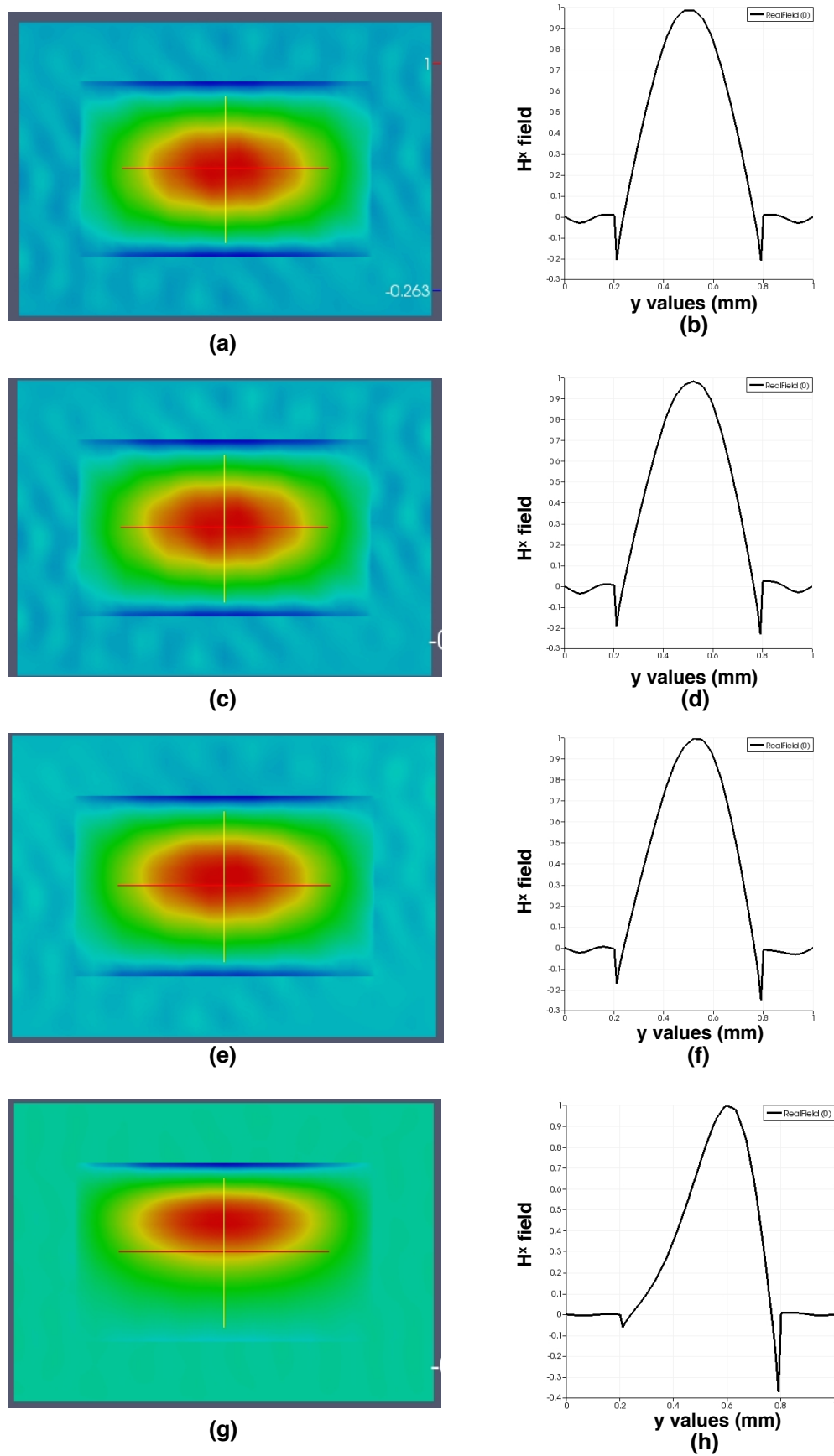


FIGURE 5.20: Contour field profile and the normalized field profile in the vertical (y) direction of the H_{12}^x mode for bending radius of a) and b) $R = 1000 \text{ mm}$, c) and d) $R = 100 \text{ mm}$, e) and f) $R = 50 \text{ mm}$ and g) and h) $R = 10 \text{ mm}$ respectively

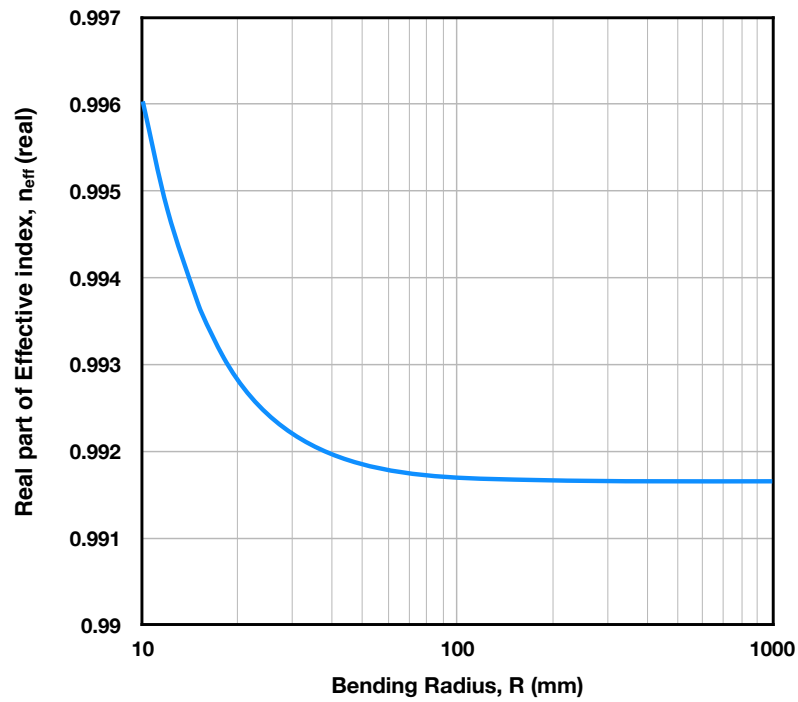


FIGURE 5.21: Variation of the real part of effective index of the H_{12}^x mode as a function of bending radius R

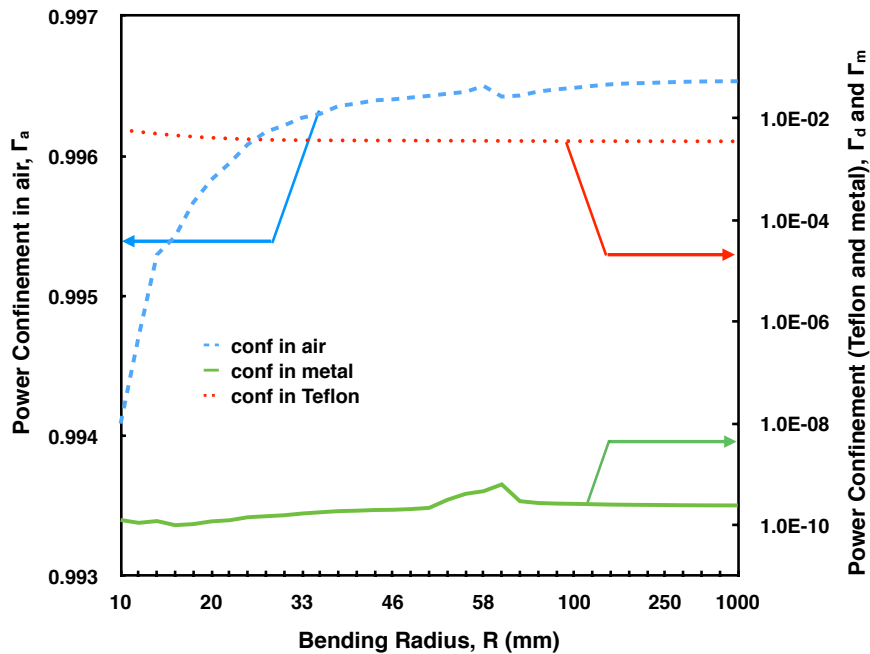


FIGURE 5.22: Power confinement factors in air (Γ_a), in Teflon (Γ_d) and in metal (Γ_m) as a function of bending radius R for the H_{12}^x mode when $W = 1.0 \text{ mm}$, $H = 0.6 \text{ mm}$, $t_d = 18 \text{ }\mu\text{m}$ and $t_m = 2.9 \text{ }\mu\text{m}$.

Figure 5.22 shows the power confinement of the guide in air, Teflon and in metal. As can be seen in the figure, power confinement of the air core exponentially decreases with the reduction of bending radius whereas the confinement in air is more or less unchanged with higher bending radius. The confinement in the Teflon layer slightly increases when the bending radius is reduced. The increase in this layer happens in almost a linear manner. Although the decrease in the air confinement is exponential the drop of confinement is at the scale of 10^{-3} and the increase in power confinement in Teflon layer is at the scale of 10^{-2} . Power confinement in metal was unchanged from 1000 mm to 70 mm and after that it started to decrease slightly. But the scale is negligible compared to the air and Teflon layer.

Although the power confinement change for the bending is very little, the impact of the change in confinement is significant when the bending radius reduces greatly. This is due to the movement of power near one of the metal dielectric interfaces.

Figure 5.21 shows the change in real part of effective index of the H_{12}^x mode. As can be seen, the real part of the effective index increases slightly as the bending radius is decreased. Figure 5.23 shows the loss characteristics for bending. It shows both the total loss of the guide and the bending loss. It can be observed that from 1000 mm to 100 mm there is no significant increase in loss. Just after 100 mm from 60 – 55 mm there is a local maximum. After that when the bending radius is further reduced, both the losses follow the same function they were following before the hump and with the increase in bending loss, total loss increases sharply after the hump.

Bending Loss Comparison between H_{10}^x and H_{12}^x modes

To compare the bending characteristics of the H_{10}^x and H_{12}^x modes, the bending losses of the two modes were compared. Figure 5.24 shows the bending losses of the two modes for the bending radius range 100 – 1000 mm (H_{10}^x mode starting at 150 mm). As it can be seen that bending loss for the H_{10}^x mode rapidly increases with the reduction of bending radius. On the other hand, bending loss for the H_{12}^x shows negligible increase at 150 mm. Therefore, the H_{10}^x mode is more affected by bending compared to the H_{12}^x mode. At this radius the bending loss for the H_{10}^x mode is 1.31 dB/m and that for H_{12}^x mode is 0.0076 dB/m . As shown in Fig. 5.23 the bending loss for the H_{12}^x mode reaches 1.3 dB/m for a bending radius of 15 mm, which is 10 times smaller. Therefore, when bending loss is considered the H_{12}^x mode is preferable over the H_{10}^x mode.

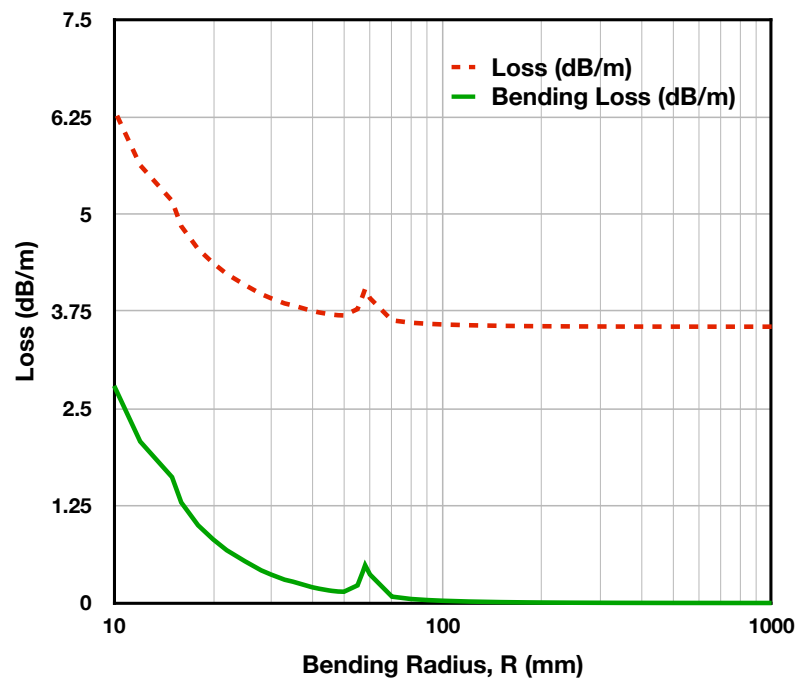


FIGURE 5.23: Variation of total loss and bending loss of the H_{12}^x mode as a function of bending radius R

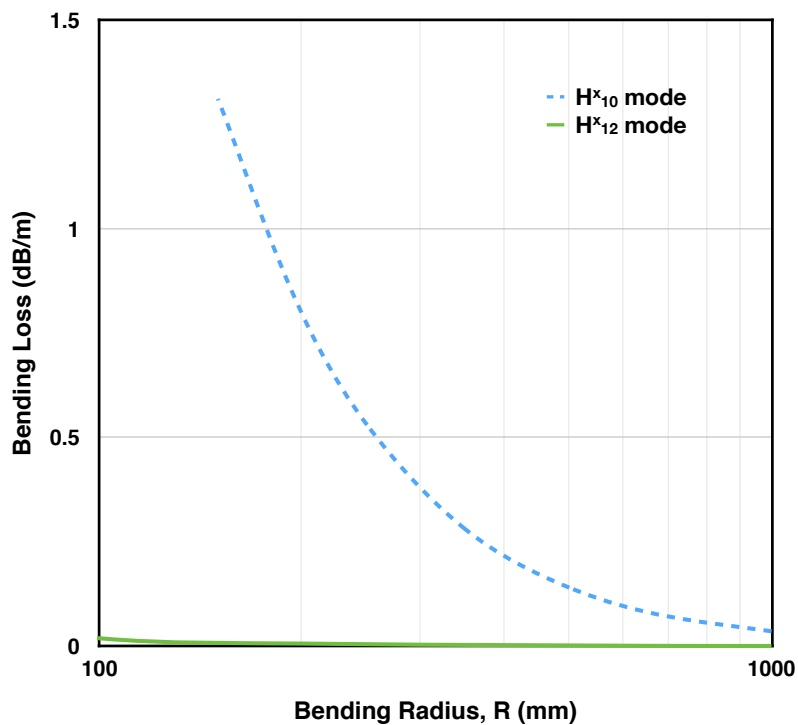


FIGURE 5.24: Comparison of bending loss from bending radius 150 mm to 1000 mm for H_{10}^x and H_{12}^x modes

5.4 Analysis of bigger rectangular guides

In the previous section, the metals used were gold, copper and silver. In that analysis the effects of change of height, width, metal thickness and dielectric thickness on the loss property of the guide were studied for the H_{10}^x , H_{20}^x , H_{30}^x , H_{11}^x and H_{12}^x modes at 2.5 THz. It was found that for a Silver guide with width 1 mm, height 0.6 mm, metal thickness 2.9 μm and Teflon thickness 18 μm the loss for the H_{12}^x mode reduced to the minimum to 2.07 dB/m. The loss obtained compares much favourably with the circular hollow core Polystyrene coated guide, which shows minimum loss value both experimentally [230] and numerically [218]. The loss can be further reduced by considering a larger waveguide with increased height and width. Due to the rectangular shape of the guide, the horizontally and vertically polarized modes will not be degenerate. Hence such a low-loss rectangular waveguide, which can be made flexible, would be able to maintain the polarization state of the input wave and may be easier to integrate with other components than would a circular structure.

In this section only the guide with Silver cladding is considered for analysis as it produces minimum loss and the effect of change in dimension is studied. All the analyses of this section are for the H_{12}^x mode only. This is because in [218, 246] it is already shown that for both circular and rectangular structures, with the optimal thickness of dielectric layer, the H_{12}^x mode shows far lower loss than any other mode.

5.4.1 Effect of Dimension

In the previous analysis the effect of height and width variations were studied. But the effect of change of the cross sectional dimensions is now presented. In [246] it was predicted that increase in the dimension (cross sectional area) of the guide could lead to lower losses. As mentioned in the previous section the goal of the previous analysis was to obtain a rectangular guide with equal loss to [218]. The guide proposed in that work had slightly lower loss but with only 20% of the cross-sectional area.

To evaluate the lower loss prediction a rectangular guide is considered with the dimensions 2.5 mm \times 1.25 mm (width 2.5 mm and height 1.25 mm) which has a cross section very close to the circular guide of [218]. To optimise the loss of the guide the dielectric thickness was varied from 0 to 28 μm . Figure 5.25 shows the variation of loss of the H_{12}^x mode with the dielectric thickness. As can be observed there are three major features of the curve. The loss value is

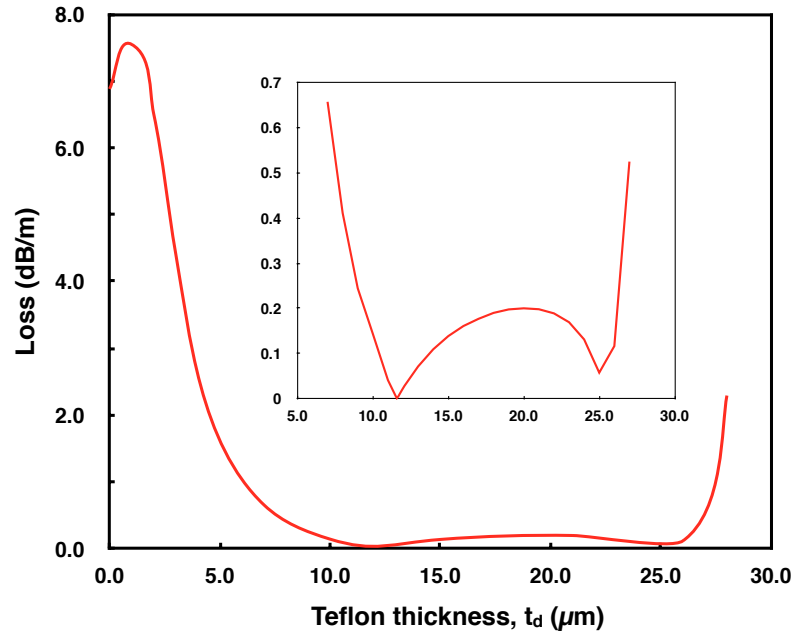


FIGURE 5.25: Variation of loss for $2.5\text{ mm} \times 1.25\text{ mm}$ guide with varying dielectric thickness. The inset shows a zoomed in view of the curve for a range of $7.0\text{ }\mu\text{m}$ to $27\text{ }\mu\text{m}$

extremely low, unlike [246]. The new observation is that there are 2 minima in the loss curve. The loss curve also shows a large valley which has almost loss free operative regions. The inset inside the figure shows the 2 minima clearly. It can also clearly be seen that the first minimum is at $t_d = 11.6\text{ }\mu\text{m}$ and the second minimum is at $t_d = 25\text{ }\mu\text{m}$. The first minimum loss found for the $2.5\text{ mm} \times 1.25\text{ mm}$ guide was 0.008 dB/m at $11.6\text{ }\mu\text{m}$ Teflon thickness whereas the second minimum was found to be 0.008 dB/m at $25\text{ }\mu\text{m}$ Teflon thickness.

Another new interesting phenomenon which can be observed is the change of field distribution with the change of dielectric thickness when width of the dielectric layer is further extended up to $29\text{ }\mu\text{m}$. As can be seen in Fig. 5.26 the field distribution along the horizontal direction is changing with the increase of the dielectric thickness.

Figure 5.26(a) shows the field when Teflon thickness is $t_d = 25\text{ }\mu\text{m}$. The H_x field is totally confined in the air core. There is very little interaction with the metal cladding. The contour field profile in Fig. 5.26(b) shows that for $28\text{ }\mu\text{m}$ thickness of the Teflon layer, there is significant interaction of the field distribution with the metal cladding in the horizontal direction. Interaction in the vertical direction is insignificant. For $28.8\text{ }\mu\text{m}$ thickness of the Teflon coating Fig. 5.26(c) shows even more interaction in the horizontal direction causing the field distribution becoming almost uniform in the horizontal direction inside

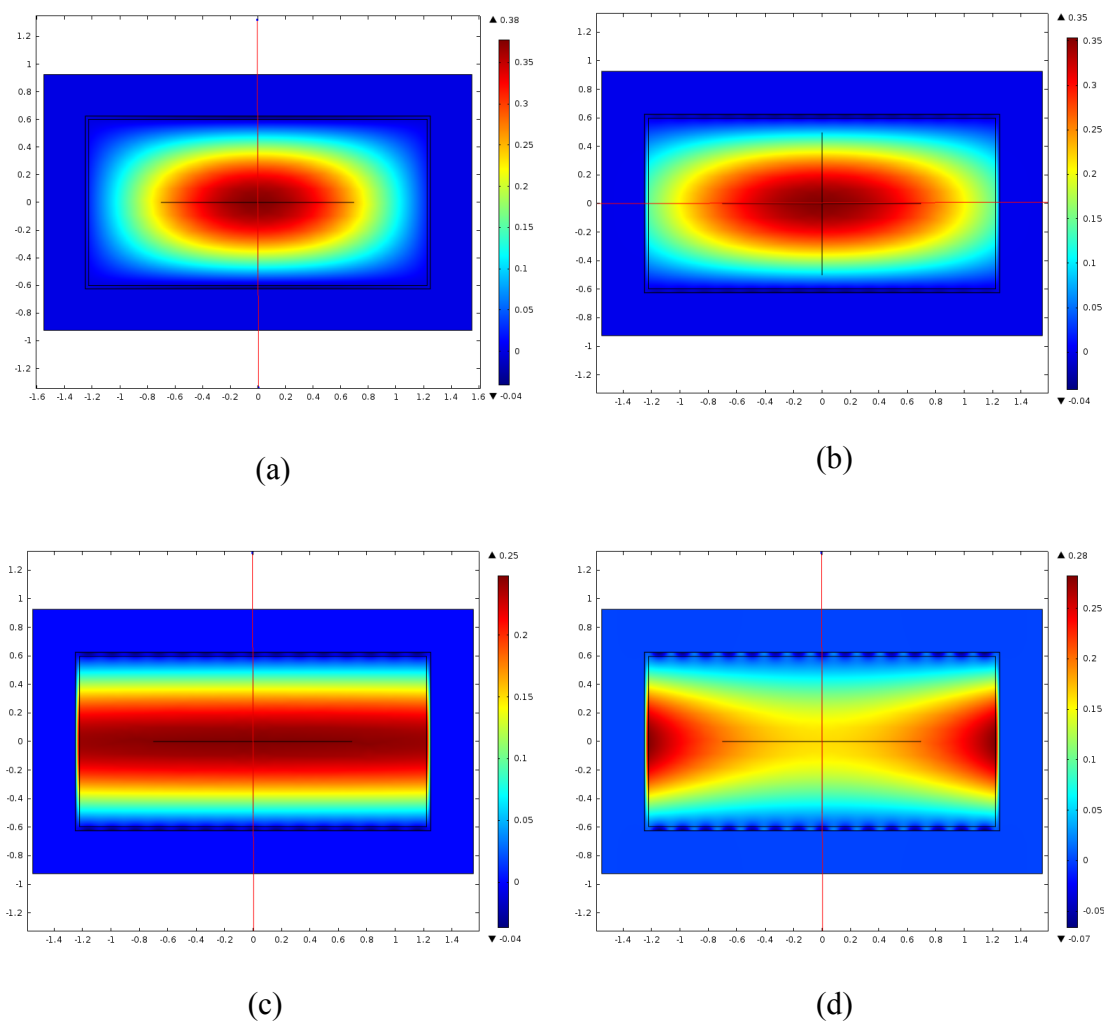


FIGURE 5.26: H_x field of the H_{12}^x mode of the $2.5 \text{ mm} \times 1.25 \text{ mm}$ guide for dielectric thicknesses of (a) $25 \mu\text{m}$, (b) $28 \mu\text{m}$, (c) $28.8 \mu\text{m}$ and (d) $29 \mu\text{m}$

the air core. Figure 5.26(d) shows the H_x distribution with $29 \mu m$ thickness. As shown the field in this case has moved to the side of the air core. The horizontal distribution of the field component is plasmonic in nature. For all the profiles shown in Fig. 5.26 the vertical interactions are not noticeable.

To understand the behaviour better, variation of the H_x field along the x and y directions through the centre of the guide for different Teflon thicknesses are also shown. Figure 5.27 shows the horizontal and vertical line plots for Teflon thicknesses of 0 , $11.6 \mu m$ and $20 \mu m$. It can be seen in Figs. 5.27(b), (d) and (f) that with the increase in thickness the interaction of the side-lobes with the Silver cladding reduces. As mentioned in section 5.3.2, the reduction in the side-lobes is the main reason for the loss reduction in this range. The first minimum we observed was at $11.6 \mu m$ thickness. Although the size of the side lobes continue to fall, the loss starts to rise. The explanation of the rise in loss can be explained by using Figs. 5.27(a), (c) and (e). In Figs. 5.27(a) and (c) the horizontal field component does not interfere with the Silver or Teflon layers as there is no visible change of slope at the corners of the line plots. But in Fig. 5.27(e) a small change in slope can be observed at the corner. A zoomed in version can be seen in the inset of Fig. 5.27(e).

Figure 5.28 shows the vertical and horizontal cross sectional profiles of the H_{12}^x mode for larger Teflon thicknesses of $25 \mu m$, $27 \mu m$, $28.8 \mu m$ and $28.9 \mu m$. In Fig. 5.25, the second minimum was observed at $25 \mu m$ Teflon thickness. As shown in Fig. 5.28(b) the side lobes are minimum at $25 \mu m$ thickness. But horizontal interaction is more prominent in Fig. 5.28(a). In fact, from $11.6 \mu m$ to $25 \mu m$ of Teflon thickness, the side interaction increased in the horizontal direction and the side lobes in the vertical direction reduced in amplitude. The loss property in this section can be explained as follows.

After $11.6 \mu m$ the side interaction in the horizontal direction started. Therefore, the loss started to increase. The loss reduction due to reduction of side lobe in the vertical direction started to compensate the loss increase due to the horizontal side interaction. As a result the initial increase in loss was suppressed and another minimum was found at $25 \mu m$ thickness.

As can be seen in Figs. 5.28(b), (d), (f) and (h), there is no significant change in the side lobe sizes when the thickness is further increased. But in Figs. 5.28(a), (c) and (e) the horizontal side interaction has increased significantly with the increase in Teflon thickness. In Fig. 5.28(g) the shape of the horizontal field changed from convex to concave. In this section due to the increase in horizontal side interaction, the loss increases very rapidly.

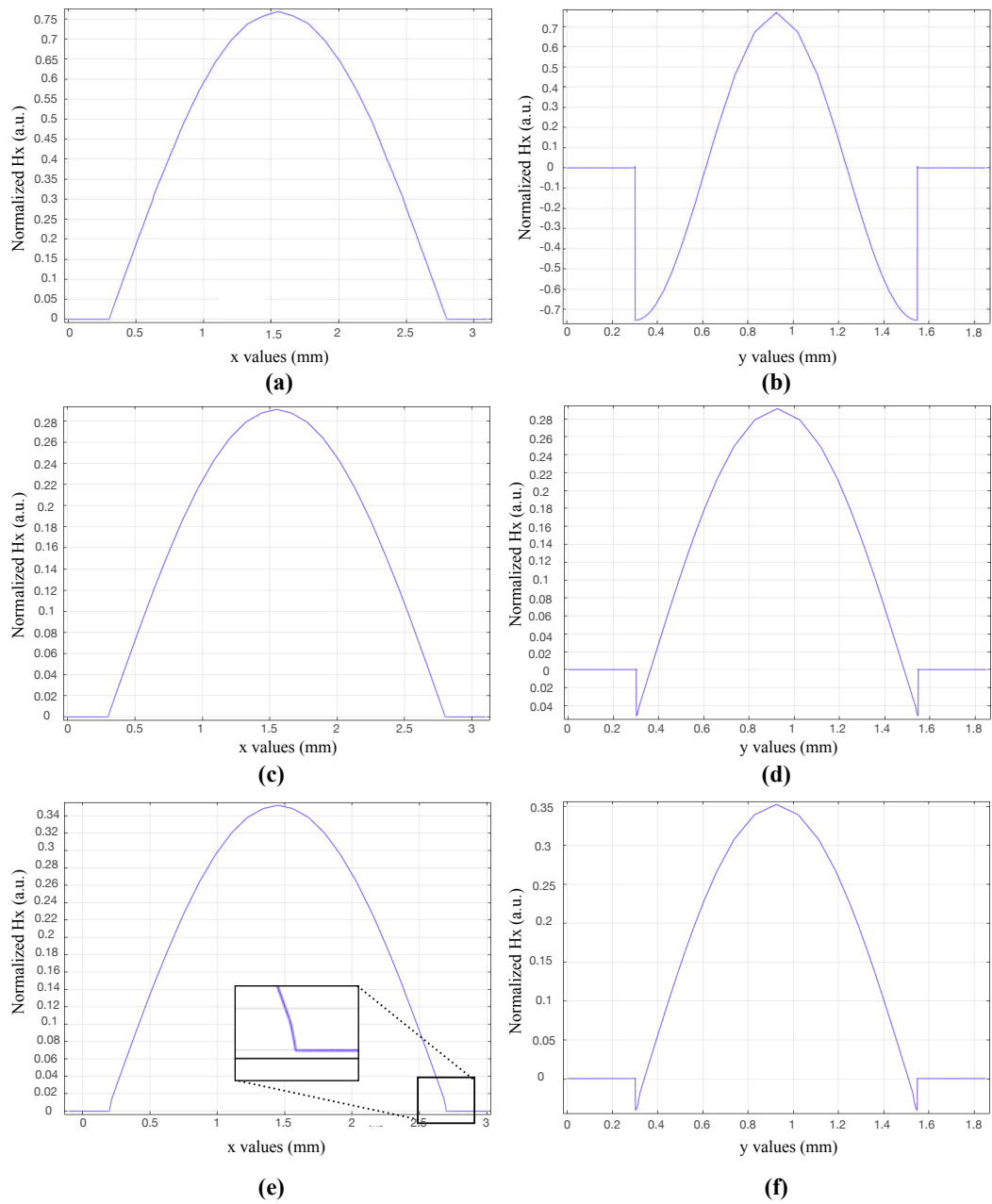


FIGURE 5.27: Line plots of the H_x field of the H_{12}^x mode (a) horizontal cross section with no Tefflon layer, (b) vertical cross section with no Tefflon layer, (c) horizontal cross section with $11.6 \mu\text{m}$ Tefflon thickness, (d) vertical cross section with $11.6 \mu\text{m}$ Tefflon thickness, (e) horizontal cross section with $20 \mu\text{m}$ Tefflon thickness, (f) vertical cross section with $20 \mu\text{m}$ Tefflon thickness

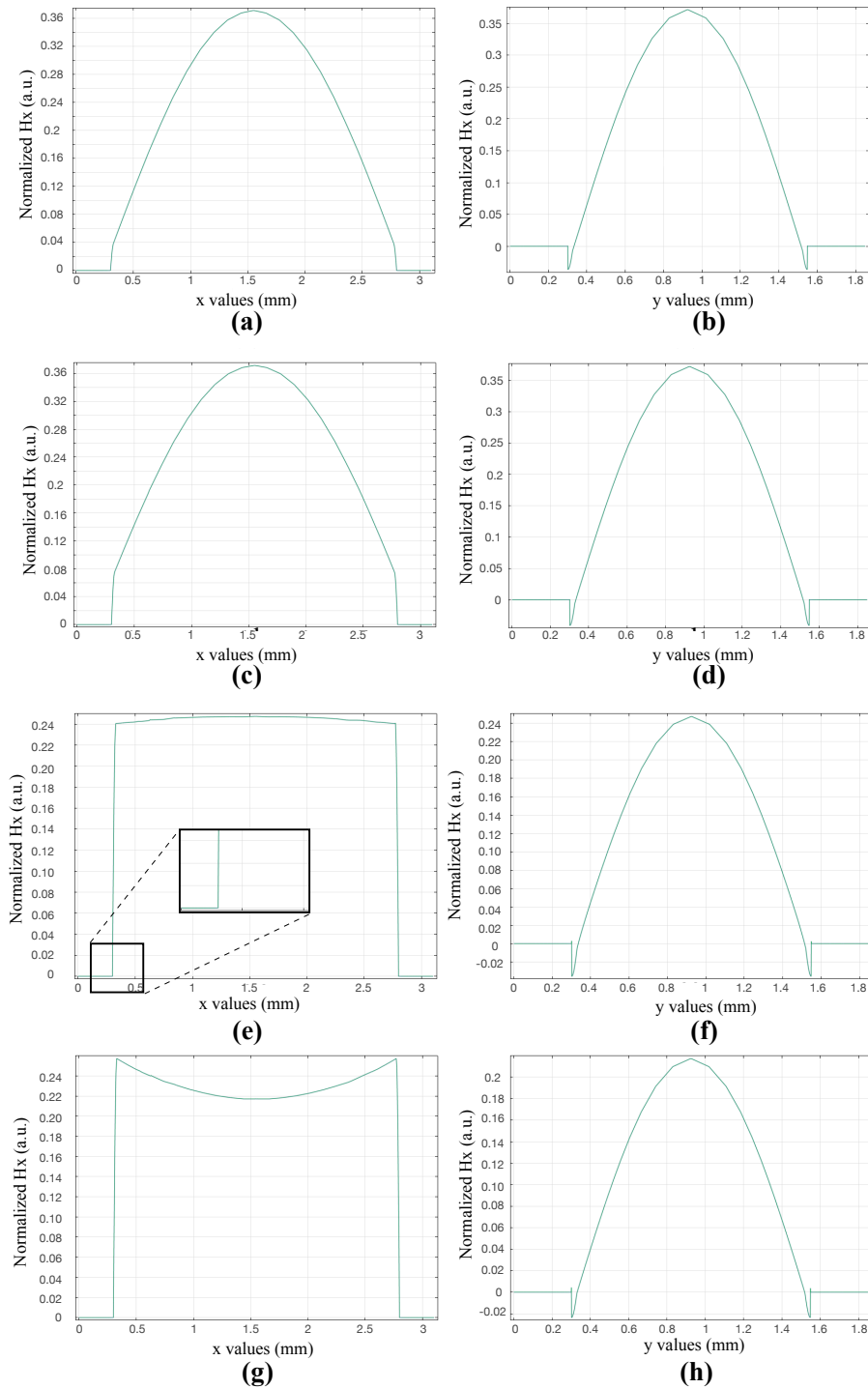


FIGURE 5.28: Line plots of H_{12}^x field for Tefflon thickness (a), (b) $25 \mu\text{m}$, (c), (d) $27 \mu\text{m}$, (e), (f) $28.8 \mu\text{m}$ and (g), (h) $28.9 \mu\text{m}$. Among these plots a), c), e), g) show the line plots along the horizontal direction and b), d), f), h) show the line plots along the vertical direction

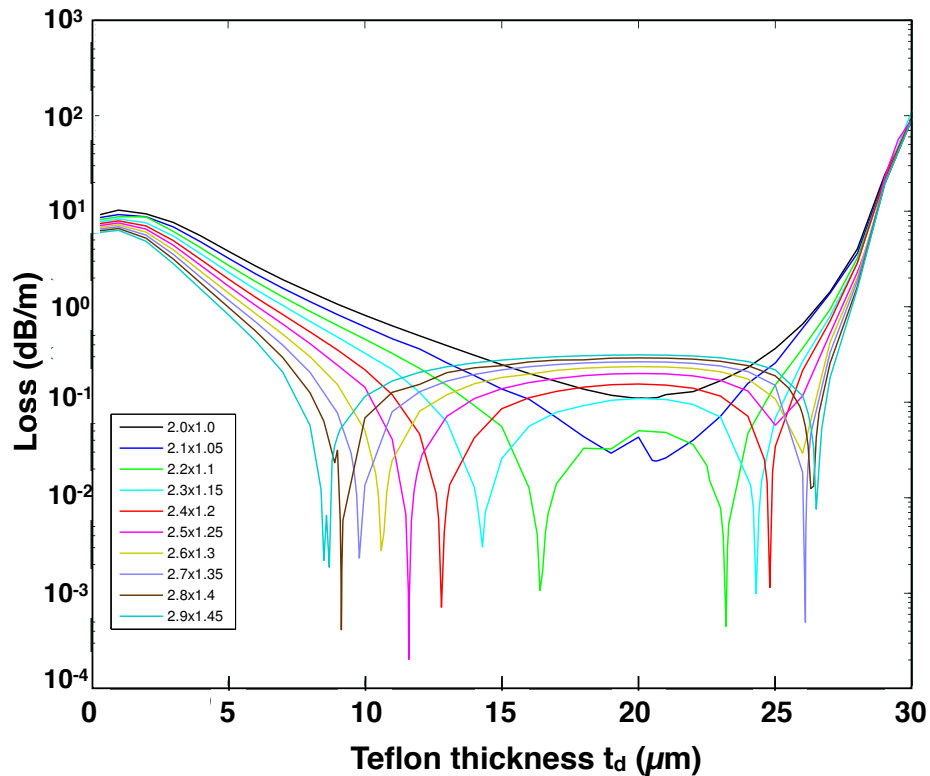


FIGURE 5.29: Loss characteristics of guides from $2.0\text{ mm} \times 1.0\text{ mm}$ to $2.9\text{ mm} \times 1.45\text{ mm}$

In the previous section, for a smaller rectangular guide, only one minimum was observed. But for a larger guide, 2 different minima were identified. To make the explanation consistent with the previous work, the effect of dimension was observed by keeping both the aspect ratio and the Silver thickness fixed and changing the cross sectional area between $2.9\text{ mm} \times 1.45\text{ mm}$ to $2.0\text{ mm} \times 1.0\text{ mm}$. The thickness of the Teflon layer was also varied from 0 to $30\text{ }\mu\text{m}$ to find the loss characteristics curve for all of the guide dimensions considered. It can be observed in Fig. 5.29 that the 2 minima are present in rectangular waveguides with larger cross section and they are further apart from each other when the cross sectional area is large. As the cross sectional area reduces, the two minima move towards each other and they start to merge when the cross sectional area was $2.1\text{ mm} \times 1.05\text{ mm}$. When the cross sectional area is $2.0\text{ mm} \times 1.0\text{ mm}$, the two minima merge completely to become a single minimum. The previously studied dimension $1.0\text{ mm} \times 0.6\text{ mm}$ is lower than this dimension. Therefore, the finding in this section is consistent with the previously found phenomenon of single minimum.

However, for smaller thicknesses of the Teflon layer, the field profile has significant side lobes of negative polarity and they interact mainly with the

metal cladding. But when the Teflon thickness increases, a significant part of the field moves into the central air core, with the side lobes reducing in amplitude.

The reason for the two minima for the higher dimension guides and later on for the single minima for the lower dimension guides can be explained using the field profiles of the H_{12}^x mode for varying Teflon thicknesses. It can be observed from Fig. 5.29 that when the cross-sectional dimension of the guide is varied, the H_{12}^x follows the similar pattern as that of Fig. 5.25. It was previously mentioned that for this mode the two minor lobes of opposite polarity contain a significant amount of power. For lower values of Teflon thickness, these two lobes interact mainly with the metal cladding, Hence, for lower Teflon thicknesses, the total loss is mainly governed by the attenuation in the metal layer and the loss of this mode is much higher. However, as the Teflon thickness increases, a higher proportion of the field is shifted from the metal to the lower loss Teflon layer and the loss in the metal layer starts to fall. Interaction of the Teflon layer with the metal cladding starts to increase and the side lobes of the modal field profile start to reduce in amplitude. The air core has more field trapped inside it and the central Gaussian lobe becomes predominant. The reduction in the side-lobes leads to lower confinements in the metal and the Teflon layers which eventually result in a reduction of the total loss.

When the Teflon thickness is further increased, the loss in the Teflon layer reaches the same order of magnitude of the metal losses and crosses it (the metal loss) and the first minimum loss point is achieved. For example, at a Teflon layer thickness of $11.6 \mu\text{m}$, the first minimum loss is achieved for the $2.5\text{mm} \times 1.25\text{mm}$ guide. The horizontal field component does not interfere with the Silver or the Teflon layers upto this Teflon thickness (corresponding to the first minimum loss value) as there is no visible change of slope at the corners of the line plots. Beyond this thickness, the loss in the Teflon starts to increase. The high refractive index of Teflon compared to that of air draws away power from the central Gaussian lobe and the confinement in Teflon becomes predominant, compared to that in metal. Although the size of the side lobes continue to fall, but after the first minimum, the side interaction in the horizontal direction started to build up and a small change in slope can be observed at the corner of the field plots. Increase in Teflon loss and also the horizontal side interaction make the total loss to increase again after the first minimum.

Although the horizontal interaction gets more prominent for increasing values of Teflon thickness, the side lobes in the vertical direction continue to get reduced in amplitude. As the Teflon layer thickness increases, the decrease in

loss due to reduction of side lobe amplitude in the vertical direction started to compensate the increase in loss due to the horizontal side interaction. As a result the initial increase in loss, that started after the first minimum, was suppressed and a second minimum was found. For the $2.5\text{ mm} \times 1.25\text{ mm}$ guide the second minimum is achieved at $25\ \mu\text{m}$ Teflon thickness. After the second minimum, it can be observed from the field plots in Fig. 5.28 that there is no significant change in the side lobe sizes when the thickness of Teflon is further increased. But the horizontal side interaction increases significantly with the increase in Teflon thickness and the field shapes also change. Due to the rapid increase in horizontal side interaction, the loss also increases very rapidly.

However, one significant contribution of this work is to identify that all of the curves show extremely low loss at the central part of the figure. The loss is stable for a large range of Teflon thickness for guides $2.3\text{ mm} \times 1.15\text{ mm}$ to $2.9\text{ mm} \times 1.45\text{ mm}$. *i.e.* Among them, the stable section is the largest for the $2.9\text{ mm} \times 1.45\text{ mm}$ guide as shown in Fig. 5.29. For the $2.9\text{ mm} \times 1.45\text{ mm}$ guide, the loss is comparatively stable in the $12\ \mu\text{m}$ to $25\ \mu\text{m}$ range. For this section the minimum loss was 0.2 dB/m and the maximum was 0.3 dB/m . Although the minimum loss found for the $2.9\text{ mm} \times 1.45\text{ mm}$ guide was 0.04 dB/m at $9\ \mu\text{m}$ thickness of the Teflon layer, the thickness range $12\ \mu\text{m}$ to $25\ \mu\text{m}$ might be more interesting as it will provide manufacturing flexibility for the Teflon thickness. Increasing the dimension further could produce a larger stable section, however then the loss value in the stable region would be slightly higher. This can be explained from Fig. 5.29. In the figure, it can be observed that as the waveguide dimension is increasing, the loss values within the stable mid-valley region show an increasing pattern, though the rate of increase is very low and the loss values are gradually going to a saturation. As the window of the low loss region remains similar and the maximum loss for the stable section saturates and stabilises around 0.3 dB/m we have shown our simulations up to $2.9\text{ mm} \times 1.45\text{ mm}$.

The curves also show a stable and extremely low loss behaviour across the dimensions. For example, for the Teflon thickness of $20\ \mu\text{m}$ the losses for the guides ranging from $2.3\text{ mm} \times 1.15\text{ mm}$ to $2.9\text{ mm} \times 1.45\text{ mm}$, vary from 0.1 dB/m to 0.3 dB/m only. This phenomenon is true for the whole of the stable range mentioned in the previous paragraph. This should also provide some manufacturing flexibility for the dimension of the guide.

Although the stable section for the Teflon thickness becomes shorter with decreasing dimension and disappears below a dimension of $2.2\text{ mm} \times 1.1\text{ mm}$,

the guide $2.5 \text{ mm} \times 1.25 \text{ mm}$ chosen for study is within the flexible range. Therefore, it should produce stable loss characteristics even with some manufacturing shortcomings.

5.5 Dispersion Characteristics of the Rectangular Guides

Modal dispersion of a guide is a very important parameter to study information propagation through it. This is because information always has a bandwidth. In a dispersive guide the shape of the information signal changes with propagation distance. On the other hand a low dispersion or dispersion free guide allows the unmodified shape of the pulse for a longer length. To consider a guide for information transmission, the dispersion properties of the guide should be known alongside its loss characteristics. The loss property determines the length of propagation of a signal for a given input power. The dispersion property measures the quality of the signal after a specific distance. If the signal gets weaker this can be compensated by using an amplifier, but if the signal gets distorted by dispersion, it cannot be mitigated.

To calculate the dispersion characteristics of the structure, the modal solution of the H_{12}^x mode has been considered. The real part of the effective index of the structure for a specific mode and wavelength has been taken into consideration. If the effective indices are calculated for a specific range of wavelengths $[\lambda_1, \lambda_2]$ with the fixed wavelength division $\Delta\lambda$, the following equation can be used to calculate the dispersion relation of the structure.

$$D = -\frac{\lambda}{c} \frac{d^2 n}{d\lambda^2} \quad (5.2)$$

Here, c is the speed of light, λ is the wavelength and n is the real part of effective index.

To study the dispersion property of the guide, both the rectangular guides analysed so far of dimension $1.0 \text{ mm} \times 0.6 \text{ mm}$ and $2.5 \text{ mm} \times 1.25 \text{ mm}$ have been considered. The frequency range for the dispersion characteristics were taken from 2.0 THz to 3.0 THz.

The thicknesses of the Teflon layers were set to minimum loss thickness for each guide. The frequency range chosen for the study was 2.0 THz–3.0 THz. The complex refractive indices of the metal were calculated using the Drude model and the dielectric properties are taken from [237, 202]. The dispersion calculation was carried out by using the formula described in Eq. 5.2 and the results are presented in Fig. 5.30.

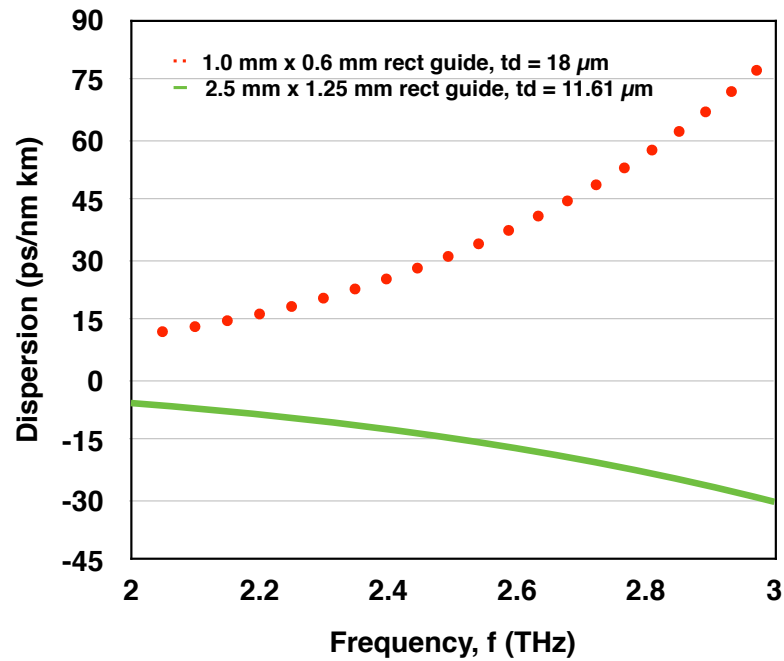


FIGURE 5.30: Dispersion curves for 1.0 mm \times 0.6 mm rectangular guide (red dotted line) and the 2.5 mm \times 1.25 mm rectangular guide (green solid line).

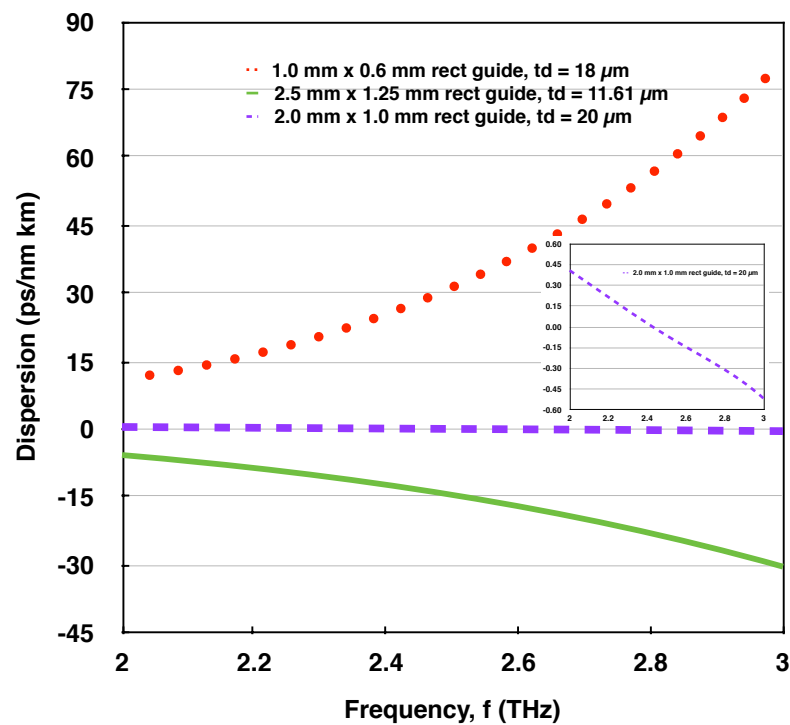


FIGURE 5.31: Dispersion curves for 1.0 mm \times 0.6 mm rectangular guide (red dotted line), the 2.5 mm \times 1.25 mm rectangular guide (green solid line) and the 2.0 mm \times 1.0 mm rectangular guide (purple dashed line). The inset shows a closer look of the dispersion characteristics of the 2.0 mm \times 1.0 mm rectangular guide

The dispersion for the $1.0\text{ mm}\times 0.6\text{ mm}$ rectangular guide is the highest between the two guides considered in Fig. 5.30. The dispersion remains positive in the range considered here and increases non-linearly when frequency is increased. The rate of increase is also highest between the two guides. The dispersion for the $2.5\text{ mm}\times 1.25\text{ mm}$ rectangular guide comes next. But this guide shows negative dispersion and the value of dispersion becomes more negative in a non-linear function with the increase of frequency.

It can be observed that the dispersion of the $1.0\text{ mm}\times 0.6\text{ mm}$ is completely in the positive side and $2.5\text{ mm}\times 1.25\text{ mm}$ is completely in the negative side. The major difference between these two guides is the dimension of the guide. Therefore, it can be assumed that there could be a dimension in between the above mentioned two where the dispersion will be less than both of them.

To check the hypothesis the dispersion characteristics of $2.0\text{ mm}\times 1.0\text{ mm}$ guide was considered. Figure 5.31 plots the dispersion characteristics of the $2.0\text{ mm}\times 1.0\text{ mm}$ rectangular guide with the earlier presented guides in Fig. 5.30. It can be noticed that the dispersion characteristic for the $2.0\text{ mm}\times 1.0\text{ mm}$ guide almost overlaps the x-axis of the figure. Therefore, a close look at the characteristics of the $2.0\text{ mm}\times 1.0\text{ mm}$ guide is needed. The inset of Fig. 5.31 shows a closer view of dispersion of the $2.0\text{ mm}\times 1.0\text{ mm}$ guide.

The dispersion of the guide starts with a very low positive dispersion value at 2.0 THz frequency and the value reduces as the frequency is increased. It crosses zero dispersion at 2.43 THz and continue to reduce in value and becomes negative. As can be seen in the Fig. 5.31 inset the dispersion is almost a linear function of frequency within our band of interest, 2.0 THz to 3.0 THz.

5.5.1 Effect of Frequency on Loss

To see the full picture for a propagating signal through a guide requires study of the loss at the modulating frequency and the dispersion relation. It also requires the study of loss over the frequency band. This is because, the loss at the modulating frequency does not show the loss property for a signal which must have a bandwidth. To see the effect of frequency on loss of the optimal $2.5\text{ mm}\times 1.25\text{ mm}$ guide, loss values for the frequency band 2.0 THz to 3.0 THz has been calculated.

Figure 5.32 shows the loss characteristics of the guide. As can be seen the guide has its minimum loss at 2.48 THz and the loss increases with both the increase or decrease of the frequency. The increase in loss is almost linear beyond

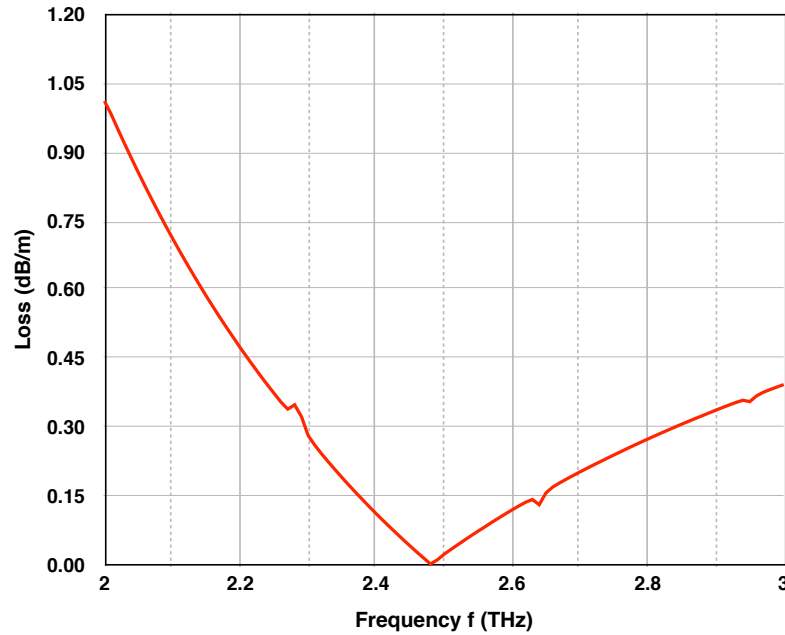
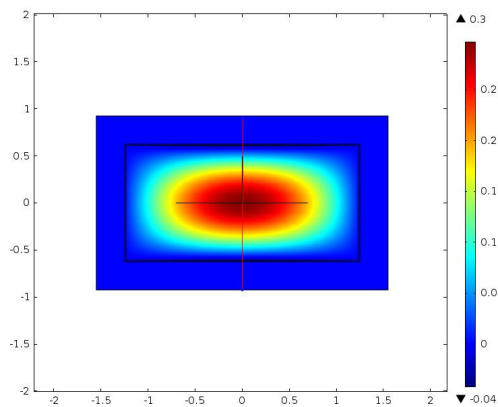


FIGURE 5.32: Loss of the optimal 2.5 mm \times 1.25 mm guide for the frequency band 2.0 THz to 3.0 THz

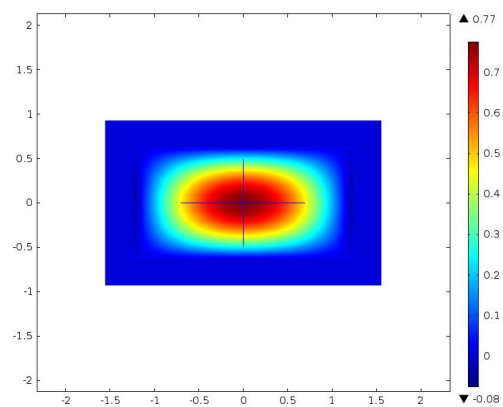
the minimum loss frequency but shows a non-linear pattern before 2.48 THz. Some small local peaks were detected.

Further investigation was performed on the left most local peak in Fig. 5.32. To find the cause of the sudden rise in the loss profile, the effective indices and losses of the H_{21}^y mode were calculated over the same frequency range. Fig. 5.33 shows the contour profile of the H_{12}^x and the H_{21}^y modes along with their vertical and horizontal cross-sections.. Although in the contour profile, the distribution of the H_{21}^y mode looks similar to that of the H_{12}^x mode, the cross sectional line plots show that unlike the H_{12}^x mode the plasmonic interaction with the metal cladding for the H_{21}^y mode happens in the horizontal x -direction.

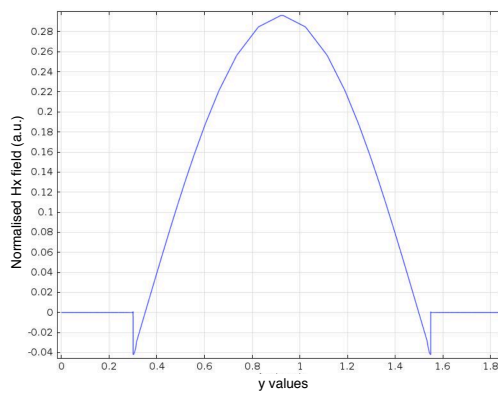
Figure. 5.34 and Fig. 5.35 show the effective indices and the loss curves of both the modes. It can clearly be observed that as the effective index curves cross each other at $f = 2.28$ THz, the loss curves of both the modes also experience a sudden change around that frequency. This sudden change in loss could be due to the degeneration of the H_{12}^x and H_{21}^y modes. Due to the degeneration, the two modes get mixed up and the loss values change rapidly. Similar to the leftmost local peak, the other local peaks could also be caused by degeneration of the H_{12}^x mode with other modes.



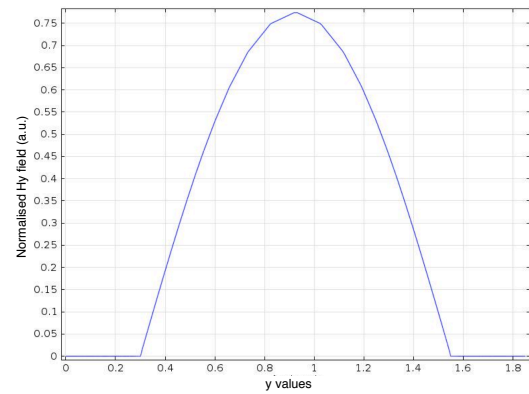
(a) Contour field profile of the H_{12}^x mode at $f = 2.50$ THz



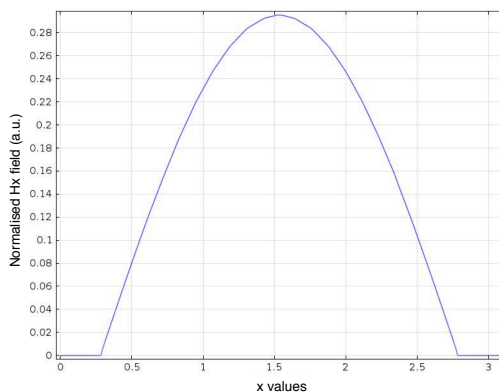
(b) Contour field profile of the H_{21}^y mode at $f = 2.50$ THz



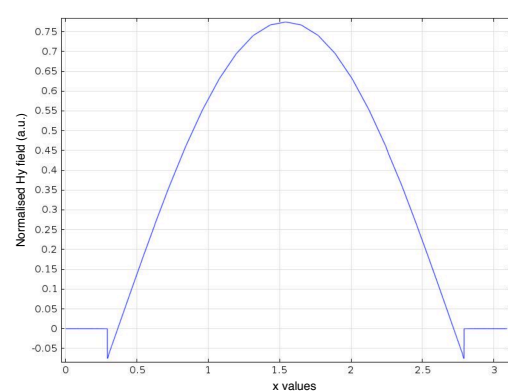
(c) Vertical cross-section of the H_x field profile of the H_{12}^x mode at $f = 2.50$ THz



(d) Vertical cross-section of the H_y field profile of the H_{21}^y mode at $f = 2.50$ THz



(e) Horizontal cross-section of the H_x field profile of the H_{12}^x mode at $f = 2.50$ THz



(f) Horizontal cross-section of the H_y field profile of the H_{21}^y mode at $f = 2.50$ THz

FIGURE 5.33: Contour field profile along with the vertical and horizontal cross-sections of the H_{12}^x and the H_{21}^y modes

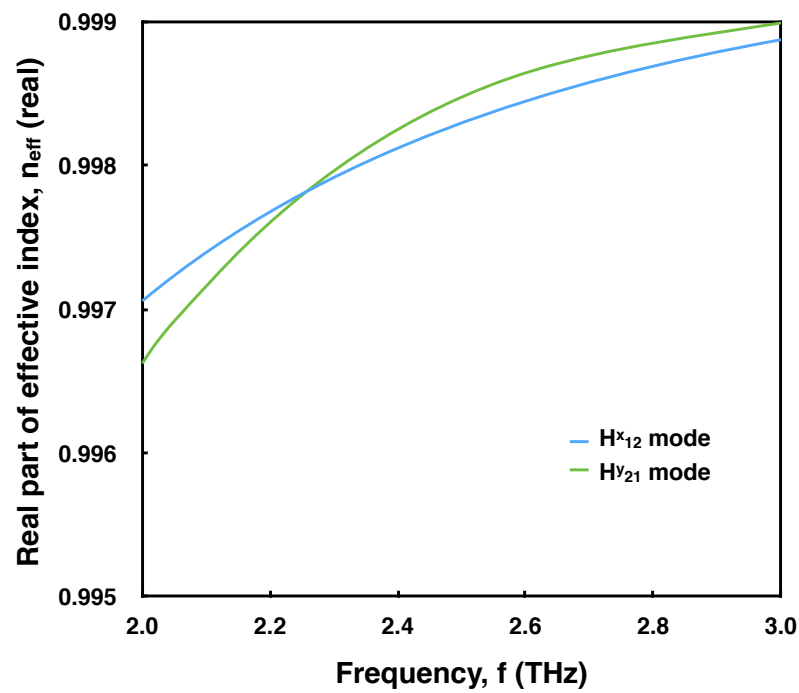


FIGURE 5.34: Real part of effective indices of the H_{12}^x and the H_{21}^y modes of the optimal $2.5 \text{ mm} \times 1.25 \text{ mm}$ guide for the frequency band 2.0 THz to 3.0 THz

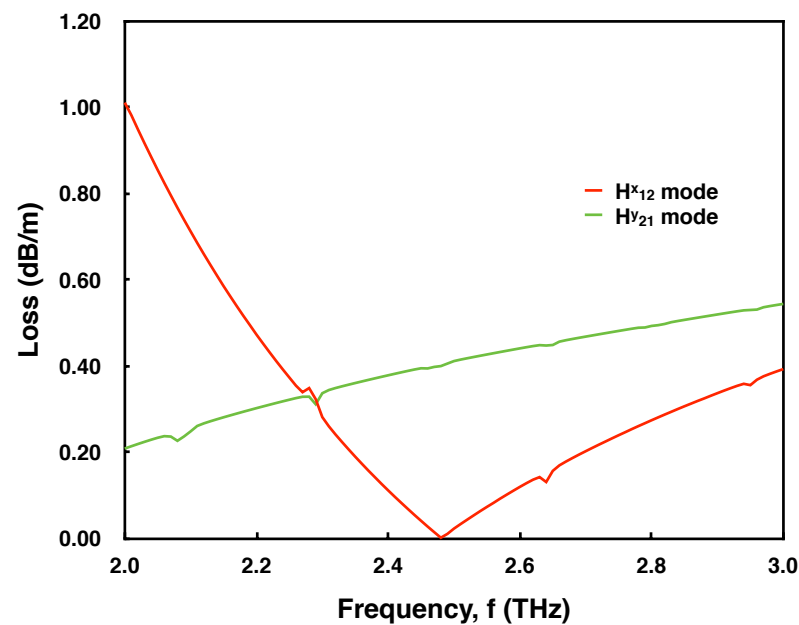


FIGURE 5.35: Loss comparison of the H_{12}^x and the H_{21}^y modes of the optimal $2.5 \text{ mm} \times 1.25 \text{ mm}$ guide for the frequency band 2.0 THz to 3.0 THz

5.6 Selective coupling to the H_{12}^x mode

When an input beam is coupled to such a waveguide, it is predominantly the H_{12}^x mode which would be excited and guided, and the first mode H_{10}^x of smaller magnitude (which may also be excited) would dissipate very quickly due to its higher modal loss. Therefore the mode selection will happen automatically due to the difference in losses of different modes. As the H_{12}^x mode has very low loss, it will sustain in the guide for longer distances.

Evanescent coupling technique from a dielectric waveguide [247, 98, 248, 249] could be used to excite the metal dielectric interface having the SPPs. Either a conventional tapered waveguide [247, 98] or, a dielectric waveguide attached to the metal cladding of the plasmonic waveguide can be used [248, 249]. In both the techniques, the evanescent tail outside the dielectric waveguide could be coupled with the metal dielectric interface to excite the surface plasmon on both sides of the hollow core guide. As the coupled wave continues to propagate through the guide, the H_{12}^x mode will eventually be selected because the loss of the mode is far lower than all the other modes.

5.7 Summary

In this chapter, the characterization and optimization of a dielectric coated hollow core rectangular waveguide is presented. The goal was to find an optimized condition of the guide so that it supports low-loss propagation at THz frequencies and also which will be small in size and easy to fabricate. Several surface plasmonic modes have been studied in the waveguide under two main conditions: with and without dielectric coating inside the metal cladding. To obtain strong field confinement and low loss propagation at THz frequencies, several parameters of the structure were varied. The analysis carried out has revealed that introducing the dielectric coating minimizes the loss of the H_{12}^x mode of the guide significantly and transforms the mode shape into one that is Gaussian like, which should be easier to couple to transmitters and receivers. It has also been revealed that, by choosing appropriate parameters for dimension, the guide shows very low loss with a relatively small guide size.

Chapter 6

Discussion and Future Works

A general evaluation of the work carried out during the course of this study, in terms of the methodology used and the validity of the results presented, is attempted in the following discussion, which eventually leads to the conclusion that the objectives set out at the beginning of this research were essentially achieved.

The primary objective of this research work has been to design and characterise waveguides using surface plasmon polaritons. The objectives outlined at the beginning of the study have been successfully achieved with a detailed analysis of results during the entire work. In this work, a numerical method based on the finite element formulation has been extensively used to accurately characterise various types of plasmonic waveguide in THz and optical frequencies and study their propagation properties.

Following the fundamental studies of light-metal interaction in the early days (late 1950s to late 1960s), SPs have been extensively explored in thin film characterization, chemical sensing and biodetection since late 1970s. In recent years interest in SPs has expanded from sensing technology to a wide range of fields, including subwavelength optics, nanophotonics, information storage, nanolithography, light generation and engineering left-handed metamaterials at optical wavelengths, etc. The reformed interest was stimulated by the recent progress in electromagnetic simulations, micro/nanofabrication and characterization techniques, which provide the necessary tools to revive and exploit remarkable properties of SPs in the domains of both fundamental physics and application development.

Waveguides used in many THz systems incorporate materials which experience high intrinsic losses at longer wavelengths due to free carrier effects. A suitable waveguide that aims to reduce these losses is often the key challenge that needs to be addressed before designing any THz systems. This issue is even more critical in plasmonic waveguides as these are utilised to miniaturise

the overall device sizes. Most plasmonic waveguides consist of either noble metals or doped semiconductors, both of which exhibit a staggering amount of losses at THz frequencies. Hence designing a low loss waveguide is one of the most critical steps in the fabrication process of plasmonic waveguides. Computer aided simulation plays a key role in waveguide designs in many optoelectronic systems and over the years several available techniques have been proposed. The finite element method has evolved as the most powerful, versatile and accurate method in analysing propagation characteristics of waveguides. This method can handle a wide variety of waveguide problems with arbitrary cross section, complex and arbitrary refractive index profile, anisotropy and nonlinearity, thus enabling the development of efficient and flexible computer programs. In this work, the emphasis has been on the usage of a customised finite element based technique to handle complex refractive index of materials used in THz and optical plasmonic waveguides.

The chapters presented in this thesis have dealt with the basic principles and theory of the numerical methods, and the characteristic simulations of various quantum cascade laser waveguides by employing full vectorial H-field finite element method.

Chapter. 2 was devoted to the mathematical background for the finite element method. The full vectorial H-field based variational formulation has been implemented in the numerical tool utilised in the work carried out here. In this formulation, the magnetic field vector \mathbf{H} is naturally continuous across the waveguide interfaces and also the associated natural boundary condition is that of an electric wall, which is very convenient to implement in many practical waveguide problems. Key primary concepts such as discretisation of the domain, the shape functions and the element matrices were explained in detail in this chapter. Since the shape functions provide only an approximate representation of the true fields, it is necessary to increase the number of elements or nodal points to reduce the resulting error. In doing so, the numerical model becomes a closer representation of the real physical problem. However, with this H-field formulation, the appearance of the spurious (non-physical) modes along with the physical modes is a key problem. The penalty function method was incorporated to eliminate these spurious modes by imposing the condition ($\nabla \cdot \mathbf{H} = 0$). The finite element method has been proven to be a very powerful method of finding the field profiles and propagation characteristics of the guided modes of most waveguides used across the broader electromagnetic spectrum.

Analysing the dynamics of the mode formation is a key step that must be carried out before designing waveguides for any systems. Such an analysis aimed at revealing the process of mode formation in plasmonic waveguides was shown in Chapter. 3. The chapter begins with an insight on the development of surface plasmons at single interfaces. Analysis of the physics underpinning the operation of plasmonic waveguides are presented which laid the foundation for the discussion on two basic type of planar plasmonic waveguides *i.e* IMI and MIM. The coupling between the plasmon modes on the single interfaces results in formation of a supermode. The thickness of the core layer was adjusted for the IMI and MIM structures to tailor the phase velocities of the different plasmon modes supported by the interfaces of these waveguides. The simulation results revealing the propagation and loss characteristics of these waveguides formed the basis of this chapter. The knowledge gained from the determination of the fundamental properties of the 3-layer plasmonic waveguide structures, which are the basic elements of the several integrated optics applications, enabled the extension of the analysis to optical waveguides with more complex geometry, whose solutions are of significant practical interest in the optoelectronics industry. The rigorous modal analysis of a 6-layer planar structure, where surface plasmon modes and attenuation characteristics take place due to the interaction of metal and dielectric elements, was carried out by using the full vectorial finite element method. The variation of certain parameters of the structure were carried out to examine the propagation and loss characteristics. Among the list of objectives outlined in the first chapter, the second objective was fulfilled through the analysis and discussion of the simulation results presented in this chapter.

In Chapter 4 a rigorous characterisation of the hybrid plasmonic waveguide was presented using a full- vectorial H field based FEM formulation. The HPWG offers sub-wavelength confinement in the low index region, offers a better compromise between confinement and loss compared to pure plasmonic waveguides, and is compatible with SOI technology. In addition, the propagation of the TE and TM modes can be independently controlled which opens up the possibility of implementing compact devices for manipulating polarization. In this chapter, we have analysed the properties of the HPWG by observing the confinement and propagation loss of the HPWG. The HPWG combines both dielectric and plasmonic guiding schemes, and it provides good confinement with moderate propagation loss. The HPWG supports both the TE and TM modes which can be utilized for many applications.

In Chapter 5 a rigorous finite element approach based on a full-vectorial \mathbf{H} -field formulation has been used to study the characteristics of a hollow core Teflon coated rectangular plasmonic waveguide at THz wavelengths. The goal of the work was to find the mode with the minimum loss and the optimal configuration of the waveguide for that mode. At the beginning of the chapter, detailed studies have been performed by varying the height and width of the waveguide and the thickness of the metal layer for several different modes. Then it was shown that introducing the Teflon coating causes significant change in the performance of the guide. The thickness of the Teflon layer and that of the metal cladding were varied to optimize the waveguide. By performing a rigorous modal analysis, it was revealed that the loss can be minimized by selecting a suitable low-loss dielectric coating, a metal and its thickness for a given dimension of the THz waveguide. After the design optimization, the H_{12}^x mode was found to have the lowest loss amongst all the modes considered here. Moreover, in the optimum configuration, this mode resembles a near Gaussian shape in both the transverse directions and using this would facilitate better coupling to the input and output sections. Different metals were also used to design the guide and determine the minimum loss conditions. A study using Polystyrene as the coating dielectric was also performed to compare the loss characteristics with those of Teflon. Finally, it was shown in this chapter that by altering the dimension *i.e.* the width and height of the dielectric coated metal clad hollow core guide, it is possible to substantially minimize the loss of the guide to a virtually negligible value. Analysis of the dispersion characteristics with the dimension has also been presented. It showed interesting dispersion characteristics as the dispersion of the guide can be controlled from highly dispersive to near zero dispersion just by varying the dimension.

Therefore, the guide is manufacturing friendly with consistent loss. Combination of low and consistent loss and controllable dispersion makes the guide eligible for many interesting devices and guide designs which includes compact interchip communication, sensing, dispersion compensators etc.

6.1 Proposals for future work

In chapter 3, the full vectorial finite element method was used to study and analyse properties of the six layer planar contra-directional coupler. It revealed the loss characteristics of different modes and also showed a path to optimise the loss and coupling length of the structure. Although the loss and the coupling length were optimised, the dispersion characteristics of the structure need to be analysed in future.

The effect of finite length and finite width of the device was not considered in this study. This will be crucial for integrated circuits as there will be limited space around the device.

An input output characteristics (S-parameter) analysis could be performed on a minimum length (based on coupling length) to see the reverse flow of the power for a frequency range. Further investigation can be performed by changing the metal and the dielectrics involved.

In chapter 4, the hybrid plasmonic waveguide at optical frequency was analysed. A further study could be performed using these results to observe the performances of TE/TM pass polarizers, biosensors and a polarization independent hybrid plasmonic coupler. We can continue further research on the integrated optical circuits, and investigate the possibility of finding an efficient way to integrate optical circuits with electronic circuits.

In chapter 5, the dielectric coated waveguide at THz frequency was analysed. The core of the guide is filled with air. A study of the guide as a gas sensor can be evaluated in future.

As the core is hollow, it can be filled with liquid and could be used as a liquid or bio-sensor. Therefore, a study could be performed to design a liquid/bio-sensor with this structure.

It has been discovered that the dispersion characteristics could be controlled by changing the dimension of the structure. Hence multiple dispersion compensation devices can be designed using the dielectric coated rectangular guide at THz frequency range.

Appendix A

Evaluation of Element Matrices

The elements of the matrices $[\mathbf{A}]_e$ and $[\mathbf{B}]_e$ in equation (2.58) can be evaluated by expressing the derivatives of the shape function vectors in terms of the shape function coefficients, as determined in equations (A.1) and (2.58), and by performing the integration of the shape functions

$$[\mathbf{A}]\{\mathbf{H}\} - \omega^2[\mathbf{B}]\{\mathbf{H}\} = 0 \quad (\text{A.1})$$

The matrices $[\mathbf{A}]$ and $[\mathbf{B}]$ are expressed as:

$$[\mathbf{A}] = \sum_{e=1}^n [\mathbf{A}]_e = \sum_{e=1}^n \int_{\Delta} \frac{1}{\hat{c}} [Q]^* [Q] d\Omega \quad (\text{A.2})$$

and

$$[\mathbf{B}] = \sum_{e=1}^n [\mathbf{B}]_e = \sum_{e=1}^n \hat{\mu} \int_{\Delta} [N]^T [N] d\Omega \quad (\text{A.3})$$

In equation A.2, the matrix $[\mathbf{A}]$ has matrices Q and Q^* which can be written as follows:

$$[Q] = \begin{bmatrix} [0] & \frac{-\partial[N]}{\partial z} & \frac{\partial[N]}{\partial y} \\ \frac{\partial[N]}{\partial z} & [0] & \frac{-\partial[N]}{\partial x} \\ \frac{-\partial[N]}{\partial y} & \frac{\partial[N]}{\partial x} & [0] \end{bmatrix} \quad (\text{A.4})$$

Replacing $\frac{\partial}{\partial z}$ with $-j\beta$, the following $[Q]$ matrix is obtained:

$$[Q] = \begin{bmatrix} [0] & j\beta[N] & \frac{\partial[N]}{\partial y} \\ -j\beta[N] & [0] & \frac{-\partial[N]}{\partial x} \\ \frac{-\partial[N]}{\partial y} & \frac{\partial[N]}{\partial x} & [0] \end{bmatrix} \quad (\text{A.5})$$

Consequently, the Q^* matrix is defined as:

$$[Q]^* = \begin{bmatrix} [0] & j\beta[N]^T & \frac{\partial[N]^T}{\partial y} \\ -j\beta[N]^T & [0] & \frac{-\partial[N]^T}{\partial x} \\ \frac{-\partial[N]^T}{\partial y} & \frac{\partial[N]^T}{\partial x} & [0] \end{bmatrix} \quad (\text{A.6})$$

where $[N]$ is defined as

$$[N] = \begin{bmatrix} N_1 & N_2 & N_3 \end{bmatrix} \quad (\text{A.7})$$

$$\therefore j\beta[N] = \begin{bmatrix} j\beta N_1 & j\beta N_2 & j\beta N_3 \end{bmatrix} \quad (\text{A.8})$$

This results in the formation of the $[A]_e$ matrix as:

$$[\mathbf{A}]_e = \frac{1}{\hat{\epsilon}} \int_{\Delta} [Q]^* [Q] d\Omega \quad (\text{A.9})$$

$$= \frac{1}{\hat{\epsilon}} \int_{\Delta} \begin{bmatrix} [0] & j\beta[N]^T & \frac{\partial[N]^T}{\partial y} \\ -j\beta[N]^T & [0] & \frac{-\partial[N]^T}{\partial x} \\ \frac{-\partial[N]^T}{\partial y} & \frac{\partial[N]^T}{\partial x} & [0] \end{bmatrix} \times \begin{bmatrix} [0] & j\beta[N] & \frac{\partial[N]}{\partial y} \\ -j\beta[N] & [0] & \frac{-\partial[N]}{\partial x} \\ \frac{-\partial[N]}{\partial y} & \frac{\partial[N]}{\partial x} & [0] \end{bmatrix} d\Omega \quad (\text{A.10})$$

$$= \frac{1}{\hat{\epsilon}} \int_{\Delta} \begin{bmatrix} \beta^2 [N]^T [N] + \frac{\partial [N]^T}{\partial y} \frac{\partial [N]}{\partial y} & -\frac{\partial [N]^T}{\partial y} \frac{\partial [N]}{\partial x} & -j\beta [N]^T \frac{\partial [N]}{\partial x} \\ -\frac{\partial [N]^T}{\partial x} \frac{\partial [N]}{\partial y} & \beta^2 [N]^T [N] + \frac{\partial [N]^T}{\partial x} & -j\beta [N]^T \frac{\partial [N]}{\partial y} \\ j\beta \frac{\partial [N]}{\partial x} [N] & j\beta \frac{\partial [N]^T}{\partial y} [N] & \frac{\partial [N]^T}{\partial y} \frac{\partial [N]}{\partial y} + \frac{\partial [N]^T}{\partial x} \frac{\partial [N]}{\partial x} \end{bmatrix} d\Omega \quad (\text{A.11})$$

The $[B]_e$ element matrix of equation A.3 can be defined as:

$$[B]_e = \mu \int_{\Delta} [\mathbf{N}]^T [\mathbf{N}] d\Omega \quad (\text{A.12})$$

where the matrix $[\mathbf{N}]$ is defined as:

$$[\mathbf{N}] = \begin{bmatrix} N_1 & N_2 & N_3 & 0 & 0 & 0 & 0 & 0 & 0 \\ 0 & 0 & 0 & N_1 & N_2 & N_3 & 0 & 0 & 0 \\ 0 & 0 & 0 & 0 & 0 & 0 & N_1 & N_2 & N_3 \end{bmatrix} \quad (\text{A.13})$$

which can also be written as

$$[\mathbf{N}] = \begin{bmatrix} [N] & [0] & [0] \\ [0] & [N] & [0] \\ [0] & [0] & [N] \end{bmatrix} \quad (\text{A.14})$$

where $[N]$ is a row vector defined as $[N] = [N_1 \ N_2 \ N_3]$. The transpose of $[N]$ can be defined as $[N]^T$ which can be represented as:

$$[N]^T = \begin{bmatrix} N_1 & 0 & 0 \\ N_2 & 0 & 0 \\ N_3 & 0 & 0 \\ 0 & N_1 & 0 \\ 0 & N_2 & 0 \\ 0 & N_3 & 0 \\ 0 & 0 & N_1 \\ 0 & 0 & N_2 \\ 0 & 0 & N_3 \end{bmatrix} \quad (\text{A.15})$$

$$= \begin{bmatrix} [N]^T & [0]^T & [0]^T \\ [0]^T & [N]^T & [0]^T \\ [0]^T & [0]^T & [N]^T \end{bmatrix}$$

Hence the $[B]_e$ matrix in equation A.12 can be written as:

$$[B]_e = \mu \int_{\Delta} \begin{bmatrix} [N]^T & [0]^T & [0]^T \\ [0]^T & [N]^T & [0]^T \\ [0]^T & [0]^T & [N]^T \end{bmatrix} \times \begin{bmatrix} [N] & [0] & [0] \\ [0] & [N] & [0] \\ [0] & [0] & [N] \end{bmatrix} d\Omega \quad (\text{A.16})$$

$$= \mu \int_{\Delta} \begin{bmatrix} [N]^T[N] & [0]^T[0] & [0]^T[0] \\ [0]^T[0] & [N]^T[N] & [0]^T[0] \\ [0]^T[0] & [0]^T[0] & [N]^T[N] \end{bmatrix} d\Omega$$

Now, integrating the individual shape functions inside the matrix will result:

$$\begin{aligned}
 \int_{\Delta} [N]^T [N] d\Omega &= \int_{\Delta} \begin{bmatrix} N_1 \\ N_2 \\ N_3 \end{bmatrix} \begin{bmatrix} N_1 & N_2 & N_3 \end{bmatrix} d\Omega \\
 &= \int_{\Delta} \begin{bmatrix} (N_1)^2 & N_1 N_2 & N_1 N_3 \\ N_2 N_1 & (N_2)^2 & N_2 N_3 \\ N_3 N_1 & N_3 N_2 & (N_3)^2 \end{bmatrix} d\Omega \tag{A.17} \\
 &= \begin{bmatrix} \int_{\Delta} (N_1)^2 d\Omega & \int_{\Delta} N_1 N_2 d\Omega & \int_{\Delta} N_1 N_3 d\Omega \\ \int_{\Delta} N_2 N_1 d\Omega & \int_{\Delta} (N_2)^2 d\Omega & \int_{\Delta} N_2 N_3 d\Omega \\ \int_{\Delta} N_3 N_1 d\Omega & \int_{\Delta} N_3 N_2 d\Omega & \int_{\Delta} (N_3)^2 d\Omega \end{bmatrix}
 \end{aligned}$$

For a triangular element, the shape functions can be integrated using the relation:

$$\int_{\Delta} N_1^l N_2^m N_3^n d\Omega = \frac{l! m! n!}{(l+m+n+2)!} 2A_e \tag{A.18}$$

Hence the integral elements in the matrix relation shown in equation A.17 can be expressed as:

$$\begin{aligned}
\int_{\Delta} N_1^2 d\Omega &= \frac{2! 0! 0!}{4!} \cdot 2A_e = \frac{A_e}{6} = \int_{\Delta} N_1^2 d\Omega = \int_{\Delta} N_1^2 d\Omega \\
\int_{\Delta} N_1 N_2 d\Omega &= \frac{1! 1! 0!}{4!} \cdot 2A_e = \frac{A_e}{12} = \int_{\Delta} N_2 N_1 d\Omega \\
\int_{\Delta} N_1 N_3 d\Omega &= \frac{1! 0! 1!}{4!} \cdot 2A_e = \frac{A_e}{12} = \int_{\Delta} N_3 N_1 d\Omega \\
\int_{\Delta} N_2 N_3 d\Omega &= \frac{0! 1! 1!}{4!} \cdot 2A_e = \frac{A_e}{12} = \int_{\Delta} N_2 N_3 d\Omega
\end{aligned} \tag{A.19}$$

Now, if we consider a matrix $[K]$, where $[K]$ can be defined in terms of the shape function integrals as:

$$[K] = \mu \int_{\Delta} [N]^T [N] d\Omega \tag{A.20}$$

Thus using the shape function definition in equation A.19 the above relation for $[K]$ can be expressed as:

$$[K] = \begin{bmatrix} \mu \frac{A_e}{6} & \mu \frac{A_e}{12} & \mu \frac{A_e}{12} \\ \mu \frac{A_e}{12} & \mu \frac{A_e}{6} & \mu \frac{A_e}{12} \\ \mu \frac{A_e}{12} & \mu \frac{A_e}{12} & \mu \frac{A_e}{6} \end{bmatrix} \tag{A.21}$$

Therefore the $[B]$ matrix in equation A.16 can be represented in terms of the $[K]$ matrix as:

$$[B]_e = \begin{bmatrix} [K] & [0]^T [0] & [0]^T [0] \\ [0]^T [0] & [K] & [0]^T [0] \\ [0]^T [0] & [0]^T [0] & [K] \end{bmatrix} \tag{A.22}$$

The integral elements of the $[A]_e$ matrix in equation A.11 can be further expressed as:

$$\int_{\Delta} \beta^2 [N]^T [N] d\Omega = \begin{bmatrix} \beta^2 \frac{A_e}{6} & \beta^2 \frac{A_e}{12} & \beta^2 \frac{A_e}{12} \\ \beta^2 \frac{A_e}{12} & \beta^2 \frac{A_e}{6} & \beta^2 \frac{A_e}{12} \\ \beta^2 \frac{A_e}{12} & \beta^2 \frac{A_e}{12} & \beta^2 \frac{A_e}{6} \end{bmatrix} \quad (\text{A.23})$$

Now

$$\int_{\Delta} \frac{\partial [N]^T}{\partial y} \frac{\partial [N]}{\partial y} d\Omega = \int_{\Delta} \begin{bmatrix} \frac{\partial N_1}{\partial y} \\ \frac{\partial N_2}{\partial y} \\ \frac{\partial N_3}{\partial y} \end{bmatrix} \times \begin{bmatrix} \frac{\partial N_1}{\partial y} & \frac{\partial N_2}{\partial y} & \frac{\partial N_3}{\partial y} \end{bmatrix} d\Omega \quad (\text{A.24})$$

$$= \int_{\Delta} \begin{bmatrix} \left(\frac{\partial N_1}{\partial y} \right)^2 & \frac{\partial N_1}{\partial y} \frac{\partial N_2}{\partial y} & \frac{\partial N_1}{\partial y} \frac{\partial N_3}{\partial y} \\ \frac{\partial N_2}{\partial y} \frac{\partial N_1}{\partial y} & \left(\frac{\partial N_2}{\partial y} \right)^2 & \frac{\partial N_2}{\partial y} \frac{\partial N_3}{\partial y} \\ \frac{\partial N_3}{\partial y} \frac{\partial N_1}{\partial y} & \frac{\partial N_3}{\partial y} \frac{\partial N_2}{\partial y} & \left(\frac{\partial N_3}{\partial y} \right)^2 \end{bmatrix} d\Omega \quad (\text{A.25})$$

The elements of the matrix in equation A.25 can be expressed after integration as:

$$\begin{aligned}
 \int_{\Delta} \left(\frac{\partial N_1}{\partial y} \right)^2 d\Omega &= \int_{\Delta} c_1^2 d\Omega = c_1^2 A_e \\
 \int_{\Delta} \frac{\partial N_1}{\partial y} \frac{\partial N_2}{\partial y} d\Omega &= \int_{\Delta} c_1 c_2 d\Omega = c_1 c_2 A_e \\
 \int_{\Delta} \frac{\partial N_1}{\partial y} \frac{\partial N_3}{\partial y} d\Omega &= \int_{\Delta} c_1 c_3 d\Omega = c_1 c_3 A_e \\
 \\
 \int_{\Delta} \frac{\partial N_2}{\partial y} \frac{\partial N_1}{\partial y} d\Omega &= \int_{\Delta} c_2 c_1 d\Omega = c_2 c_1 A_e \\
 \int_{\Delta} \left(\frac{\partial N_2}{\partial y} \right)^2 d\Omega &= \int_{\Delta} c_2^2 d\Omega = c_2^2 A_e \\
 \int_{\Delta} \frac{\partial N_2}{\partial y} \frac{\partial N_3}{\partial y} d\Omega &= \int_{\Delta} c_2 c_3 d\Omega = c_2 c_3 A_e \\
 \\
 \int_{\Delta} \frac{\partial N_3}{\partial y} \frac{\partial N_1}{\partial y} d\Omega &= \int_{\Delta} c_3 c_1 d\Omega = c_3 c_1 A_e \\
 \int_{\Delta} \frac{\partial N_3}{\partial y} \frac{\partial N_2}{\partial y} d\Omega &= \int_{\Delta} c_3 c_2 d\Omega = c_3 c_2 A_e \\
 \int_{\Delta} \left(\frac{\partial N_3}{\partial y} \right)^2 d\Omega &= \int_{\Delta} c_3^2 d\Omega = c_3^2 A_e
 \end{aligned} \tag{A.26}$$

Hence the matrix in equation A.25 can be re-written as:

$$\int_{\Delta} \frac{\partial [N]^T}{\partial y} \frac{\partial [N]}{\partial y} d\Omega = \int_{\Delta} \begin{bmatrix} c_1^2 A_e & c_1 c_2 A_e & c_1 c_3 A_e \\ c_2 c_1 A_e & c_2^2 A_e & c_2 c_3 A_e \\ c_3 c_1 A_e & c_3 c_2 A_e & c_3^2 A_e \end{bmatrix} d\Omega \tag{A.27}$$

Similarly, the $\int_{\Delta} -\frac{\partial [N]^T}{\partial y} \frac{\partial [N]}{\partial x} d\Omega$ term in equation A.20 can be expressed as:

$$\int_{\Delta} \frac{\partial [N]^T}{\partial y} \frac{\partial [N]}{\partial x} d\Omega = \int_{\Delta} \begin{bmatrix} -\frac{\partial N_1}{\partial y} \\ -\frac{\partial N_2}{\partial y} \\ -\frac{\partial N_3}{\partial y} \end{bmatrix} \times \begin{bmatrix} -\frac{\partial N_1}{\partial x} & -\frac{\partial N_2}{\partial x} & -\frac{\partial N_3}{\partial x} \end{bmatrix} d\Omega \tag{A.28}$$

This results in the formation of the following matrix:

$$\int_{\Delta} \frac{\partial[N]^T}{\partial y} \frac{\partial[N]}{\partial x} d\Omega = \int_{\Delta} \begin{bmatrix} -\frac{\partial N_1}{\partial y} \frac{\partial N_1}{\partial x} & -\frac{\partial N_1}{\partial y} \frac{\partial N_2}{\partial x} & -\frac{\partial N_1}{\partial y} \frac{\partial N_3}{\partial x} \\ -\frac{\partial N_2}{\partial y} \frac{\partial N_1}{\partial x} & -\frac{\partial N_2}{\partial y} \frac{\partial N_2}{\partial x} & -\frac{\partial N_2}{\partial y} \frac{\partial N_3}{\partial x} \\ -\frac{\partial N_3}{\partial y} \frac{\partial N_1}{\partial x} & -\frac{\partial N_3}{\partial y} \frac{\partial N_2}{\partial x} & -\frac{\partial N_3}{\partial y} \frac{\partial N_3}{\partial x} \end{bmatrix} d\Omega \quad (\text{A.29})$$

The components in the above matrix shown in equation A.29 can be rearranged by substituting the relation of equation 2.51:

$$\int_{\Delta} \frac{\partial[N]^T}{\partial y} \frac{\partial[N]}{\partial x} d\Omega = \int_{\Delta} \begin{bmatrix} -b_1 c_1 A_e & -b_2 c_1 A_e & b_3 c_1 A_e \\ -b_1 c_2 A_e & -b_2 c_2 A_e & b_3 c_2 A_e \\ -b_1 c_3 A_e & -b_2 c_3 A_e & b_3 c_3 A_e \end{bmatrix} d\Omega \quad (\text{A.30})$$

Similarly other terms of equation A.11 such as $-j\beta \int_{\Delta} [N]^T \frac{\partial[N]}{\partial x} d\Omega$ can also be expressed as:

$$\begin{aligned} -j\beta \int_{\Delta} [N]^T \frac{\partial[N]}{\partial x} d\Omega &= -j\beta \int_{\Delta} \begin{bmatrix} N_1 \\ N_2 \\ N_3 \end{bmatrix} \times \begin{bmatrix} \frac{\partial N_1}{\partial x} & \frac{\partial N_2}{\partial x} & \frac{\partial N_3}{\partial x} \end{bmatrix} d\Omega \\ &= -j\beta \int_{\Delta} \begin{bmatrix} N_1 \frac{\partial N_1}{\partial x} & N_1 \frac{\partial N_2}{\partial x} & N_1 \frac{\partial N_3}{\partial x} \\ N_2 \frac{\partial N_1}{\partial x} & N_2 \frac{\partial N_2}{\partial x} & N_2 \frac{\partial N_3}{\partial x} \\ N_3 \frac{\partial N_1}{\partial x} & N_3 \frac{\partial N_2}{\partial x} & N_3 \frac{\partial N_3}{\partial x} \end{bmatrix} d\Omega \quad (\text{A.31}) \\ &= -j\beta \begin{bmatrix} b_1 \frac{A_e}{3} & b_2 \frac{A_e}{3} & b_3 \frac{A_e}{3} \\ b_1 \frac{A_e}{3} & b_2 \frac{A_e}{3} & b_3 \frac{A_e}{3} \\ b_1 \frac{A_e}{3} & b_2 \frac{A_e}{3} & b_3 \frac{A_e}{3} \end{bmatrix} \end{aligned}$$

Similarly

$$-j\beta \int_{\Delta} [N]^T \frac{\partial [N]}{\partial y} d\Omega = -j\beta \begin{bmatrix} c_1 \frac{A_e}{3} & c_2 \frac{A_e}{3} & c_3 \frac{A_e}{3} \\ c_1 \frac{A_e}{3} & c_2 \frac{A_e}{3} & c_3 \frac{A_e}{3} \\ c_1 \frac{A_e}{3} & c_2 \frac{A_e}{3} & c_3 \frac{A_e}{3} \end{bmatrix} \quad (\text{A.32})$$

Other terms such as $-\int_{\Delta} \frac{\partial [N]^T}{\partial x} \frac{\partial [N]}{\partial y} d\Omega$ and $\int_{\Delta} \frac{\partial [N]^T}{\partial x} \frac{\partial [N]}{\partial x} d\Omega$ can also be expressed as follows:

$$\begin{aligned} -\int_{\Delta} \frac{\partial [N]^T}{\partial x} \frac{\partial [N]}{\partial y} d\Omega &= \int_{\Delta} \begin{bmatrix} -\frac{\partial N_1}{\partial x} \\ -\frac{\partial N_2}{\partial x} \\ -\frac{\partial N_3}{\partial x} \end{bmatrix} \times \begin{bmatrix} \frac{\partial N_1}{\partial y} & \frac{\partial N_2}{\partial y} & \frac{\partial N_3}{\partial y} \end{bmatrix} d\Omega \\ &= \int_{\Delta} \begin{bmatrix} -\frac{\partial N_1}{\partial x} \frac{\partial N_1}{\partial y} & -\frac{\partial N_1}{\partial x} \frac{\partial N_2}{\partial y} & -\frac{\partial N_1}{\partial x} \frac{\partial N_3}{\partial y} \\ -\frac{\partial N_2}{\partial x} \frac{\partial N_1}{\partial y} & -\frac{\partial N_2}{\partial x} \frac{\partial N_2}{\partial y} & -\frac{\partial N_2}{\partial x} \frac{\partial N_3}{\partial y} \\ -\frac{\partial N_3}{\partial x} \frac{\partial N_1}{\partial y} & -\frac{\partial N_3}{\partial x} \frac{\partial N_2}{\partial y} & -\frac{\partial N_3}{\partial x} \frac{\partial N_3}{\partial y} \end{bmatrix} d\Omega \quad (\text{A.33}) \\ &= \begin{bmatrix} -b_1 c_1 A_e & -b_1 c_2 A_e & -b_1 c_3 A_e \\ -b_2 c_1 A_e & -b_2 c_2 A_e & -b_2 c_3 A_e \\ -b_3 c_1 A_e & -b_3 c_2 A_e & -b_3 c_3 A_e \end{bmatrix} \end{aligned}$$

$$\begin{aligned}
 \int_{\Delta} \frac{\partial[N]^T}{\partial x} \frac{\partial[N]}{\partial x} d\Omega &= \int_{\Delta} \begin{bmatrix} \frac{\partial N_1}{\partial x} \\ \frac{\partial N_2}{\partial x} \\ \frac{\partial N_3}{\partial x} \end{bmatrix} \times \begin{bmatrix} \frac{\partial N_1}{\partial x} & \frac{\partial N_2}{\partial x} & \frac{\partial N_3}{\partial x} \end{bmatrix} d\Omega \\
 &= \int_{\Delta} \begin{bmatrix} \left(\frac{\partial N_1}{\partial x}\right)^2 & \frac{\partial N_1}{\partial x} \frac{\partial N_2}{\partial x} & \frac{\partial N_1}{\partial x} \frac{\partial N_3}{\partial x} \\ \frac{\partial N_2}{\partial x} \frac{\partial N_1}{\partial x} & \left(\frac{\partial N_2}{\partial x}\right)^2 & \frac{\partial N_2}{\partial x} \frac{\partial N_3}{\partial x} \\ \frac{\partial N_3}{\partial x} \frac{\partial N_1}{\partial x} & \frac{\partial N_3}{\partial x} \frac{\partial N_2}{\partial x} & \left(\frac{\partial N_3}{\partial x}\right)^2 \end{bmatrix} d\Omega \quad (\text{A.34}) \\
 &= \begin{bmatrix} b_1^2 A_e & b_1 b_2 A_e & b_1 b_3 A_e \\ b_2 b_1 A_e & b_2^2 A_e & b_2 b_3 A_e \\ b_3 b_1 A_e & b_3 b_2 A_e & b_3^2 A_e \end{bmatrix}
 \end{aligned}$$

Hence

$$\int_{\Delta} \left(\frac{\partial[N]^T}{\partial y} \frac{\partial[N]}{\partial y} + \frac{\partial[N]^T}{\partial x} \frac{\partial[N]}{\partial x} \right) d\Omega = \begin{bmatrix} (b_1^2 + c_1^2) A_e & (b_1 b_2 + c_1 c_2) A_e & (b_1 b_3 + c_1 c_3) A_e \\ (b_1 b_2 + c_1 c_2) A_e & (b_2^2 + c_2^2) A_e & (b_2 b_3 + c_2 c_3) A_e \\ (b_1 b_3 + c_1 c_3) A_e & (b_2 b_3 + c_2 c_3) A_e & (b_3^2 + c_3^2) A_e \end{bmatrix} \quad (\text{A.35})$$

Therefore from equation A.11, the $9 \times 9 [A]_e$ matrix can be evaluated as:

$$[A]_e = \begin{bmatrix} A_{e(1,1)} & A_{e(1,2)} & A_{e(1,3)} & A_{e(1,4)} & A_{e(1,5)} & A_{e(1,6)} & A_{e(1,7)} & A_{e(1,8)} & A_{e(1,9)} \\ A_{e(2,1)} & A_{e(2,2)} & A_{e(2,3)} & A_{e(2,4)} & A_{e(2,5)} & A_{e(2,6)} & A_{e(2,7)} & A_{e(2,8)} & A_{e(2,9)} \\ A_{e(3,1)} & A_{e(3,2)} & A_{e(3,3)} & A_{e(3,4)} & A_{e(3,5)} & A_{e(3,6)} & A_{e(3,7)} & A_{e(3,8)} & A_{e(3,9)} \\ A_{e(4,1)} & A_{e(4,2)} & A_{e(4,3)} & A_{e(4,4)} & A_{e(4,5)} & A_{e(4,6)} & A_{e(4,7)} & A_{e(4,8)} & A_{e(4,9)} \\ A_{e(5,1)} & A_{e(5,2)} & A_{e(5,3)} & A_{e(5,4)} & A_{e(5,5)} & A_{e(5,6)} & A_{e(5,7)} & A_{e(5,8)} & A_{e(5,9)} \\ A_{e(6,1)} & A_{e(6,2)} & A_{e(6,3)} & A_{e(6,4)} & A_{e(6,5)} & A_{e(6,6)} & A_{e(6,7)} & A_{e(6,8)} & A_{e(6,9)} \\ A_{e(7,1)} & A_{e(7,2)} & A_{e(7,3)} & A_{e(7,4)} & A_{e(7,5)} & A_{e(7,6)} & A_{e(7,7)} & A_{e(7,8)} & A_{e(7,9)} \\ A_{e(8,1)} & A_{e(8,2)} & A_{e(8,3)} & A_{e(8,4)} & A_{e(8,5)} & A_{e(8,6)} & A_{e(8,7)} & A_{e(8,8)} & A_{e(8,9)} \\ A_{e(9,1)} & A_{e(9,2)} & A_{e(9,3)} & A_{e(9,4)} & A_{e(9,5)} & A_{e(9,6)} & A_{e(9,7)} & A_{e(9,8)} & A_{e(9,9)} \end{bmatrix} \quad (\text{A.36})$$

Thus some of the elements of the $9 \times 9 [A]_e$ matrix can be evaluated as:

$$\begin{aligned}
 [A]_{e(1,1)} &= \frac{1}{\epsilon} \left[\frac{\beta^2 A_e}{6} + c_1^2 A_e \right] \\
 [A]_{e(1,2)} &= \frac{1}{\epsilon} \left[\frac{\beta^2 A_e}{12} + c_1 c_2 A_e \right] \\
 [A]_{e(1,3)} &= \frac{1}{\epsilon} \left[\frac{\beta^2 A_e}{12} + c_1 c_2 A_e \right] \\
 [A]_{e(1,4)} &= \frac{1}{\epsilon} [-b_1 c_1 A_e] \\
 [A]_{e(1,5)} &= \frac{1}{\epsilon} [-b_2 c_1 A_e] \\
 [A]_{e(1,6)} &= \frac{1}{\epsilon} [-b_3 c_1 A_e] \\
 [A]_{e(1,7)} &= \frac{1}{\epsilon} \left[-j \beta b_1 \frac{A_e}{3} \right] \\
 [A]_{e(1,8)} &= \frac{1}{\epsilon} \left[-j \beta b_2 \frac{A_e}{3} \right] \\
 [A]_{e(1,9)} &= \frac{1}{\epsilon} \left[-j \beta b_3 \frac{A_e}{3} \right]
 \end{aligned} \tag{A.37}$$

Similarly 72 other elements of the $9 \times 9 [A]_e$ matrix can be evaluated.

Appendix B

Calculation of Confinement Factor

The Power in an electromagnetic field can be deduced using the Poynting vector relation

$$S = \int_{\Delta} (\mathbf{E}^* \times \mathbf{H}) d\Omega \quad (\text{B.1})$$

Where the cross product relation in the above equation B.1 is given as:

$$\mathbf{E}^* \times \mathbf{H} = \begin{vmatrix} \bar{a}_x & \bar{a}_y & \bar{a}_z \\ E_x^* & E_y^* & E_z^* \\ H_x & H_y & H_z \end{vmatrix} \quad (\text{B.2})$$

$$= \bar{a}_x(E_y^*H_z - E_z^*H_y) - \bar{a}_y(E_x^*H_z - E_z^*H_x) + \bar{a}_z(E_x^*H_y - E_y^*H_x)$$

In equation B.1, integration is carried out over each element cross section, however, only the variation in the propagation direction is of particular interest. Hence the z -component of the Poynting vector relation may be expressed as:

$$S = \int_{\Delta} (E_x^*H_y - E_y^*H_x) d\Omega \quad (\text{B.3})$$

The above equation can be simplified by establishing a relation between the \mathbf{E} and \mathbf{H} components so that the final expression is one variable only. From

Maxwell's equations, the following can be derived:

$$\nabla \times \mathbf{H}^* = j\omega\epsilon\mathbf{E}^* \begin{vmatrix} \bar{x} & \bar{y} & \bar{z} \\ \partial_x & \partial_y & \partial_z \\ H_x^* & H_y^* & H_z^* \end{vmatrix} \quad (\text{B.4})$$

from which the following is obtained:

$$j\omega\epsilon(E_x^*\bar{x} + E_y^*\bar{y} + E_z^*\bar{z}) = \left(\frac{\partial H_z^*}{\partial y} - \frac{\partial H_y^*}{\partial z}\right)\bar{x} - \left(\frac{\partial H_z^*}{\partial x} - \frac{\partial H_x^*}{\partial z}\right)\bar{y} + \left(\frac{\partial H_y^*}{\partial x} - \frac{\partial H_x^*}{\partial y}\right)\bar{z} \quad (\text{B.5})$$

Equating terms with like coefficients:

$$j\omega\epsilon E_x^* = \left(\frac{\partial H_z^*}{\partial y} - \frac{\partial H_y^*}{\partial z}\right) \quad (\text{B.6})$$

$$j\omega\epsilon E_y^* = -\left(\frac{\partial H_z^*}{\partial x} - \frac{\partial H_x^*}{\partial z}\right)$$

Replacing the $\partial/\partial z$ component with $-j\beta$ the following relation can be obtained:

$$j\omega\epsilon E_x^* = \frac{\partial H_z^*}{\partial y} + j\beta H_y^* \Rightarrow E_x^* = \frac{1}{j\omega\epsilon} \frac{\partial H_z^*}{\partial y} + \frac{\beta}{\omega\epsilon} H_y^* \quad (\text{B.7})$$

$$j\omega\epsilon E_y^* = -\frac{\partial H_z^*}{\partial x} - j\beta H_x^* \Rightarrow E_y^* = -\frac{1}{j\omega\epsilon} \frac{\partial H_z^*}{\partial x} - \frac{\beta}{\omega\epsilon} H_x^*$$

Substituting E_x^* and E_y^* from the above expression into the Poynting vector relation of equation B.3, the following can be obtained:

$$S_z = \int_{\Delta} \frac{1}{\omega\epsilon} \left(\beta H_y^* + \frac{1}{j} \frac{\partial H_z^*}{\partial y} \right) H_y + \frac{1}{\omega\epsilon} \left(\beta H_x^* + \frac{1}{j} \frac{\partial H_z^*}{\partial x} \right) H_x d\Omega \quad (\text{B.8})$$

$$\therefore S_z = \int_{\Delta} \left[\frac{1}{\omega\epsilon} (\beta H_y^* H_y + \beta H_x^* H_x) - \frac{1}{\omega\epsilon} \left(j \frac{\partial H_z^*}{\partial x} H_x + j \frac{\partial H_z^*}{\partial y} H_y \right) \right] d\Omega$$

For plasmonic medium with a complex propagation constant $\beta = \beta' + j\beta''$ and dielectric permittivity $\epsilon = \epsilon' + j\epsilon''$, the eigen value solutions obtained are

also complex. Due to which the resultant fields are also complex as $H_x = H'_x + jH_x''$, $H_y = H'_y + jH_y''$, $H_z = H'_z + jH_z''$, and the conjugate fields are as: $H_x^* = H'_x - jH_x''$, $H_y^* = H'_y - jH_y''$, $H_z^* = H'_z - jH_z''$.

Representing the fields in a triangular element using the shape function description, the following can be written:

$$\mathbf{H} = [N]\{\mathbf{H}\}_e \quad \text{and} \quad \mathbf{H}^* = \{\mathbf{H}\}_e^T [N]^T \quad (\text{B.9})$$

Thus using the field representation in equation B.9, the Poynting vector relation in equation B.8 can be represented as:

$$S_z = \int_{\Delta} \left[\frac{\beta}{\omega\epsilon} (\{H_y\}_e^T [N]^T [N] \{H_y\}_e + \{H_x\}_e^T [N]^T [N] \{H_x\}_e) - \frac{j}{\omega\epsilon} \left(\{H_z\}_e^T \frac{\partial [N]^T [N]}{\partial x} \{H_x\}_e + \{H_z\}_e^T \frac{\partial [N]^T [N]}{\partial y} \{H_y\}_e \right) \right] d\Omega \quad (\text{B.10})$$

The shape function derivatives can be expressed as:

$$\frac{\partial [N]^T}{\partial x} [N] = \begin{bmatrix} \frac{\partial N_1}{\partial x} N_1 & \frac{\partial N_1}{\partial x} N_2 & \frac{\partial N_1}{\partial x} N_3 \\ \frac{\partial N_2}{\partial x} N_1 & \frac{\partial N_2}{\partial x} N_2 & \frac{\partial N_2}{\partial x} N_3 \\ \frac{\partial N_3}{\partial x} N_1 & \frac{\partial N_3}{\partial x} N_2 & \frac{\partial N_3}{\partial x} N_3 \end{bmatrix} \quad (\text{B.11})$$

Using the shape function approximation derived from equation B.6, the above equation can be expressed as:

$$\frac{\partial [N]^T}{\partial x} [N] = \begin{bmatrix} b_1 N_1 & b_1 N_2 & b_1 N_3 \\ b_2 N_1 & b_2 N_2 & b_2 N_3 \\ b_3 N_1 & b_3 N_2 & b_3 N_3 \end{bmatrix} \quad (\text{B.12})$$

Similarly $\frac{\partial[N]^T}{\partial y}[N]$ can be expressed as

$$\frac{\partial[N]^T}{\partial x}[N] = \begin{bmatrix} c_1 N_1 & c_1 N_2 & c_1 N_3 \\ c_2 N_1 & c_2 N_2 & c_2 N_3 \\ c_3 N_1 & c_3 N_2 & c_3 N_3 \end{bmatrix} \quad (\text{B.13})$$

where the coefficients b_1, b_2, b_3, c_1, c_2 and c_3 can be defined as:

$$\frac{\partial N_1}{\partial x} = b_1; \quad \frac{\partial N_2}{\partial x} = b_2; \quad \frac{\partial N_3}{\partial x} = b_3 \quad (\text{B.14})$$

$$\frac{\partial N_1}{\partial y} = c_1; \quad \frac{\partial N_2}{\partial y} = c_2; \quad \frac{\partial N_3}{\partial y} = c_3$$

Thus the power equation can be written as:

$$S_z = \frac{\beta}{\omega\epsilon} \left(\begin{array}{c} \{H_y\}_e^T \begin{bmatrix} \frac{A_e}{6} & \frac{A_e}{12} & \frac{A_e}{12} \\ \frac{A_e}{12} & \frac{A_e}{6} & \frac{A_e}{12} \\ \frac{A_e}{12} & \frac{A_e}{12} & \frac{A_e}{6} \end{bmatrix} \{H_y\}_e + \{H_x\}_e^T \begin{bmatrix} \frac{A_e}{6} & \frac{A_e}{12} & \frac{A_e}{12} \\ \frac{A_e}{12} & \frac{A_e}{6} & \frac{A_e}{12} \\ \frac{A_e}{12} & \frac{A_e}{12} & \frac{A_e}{6} \end{bmatrix} \{H_x\}_e \end{array} \right) \\ - \frac{j}{\omega\epsilon} \left(\begin{array}{c} \{H_z\}_e^T \frac{A_e}{3} \begin{bmatrix} b_1 & b_1 & b_1 \\ b_2 & b_2 & b_2 \\ b_3 & b_3 & b_3 \end{bmatrix} \{H_x\}_e + \{H_z\}_e^T \frac{A_e}{3} \begin{bmatrix} c_1 & c_1 & c_1 \\ c_2 & c_2 & c_2 \\ c_3 & c_3 & c_3 \end{bmatrix} \{H_y\}_e \end{array} \right) \quad (\text{B.15})$$

Appendix C

List of Associated Publications

This is a list of publications by the author which are associated with this work.

Journal

- [1] B. M. A. Rahman, A. Quadir, H. Tanvir, and K. T. V Grattan, "Characterization of plasmonic modes in a low-loss dielectric-coated hollow core rectangular waveguide at terahertz frequency," *Photonics Journal, IEEE*, vol. 3, no. 6, pp. 1054–1066, 2011.
- [2] A. Quadir and B. M. A. Rahman, "Almost Loss free and Dispersion free Dielectric coated plasmonic guide," *Photonics Journal, IEEE*, submitted.
- [3] B. M. A. Rahman, C. Markides, M. Uthman, A. Quadir, N. Kejalakshmy, and C. Themistos, "Characterization of low-loss waveguides and devices for terahertz radiation," *Optical Engineering*, vol. 53, no. 3, pp. 031210–031210, 2014.

Conference

- [1] B. M. A. Rahman, A. Quadir, H. Tanvir, and K. T. V. Grattan, "Low-loss dielectric-coated hollow rectangular plasmonic waveguide supporting THz guidance," in *Integrated Photonics Research, Silicon and Nanophotonics*, p. IMA6, Optical Society of America, 2011.
- [2] B. M. A. Rahman, A. Quadir, N. Kejalakshmy, and K. Grattan, "Design optimization of low-loss waveguides for THz guidance," in *SPIE Defense, Security, and Sensing*, pp. 83630H–83630H, International Society for Optics and Photonics, 2012.

- [3] B. M. A. Rahman, H. Tanvir, N. Kejalakshmy, A. Quadir, and K. T. V. Grattan, "Rigorous characterization of surface plasmon modes by using the finite element method," in *SPIE OPTO*, pp. 79410W–79410W, International Society for Optics and Photonics, 2011.
- [4] C. Themistos, K. Kalli, M. Komodromos, C. Markides, A. Quadir, B. M. A. Rahman, and K. T. V. Grattan, "Low-loss multimode interference couplers for terahertz waves," in *SPIE Photonics Europe*, pp. 84260X–84260X, International Society for Optics and Photonics, 2012.
- [5] C. Markides, C. Viphavakit, C. Themistos, M. Komodromos, K. Kalli, A. Quadir, and B. M. A. Rahman, "Dispersion characteristics of plasmonic waveguides for THz waves," in *SPIE Optics+ Optoelectronics*, pp. 87750J–87750J, International Society for Optics and Photonics, 2013.

Bibliography

- [1] R. S. Woodbury, T. Derry, and T. I. Williams. "A Short History of Technology from the Earliest Times to AD 1900". In: *Speculum* 37.02 (1962), pp. 270–271.
- [2] J. Hecht. *City of light: the story of fiber optics*. Oxford university press, 2004.
- [3] N. S. Kapany. *Fiber optics*. Academic press, 1967.
- [4] D. Hondros and P. Debye. "Elektromagnetische Wellen an dielektrischen Drähten". In: *Annalen der Physik* 337.8 (1910), pp. 465–476.
- [5] W. M. Elsasser. "Attenuation in a dielectric circular rod". In: *Journal of Applied Physics* 20.12 (1949), pp. 1193–1196.
- [6] E. Snitzer and H. Osterberg. "Observed Dielectric Waveguide Modes in the Visible Spectrum*". In: *JOSA* 51.5 (1961), pp. 499–505.
- [7] N. Kapany and J. Burke. "Light conduction along absorbing fiber by evanescent boundary wave". In: *J. opt. Soc. Amer.(Abstr.)* 51 (1961), p. 1474.
- [8] K. Kao and G. A. Hockham. "Dielectric-fibre surface waveguides for optical frequencies". In: *Proceedings of the Institution of Electrical Engineers*. Vol. 113. 7. IET. 1966, pp. 1151–1158.
- [9] T. Maiman. "Stimulated Optical Radiation in Ruby". In: *Nature* 187 (1960), pp. 493–494.
- [10] T. Miya, Y Terunuma, T. Hosaka, and T. Miyashita. "Ultimate low-loss single-mode fibre at 1.55 μm ". In: *Electronics Letters* 15.4 (1979), pp. 106–108.
- [11] H. Osterberg and L. W. Smith. "Transmission of optical energy along surfaces: Part ii, inhomogeneous media". In: *JOSA* 54.9 (1964), pp. 1078–1079.
- [12] R. Shubert and H Harris. "Optical surface waves on thin films and their application to integrated data processors". In: *Microwave Theory and Techniques, IEEE Transactions on* 16.12 (1968), pp. 1048–1054.
- [13] S. E. Miller. "Integrated optics: an introduction". In: *Bell System Technical Journal* 48.7 (1969), pp. 2059–2069.

- [14] S. M. R. Kabir, B. M. A. Rahman, A. Agrawal, and K. T. V. Grattan. "Elimination of numerical dispersion from electromagnetic time domain analysis by using resource efficient finite element technique". In: *Progress In Electromagnetics Research* 137 (2013), pp. 487–512.
- [15] I. Malitson. "Interspecimen comparison of the refractive index of fused silica". In: *J. Opt. Soc. Am* 54.11 (1964), p. 1401.
- [16] C. D. Salzberg and J. J. Villa. "Infrared refractive indexes of silicon germanium and modified selenium glass". In: *JOSA* 47.3 (1957), pp. 244–246.
- [17] T. W. Ebbesen, H. Lezec, H. Ghaemi, T. Thio, and P. Wolff. "Extraordinary optical transmission through sub-wavelength hole arrays". In: *Nature* 391.6668 (1998), pp. 667–669.
- [18] E. Hendry, F. Garcia-Vidal, L. Martin-Moreno, J. G. Rivas, M. Bonn, A. P. Hibbins, and M. J. Lockyear. "Optical control over surface-plasmon-polariton-assisted THz transmission through a slit aperture". In: *Physical review letters* 100.12 (2008), p. 123901.
- [19] R. Wood. "XLII. On a remarkable case of uneven distribution of light in a diffraction grating spectrum". In: *The London, Edinburgh, and Dublin Philosophical Magazine and Journal of Science* 4.21 (1902), pp. 396–402.
- [20] R. Wood. "XXVII. Diffraction gratings with controlled groove form and abnormal distribution of intensity". In: *The London, Edinburgh, and Dublin Philosophical Magazine and Journal of Science* 23.134 (1912), pp. 310–317.
- [21] J. M. Garnett. "Colours in Metal Glasses and in Metallic Films". In: *Proceedings of the Royal Society of London* (1904), pp. 443–445.
- [22] L. Rayleigh. "On the dynamical theory of gratings". In: *Proceedings of the Royal Society of London. Series A, Containing Papers of a Mathematical and Physical Character* 79.532 (1907), pp. 399–416.
- [23] A Hessel and A. A. Oliner. "A new theory of Woods anomalies on optical gratings". In: *Applied Optics* 4.10 (1965), pp. 1275–1297.
- [24] R. Ritchie. "Plasma losses by fast electrons in thin films". In: *Physical Review* 106.5 (1957), p. 874.
- [25] C. Powell and J. Swan. "Effect of oxidation on the characteristic loss spectra of aluminum and magnesium". In: *Physical Review* 118.3 (1960), p. 640.

- [26] D Bohm and D Pines. "A collective description of electron interactions. I. Magnetic interactions". In: *Physical Review* 82.5 (1951), p. 625.
- [27] D Pines and D Bohm. "A collective description of electron interactions: II. Collective vs individual particle aspects of the interactions". In: *Physical Review* 85.2 (1952), p. 338.
- [28] D Bohm and D Pines. "A collective description of electron interactions: III. Coulomb interactions in a degenerate electron gas". In: *Physical Review* 92.3 (1953), p. 609.
- [29] E Burstein, W. P. Chen, Y. J. Chen, and A Hartstein. "Surface polariton-propagating electromagnetic modes at interfaces". In: *Journal of Vacuum Science & Technology* 11.6 (1974), pp. 1004–1019.
- [30] E. Kretschmann and H. Raether. "Notizen: Radiative Decay of Non Radiative Surface Plasmons Excited by Light". In: *Zeitschrift für Naturforschung A* 23.12 (1968), pp. 2135–2136.
- [31] E. Kretschmann. "Die bestimmung optischer konstanten von metallen durch anregung von oberflächenplasmaschwingungen". In: *Zeitschrift für Physik* 241.4 (1971), pp. 313–324.
- [32] A. Otto. "Excitation of nonradiative surface plasma waves in silver by the method of frustrated total reflection". In: *Zeitschrift für Physik* 216.4 (1968), pp. 398–410.
- [33] U. Kreibig and P. Zacharias. "Surface plasma resonances in small spherical silver and gold particles". In: *Zeitschrift für Physik* 231.2 (1970), pp. 128–143.
- [34] S. Cunningham, A. Maradudin, and R. Wallis. "Effect of a charge layer on the surface-plasmon-polariton dispersion curve". In: *Physical Review B* 10.8 (1974), p. 3342.
- [35] M. Fleischmann, P. J. Hendra, and A. McQuillan. "Raman spectra of pyridine adsorbed at a silver electrode". In: *Chemical Physics Letters* 26.2 (1974), pp. 163–166.
- [36] S. P. Nanophotonics. "ML Brongersma and PG Kik". In: *Springer Series in Optical Sciences* (2007).
- [37] H. E. de Bruijn, R. P. Kooyman, and J. Greve. "Determination of dielectric permittivity and thickness of a metal layer from a surface plasmon resonance experiment". In: *Applied optics* 29.13 (1990), pp. 1974–1978.

- [38] K. Matsubara, S. Kawata, and S. Minami. "Optical chemical sensor based on surface plasmon measurement". In: *Applied Optics* 27.6 (1988), pp. 1160–1163.
- [39] U Jönsson, L Fägerstam, B Ivarsson, B Johnsson, R Karlsson, K Lundh, S Löfås, B Persson, H Roos, and I Rönnerberg. "Real-time biospecific interaction analysis using surface plasmon resonance and a sensor chip technology." In: *Biotechniques* 11.5 (1991), pp. 620–627.
- [40] C. Nylander, B. Liedberg, and T. Lind. "Gas detection by means of surface plasmon resonance". In: *Sensors and Actuators* 3 (1983), pp. 79–88.
- [41] B. Liedberg, C. Nylander, and I. Lunström. "Surface plasmon resonance for gas detection and biosensing". In: *Sensors and Actuators* 4 (1983), pp. 299–304.
- [42] D. R. Shankaran, K. V. Gobi, and N. Miura. "Recent advancements in surface plasmon resonance immunosensors for detection of small molecules of biomedical, food and environmental interest". In: *Sensors and Actuators B: Chemical* 121.1 (2007), pp. 158–177.
- [43] A. Christ, T. Zentgraf, S. G. Tikhodeev, N. A. Gippius, J. Kuhl, and H. Giessen. "Detection of immunocomplex formation via surface plasmon resonance on gold-coated diffraction gratings". In: *Biosensors* 3 (1987), pp. 211–225.
- [44] R. Jorgenson and S. Yee. "A fiber-optic chemical sensor based on surface plasmon resonance". In: *Sensors and Actuators B: Chemical* 12.3 (1993), pp. 213–220.
- [45] C. R. Lavers and J. S. Wilkinson. "A waveguide-coupled surface-plasmon sensor for an aqueous environment". In: *Sensors and Actuators B: Chemical* 22.1 (1994), pp. 75–81.
- [46] J. Homola, S. S. Yee, and G. Gauglitz. "Surface plasmon resonance sensors: review". In: *Sensors and Actuators B: Chemical* 54.1 (1999), pp. 3–15.
- [47] C. L. Baird and D. G. Myszka. "Current and emerging commercial optical biosensors". In: *Journal of Molecular Recognition* 14.5 (2001), pp. 261–268.
- [48] J. Takahara, S. Yamagishi, H. Taki, A. Morimoto, and T. Kobayashi. "Guiding of a one-dimensional optical beam with nanometer diameter". In: *Optics Letters* 22.7 (1997), pp. 475–477.

- [49] P. Kapur, G. Chandra, J. P. McVittie, and K. C. Saraswat. "Technology and reliability constrained future copper interconnects. II. Performance implications". In: *Electron Devices, IEEE Transactions on* 49.4 (2002), pp. 598–604.
- [50] M. J. Kobrinsky, B. A. Block, J. F. Zheng, B. C. Barnett, E. Mohammed, M. Reshotko, F. Robertson, S. List, I. Yang, and K. Cadien. "On-chip optical interconnects". In: *intel Technology Journal* 8.2 (2004), pp. 129–141.
- [51] R. Charbonneau, P. Berini, E. Berolo, and E. Lisicka-Shrzek. "Experimental observation of plasmon polariton waves supported by a thin metal film of finite width". In: *Optics letters* 25.11 (2000), pp. 844–846.
- [52] J. R. Krenn and J. C. Weeber. "Surface plasmon polaritons in metal stripes and wires". In: *Philosophical Transactions of the Royal Society of London A: Mathematical, Physical and Engineering Sciences* (2004), pp. 739–756.
- [53] P. Berini, R. Charbonneau, N. Lahoud, and G. Mattiussi. "Characterization of long-range surface-plasmon-polariton waveguides". In: *Journal of Applied Physics* 98.4 (2005), p. 043109.
- [54] R. Zia, J. A. Schuller, A. Chandran, and M. L. Brongersma. "Plasmonics: the next chip-scale technology". In: *Materials today* 9.7 (2006), pp. 20–27.
- [55] T. Yatsui, T. Abe, M. Kourogi, and M. Ohtsu. "Plasmon waveguide for optical far/near-field conversion". In: *Lasers and Electro-Optics, 2002. CLEO'02. Technical Digest. Summaries of Papers Presented at the. IEEE. 2002*, pp. 76–77.
- [56] D. F. Pile, T. Ogawa, D. K. Gramotnev, T. Okamoto, M. Haraguchi, M. Fukui, and S. Matsuo. "Theoretical and experimental investigation of strongly localized plasmons on triangular metal wedges for subwavelength waveguiding". In: *Applied Physics Letters* 87.6 (2005), p. 061106.
- [57] D. F. Pile, T. Ogawa, D. K. Gramotnev, Y. Matsuzaki, K. C. Vernon, K. Yamaguchi, T. Okamoto, M. Haraguchi, and M. Fukui. "Two-dimensionally localized modes of a nanoscale gap plasmon waveguide". In: *Applied Physics Letters* 87.26 (2005), p. 261114.
- [58] L. Chen, J. Shakya, and M. Lipson. "Subwavelength confinement in an integrated metal slot waveguide on silicon". In: *Optics Letters* 31.14 (2006), pp. 2133–2135.

- [59] S. I. Bozhevolnyi, V. S. Volkov, E Devaux, and T. W. Ebbesen. "Channel plasmon-polariton guiding by subwavelength metal grooves". In: *Physical Review Letters* 95.4 (2005), p. 046802.
- [60] R. Charbonneau, C. Scales, I. Breukelaar, S. Fafard, N. Lahoud, G. Matiusi, and P. Berini. "Passive integrated optics elements based on long-range surface plasmon polaritons". In: *Journal of Lightwave Technology* 24.1 (2006), p. 477.
- [61] I. I. Smolyaninov, D. L. Mazzoni, J. Mait, and C. C. Davis. "Experimental study of surface-plasmon scattering by individual surface defects". In: *Physical Review B* 56.3 (1997), p. 1601.
- [62] H Ditlbacher, J. Krenn, G Schider, A Leitner, and F. Aussenegg. "Two-dimensional optics with surface plasmon polaritons". In: *Applied Physics Letters* 81.10 (2002), pp. 1762–1764.
- [63] S. E. Ralph and D Grischkowsky. "THz spectroscopy and source characterization by optoelectronic interferometry". In: *Applied Physics Letters* 60.9 (1992), pp. 1070–1072.
- [64] K. P. Cheung and D. H. Auston. "Excitation of coherent phonon polaritons with femtosecond optical pulses". In: *Physical Review Letters* 55.20 (1985), p. 2152.
- [65] K. P. Cheung and D. H. Auston. "A novel technique for measuring far-infrared absorption and dispersion". In: *Infrared Physics* 26.1 (1986), pp. 23–27.
- [66] B. B. Hu and M. C. Nuss. "Imaging with terahertz waves". In: *Optics Letters* 20.16 (1995), pp. 1716–1718.
- [67] D. M. Mittleman, S Hunsche, L Boivin, and M. C. Nuss. "T-ray tomography". In: *Optics Letters* 22.12 (1997), pp. 904–906.
- [68] T. D. Dorney, J. L. Johnson, J Van Rudd, R. G. Baraniuk, W. W. Symes, and D. M. Mittleman. "Terahertz reflection imaging using Kirchhoff migration". In: *Optics Letters* 26.19 (2001), pp. 1513–1515.
- [69] K McClatchey, M. T. Reiten, and R. A. Cheville. "Time resolved synthetic aperture terahertz impulse imaging". In: *Applied Physics Letters* 79.27 (2001), pp. 4485–4487.
- [70] J. O'Hara and D Grischkowsky. "Quasi-optic synthetic phased-array terahertz imaging". In: *JOSA B* 21.6 (2004), pp. 1178–1191.

- [71] D. M. Mittleman, R. H. Jacobsen, and M. C. Nuss. "T-ray imaging". In: *IEEE Journal of Selected Topics in Quantum Electronics* 2.3 (1996), pp. 679–692.
- [72] P. H. Siegel. "Terahertz technology in biology and medicine". In: *Microwave Symposium Digest, 2004 IEEE MTT-S International*. Vol. 3. IEEE. 2004, pp. 1575–1578.
- [73] B. Fischer, M. Hoffmann, H. Helm, R. Wilk, F. Rutz, T. Kleine-Ostmann, M. Koch, and P. Jepsen. "Terahertz time-domain spectroscopy and imaging of artificial RNA". In: *Optics Express* 13.14 (2005), pp. 5205–5215.
- [74] H Yoshida, Y Ogawa, Y Kawai, S Hayashi, A Hayashi, C Otani, E Kato, F Miyamaru, and K Kawase. "Terahertz sensing method for protein detection using a thin metallic mesh". In: *Applied Physics Letters* 91.25 (2007), p. 253901.
- [75] P. H. Bolivar, M Brucherseifer, M Nagel, H Kurz, A Bosserhoff, et al. "Label-free probing of genes by time-domain terahertz sensing". In: *Physics in Medicine and Biology* 47.21 (2002), p. 3815.
- [76] P. H. Bolívar, M. Nagel, F. Richter, M. Brucherseifer, H. Kurz, A. Bosserhoff, and R. Büttner. "Label-free THz sensing of genetic sequences: towards THz biochips". In: *Philosophical Transactions of the Royal Society of London A: Mathematical, Physical and Engineering Sciences* 362.1815 (2004), pp. 323–335.
- [77] M Nagel, P. H. Bolivar, M Brucherseifer, H Kurz, A Bosserhoff, and R Büttner. "Integrated THz technology for label-free genetic diagnostics". In: *Applied Physics Letters* 80.1 (2002), pp. 154–156.
- [78] R. Woodward, V. Wallace, D. Arnone, E. Linfield, and M Pepper. "Terahertz pulsed imaging of skin cancer in the time and frequency domain". In: *Journal of Biological Physics* 29.2-3 (2003), pp. 257–259.
- [79] R. M. Woodward, B. E. Cole, V. P. Wallace, R. J. Pye, D. D. Arnone, E. H. Linfield, and M. Pepper. "Terahertz pulse imaging in reflection geometry of human skin cancer and skin tissue". In: *Physics in Medicine and Biology* 47.21 (2002), p. 3853.
- [80] M. Tonouchi. "Cutting-edge terahertz technology". In: *Nature Photonics* 1.2 (2007), pp. 97–105.

- [81] J. F. Federici, B. Schulkin, F. Huang, D. Gary, R. Barat, F. Oliveira, and D. Zimdars. "THz imaging and sensing for security applications—explosives, weapons and drugs". In: *Semiconductor Science and Technology* 20.7 (2005), S266.
- [82] K. Kawase, Y. Ogawa, Y. Watanabe, and H. Inoue. "Non-destructive terahertz imaging of illicit drugs using spectral fingerprints". In: *Optics Express* 11.20 (2003), pp. 2549–2554.
- [83] B. Ferguson and X.-C. Zhang. "Materials for terahertz science and technology". In: *Nature Materials* 1.1 (2002), pp. 26–33.
- [84] D. Grischkowsky, S. Keiding, M. Van Exter, and C. Fattinger. "Far-infrared time-domain spectroscopy with terahertz beams of dielectrics and semiconductors". In: *JOSA B* 7.10 (1990), pp. 2006–2015.
- [85] G. Klatt, R. Gebbs, H. Schafer, M. Nagel, C. Janke, A. Bartels, and T. Dekorsy. "High-resolution terahertz spectrometer". In: *Selected Topics in Quantum Electronics, IEEE Journal of* 17.1 (2011), pp. 159–168.
- [86] G. Klatt, R. Gebbs, C. Janke, T. Dekorsy, and A. Bartels. "Rapid-scanning terahertz precision spectrometer with more than 6 THz spectral coverage". In: *Optics Express* 17.25 (2009), pp. 22847–22854.
- [87] D. M. Mittleman, R. H. Jacobsen, R. Neelamani, R. G. Baraniuk, and M. C. Nuss. "Gas sensing using terahertz time-domain spectroscopy". In: *Applied Physics B: Lasers and Optics* 67.3 (1998), pp. 379–390.
- [88] S. Komiyama, O. Astafiev, V. Antonov, T. Kutsuwa, and H. Hirai. "A single-photon detector in the far-infrared range". In: *Nature* 403.6768 (2000), pp. 405–407.
- [89] G. Dyer, J. Crossno, G. Aizin, E. Shaner, M. Wanke, J. Reno, and S. Allen. "A plasmonic terahertz detector with a monolithic hot electron bolometer". In: *Journal of Physics: Condensed Matter* 21.19 (2009), p. 195803.
- [90] Y.-S. Lee. *Principles of terahertz science and technology*. Vol. 170. Springer Science & Business Media, 2009.
- [91] Q. Wu and X.-C. Zhang. "Free-space electro-optic sampling of terahertz beams". In: *Applied Physics Letters* 67.24 (1995), pp. 3523–3525.
- [92] H. Eisele, A. Rydberg, G. Haddad, et al. "Recent advances in the performance of InP Gunn devices and GaAs TUNNETT diodes for the 100-300-GHz frequency range and above". In: *IEEE Transactions on Microwave Theory and Techniques* 48.4 (2000), pp. 626–631.

- [93] G. Gallerano, S Biedron, et al. "Overview of terahertz radiation sources". In: *Proceedings of the 2004 FEL Conference*. 2004, pp. 216–221.
- [94] D. Auston, K. Cheung, J. Valdmanis, and D. Kleinman. "Cherenkov radiation from femtosecond optical pulses in electro-optic media". In: *Physical Review Letters* 53.16 (1984), p. 1555.
- [95] Z. Jiang and X.-C. Zhang. "Terahertz imaging via electrooptic effect". In: *IEEE Transactions on Microwave Theory and Techniques* 47.12 (1999), pp. 2644–2650.
- [96] G. Williams. "FAR-IR/THz radiation from the Jefferson Laboratory, energy recovered linac, free electron laser". In: *Review of Scientific Instruments* 73.3 (2002), pp. 1461–1463.
- [97] J. Faist, F. Capasso, D. L. Sivco, C. Sirtori, A. L. Hutchinson, and A. Y. Cho. "Quantum cascade laser". In: *Science* 264.5158 (1994), pp. 553–556.
- [98] S. A. Maier. *Plasmonics: fundamentals and applications*. Springer Science & Business Media, 2007.
- [99] G. Goubau. "Surface waves and their application to transmission lines". In: *Journal of Applied Physics* 21.11 (1950), pp. 1119–1128.
- [100] J. R. Wait. "The ancient and modern history of EM ground-wave propagation". In: *Antennas and Propagation Magazine, IEEE* 40.5 (1998), pp. 7–24.
- [101] J. G. Rivas, M Kuttge, P. H. Bolivar, H Kurz, and J. Sánchez-Gil. "Propagation of surface plasmon polaritons on semiconductor gratings". In: *Physical Review Letters* 93.25 (2004), p. 256804.
- [102] J. G. Rivas, M Kuttge, H Kurz, P. H. Bolivar, and J. Sánchez-Gil. "Low-frequency active surface plasmon optics on semiconductors". In: *Applied Physics Letters* 88.8 (2006), p. 082106.
- [103] J Saxler, J. G. Rivas, C Janke, H. Pellemans, P. H. Bolívar, and H Kurz. "Time-domain measurements of surface plasmon polaritons in the terahertz frequency range". In: *Physical Review B* 69.15 (2004), p. 155427.
- [104] K. Wang and D. M. Mittleman. "Guided propagation of terahertz pulses on metal wires". In: *JOSA B* 22.9 (2005), pp. 2001–2008.
- [105] L. Qiao and J. Wang. "A modified ray-optic method for arbitrary dielectric waveguides". In: *IEEE Journal of Quantum Electronics*, 28.12 (1992), pp. 2721–2727.

- [106] R. Srivastava, C. Kao, and R. V. Ramaswamy. "WKB analysis of planar surface waveguides with truncated index profiles". In: *Journal of Lightwave Technology* 5.11 (1987), pp. 1605–1609.
- [107] E. A. Marcatili. "Dielectric rectangular waveguide and directional coupler for integrated optics". In: *Bell System Technical Journal* 48.7 (1969), pp. 2071–2102.
- [108] R. Knox and P. Toullos. *Proceedings of MRI symposium on submillimetre waves*. 1970.
- [109] R. Chandrasekaran and A. Tamir. "Algebraic optimization: the Fermat-Weber location problem". In: *Mathematical Programming* 46.1-3 (1990), pp. 219–224.
- [110] C.-J. Chang, T.-T. Su, and Y.-Y. Chiang. "Analysis of a cutoff priority cellular radio system with finite queueing and reneging/dropping". In: *IEEE/ACM Transactions on Networking (TON)* 2.2 (1994), pp. 166–175.
- [111] W.-B. Zhou et al. "Analysis of trapped image guides using effective dielectric constant and surface impedances". In: *IEEE Transactions on Microwave Theory and Techniques* 30.12 (1982), pp. 2163–2166.
- [112] K. S. Chiang. "Analysis of the effective-index method for the vector modes of rectangular-core dielectric waveguides". In: *IEEE Transactions on Microwave Theory and Techniques* 44.5 (1996), pp. 692–700.
- [113] K. S. Chiang, K. M. Lo, and K. S. Kwok. "Effective-index method with built-in perturbation correction for integrated optical waveguides". In: *Journal of Lightwave Technology* 14.2 (1996), pp. 223–228.
- [114] M. Koshiba. *Optical Waveguide Analysis*. McGraw-Hill New York etc., 1992.
- [115] E. Yamashita. *Analysis Methods for Electromagnetic Wave Problems*. Vol. 1. Artech House on Demand, 1990.
- [116] I. C. Goyal, R. L. Gallawa, and A. K. Ghatak. "Improved variational analysis of inhomogeneous optical waveguides using Airy functions". In: *Journal of Lightwave Technology* 11.10 (1993), pp. 1575–1578.
- [117] A. Wexler. "Computation of electromagnetic fields". In: *IEEE Transactions on Microwave Theory and Techniques* 17.8 (1969), pp. 416–439.
- [118] J. E. Goell. "A circular-harmonic computer analysis of rectangular dielectric waveguides". In: *Bell System Technical Journal* 48.7 (1969), pp. 2133–2160.

- [119] E Yamashita and K Atsuki. "The point matching method". In: *Analysis Methods for Electromagnetic Wave Problems* (1990).
- [120] A. Cullen, O Özkan, and L. Jackson. "Point-matching technique for rectangular-cross-section dielectric rod". In: *Electronics Letters* 7.17 (1971), pp. 497–499.
- [121] R. H. T. Bates and F. L. Ng. "Point matching computation of transverse resonances". In: *International Journal for Numerical Methods in Engineering* 6.2 (1973), pp. 155–168.
- [122] N. Morita. "The boundary-element method". In: *Analysis Methods for Electromagnetic Wave Problems* (1990), pp. 33–77.
- [123] T. Zhu, J. Zhang, and S. Atluri. "A meshless local boundary integral equation (LBIE) method for solving nonlinear problems". In: *Computational Mechanics* 22.2 (1998), pp. 174–186.
- [124] C. D. Nallo, F. Frezza, and A. Galli. "Full-wave modal analysis of arbitrarily-shaped dielectric waveguides through an efficient boundary-element-method formulation". In: *IEEE Transactions on Microwave Theory and Techniques* 43.12 (1995), pp. 2982–2990.
- [125] S. T. Peng and A. A. Oliner. "Guidance and leakage properties of a class of open dielectric waveguides: Part I-Mathematical Formulations". In: *IEEE Transactions on Microwave Theory and Techniques* 29.9 (1981), pp. 843–855.
- [126] M. Koshiya and M. Suzuki. "Vectorial wave analysis of dielectric waveguides for optical-integrated circuits using equivalent network approach". In: *Journal of Lightwave Technology* 4.6 (1986), pp. 656–664.
- [127] N. Dagli and C. G. Fonstad. "A New Method of Analyzing and Modeling Integrated Optoelectronic Components". In: *Microwave and Millimeter-Wave Monolithic Circuits*. Vol. 87. 1. IEEE. 1987, pp. 39–41.
- [128] M. Koshiya, K. Hayata, and M. Suzuki. "Improved finite-element formulation in terms of the magnetic field vector for dielectric waveguides". In: *IEEE Transactions on Microwave Theory and Techniques* 33.3 (1985), pp. 227–233.
- [129] P. Kendall, P. McIlroy, and M. Stern. "Spectral index method for rib waveguide analysis". In: *Electronics Letters* 25.2 (1989), pp. 107–108.

- [130] M. S. Stern, P. C. Kendall, and P. W. A. McIlroy. "Analysis of the spectral index method for vector modes of rib waveguides". In: *IEE Proceedings J (Optoelectronics)* 137.1 (1990), pp. 21–26.
- [131] S. V. Burke. "Spectral index method applied to rib and strip-loaded directional couplers". In: *IEE Proceedings J (Optoelectronics)* 137.1 (1990), pp. 7–10.
- [132] J. R. P. Pola, W Biehlig, and F Lederer. "A generalization of the spectral index method toward multiple rib waveguides". In: *Journal of Lightwave Technology* 14.3 (1996), pp. 454–461.
- [133] A. S. Sudbø. "Why are accurate computations of mode fields in rectangular dielectric waveguides difficult?" In: *Journal of Lightwave Technology* 10.4 (1992), pp. 418–419.
- [134] U. Schulz and R. Pregla. "A new technique for the analysis of the dispersion characteristics of planar waveguides and its application to microstrips with tuning septums". In: *Radio Science* 16.6 (1981), pp. 1173–1178.
- [135] B. M. Sherrill and N. G. Alexopoulos. "The method of lines applied to a finline/strip configuration on an anisotropic substrate". In: *IEEE Transactions on Microwave Theory and Techniques* 35.6 (1987), pp. 568–575.
- [136] U Rogge and R Pregla. "Method of lines for the analysis of strip-loaded optical waveguides". In: *JOSA B* 8.2 (1991), pp. 459–463.
- [137] J. Gerdes, K. H. Helf, and R. Pregla. "Full-wave analysis of traveling-wave electrodes with finite thickness for electro-optic modulators by the method of lines". In: *Journal of Lightwave Technology* 9.4 (1991), pp. 461–467.
- [138] R Pregla. "Method of lines for the analysis of multilayered gyrotropic waveguide structures". In: *IEE Proceedings H (Microwaves, Antennas and Propagation)*. Vol. 140. 3. IET. 1993, pp. 183–192.
- [139] P. Berini and K. Wu. "Modeling lossy anisotropic dielectric waveguides with the method of lines". In: *IEEE Transactions on Microwave Theory and Techniques* 44.5 (1996), pp. 749–759.
- [140] R Pregla and E Ahlers. "Method of lines for analysis of discontinuities in optical waveguides". In: *Electronics Letters* 29.21 (1993), pp. 1845–1847.

- [141] K. Chiang. "Review of numerical and approximate methods for the modal analysis of general optical dielectric waveguides". In: *Optical and Quantum Electronics* 26.3 (1994), S113–S134.
- [142] M. Feit and J. Fleck. "Computation of mode properties in optical fiber waveguides by a propagating beam method". In: *Applied Optics* 19.7 (1980), pp. 1154–1164.
- [143] H. P. Nolting and R. März. "Results of benchmark tests for different numerical BPM algorithms". In: *Journal of Lightwave Technology* 13.2 (1995), pp. 216–224.
- [144] D. Yevick and B. Hermansson. "New formulations of the matrix beam propagation method: application to rib waveguides". In: *IEEE Journal of Quantum Electronics* 25.2 (1989), pp. 221–229.
- [145] P. A. Buah, B. M. A. Rahman, and K. T. V. Grattan. "Numerical study of soliton switching in active three-core nonlinear fiber couplers". In: *IEEE Journal of Quantum Electronics* 33.5 (1997), pp. 874–878.
- [146] T. Itoh. *Numerical Techniques for Microwave and Millimeter-wave Passive Structures*. Wiley-Interscience, 1989.
- [147] K. Yee. "Numerical solution of initial boundary value problems involving Maxwell's equations in isotropic media". In: *Antennas and Propagation, IEEE Transactions on* 14.3 (1966), pp. 302–307.
- [148] T. Weiland. "A discretization model for the solution of Maxwell's equations for six-component fields". In: *Archiv Elektronik und Uebertragungstechnik* 31 (1977), pp. 116–120.
- [149] M. C. T. Weiland. "Discrete electromagnetism with the finite integration technique". In: *Progress In Electromagnetics Research* 32 (2001), pp. 65–87.
- [150] M. Clemens and T. Weiland. "Magnetic field simulation using conformal FIT formulations". In: *Magnetics, IEEE Transactions on* 38.2 (2002), pp. 389–392.
- [151] D. Pinto and S. Obayya. "Accurate perfectly matched layer finite-volume time-domain method for photonic bandgap devices". In: *Photonics Technology Letters, IEEE* 20.5 (2008), pp. 339–341.
- [152] S. Obayya. *Computational photonics*. John Wiley & Sons, 2011.
- [153] M Koshiha, K Hayata, and M Suzuki. "Approximate scalar finite-element analysis of anisotropic optical waveguides". In: *Electronics Letters* 18.10 (1982), pp. 411–413.

- [154] A. Cangellaris, C. Lin, and K. Mei. "Point-matched time domain finite element methods for electromagnetic radiation and scattering". In: *Antennas and Propagation, IEEE Transactions on* 35.10 (1987), pp. 1160–1173.
- [155] M. Feliziani and E. Maradei. "Point matched finite element-time domain method using vector elements". In: *Magnetics, IEEE Transactions on* 30.5 (1994), pp. 3184–3187.
- [156] J. Lee, R. Lee, and A. Cangellaris. "Time-domain finite-element methods". In: *Antennas and Propagation, IEEE Transactions on* 45.3 (1997), pp. 430–442.
- [157] S. Obayya. "Efficient finite-element-based time-domain beam propagation analysis of optical integrated circuits". In: *Quantum Electronics, IEEE Journal of* 40.5 (2004), pp. 591–595.
- [158] F. Teixeira. "Time-Domain Finite-Difference and Finite-Element Methods for Maxwell Equations in Complex Media". In: *Antennas and Propagation, IEEE Transactions on* 56.8 (2008), pp. 2150–2166. ISSN: 0018-926X. DOI: 10.1109/TAP.2008.926767.
- [159] H. Songoro, M. Vogel, and Z. Cendes. "Keeping Time with Maxwell's Equations". In: *Microwave Magazine, IEEE* 11.2 (2010), pp. 42–49.
- [160] J. S. Hesthaven and T. Warburton. *Nodal discontinuous Galerkin methods: algorithms, analysis, and applications*. Vol. 54. Springer, 2007.
- [161] M. Koshiya, Y. Tsuji, and M. Hikari. "Time-domain beam propagation method and its application to photonic crystal circuits". In: *Journal of lightwave technology* 18.1 (2000), p. 102.
- [162] T. W. J.S. Hesthaven. *High-order/Spectral Methods on Unstructured Grids I. Time-domain Solution of Maxwell's Equations*. Tech. rep. 2001-6. Hampton, Virginia: ICASE NASA Langley Research Center, 2001.
- [163] S. Gedney and U. Navsariwala. "An unconditionally stable finite element time-domain solution of the vector wave equation". In: *Microwave and Guided Wave Letters, IEEE* 5.10 (1995), pp. 332–334.
- [164] J. M. Jin. *The Finite Element Method in Electromagnetics*. John Wiley & Sons, 2014.
- [165] R. März. *Integrated Optics: Design and Modeling*. Artech House on Demand, 1995.

- [166] N. Mabaya, P. E. Lagasse, and P. Vandenbulcke. "Finite Element Analysis Waveguides of Optical". In: *IEEE Transactions on Microwave Theory and Techniques* 29.6 (1981), pp. 600–605.
- [167] P. Daly. "Finite element approach to propagation in elliptical and parabolic waveguides". In: *International Journal for Numerical Methods in Engineering* 20.4 (1984), pp. 681–688.
- [168] R.-B. Wu and C. H. Chen. "A scalar variational conformal mapping technique for weakly guiding dielectric waveguides". In: *IEEE Journal of Quantum Electronics* 22.5 (1986), pp. 603–609.
- [169] M. Koshiya, K. Hayata, and M. Suzuki. "Approximate scalar finite-element analysis of anisotropic optical waveguides with off-diagonal elements in a permittivity tensor". In: *IEEE Transactions on Microwave Theory and Techniques* 32.6 (1984), pp. 587–593.
- [170] Z. J. Csendes and P. Silvester. "Numerical solution of dielectric loaded waveguides: I-finite-element analysis". In: *IEEE Transactions on Microwave Theory and Techniques* 18.12 (1970), pp. 1124–1131.
- [171] W. J. English and F. J. Young. "An E vector variational formulation of the Maxwell equations for cylindrical waveguide problems". In: *IEEE Transactions on Microwave Theory and Techniques* 19.1 (1971), pp. 40–46.
- [172] M. Hano. "Finite-element analysis of dielectric-loaded waveguides". In: *IEEE Transactions on Microwave Theory and Techniques* 32.10 (1984), pp. 1275–1279.
- [173] M. Koshiya, K. Hayata, and M. Suzuki. "Finite-element formulation in terms of the electric-field vector for electromagnetic waveguide problems". In: *IEEE Transactions on Microwave Theory and Techniques* 33.10 (1985), pp. 900–905.
- [174] B. M. A. Rahman and J. B. Davies. "Finite-element analysis of optical and microwave waveguide problems". In: *IEEE Transactions on Microwave Theory and Techniques* 32.1 (1984), pp. 20–28.
- [175] A. Berk. "Variational principles for electromagnetic resonators and waveguides". In: *IEEE Transactions on Antennas and Propagation* 4.2 (1956), pp. 104–111.
- [176] A. Konrad. "High-order triangular finite elements for electromagnetic waves in anisotropic media". In: *IEEE Transactions on Microwave Theory and Techniques* 25.5 (1977), pp. 353–360.

- [177] B. M. A. Rahman and J. B. Davies. "Penalty function improvement of waveguide solution by finite elements". In: *IEEE Transactions on Microwave Theory and Techniques* 32.8 (1984), pp. 922–928.
- [178] B. Rahman, M. Rahman, S Sriratanavaree, N Kejalakshmy, and K. Grat-tan. "Rigorous analysis of the transverse acoustic modes in optical waveg-uides by exploiting their structural symmetry". In: *Applied optics* 53.29 (2014), pp. 6797–6803.
- [179] B. Rahman and J. Davies. "Vector–H finite element solution of GaAs/GaAlAs rib waveguides". In: *IEE Proceedings J (Optoelectronics)* 132.6 (1985), pp. 349–353.
- [180] M. L. Brongersma, J. W. Hartman, and H. A. Atwater. "Electromagnetic energy transfer and switching in nanoparticle chain arrays below the diffraction limit". In: *Physical Review B* 62.24 (2000), R16356.
- [181] W. L. Barnes, A. Dereux, and T. W. Ebbesen. "Surface plasmon subwave-length optics". In: *Nature* 424.6950 (2003), pp. 824–830.
- [182] R. Zia, M. D. Selker, and M. L. Brongersma. "Leaky and bound modes of surface plasmon waveguides". In: *Physical Review B* 71.16 (2005), p. 165431.
- [183] H. Raether. *Surface Plasmons on Smooth Surfaces*. Springer, 1988.
- [184] B Steinberger, A Hohenau, H Ditlbacher, A. Stepanov, A Drezet, F. Aussenegg, A Leitner, and J. Krenn. "Dielectric stripes on gold as surface plasmon waveguides". In: *Applied Physics Letters* 88.9 (2006), pp. 94104–94104.
- [185] A. Krasavin and A. Zayats. "Passive photonic elements based on dielectric-loaded surface plasmon polariton waveguides". In: *Applied Physics Let-ters* 90.21 (2007), p. 211101.
- [186] V Giannini, Y Zhang, M Forcales, and J G mez Rivas. "Long-range sur-face polaritons in ultra-thin films of silicon". In: *Optics Express* 16.24 (2008), pp. 19674–19685.
- [187] R. F. Oulton, V. J. Sorger, D. Genov, D. Pile, and X Zhang. "A hybrid plasmonic waveguide for subwavelength confinement and long-range propagation". In: *Nature Photonics* 2.8 (2008), pp. 496–500.
- [188] S. A. Maier, P. G. Kik, H. A. Atwater, S. Meltzer, E. Harel, B. E. Koel, and A. A. Requicha. "Local detection of electromagnetic energy transport below the diffraction limit in metal nanoparticle plasmon waveguides". In: *Nature Materials* 2.4 (2003), pp. 229–232.

- [189] C. Themistos, B. M. A. Rahman, and K. T. V. Grattan. "Finite-element analysis of lossy TE–TM modes in metal-clad optical waveguides". In: *Applied Optics* 37.24 (1998), pp. 5747–5754.
- [190] Q. Cao and J. Jahns. "Azimuthally polarized surface plasmons as effective terahertz waveguides". In: *Optics Express* 13.2 (2005), pp. 511–518.
- [191] G Gallot, S. Jamison, R. McGowan, and D Grischkowsky. "Terahertz waveguides". In: *JOSA B* 17.5 (2000), pp. 851–863.
- [192] S. A. Maier and H. A. Atwater. "Plasmonics: Localization and guiding of electromagnetic energy in metal/dielectric structures". In: *Journal of Applied Physics* 98.1 (2005), p. 011101.
- [193] M. H. Huang, S. Mao, H. Feick, H. Yan, Y. Wu, H. Kind, E. Weber, R. Russo, and P. Yang. "Room-temperature ultraviolet nanowire nanolasers". In: *Science* 292.5523 (2001), pp. 1897–1899.
- [194] M. T. Hill, Y.-S. Oei, B. Smalbrugge, Y. Zhu, T. De Vries, P. J. Van Veldhoven, F. W. Van Otten, T. J. Eijkemans, J. P. Turkiewicz, H. De Waardt, et al. "Lasing in metallic-coated nanocavities". In: *Nature Photonics* 1.10 (2007), pp. 589–594.
- [195] B. S. Williams. "Terahertz quantum-cascade lasers". In: *Nature Photonics* 1.9 (2007), pp. 517–525.
- [196] P. Berini. "Plasmon-polariton waves guided by thin lossy metal films of finite width: Bound modes of symmetric structures". In: *Physical Review B* 61.15 (2000), p. 10484.
- [197] A. D. Boardman. *Electromagnetic Surface Modes*. John Wiley & Sons, 1982.
- [198] I Pockrand and H Raether. "Surface plasma oscillations at sinusoidal silver surfaces". In: *Applied Optics* 16.7 (1977), pp. 1784–1786.
- [199] G Kovacs. "Optical excitation of surface plasmon-polaritons in layered media". In: *Electromagnetic Surface Modes* (1982), pp. 143–200.
- [200] P Halevi and A. Boardman. *Electromagnetic surface modes*. 1982.
- [201] D. Nash and J. Sambles. "Surface plasmon-polariton study of the optical dielectric function of silver". In: *Journal of Modern Optics* 43.1 (1996), pp. 81–91.
- [202] E. Palik. "Handbook of Optical Constants of Solids II Academic". In: *New York* 19912 (1991).

- [203] Y. Wang, R. Islam, and G. V. Eleftheriades. "An ultra-short contra-directional coupler utilizing surface plasmon-polaritons at optical frequencies". In: *Optics Express* 14.16 (2006), pp. 7279–7290.
- [204] D. Dai, Y. Shi, and S. He. "Characteristic analysis of nanosilicon rectangular waveguides for planar light-wave circuits of high integration". In: *Applied Optics* 45.20 (2006), pp. 4941–4946.
- [205] F. F. Lu, T Li, J Xu, Z. Xie, L Li, S. N. Zhu, and Y. Y. Zhu. "Surface plasmon polariton enhanced by optical parametric amplification in nonlinear hybrid waveguide". In: *Optics Express* 19.4 (2011), pp. 2858–2865.
- [206] F Bahrami, M. Alam, J. Aitchison, and M Mojahedi. "Dual polarization measurements in the hybrid plasmonic biosensors". In: *Plasmonics* 8.2 (2013), pp. 465–473.
- [207] A. Shalabney and I. Abdulhalim. "Electromagnetic fields distribution in multilayer thin film structures and the origin of sensitivity enhancement in surface plasmon resonance sensors". In: *Sensors and Actuators A: Physical* 159.1 (2010), pp. 24–32.
- [208] A. V. Krasavin and A. V. Zayats. "Silicon-based plasmonic waveguides". In: *Optics Express* 18.11 (2010), pp. 11791–11799.
- [209] G. Veronis and S. Fan. "Guided subwavelength plasmonic mode supported by a slot in a thin metal film". In: *Optics Letters* 30.24 (2005), pp. 3359–3361.
- [210] M. Alam, J Meier, J. S. Aitchison, and M Mojahedi. "Propagation characteristics of hybrid modes supported by metal-low-high index waveguides and bends". In: *Optics Express* 18.12 (2010), pp. 12971–12979.
- [211] D. Dai and S. He. "A silicon-based hybrid plasmonic waveguide with a metal cap for a nano-scale light confinement". In: *Optics Express* 17.19 (2009), pp. 16646–16653.
- [212] M. Alam, J. S. Aitchison, and M. Mojahedi. "Compact hybrid TM-pass polarizer for silicon-on-insulator platform". In: *Applied Optics* 50.15 (2011), pp. 2294–2298.
- [213] C. Multiphysics. "version 4.2". In: *Heat Transfer Module* (2011).
- [214] P. B. Johnson and R.-W. Christy. "Optical constants of the noble metals". In: *Physical Review B* 6.12 (1972), p. 4370.
- [215] Q Chen, Z. Jiang, G. Xu, and X.-C. Zhang. "Near-field terahertz imaging with a dynamic aperture". In: *Optics Letters* 25.15 (2000), pp. 1122–1124.

- [216] R. H. Jacobsen, D. Mittleman, and M. Nuss. "Chemical recognition of gases and gas mixtures with terahertz waves". In: *Optics Letters* 21.24 (1996), pp. 2011–2013.
- [217] J. Zhang and D Grischkowsky. "Waveguide terahertz time-domain spectroscopy of nanometer water layers". In: *Optics Letters* 29.14 (2004), pp. 1617–1619.
- [218] C. Themistos, B. M. A. Rahman, M. Rajarajan, K. T. V. Grattan, B Bowden, and J. A. Harrington. "Characterization of silver/polystyrene (PS)-coated hollow glass waveguides at THz frequency". In: *Journal of Light-wave Technology* 25.9 (2007), pp. 2456–2462.
- [219] P. H. Siegel et al. "Terahertz technology". In: *IEEE Transactions on microwave theory and techniques* 50.3 (2002), pp. 910–928.
- [220] C. Yeh, F. Shimabukuro, and P. H. Siegel. "Low-loss terahertz ribbon waveguides". In: *Applied Optics* 44.28 (2005), pp. 5937–5946.
- [221] B. Ung, A. Dupuis, K. Stoeffler, C. Dubois, and M. Skorobogatiy. "High-refractive-index composite materials for terahertz waveguides: trade-off between index contrast and absorption loss". In: *JOSA B* 28.4 (2011), pp. 917–921.
- [222] C.-H. Lai, B. You, J.-Y. Lu, T.-A. Liu, J.-L. Peng, C.-K. Sun, and H.-C. Chang. "Modal characteristics of antiresonant reflecting pipe waveguides for terahertz waveguiding". In: *Optics Express* 18.1 (2010), pp. 309–322.
- [223] K. Nielsen, H. K. Rasmussen, A. J. Adam, P. C. Planken, O. Bang, and P. U. Jepsen. "Bendable, low-loss Topas fibers for the terahertz frequency range". In: *Optics Express* 17.10 (2009), pp. 8592–8601.
- [224] H Han, H Park, M Cho, and J Kim. "Terahertz pulse propagation in a plastic photonic crystal fiber". In: *Applied Physics Letters* 80.15 (2002), pp. 2634–2636.
- [225] A. Dupuis, A. Mazhorova, F. Désévéday, M. Rozé, and M. Skorobogatiy. "Spectral characterization of porous dielectric subwavelength THz fibers fabricated using a microstructured molding technique". In: *Optics Express* 18.13 (2010), pp. 13813–13828.

- [226] A. Dupuis, J.-F. Allard, D. Morris, K. Stoeffler, C. Dubois, and M. Skorobogatiy. "Fabrication and THz loss measurements of porous subwavelength fibers using a directional coupler method". In: *Optics Express* 17.10 (2009), pp. 8012–8028.
- [227] A. Hassani, A. Dupuis, and M. Skorobogatiy. "Low loss porous terahertz fibers containing multiple subwavelength holes". In: *Applied Physics Letters* 92.7 (2008), p. 071101.
- [228] M. Skorobogatiy and A. Dupuis. "Ferroelectric all-polymer hollow Bragg fibers for terahertz guidance". In: *Applied Physics Letters* 90.11 (2007), p. 113514.
- [229] T. Ito, Y. Matsuura, M. Miyagi, H. Minamide, and H. Ito. "Flexible terahertz fiber optics with low bend-induced losses". In: *JOSA B* 24.5 (2007), pp. 1230–1235.
- [230] J. Harrington, R. George, P. Pedersen, and E. Mueller. "Hollow polycarbonate waveguides with inner Cu coatings for delivery of terahertz radiation". In: *Optics Express* 12.21 (2004), pp. 5263–5268.
- [231] B. Bowden, J. A. Harrington, and O. Mitrofanov. "Silver/polystyrene-coated hollow glass waveguides for the transmission of terahertz radiation". In: *Optics Letters* 32.20 (2007), pp. 2945–2947.
- [232] T. Hidaka, H. Minamide, H. Ito, J.-i. Nishizawa, K. Tamura, and S. Ichikawa. "Ferroelectric PVDF cladding terahertz waveguide". In: *Journal of Lightwave Technology* 23.8 (2005), p. 2469.
- [233] M Miyagi and S Karasawa. "A comparative study of rectangular and circular dielectric-coated metallic waveguides for CO₂ laser light: Theory". In: *Optics Communications* 68.1 (1988), pp. 18–20.
- [234] H. Machida, Y. Matsuura, H. Ishikawa, and M. Miyagi. "Transmission properties of rectangular hollow waveguides for CO₂ laser light". In: *Applied Optics* 31.36 (1992), pp. 7617–7622.
- [235] M. Ordal, L. Long, R. Bell, S. Bell, R. Bell, R. Alexander, and C. Ward. "Optical properties of the metals al, co, cu, au, fe, pb, ni, pd, pt, ag, ti, and w in the infrared and far infrared". In: *Applied Optics* 22.7 (1983), pp. 1099–1119.
- [236] K. H. Schlereth and M Tacke. "The complex propagation constant of multilayer waveguides-An algorithm for a personal computer". In: *IEEE Journal of Quantum Electronics* 26 (1990), pp. 627–630.

- [237] Y.-S. Jin, G.-J. Kim, and S.-G. Jeon. "Terahertz dielectric properties of polymers". In: (2006).
- [238] C. Winnewisser, F. Lewen, and H. Helm. "Transmission characteristics of dichroic filters measured by THz time-domain spectroscopy". In: *Applied Physics A: Materials Science & Processing* 66.6 (1998), pp. 593–598.
- [239] R. W. McGowan, G Gallot, and D Grischkowsky. "Propagation of ultrawideband short pulses of terahertz radiation through submillimeter-diameter circular waveguides". In: *Optics Letters* 24.20 (1999), pp. 1431–1433.
- [240] B. E. Little, S. T. Chu, H. A. Haus, J Foresi, and J.-P. Laine. "Microring resonator channel dropping filters". In: *Journal of Lightwave Technology* 15.6 (1997), pp. 998–1005.
- [241] M Zirngibl, C. H. Joyner, L. Stulz, T. Gaiffe, and C Dragone. "Polarisation independent 8×8 waveguide grating multiplexer on InP". In: *Electronics Letters* 29.2 (1993), pp. 201–202.
- [242] R. R. Hayes and D. Yap. "GaAs spiral optical waveguides for delay-line applications". In: *Journal of Lightwave Technology* 11.3 (1993), pp. 523–528.
- [243] X. Jiang, W. Qi, H. Zhang, Y. Tang, Y. Hao, J. Yang, and M. Wang. "Low crosstalk $1/\text{spl times}/2$ thermo-optic digital optical switch with integrated S-bend attenuator". In: *IEEE Photonics Technology Letters* 18.4 (2006), pp. 610–612.
- [244] W. Gambling, H. Matsumura, and C. Ragdale. "Field deformation in a curved single-mode fibre". In: *Electronics Letters* 14.5 (1978), pp. 130–132.
- [245] M. Heiblum and J. H. Harris. "Analysis of curved optical waveguides by conformal transformation". In: *IEEE Journal of Quantum Electronics* 11 (1975), pp. 75–83.
- [246] B. M. A. Rahman, A. Quadir, H. Tanvir, and K. T. V. Grattan. "Characterization of plasmonic modes in a low-loss dielectric-coated hollow core rectangular waveguide at terahertz frequency". In: *IEEE Photonics Journal* 3.6 (2011), pp. 1054–1066.
- [247] S. A. Maier, P. E. Barclay, T. J. Johnson, M. D. Friedman, and O. Painter. "Low-loss fiber accessible plasmon waveguide for planar energy guiding and sensing". In: *Applied Physics Letters* 84.20 (2004), pp. 3990–3992.

-
- [248] H Ditlbacher, N Galler, D. Koller, A Hohenau, A Leitner, F. Aussenegg, and J. Krenn. "Coupling dielectric waveguide modes to surface plasmon polaritons". In: *Optics express* 16.14 (2008), pp. 10455–10464.
- [249] S Hayashi, D. Nesterenko, and Z Sekkat. "Waveguide-coupled surface plasmon resonance sensor structures: Fano lineshape engineering for ultrahigh-resolution sensing". In: *Journal of Physics D: Applied Physics* 48.32 (2015), p. 325303.